

Artificial Intelligence in *Medical Imaging*

Artif Intell Med Imaging 2020 June 28; 1(1): 1-69





Artificial Intelligence in Medical Imaging

Contents

Bimonthly Volume 1 Number 1 June 28, 2020

EDITORIAL

- 1 Rising role of artificial intelligence in image reconstruction for biomedical imaging
Chen XL, Yan TY, Wang N, von Deneen KM

REVIEW

- 6 Breast dynamic contrast-enhanced-magnetic resonance imaging and radiomics: State of art
Orlando A, Dimarco M, Cannella R, Bartolotta TV

MINIREVIEWS

- 19 Artificial intelligence in pancreatic disease
Chen BB
- 31 Machine learning for diagnosis of coronary artery disease in computed tomography angiography: A survey
Zhao FJ, Fan SQ, Ren JF, von Deneen KM, He XW, Chen XL
- 40 Acute pancreatitis: A pictorial review of early pancreatic fluid collections
Xiao B

ORIGINAL ARTICLE

Basic Study

- 50 Acoustic concept based on an autonomous capsule and a wideband concentric ring resonator for pathophysiological prevention
Medjdoub A, Lefebvre F, Saad N, Soudani S, Nassar G

CASE REPORT

- 65 Cerebral amyloid angiopathy vs Alzheimer's dementia: Diagnostic conundrum
Arberry J, Singh S, Mizoguchi RA

ABOUT COVER

Editor-in-Chief of *Artificial Intelligence in Medical Imaging*, Professor Xue-Li Chen is an expert in the field of biomedical photonics imaging as well as its application in early detection and accurate diagnosis of gastric cancer. Professor Chen has co-led the development of Cerenkov luminescence endoscope and further explored the application in early detection of clinical gastrointestinal tumors. Professor Chen has also developed the stimulated Raman projection tomography technology which can perform the volumetric imaging of single cells in a label-free manner. Professor Chen has served as the member of SPIE, OSA, IEEE, and as a committee member of the Branch of Contrast Technology in China Medicinal Biotech Association, the Nuclear Medicine Committee of Shaanxi Cancer Association, and the Shaanxi Society of Biomedical Engineering.

AIMS AND SCOPE

The primary aim of *Artificial Intelligence in Medical Imaging* (AIMI, *Artif Intell Med Imaging*) is to provide scholars and readers from various fields of artificial intelligence in medical imaging with a platform to publish high-quality basic and clinical research articles and communicate their research findings online.

AIMI mainly publishes articles reporting research results obtained in the field of artificial intelligence in medical imaging and covering a wide range of topics, including artificial intelligence in radiology, pathology image analysis, endoscopy, molecular imaging, and ultrasonography.

INDEXING/ABSTRACTING

There is currently no indexing.

RESPONSIBLE EDITORS FOR THIS ISSUE

Electronic Editor: *Yan-Xia Xing*, Production Department Director: *Yun-Xiaojuan Wu*, Editorial Office Director: *Jin-Lei Wang*.

NAME OF JOURNAL

Artificial Intelligence in Medical Imaging

ISSN

ISSN 2644-3260 (online)

LAUNCH DATE

June 28, 2020

FREQUENCY

Bimonthly

EDITORS-IN-CHIEF

Xue-Li Chen, Ahmed Abd El-Razek, Jun Shen

EDITORIAL BOARD MEMBERS

<https://www.wjgnet.com/2644-3260/editorialboard.htm>

PUBLICATION DATE

June 28, 2020

COPYRIGHT

© 2020 Baishideng Publishing Group Inc

INSTRUCTIONS TO AUTHORS

<https://www.wjgnet.com/bpg/gerinfo/204>

GUIDELINES FOR ETHICS DOCUMENTS

<https://www.wjgnet.com/bpg/GerInfo/287>

GUIDELINES FOR NON-NATIVE SPEAKERS OF ENGLISH

<https://www.wjgnet.com/bpg/gerinfo/240>

PUBLICATION ETHICS

<https://www.wjgnet.com/bpg/GerInfo/288>

PUBLICATION MISCONDUCT

<https://www.wjgnet.com/bpg/gerinfo/208>

ARTICLE PROCESSING CHARGE

<https://www.wjgnet.com/bpg/gerinfo/242>

STEPS FOR SUBMITTING MANUSCRIPTS

<https://www.wjgnet.com/bpg/GerInfo/239>

ONLINE SUBMISSION

<https://www.f6publishing.com>

Rising role of artificial intelligence in image reconstruction for biomedical imaging

Xue-Li Chen, Tian-Yu Yan, Nan Wang, Karen M von Deneen

ORCID number: Xue-Li Chen [0000-0002-3898-9892](https://orcid.org/0000-0002-3898-9892); Tian-Yu Yan [0000-0002-2245-1537](https://orcid.org/0000-0002-2245-1537); Nan Wang [0000-0002-6780-3401](https://orcid.org/0000-0002-6780-3401); Karen M von Deneen [0000-0002-5310-1003](https://orcid.org/0000-0002-5310-1003).

Author contributions: Chen XL designed the overall outline of the manuscript; Yan TY and Wang N performed the literature review and summary; Chen XL contributed to the writing and editing of the manuscript; von Deneen KM polished the language of the paper.

Supported by The National Key R&D Program of China, No. 2018YFC0910600; the National Natural Science Foundation of China No. 81627807 and 11727813; Shaanxi Science Funds for Distinguished Young Scholars, No. 2020JC-27; the Fok Ying Tung Education Foundation, No. 161104; and Program for the Young Top-notch Talent of Shaanxi Province.

Conflict-of-interest statement: The authors declare that they have no conflicts of interest.

Open-Access: This article is an open-access article that was selected by an in-house editor and fully peer-reviewed by external reviewers. It is distributed in accordance with the Creative Commons Attribution NonCommercial (CC BY-NC 4.0)

Xue-Li Chen, Tian-Yu Yan, Nan Wang, Karen M von Deneen, Engineering Research Center of Molecular and Neuro Imaging of Ministry of Education, School of Life Science and Technology, Xidian University, Xi'an 710126, Shaanxi Province, China

Corresponding author: Xue-Li Chen, PhD, Professor, Engineering Research Center of Molecular and Neuro Imaging of Ministry of Education, School of Life Science and Technology, Xidian University, No. 266, Xinglong Section of Xifeng Road, Xi'an 710126, Shaanxi Province, China. xlchen@xidian.edu.cn

Abstract

In this editorial, we review recent progress on the applications of artificial intelligence (AI) in image reconstruction for biomedical imaging. Because it abandons prior information of traditional artificial design and adopts a completely data-driven mode to obtain deeper prior information *via* learning, AI technology plays an increasingly important role in biomedical image reconstruction. The combination of AI technology and the biomedical image reconstruction method has become a hotspot in the field. Favoring AI, the performance of biomedical image reconstruction has been improved in terms of accuracy, resolution, imaging speed, *etc*. We specifically focus on how to use AI technology to improve the performance of biomedical image reconstruction, and propose possible future directions in this field.

Key words: Biomedical imaging; Image reconstruction; Artificial intelligence; Machine learning; Deep learning; Tomography

©The Author(s) 2020. Published by Baishideng Publishing Group Inc. All rights reserved.

Core tip: Three-dimensional biomedical imaging plays an important role in biology and medicine. We review recent progress on the applications of artificial intelligence (AI) in image reconstruction for biomedical imaging. We specifically focus on how to use AI technology to improve the performance of biomedical image reconstruction and propose possible future directions in this field. We believe that, with further development, AI technology will play an increasingly important role in biomedical image reconstruction.

Citation: Chen XL, Yan TY, Wang N, von Deneen KM. Rising role of artificial intelligence in

license, which permits others to distribute, remix, adapt, build upon this work non-commercially, and license their derivative works on different terms, provided the original work is properly cited and the use is non-commercial. See: <http://creativecommons.org/licenses/by-nc/4.0/>

Manuscript source: Invited manuscript

Received: May 7, 2020

Peer-review started: May 7, 2020

First decision: May 15, 2020

Revised: June 9, 2020

Accepted: June 17, 2020

Article in press: June 17, 2020

Published online: June 28, 2020

P-Reviewer: Tomizawa N

S-Editor: Wang JL

L-Editor: Filipodia

E-Editor: Ma YJ



image reconstruction for biomedical imaging. *Artif Intell Med Imaging* 2020; 1(1): 1-5

URL: <https://www.wjgnet.com/2644-3260/full/v1/i1/1.htm>

DOI: <https://dx.doi.org/10.35711/aimi.v1.i1.1>

BACKGROUND

Biomedical imaging plays an important role in biology and medicine. In particular, three-dimensional (3D) imaging mode based on an image reconstruction technique, such as computed tomography (CT), magnetic resonance imaging (MRI), positron emission tomography (PET), photoacoustic tomography (PAT), and 3D optical imaging, allow biologists and physicians to visualize the structural, cellular, and functional information stereoscopically. Image reconstruction in 3D biomedical imaging is a type of inverse problem, which is used to reconstruct the distribution of this information in the living body by using the physical signals acquired from outside of the body. Research on the image reconstruction algorithm has always been an important issue to promote the development and innovation of biomedical imaging equipment. However, due to several reasons, such as the limitation of imaging time and dose (contrast medium or radiation dose), insufficiency of the measurements, inherent noise and other interference doping in the original signals, the traditional image reconstruction techniques cannot achieve good performance. For example, there are trade-offs in optimal imaging accuracy, spatial resolution and imaging speed, which have been challenges in the field of biomedical image reconstruction. The rapid development of artificial intelligence (AI) technology brings new opportunities for biomedical image reconstruction. AI abandons prior information of traditional artificial design, and adopts a completely data-driven mode to obtain deeper prior information *via* learning. Currently, the combination of AI and the biomedical image reconstruction method has become a hotspot in the field.

ADVANCES

Recently, AI plays an increasingly important role in image reconstruction of 3D biomedical imaging, including both clinical and preclinical biomedical imaging technologies such as CT, MRI, PET, PAT, and 3D optical imaging. In CT reconstruction, AI technology mainly focuses on solving two problems: CT reconstruction with low radiation dose and CT reconstruction with a small amount of view measurements^[1-6]. For example, Chen *et al*^[1] integrated the autoencoder, deconvolution network, and shortcut connections into the residual encoder-decoder convolutional natural network for low-dose CT imaging, which demonstrated great potential for high-speed imaging with good noise reduction, structural preservation, and lesion detection. For CT reconstruction with a small amount of view measurements, it mainly involves a small amount of view reconstruction based on limited angles^[2-4] and sparse view reconstruction based on full angles^[5-7]. With the help of the deep learning framework, researchers can obtain a much clearer edge and fine structural information through a small amount of measured data, to achieve the best imaging quality with faster imaging speed^[5-7]. The use of AI technology in MRI image reconstruction has attracted an increasing amount of attention, and much progress has been made in recent years. In these works, by means of machine learning or deep learning framework, MRI image reconstruction can be much improved by reducing noise or artifacts^[8], enhancing spatial resolution or details^[9-12], accelerating imaging speed^[13-16], and improving image accuracy and quality^[17-21]. AI-based image reconstruction techniques have also been applied to clinical studies, for example the TrueFidelity^[22], a deep learning-based image processing platform developed by General Electric Healthcare and the Advanced intelligent clear-IQ Engine^[23], developed by Canon Medical Systems Corporation.

In functional or molecular imaging, AI technology is mainly used to improve the quality of reconstructed images^[24-38]. For example, by using AI technology, high-quality PET images can be reconstructed from low-dose and ultra-low-dose radionuclides^[24,25]. The whole neural network can solve the storage space challenge in PET and realize the direct reconstruction of large-scale data^[28]. With the help of machine learning and deep learning frameworks, the problems existing in PAT image reconstruction caused by limited views or sparse view measurements, including resolution and image quality

degradation, can be solved^[29-33]. In diffuse light-based 3D optical imaging, it is necessary to establish a mathematical model to describe diffused light propagation in the living body, and then to calculate the target distribution by solving the model in reverse^[39,40]. However, this mathematical model is usually a simplified linear model that has serious ill-posedness, which results in poor quality of reconstructed images. With the help of the deep learning framework by directly learning the complicated relationship between surface measurements and target distribution inside the body, the quality of the reconstructed image can be greatly improved and the reconstruction time can be reduced^[34-38].

OUTLOOK

We present recent progresses on AI-based image reconstruction for 3D biomedical imaging. The rising role of AI in image reconstruction includes improving the quality, accuracy, and resolution of the reconstructed image as well as the imaging speed. Furthermore, with the rapid development of AI technology, such a rising role will become increasingly significant. However, there remain several central challenges facing the field. The first one is the generality of machine learning or the deep learning framework. In existing studies, the frameworks are all aimed at specific problems, such as image objects with specific features. Thus, generalization performance and the migration ability of the framework are poor. If a network framework can be developed, which can provide good image reconstruction performance for the imaging objects with various structures and properties, even for all of the biomedical imaging technologies, it will be great progress on AI-based image reconstruction for biomedical imaging. Second, current research needs to use AI technology to reconstruct the measured data into images, and then analyze these images to obtain relevant physiological or pathological information. With the help of AI, it will be significant to obtain physiological and pathological information directly from the measured data, which is also the future direction of the application of AI technology in the field of biomedical imaging. Lastly, the development of machine learning or the deep learning algorithm itself is also an important direction in the field. These efforts are expected to promote the wide applications of AI-based biomedical imaging in biology and medicine.

REFERENCES

- 1 **Chen H**, Zhang Y, Kalra MK, Lin F, Chen Y, Liao P, Zhou J, Wang G. Low-Dose CT With a Residual Encoder-Decoder Convolutional Neural Network. *IEEE Trans Med Imaging* 2017; **36**: 2524-2535 [PMID: 28622671 DOI: 10.1109/TMI.2017.2715284]
- 2 **Jiang Z**, Chen Y, Zhang Y, Ge Y, Yin FF, Ren L. Augmentation of CBCT Reconstructed From Under-Sampled Projections Using Deep Learning. *IEEE Trans Med Imaging* 2019; **38**: 2705-2715 [PMID: 31021791 DOI: 10.1109/TMI.2019.2912791]
- 3 **Bubba TA**, Kutyniok G, Lasses M, Marz M, Samek W, Siltanen S, Srinivasan V. Learning the invisible: a hybrid deep learning-shearlet framework for limited angle computed tomography. *Inverse Probl* 2019; **35**: 064002 [DOI: 10.1088/1361-6420/ab10ca]
- 4 **Fu J**, Dong J, Zhao F. A Deep Learning Reconstruction Framework for Differential Phase-Contrast Computed Tomography With Incomplete Data. *IEEE Trans Image Process* 2020; **29**: 2190-2202 [PMID: 31647435 DOI: 10.1109/TIP.2019.2947790]
- 5 **Kyong Hwan Jin**, McCann MT, Froustey E, Unser M. Deep Convolutional Neural Network for Inverse Problems in Imaging. *IEEE Trans Image Process* 2017; **26**: 4509-4522 [PMID: 28641250 DOI: 10.1109/TIP.2017.2713099]
- 6 **Han Y**, Ye JC. Framing U-Net via Deep Convolutional Framelets: Application to Sparse-View CT. *IEEE Trans Med Imaging* 2018; **37**: 1418-1429 [PMID: 29870370 DOI: 10.1109/TMI.2018.2823768]
- 7 **Nakai H**, Nishio M, Yamashita R, Ono A, Nakao KK, Fujimoto K, Togashi K. Quantitative and Qualitative Evaluation of Convolutional Neural Networks with a Deeper U-Net for Sparse-View Computed Tomography Reconstruction. *Acad Radiol* 2020; **27**: 563-574 [PMID: 31281082 DOI: 10.1016/j.acra.2019.05.016]
- 8 **Zhu B**, Liu JZ, Cauley SF, Rosen BR, Rosen MS. Image reconstruction by domain-transform manifold learning. *Nature* 2018; **555**: 487-492 [PMID: 29565357 DOI: 10.1038/nature25988]
- 9 **Chaudhari AS**, Fang Z, Kogan F, Wood J, Stevens KJ, Gibbons EK, Lee JH, Gold GE, Hargreaves BA. Super-resolution musculoskeletal MRI using deep learning. *Magn Reson Med* 2018; **80**: 2139-2154 [PMID: 29582464 DOI: 10.1002/mrm.27178]
- 10 **Sun L**, Fan Z, Fu X, Huang Y, Ding X, Paisley J. A Deep Information Sharing Network for Multi-Contrast Compressed Sensing MRI Reconstruction. *IEEE Trans Image Process* 2019; **28**: 6141-6153 [PMID: 31295112 DOI: 10.1109/TIP.2019.2925288]
- 11 **Shi J**, Li Z, Ying S, Wang C, Liu Q, Zhang Q, Yan P. MR Image Super-Resolution via Wide Residual

- Networks With Fixed Skip Connection. *IEEE J Biomed Health Inform* 2019; **23**: 1129-1140 [PMID: 29993565 DOI: [10.1109/JBHI.2018.2843819](https://doi.org/10.1109/JBHI.2018.2843819)]
- 12 **Zhang J**, Gu Y, Tang H, Wang X, Kong Y, Chen Y, Shu H, Coatrieux J. Compressed sensing MR image reconstruction via a deep frequency-division network. *Neurocomputing* 2020; **384**: 346-355 [DOI: [10.1016/j.neucom.2019.12.011](https://doi.org/10.1016/j.neucom.2019.12.011)]
 - 13 **Yang G**, Yu S, Dong H, Slabaugh G, Dragotti PL, Ye X, Liu F, Arridge S, Keegan J, Guo Y, Firmin D, Keegan J, Slabaugh G, Arridge S, Ye X, Guo Y, Yu S, Liu F, Firmin D, Dragotti PL, Yang G, Dong H. DAGAN: Deep De-Aliasing Generative Adversarial Networks for Fast Compressed Sensing MRI Reconstruction. *IEEE Trans Med Imaging* 2018; **37**: 1310-1321 [PMID: 29870361 DOI: [10.1109/TMI.2017.2785879](https://doi.org/10.1109/TMI.2017.2785879)]
 - 14 **Lee D**, Yoo J, Tak S, Ye JC. Deep Residual Learning for Accelerated MRI Using Magnitude and Phase Networks. *IEEE Trans Biomed Eng* 2018; **65**: 1985-1995 [PMID: 29993390 DOI: [10.1109/TBME.2018.2821699](https://doi.org/10.1109/TBME.2018.2821699)]
 - 15 **Xiang L**, Chen Y, Chang W, Zhan Y, Lin W, Wang Q, Shen D. Deep Learning Based Multi-Modal Fusion for Fast MR Reconstruction. *IEEE Trans Biomed Eng* 2019; **66**: 2105-2114 [PMID: 30507491 DOI: [10.1109/TBME.2018.2883958](https://doi.org/10.1109/TBME.2018.2883958)]
 - 16 **Zhang J**, Wu J, Chen S, Zhang Z, Cai S, Cai C, Chen Z. Robust Single-Shot T₂ Mapping via Multiple Overlapping-Echo Acquisition and Deep Neural Network. *IEEE Trans Med Imaging* 2019; **38**: 1801-1811 [PMID: 30714913 DOI: [10.1109/TMI.2019.2896085](https://doi.org/10.1109/TMI.2019.2896085)]
 - 17 **Schlemper J**, Caballero J, Hajnal JV, Price AN, Rueckert D. A Deep Cascade of Convolutional Neural Networks for Dynamic MR Image Reconstruction. *IEEE Trans Med Imaging* 2018; **37**: 491-503 [PMID: 29035212 DOI: [10.1109/TMI.2017.2760978](https://doi.org/10.1109/TMI.2017.2760978)]
 - 18 **Quan TM**, Nguyen-Duc T, Jeong WK. Compressed Sensing MRI Reconstruction Using a Generative Adversarial Network With a Cyclic Loss. *IEEE Trans Med Imaging* 2018; **37**: 1488-1497 [PMID: 29870376 DOI: [10.1109/TMI.2018.2820120](https://doi.org/10.1109/TMI.2018.2820120)]
 - 19 **Mardani M**, Gong E, Cheng JY, Vasanawala SS, Zaharchuk G, Xing L, Pauly JM. Deep Generative Adversarial Neural Networks for Compressive Sensing MRI. *IEEE Trans Med Imaging* 2019; **38**: 167-179 [PMID: 30040634 DOI: [10.1109/TMI.2018.2858752](https://doi.org/10.1109/TMI.2018.2858752)]
 - 20 **Qin C**, Schlemper J, Caballero J, Price AN, Hajnal JV, Rueckert D. Convolutional Recurrent Neural Networks for Dynamic MR Image Reconstruction. *IEEE Trans Med Imaging* 2019; **38**: 280-290 [PMID: 30080145 DOI: [10.1109/TMI.2018.2863670](https://doi.org/10.1109/TMI.2018.2863670)]
 - 21 **Kofler A**, Dewey M, Schaeffter T, Wald C, Kolbitsch C. Spatio-Temporal Deep Learning-Based Undersampling Artefact Reduction for 2D Radial Cine MRI With Limited Training Data. *IEEE Trans Med Imaging* 2020; **39**: 703-717 [PMID: 31403407 DOI: [10.1109/TMI.2019.2930318](https://doi.org/10.1109/TMI.2019.2930318)]
 - 22 **Hsieh J**, Liu E, Nett B, Tang J, Thibault JB, Sahney S. A new era of image reconstruction: TrueFidelityTM - Technical white paper on deep learning imaging reconstruction. New York: General Electric Company, 2019: 1-14
 - 23 **Boedeker K**. AiCE deep learning reconstruction: bringing the power of ultra-high resolution CT to routine imaging. Tochigi: Canon Medical Systems Corporation, 2019
 - 24 **Kim K**, Wu D, Gong K, Dutta J, Kim JH, Son YD, Kim HK, El Fakhri G, Li Q. Penalized PET Reconstruction Using Deep Learning Prior and Local Linear Fitting. *IEEE Trans Med Imaging* 2018; **37**: 1478-1487 [PMID: 29870375 DOI: [10.1109/TMI.2018.2832613](https://doi.org/10.1109/TMI.2018.2832613)]
 - 25 **Ouyang J**, Chen KT, Gong E, Pauly J, Zaharchuk G. Ultra-low-dose PET reconstruction using generative adversarial network with feature matching and task-specific perceptual loss. *Med Phys* 2019; **46**: 3555-3564 [PMID: 31131901 DOI: [10.1002/mp.13626](https://doi.org/10.1002/mp.13626)]
 - 26 **Xu J**, Liu H. Three-dimensional convolutional neural networks for simultaneous dual-tracer PET imaging. *Phys Med Biol* 2019; **64**: 185016 [PMID: 31292287 DOI: [10.1088/1361-6560/ab3103](https://doi.org/10.1088/1361-6560/ab3103)]
 - 27 **Gong K**, Catana C, Qi J, Li Q. PET Image Reconstruction Using Deep Image Prior. *IEEE Trans Med Imaging* 2019; **38**: 1655-1665 [PMID: 30575530 DOI: [10.1109/TMI.2018.2888491](https://doi.org/10.1109/TMI.2018.2888491)]
 - 28 **Whiteley W**, Luk WK, Gregor J. DirectPET: full-size neural network PET reconstruction from sinogram data. *J Med Imaging (Bellingham)* 2020; **7**: 032503 [PMID: 32206686 DOI: [10.1117/1.JMI.7.3.032503](https://doi.org/10.1117/1.JMI.7.3.032503)]
 - 29 **Antholzer S**, Haltmeier M, Schwab J. Deep learning for photoacoustic tomography from sparse data. *Inverse Probl Sci Eng* 2019; **27**: 987-1005 [PMID: 31057659 DOI: [10.1080/17415977.2018.1518444](https://doi.org/10.1080/17415977.2018.1518444)]
 - 30 **Waibel D**, Grohl J, Isensee F, Kirchner T, Maier-Hein K, Maier-Hein L. Reconstruction of initial pressure from limited view photoacoustic images using deep learning. *Oraevsky A, Wang L, editors. Photons Plus Ultrasound: Imaging and Sensing*. SPIE 2018; 104942S [DOI: [10.1117/12.2288353](https://doi.org/10.1117/12.2288353)]
 - 31 **Hauptmann A**, Lucka F, Betcke M, Huynh N, Adler J, Cox B, Beard P, Ourselin S, Arridge S. Model-Based Learning for Accelerated, Limited-View 3-D Photoacoustic Tomography. *IEEE Trans Med Imaging* 2018; **37**: 1382-1393 [PMID: 29870367 DOI: [10.1109/TMI.2018.2820382](https://doi.org/10.1109/TMI.2018.2820382)]
 - 32 **Deng H**, Wang X, Cai C, Luo J, Ma C. Machine-learning enhanced photoacoustic computed tomography in a limited view configuration. In: Yuan XC, Carney PS, Shi K, Somekh MG, editors. *Advanced Optical Imaging Technologies II*. SPIE 2019; 111860J [DOI: [10.1117/12.2539148](https://doi.org/10.1117/12.2539148)]
 - 33 **Vu T**, Li M, Humayun H, Zhou Y, Yao J. A generative adversarial network for artifact removal in photoacoustic computed tomography with a linear-array transducer. *Exp Biol Med (Maywood)* 2020; **245**: 597-605 [PMID: 32208974 DOI: [10.1177/1535370220914285](https://doi.org/10.1177/1535370220914285)]
 - 34 **Gao Y**, Wang K, An Y, Jiang SX, Meng H, Tian J. Non model-based bioluminescence tomography using a machine-learning reconstruction strategy. *Optica* 2018; **5**: 1451-1454 [DOI: [10.1364/OPTICA.5.001451](https://doi.org/10.1364/OPTICA.5.001451)]
 - 35 **Guo L**, Liu F, Cai C, Liu J, Zhang G. 3D deep encoder-decoder network for fluorescence molecular tomography. *Opt Lett* 2019; **44**: 1892-1895 [PMID: 30985768 DOI: [10.1364/OL.44.001892](https://doi.org/10.1364/OL.44.001892)]
 - 36 **Zhang Z**, Cai M, Gao Y, Shi X, Zhang X, Hu Z, Tian J. A novel Cerenkov luminescence tomography approach using multilayer fully connected neural network. *Phys Med Biol* 2019; **64**: 245010 [PMID: 31770734 DOI: [10.1088/1361-6560/ab5bb4](https://doi.org/10.1088/1361-6560/ab5bb4)]
 - 37 **Li DS**, Chen CX, Li JF, Yan Q. Reconstruction of fluorescence molecular tomography based on graph convolution networks. *J Opt* 2020; **22**: 045602 [DOI: [10.1088/2040-8986/ab76a5](https://doi.org/10.1088/2040-8986/ab76a5)]

- 38 **Yoo J**, Sabir S, Heo D, Kim KH, Wahab A, Choi Y, Lee SI, Chae EY, Kim HH, Bae YM, Choi YW, Cho S, Ye JC. Deep Learning Diffuse Optical Tomography. *IEEE Trans Med Imaging* 2020; **39**: 877-887 [PMID: 31442973 DOI: 10.1109/TMI.2019.2936522]
- 39 **Cong W**, Wang G, Kumar D, Liu Y, Jiang M, Wang L, Hoffman E, McLennan G, McCray P, Zabner J, Cong A. Practical reconstruction method for bioluminescence tomography. *Opt Express* 2005; **13**: 6756-6771 [PMID: 19498692 DOI: 10.1364/OPEX.13.006756]
- 40 **Darne C**, Lu Y, Sevik-Muraca EM. Small animal fluorescence and bioluminescence tomography: a review of approaches, algorithms and technology update. *Phys Med Biol* 2014; **59**: R1-64 [PMID: 24334634 DOI: 10.1088/0031-9155/59/1/R1]

Breast dynamic contrast-enhanced-magnetic resonance imaging and radiomics: State of art

Alessia Orlando, Mariangela Dimarco, Roberto Cannella, Tommaso Vincenzo Bartolotta

ORCID number: Alessia Orlando 0000-0001-9048-1730; Mariangela Dimarco 0000-0003-0931-2302; Roberto Cannella 0000-0002-3808-0785; Tommaso Vincenzo Bartolotta 0000-0002-8808-379X.

Author contributions: Orlando A and Dimarco M wrote and revised the manuscript for important intellectual content; Cannella R and Bartolotta TV made critical revisions related to important intellectual content of the manuscript; all the authors approved the final version of the article.

Conflict-of-interest statement: No conflict of interests.

Open-Access: This article is an open-access article that was selected by an in-house editor and fully peer-reviewed by external reviewers. It is distributed in accordance with the Creative Commons Attribution NonCommercial (CC BY-NC 4.0) license, which permits others to distribute, remix, adapt, build upon this work non-commercially, and license their derivative works on different terms, provided the original work is properly cited and the use is non-commercial. See: <http://creativecommons.org/licenses/by-nc/4.0/>

Manuscript source: Invited

Alessia Orlando, Mariangela Dimarco, Roberto Cannella, Tommaso Vincenzo Bartolotta, Section of Radiology - BiND, University Hospital "Paolo Giaccone", Palermo 90127, Italy

Tommaso Vincenzo Bartolotta, Department of Radiology, Fondazione Istituto Giuseppe Giglio, Ct.da Pietrapollastra, Palermo 90015, Italy

Corresponding author: Tommaso Vincenzo Bartolotta, MD, PhD, Associate Professor, Section of Radiology - BiND, University Hospital "Paolo Giaccone", Via Del Vespro 129, Palermo 90127, Italy. tommasovincenzo.bartolotta@unipa.it

Abstract

Breast cancer represents the most common malignancy in women, being one of the most frequent cause of cancer-related mortality. Ultrasound, mammography, and magnetic resonance imaging (MRI) play a pivotal role in the diagnosis of breast lesions, with different levels of accuracy. Particularly, dynamic contrast-enhanced MRI has shown high diagnostic value in detecting multifocal, multicentric, or contralateral breast cancers. Radiomics is emerging as a promising tool for quantitative tumor evaluation, allowing the extraction of additional quantitative data from radiological imaging acquired with different modalities. Radiomics analysis may provide novel information through the quantification of lesions heterogeneity, that may be relevant in clinical practice for the characterization of breast lesions, prediction of tumor response to systemic therapies and evaluation of prognosis in patients with breast cancers. Several published studies have explored the value of radiomics with good-to-excellent diagnostic and prognostic performances for the evaluation of breast lesions. Particularly, the integrations of radiomics data with other clinical and histopathological parameters have demonstrated to improve the prediction of tumor aggressiveness with high accuracy and provided precise models that will help to guide clinical decisions and patients management. The purpose of this article is to describe the current application of radiomics in breast dynamic contrast-enhanced MRI.

Key words: Radiomics; Texture analysis; Magnetic resonance imaging; Dynamic contrast-enhanced-magnetic resonance imaging; Breast; Cancer

©The Author(s) 2020. Published by Baishideng Publishing Group Inc. All rights reserved.

manuscript

Received: June 1, 2020**Peer-review started:** June 1, 2020**First decision:** June 5, 2020**Revised:** June 17, 2020**Accepted:** June 20, 2020**Article in press:** June 20, 2020**Published online:** June 28, 2020**P-Reviewer:** Li JF**S-Editor:** Wang JL**L-Editor:** A**E-Editor:** Xing YX

Core tip: Dynamic contrast-enhanced-magnetic resonance imaging (DCE-MRI) has been evaluated in most of radiomics studies on breast cancers. However, heterogeneity in study designs related to magnetic field, contrast media used, and software available to perform radiomics challenge the comparisons of available results. In this review we will focus on the following applications of radiomics in breast DCE-MRI: characterization of breast lesions, prediction of breast cancer histological types, correlation with receptor status, prediction of lymph node metastases, prediction of tumor response to neoadjuvant systemic therapy, prognosis and recurrence risks.

Citation: Orlando A, Dimarco M, Cannella R, Bartolotta TV. Breast dynamic contrast-enhanced-magnetic resonance imaging and radiomics: State of art. *Artif Intell Med Imaging* 2020; 1(1): 6-18

URL: <https://www.wjgnet.com/2644-3260/full/v1/i1/6.htm>

DOI: <https://dx.doi.org/10.35711/aimi.v1.i1.6>

INTRODUCTION

Breast cancer represents the most common malignancy in women^[1]. It is estimated that 268600 US women were newly diagnosed with invasive breast cancer in 2019, and that 41760 US women died of breast cancer^[1]. Because of its incidence and clinical impact, early and accurate tumor detection with imaging is of utmost importance. Ultrasound, mammography, and magnetic resonance imaging (MRI) play a pivotal role in the diagnosis of breast lesions, with different levels of accuracy. Particularly, MRI has shown a greater sensitivity than mammography (92% vs 75%, respectively)^[2] and ultrasound (90% vs 39% and 49% of ultrasound alone or associated with mammography, respectively)^[3] for the diagnosis of breast cancer. Thanks to the ability to provide both morphologic and hemodynamic features, dynamic contrast-enhanced MRI (DCE-MRI) provides high sensitivity (over 90%) in the detection of breast cancer, although specificity for lesion characterization is still suboptimal (72%)^[2,3]. DCE-MRI has shown high diagnostic value in detecting multifocal, multicentric, or contralateral disease not diagnosed on physical examination, mammography or ultrasound, recognition of ductal carcinoma *in situ* (DCIS), evaluation of treatment response to neoadjuvant chemotherapy, detection of occult primary breast cancer in patients with metastatic axillary nodes (the so-called “CUP syndrome”), and detection of cancer in dense breast tissue^[4].

Recently, an increasing interest for the clinical utility of quantitative imaging is developing. In this scenario, radiomics is emerging as a promising tool for quantitative tumor evaluation. Radiomics allow to extract quantitative data from medical images that be combined to provide models for clinical decision support^[5].

The purpose of this article in to describe the current application of radiomics in breast dynamic contrast-enhanced MRI.

CONCEPTS OF RADIOMICS ANALYSIS

Radiomics is a complex process that articulates into distinct steps, including: Acquisition of images, tumor segmentation, feature extraction, exploratory analysis, and model building. The first step of radiomics is acquisition of high-quality images. Potentially, all the radiologic techniques may be used for radiomics analysis. In the field of breast imaging, all the techniques (mammography, ultrasound, and MRI) have shown promising results in radiomics studies. Particularly, breast MRI is commonly performed using T2-weighted images acquired to characterized diseased tissue, diffusion-weighted imaging (DWI), and apparent diffusion coefficient (ADC) that have an important clinical role in the evaluation of breast lesions, and post-contrast dynamic imaging that are mandatory for the differentiation of benign and malignant lesions. Next step is the segmentation of the lesion (Figure 1), with selection of a region of interest (ROI) and delineation of the borders of its volume. The ROI selection process is not yet standardized and it is linked to high levels of variability between different studies, as it can include the whole tumor or single slice segmentation^[6].

Feature extraction may be performed with different radiomics software that are able

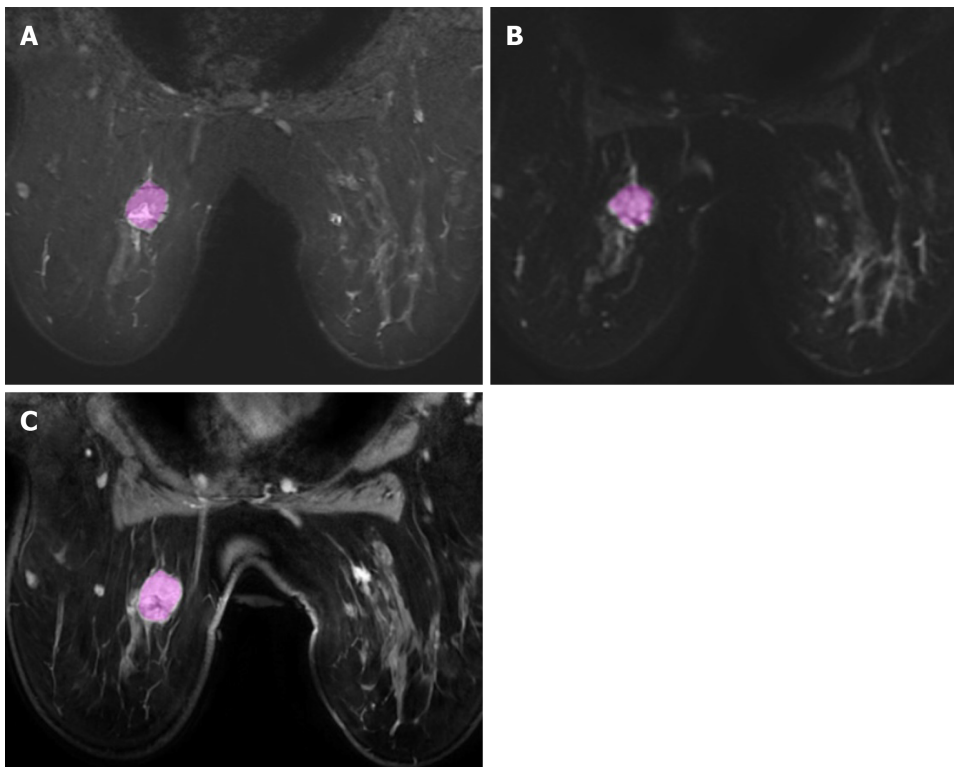


Figure 1 Examples of lesion segmentation in dynamic contrast-enhanced-magnetic resonance imaging in a 70-year-old woman with 3.0 cm breast cancer lesion. A: Short tau inversion recovery; B: Diffusion-weighted imaging; C: Contrast-enhanced sequences.

to provide a large number of quantitative features. Quantitative radiomics features can be divided into morphological (basic features that describe the shape of the ROI and its geometric properties such as volume, diameter, sphericity), and statistical (calculated using statistical methods). These features can be further divided into first order (histogram-based) features that describe the distribution of voxel values without considering the spatial relationships (*i.e.* mean, median, skewness, kurtosis, and entropy); second order texture features that are obtained by calculating the relationships between neighboring voxels (*i.e.* grey level co-occurrence matrix, grey level run length matrix, grey level size zone matrix); and third order features that are obtained by statistical methods after applying filters or mathematical transforms to the images (*i.e.* wavelet transform, Laplacian transforms of Gaussian-filtered images)^[7].

The next and last step in the workflow is building the statistical radiomics model with the purpose to predict an outcome or response variables. Different models can be evaluated to predict a specific outcome or a response using a variety of classifiers.

APPLICATION OF RADIOMICS IN BREAST DCE-MRI

The emerging field of radiomics was applied to several breast imaging modalities^[8,9]. Nevertheless, DCE-MRI was used in most studies but with heterogeneity in study designs related to magnetic field (1.5T or 3T), contrast media used, and software available to perform radiomics^[10]. In this review we will focus the following applications of radiomics in breast DCE-MRI: Characterization of breast lesions, prediction of breast cancer histological types, correlation with receptor status, prediction with lymph node metastases, prediction of tumor response to neoadjuvant systemic therapy (NST), prognosis and recurrence risks.

Characterization of breast lesions

Radiomics features extracted from multiple MRI sequences have shown to be helpful in establishing predictive models that could help differentiate between benign and malignant breast lesions. Several radiomics models were proposed with promising results, with most texture analysis performed on post-contrast T1-weighted images, alone or in association with other sequences (T2w and ADC maps).

Since the very first studies in literature, conducted on small populations analyzing

different types of features extracted (dynamic, textural, spatio-temporal) from breast contrast-enhanced MRI, the dynamic subset revealed the best performance for the characterization of breast lesions for Fusco *et al*^[11]. Testing a multi-layer perceptron neural network classifier, with an automatic ROI segmentation or ROI classification, they found an accuracy for dynamic features subset of about 80%, with the major discrimination power in differentiating benign from malignant lesions found for “basal signal”, “sum of intensities difference”, “relative enhancement slope” and “relative enhancement” features.

Nie *et al*^[12] investigated the utility of breast lesions morphology and textural features for differentiating between benign and malignant lesions, with both manual and automated segmentation and performing diagnostic feature selection using artificial neural network. They found that among morphological features “Compactness” and “Normalized Radial Length Entropy” showed significant differences between the benign and the malignant groups, whereas among “Gray Level Co-occurrence Matrices” texture features, “Gray Level Entropy” and “Gray Level Sum Average” were significantly lower in benign compared to malignant lesions. Analyzing the diagnostic performance of individual and combined features the highest AUROC (0.86) was obtained combining the following 6 features: Compactness, NRL entropy, volume, gray level entropy, gray level sum average, and homogeneity. Entropy is an important feature associated with tumor aggressiveness. It represents one of the most reliable feature to distinguish malignant from benign lesions, with the irregularity of texture reflecting the tumor heterogeneity, and tumor aggressiveness^[13-15]. Gibbs *et al*^[16], testing texture analysis with the aim to characterize breast lesions, concluded that texture features of variance, sum entropy, and entropy were the most significant when discriminating between benign and malignant lesions.

Radiomics model of quantitative pharmacokinetic maps demonstrated a strong ability to discriminate between benign and malignant breast lesions, directly reflecting the physiological properties of tissues, such as vessel permeability, perfusion, and volume of the extravascular/extracellular space^[13,17]. Nagarajan *et al*^[18] studied texture features extracted from the lesion enhancement pattern on all five post-contrast images, thus using a dynamic texture quantification approach. In this study, the highest AUROC (0.82) was achieved with texture features responsible for capturing aspects of lesion heterogeneity. Gibbs *et al*^[19] also assessed the efficacy of radiomics analysis with quantitative pharmacokinetic maps in small breast lesions (less than 1 cm). Their results showed that texture parameters calculated from initial enhancement, overall enhancement, and area under the enhancement curve maps offered similar discriminatory power in discriminating benign and malignant breast lesions, whereas texture features obtained from washout maps did not demonstrate any diagnostic value^[19].

While many studies focused on discriminatory capacities of specific texture features extracted from combining quantitative pharmacokinetic parameters of DCE-MRI sequences, few studies used a multiparametric approach analyzing also feature extracted from other sequences, such as T2-weighted and T1-weighted imaging, diffusion kurtosis imaging, and ADC maps. The multimodal MRI-based radiomics model developed by Zhang *et al*^[13] demonstrated higher diagnostic ability for differentiating benign and malignant breast lesions [Area under curve (AUC) = 0.921], increasing the discriminatory power of radiomics features extracted from DCE pharmacokinetic parameter maps alone (AUC = 0.836). In particular, analyzing textural features included in the radiomics models, malignant breast lesions had higher entropy and nonuniformity than benign lesions. The multiview IsoSVM (hybrid isomap and support vector machine) model applied by Parekh *et al*^[20] to radiomics features extracted from multiparametric breast MR imaging at 3T, classified benign and malignant breast tumors with an AUROC of 0.91, sensitivity of 93%, and specificity of 85%. In this study, entropy features maps obtained demonstrated significantly higher entropy for malignant than benign lesions on post contrast DCE-MRI and ADC maps^[20]. The same authors developed a multiparametric imaging radiomics framework for extraction of first and second order radiomics features from multiparametric radiological datasets which provided a 9%-28% increase in AUROC over single radiomics parameters. Similar results were reported by Bhooshan *et al*^[21], who found the better performance applying a multiparametric feature vector, with T2-weighted MRI textural features added to DCE-MRI kinetic ones.

Radiomics features extracted from unenhanced MRI sequences were also evaluated for the prediction of malignancies. In the study of Bickelhaupt *et al*^[22] an unenhanced, abbreviated DWI protocol (ueMRI), including T2-weighted, DWI, DWI with background suppression sequences, and corresponding ADC maps, was used to test three machine learning classifiers including univariate mean ADC model,

unconstrained radiomics model, constrained radiomics model with mandatory inclusion of mean ADC. The last two radiomics classifiers were found to be able to distinguish benign from malignant lesions more accurately (AUROC of 0.842 and 0.851) than the mean ADC parameter alone (AUROC of 0.774)^[22]. Nevertheless, the performance remained lower than that of the experienced breast radiologist using standard DCE-MRI protocol^[22]. ADC radiomics features reflect the heterogeneity of diffusion in tumors, relative to the cell density and the microenvironment distribution inside the lesion. Hu *et al*^[23] found that ADC radiomics score was more accurate than ADC values alone and they developed a prediction model based on ADC radiomics, pharmacokinetics and clinical features, which showed good diagnostic performance in differentiating benign and malignant lesions classified as BI-RADS 4. A radiomics model based on kurtosis diffusion-weighted imaging was evaluated by Bickelhaupt *et al*^[24] who conducted a multicentric and prospective study on BI-RADS 4 and 5 lesions, by using MRI scanners from different vendors, showing reliable results, with a real benefit for BI-RADS 4a and 4b breast lesions.

Finally, more recent studies are using DCE-MRI focusing their attention on peritumoural tissues inclusion during segmentation. Zhou *et al*^[25] found that the smallest bounding box, that included a small amount of peritumoral tissue adjacent to the tumor, had higher accuracy compared to tumor alone or larger input boxes.

Prediction of breast cancer histological types

Few studies employed radiomics models and texture analysis to distinguish between the heterogeneous histopathologic subtypes of breast cancer and entropy-based features from the co-occurrence matrix appear to be most crucial, with promising results. Invasive ductal (IDC) and lobular (ILC) carcinoma are the most common pathologic types. The different growth patterns may manifest with different heterogeneity of internal enhancement in DCE-MRI, and could be the basis to differentiate between these two histological types by means of textural analysis^[14,26]. Holli *et al*^[26] found that the co-occurrence matrix texture features group was statistically significant different between ductal and lobular invasive cancers on DCE-MR images. Similar conclusions were reported by Waugh *et al*^[14] analyzing differences between IDC, ILC and in situ ductal carcinoma (DCIS). Chou *et al*^[27] investigated the potential role of radiomics in classifying DCIS nuclear grade and found that only one heterogeneity metric, surface-to-volume ratio from the “shape and morphology” metrics group, was significantly different between “high nuclear grade” and “non-high nuclear grade” DCIS.

Correlation with receptor status and molecular subtypes

Expression of Ki-67, estrogen receptor (ER), progesterone receptor, human epidermal growth factor 2 receptor (HER2) are crucial factors to differentiate breast cancers into four main molecular subtypes (Luminal A, Luminal B, Her2 over-expressing, and triple negative, TN) with different outcomes and therapeutic strategies. According to the molecular subtypes different strategies, including surgery, adjuvant or neoadjuvant therapies, can be undertaken^[28-31]. Current assessment of molecular subtypes is mostly based on immunohistochemistry (IHC)^[32]. When IHC is tested in tissue specimens obtained by needle biopsy, could be not totally representative of the entire tumor or provide inconclusive results due to insufficient material. In this setting, according to prior studies, DCE-MRI may provide information suggesting the molecular subtype of breast cancer. In 2018, the American Joint Committee on Cancer updated the breast cancer staging guidelines to add other cancer characteristics to the TNM system to determine a cancer's stage, including receptor status^[33]. When developing a treatment plan, a correct assessment of receptor status is crucial. Several published studies revealed that rim enhancement, heterogeneous internal enhancement, and peritumoral edema are more frequently associated with TN than Luminal subtypes^[34,35]. In the study of Blaschke *et al*^[36] HER2-enriched tumors showed the percent volume with > 50% and > 100% early phase uptake higher than Luminal A/B lesions at kinetic assessment. TN tends to be more frequently round in shape^[32,37], Her2 cancers with smooth margins than other subtypes^[37]. Controversial results were reported for diffusion-weighted imaging, suggesting that high ADC values are associated with HER2 subtypes^[38] or with Luminal A^[39], and for spectroscopy, suggesting that high values of tCho are statistically correlated to the TN subtype for some authors^[39,40], and with non-TN and Luminal B^[41].

Several studies investigated the relationship between radiomics MRI features and breast cancer receptor status^[42-44]. Wu *et al*^[45] reported only few features significantly associated with Luminal A, Luminal B or TN in their study cohorts for distinguishing different molecular subtypes of breast cancers. Radiomics analysis conducted by Li

et al^[46] showed a statistically significant trend for the relationship between enhancement textures (entropy) and molecular subtypes in the task of distinguishing between ER+ versus ER-. Indeed, heterogeneous nature of contrast uptake within the breast tumor is related to molecular subtype. Similar observations were reported by Waugh *et al*^[14], revealing that HER2-enriched and TN cancers showed a significant increase in entropy value. In the study of Chang *et al*^[47] the quantitative region-based features extracted from breast DCE-MRI were used to interpret the intra-tumoral heterogeneity and correlated with ER, HER2, and TNBC, with better performance than morphological features (texture features and shape feature) and the pharmacokinetic model. Fan *et al*^[48] investigated the use of features extracted from DCE-MRI for the prediction of the molecular subtypes of breast cancer and observed low kurtosis and skewness for the luminal A subtype, the highest enhancement values in the normal breasts for Her 2 subtypes and the lowest for luminal A and luminal B tumors. Furthermore, other studies suggested the value of the heterogeneity of the surrounding parenchyma, including background parenchymal enhancement features in differentiating TN breast cancers from others, as observed by Wang *et al*^[49]. The evaluation of both peritumoral and intratumoral features allowed to identify HER2 subtype with better accuracy than intratumoral features alone in the study of Braman *et al*^[50]. According to the results of Leithner *et al*^[51] radiomics analysis from DWI with ADC mapping allows evaluation of breast cancer receptor status and molecular subtyping. For differentiating ER positive breast cancer molecular subtypes (Luminal A *vs* Luminal B) the two most discriminative texture parameters extracted from the dynamic T1-weighted sequences by Holli-Helenius *et al*^[52] were sum entropy and sum variance, which also showed positive correlation with higher Ki-67 index.

High Ki-67 expression is a well-known prognostic factor, related to better neo-adjuvant therapy response but poorer prognosis. Assessment of Ki-67 based on immunohistochemistry on tissue specimens obtained by needle biopsy sample may not be representative of the whole tumor because of the relatively small tissue sample size and tumor heterogeneity. In the attempt to predict the expression of Ki-67 several studies have explored the potential of radiomics imaging features, with promising results. In their retrospective study, Ma *et al*^[53] showed that texture features extracted on the first post-contrast images were associated with breast cancer Ki-67 expression. Similar results were obtained by Juan *et al*^[54]. A correlation between Ki-67 expression and radiomics features were observed also performing features extraction from T2-weighted images^[55] and ADC maps^[56].

Prediction of lymph node status

Involvement of axillary lymph nodes (LN) in patients with breast cancers represents a crucial prognostic factor, as it guides therapeutic management. Non-invasive methods to preoperatively evaluate LN metastasis are highly needed. Some promising studies suggested that radiomics models could be able to achieve this objective. In recent studies, specific lesions textural features extracted from anatomical and functional MRI images, improved the performance of radiomics models in predicting LN metastasis^[57,58]. Liu *et al*^[59] demonstrated that DCE-MRI radiomics features, particularly features extracted from peritumoral regions, associated with clinico-pathologic informations were able to predict LN metastasis in breast cancer patients. Indeed, the area surrounding tumors, is thought to carry informations such as peritumoral lymphatic vessel invasion, lymphocytic infiltration, and edema^[59,60]. Other authors reported that the best results were obtained when the features extraction was performed in the strongest phases of tumor enhancement, probably because it shows more clearly the lesion boundaries and better reflects the tumor heterogeneity and invasiveness^[61]. The radiomics nomogram developed by Han *et al*^[62] demonstrated excellent performance to predict LN metastases, and good ability in distinguishing the number of metastatic LNs. Similar performances were reported by several other evidences^[59,63-65]. Finally, only very few studies evaluated texture analysis in identified index lymph nodes in postcontrast T1-weighted images, concluding that morphologic features were more predictive than kinetic and texture features^[66,67].

Prediction of tumor response to neo-adjuvant therapy

NST is often the first line treatment for those patients diagnosed with locally advanced breast cancer, with several potential advantages, including the reduction of tumor size to allow breast-conservative surgery instead of mastectomy, as well as a prognostic indicator^[68]. The pathologic complete response (pCR) rate range from 0.3%–38.7%, depending on cancer subtype and breast cancer stage^[69]. Early identification of patients who are not likely to achieve pCR is crucial as they could benefit from changes to their initial NST regimens. DCE-MRI is considered as the most reliable technique for

evaluating the responses to NST. According to a meta-analysis based on 25 studies, breast MRI had high specificity (up to 90.7%), but low sensitivity (63.1%) in predicting pathologic complete remission after preoperative therapy in patients with breast cancer^[70]. According to another recent meta-analysis, accuracy in detection of residual malignancy with breast MRI varies also in consideration of the treatment type, with AUC values ranging from 0.83 to 0.89, and on the basis of response definition, for instance volume reduction, absence of enhancement or enhancement equal or less than breast parenchyma^[71,72]. The wide heterogeneity of studies, with controversial results, suggests to standardize definitions and primary endpoints to produce clinically significant results^[73].

The identification of pCR is still a challenge and according with several studies, radiomics can be helpful in a non-invasive prediction of response to NST^[74-78]. In most studies, GLCM features were the most predictive of therapy response, particularly entropy^[79-81]. Noteworthy, in the study of Parikh *et al.*^[82], responders to NST showed increase in lesion homogeneity after one round of therapy. Cao *et al.*^[83] demonstrated that texture analysis may help to improve the performance of post-NST MRI in identifying pCR in mass-like breast cancer, showing that entropy was an independent risk factor. Intratumoral spatial heterogeneity at perfusion MRI appeared to be an independent prognostic factor of recurrence-free survival in patients with locally advanced breast cancers treated with NST^[84]. Significant differences between pCR and non-pCR patients were found for texture parameters also by Fusco *et al.*^[85]. Peritumoral region includes prognostic informations, such as angiogenic and lymphangiogenic activity, peritumoral invasion of lymphatics and blood vessels and peritumoral lymphocytic infiltration^[86]. In their retrospective study, Braman *et al.*^[87] demonstrated that with combined intratumoral and peritumoral radiomics approach, analyzing textural features extracted from T1-weighted contrast-enhanced MRI scans, it is possible to successfully predict pCR to NST from pretreatment breast DCE-MRI, both with and without a priori knowledge of receptor status. Later, the same authors, confirmed that an intratumoral and peritumoral imaging signature was capable to predict the response to preroperative targeted therapy in another retrospective study conducted on HER2-positive breast cancers, highlighting again the relationship between immune-response and the peritumoral environment^[50]. Zhou *et al.*^[88] investigated the role of wavelet-transformed textures, which can provide comprehensive spatial, and frequency distributions for characterizing intratumoral and peritumoral regions in terms of low and high frequency signals. In their study wavelet-transformed textures outperformed volumetric and peripheral textures in the radiomics MRI prediction of pCR to NST for patients with locally advanced breast cancers.

DWI is considerably sensitive to NST-induced intratumoral changes, resulting in an additional value when associated to contrast-enhanced MRI in radiomics models. Radiomics signatures combining multi-parametric MRI achieved a good performance for predicting complete response in BC, in both Luminal and TN cancers, in the study conducted by Liu *et al.*^[89]. With a radiomics signature, combining radiomics features from DCE-MRI and ADC maps, Chen *et al.*^[90] obtained similar results, with a higher performance than the models with DCE-MRI or ADC maps alone, in predicting PCR.

Sentinel lymph node biopsy has replaced axillary lymph node dissection in patients who convert to node-negative status after NST. Several studies assessed whether breast MRI can be used to assess lymph node residual metastasis after NST allowing breast cancer patients to avoid unnecessary axillary surgery. In the study of Hyun *et al.*^[91], DCE-MRI was able to rule out the presence of advanced nodal disease with a NPV of 94% in NAC patients. Nevertheless, in the work of Mattingly *et al.*^[92], post-treatment MRI and surgical pathologic findings revealed a slight strength of agreement and DCE-MRI revealed specificity and sensitivity of 63% and 55%, respectively. Ha *et al.*^[93] found different results, with sensitivity and specificity of 57% and 72%, with positive estrogen receptor status significantly associated with misdiagnosis by MRI. These latter evidences, revealing that post-treatment MRI findings were not exactly predictive of residual axillary disease, suggest to use DCE-MRI results with caution when planning treatment and to avoid omitting sentinel lymph node biopsy or axillary lymph node dissection for staging in women determined to be node-positive pre-treatment. In this setting, convolutional neural networks (CNN), were employed to predict the likelihood of axillary LN metastasis and NAC treatment response, using MRI datasets prior to initiation of NAC in few studies with controversial results^[79,94-96]. Ha *et al.*^[96] reported an accuracy of 83% with AUC of 0.93 for CNN in predicting axillary response. Nevertheless, in the study of Golden *et al.*^[79] the GLCM texture features extracted from pre- chemotherapy MRI was able to predict pCR and residual lymph node metastasis with an AUC of 0.68.

Prognosis

Radiomics models demonstrated promising results in predicting cancer prognosis of patients with tumors of various organs, reporting that several texture features, such as uniformity and entropy, can be used in risk stratification^[15,97,98]. By using the genomic-based scores for the multigene assays MammaPrint, Oncotype DX, and PAM50 as the reference standards, Li *et al*^[99] demonstrated that breast MRI radiomics show a promising role for image-based phenotyping in assessing the risk of recurrence. Noteworthy, enhancement texture features were consistently associated with recurrence score, highlighting how microvascular density and/or central necrosis, responsible of tumor heterogeneity, play an important biological role in recurrence. Other authors confirmed these results, finding that tumors with higher entropy on T2-weighted images and lower entropy on T1w subtraction images were associated with poorer recurrence-free survival^[15]. A CNN developed by Ha *et al*^[100] was able to predict with an accuracy of up to 84%, the Oncotype Dx Recurrence Score (ODRS), an expensive but validated recurrence score, recommended by American Society of Clinical Oncology guidelines to decide on adjuvant systemic chemotherapy in ER+/HER-/node negative lesions^[101]. Nevertheless, this result was not confirmed by Saha *et al*^[102], who tested two machine learning-based models, finding only a moderate association between imaging and ODRS. The study of Park *et al*^[103] was the first performed, using ROIs drawn on entire tumors, to demonstrate that a radiomics signature can estimate survival in patients with BC. They generated a multivariate feature vector based on morphologic, histogram texture, and GLCM texture features to stratify patients at risk for recurrence. They also showed that a combined radiomics-clinical-pathological nomogram achieved superior prognostic performance than either the Rad-score-only or the clinico-pathological nomograms. Nevertheless, controversial results were recently reported applying radiomics models to predict prognosis for TN (triple-negative) breast cancers^[104,105]. While in the study conducted by Kim *et al*^[105] the radiomics score was significantly associated with worse disease free survival, but comparable in performance with the clinico-pathologic model, in both the training and validation sets, the work performed by Koh *et al*^[104] showed that their Radiomics model was able to predict systemic recurrence better than the Clinical model only in the training set.

LIMITATIONS AND FUTURE APPLICATIONS

Radiomics techniques require further studies, as they have not yet achieved widespread, demonstrated and accepted, clinical relevance and applicability. The main challenge is the standardization of MRI acquisition protocol, method of segmentation, feature extraction and selection, or classification. Another hurdle is the current lack of evidences regarding reproducibility of feature extraction systems and radiomics models. Furthermore, most studies are retrospectively designed, with relatively small sample size and wide methodological differences. Larger and prospective studies, with standardized radiomics methods are needed to prove and improve potential clinical applications of radiomics in BC. Further studies are necessary to prove and understand the relationships between image-derived texture features and histopathologic or even genomic expression data. The main future directions include the correlation between proteomic and genomic tumor analyses with radiomics features, through the field of radiogenomics. These last investigations could have a potential role in explaining tumor biology, contributing in the main future objective of personalized diagnosis and treatment of breast cancer patients.

REFERENCES

- 1 Siegel RL, Miller KD, Jemal A. Cancer statistics, 2019. *CA Cancer J Clin* 2019; **69**: 7-34 [PMID: 30620402 DOI: 10.3322/caac.21551]
- 2 Zhang Y, Ren H. Meta-analysis of diagnostic accuracy of magnetic resonance imaging and mammography for breast cancer. *J Cancer Res Ther* 2017; **13**: 862-868 [PMID: 29237918 DOI: 10.4103/jcrt.JCRT_678_17]
- 3 Kuhl CK, Schrading S, Leutner CC, Morakkabati-Spitz N, Wardelmann E, Fimmers R, Kuhn W, Schild HH. Mammography, breast ultrasound, and magnetic resonance imaging for surveillance of women at high familial risk for breast cancer. *J Clin Oncol* 2005; **23**: 8469-8476 [PMID: 16293877 DOI: 10.1200/JCO.2004.00.4960]
- 4 Menezes GL, Knuttel FM, Stehouwer BL, Pijnappel RM, van den Bosch MA. Magnetic resonance imaging in breast cancer: A literature review and future perspectives. *World J Clin Oncol* 2014;

- 5: 61-70 [PMID: [24829852](#) DOI: [10.5306/wjco.v5.i2.61](#)]
- 5 **Gillies RJ**, Kinahan PE, Hricak H. Radiomics: Images Are More than Pictures, They Are Data. *Radiology* 2016; **278**: 563-577 [PMID: [26579733](#) DOI: [10.1148/radiol.2015151169](#)]
- 6 **Tagliafico AS**, Piana M, Schenone D, Lai R, Massone AM, Houssami N. Overview of radiomics in breast cancer diagnosis and prognostication. *Breast* 2020; **49**: 74-80 [PMID: [31739125](#) DOI: [10.1016/j.breast.2019.10.018](#)]
- 7 **Rizzo S**, Botta F, Raimondi S, Origi D, Fanciullo C, Morganti AG, Bellomi M. Radiomics: the facts and the challenges of image analysis. *Eur Radiol Exp* 2018; **2**: 36 [PMID: [30426318](#) DOI: [10.1186/s41747-018-0068-z](#)]
- 8 **Valdora F**, Houssami N, Rossi F, Calabrese M, Tagliafico AS. Rapid review: radiomics and breast cancer. *Breast Cancer Res Treat* 2018; **169**: 217-229 [PMID: [29396665](#) DOI: [10.1007/s10549-018-4675-4](#)]
- 9 **Rogers W**, Thulasi Seetha S, Refaee TAG, Lieverse RIY, Granzier RWY, Ibrahim A, Keek SA, Sanduleanu S, Primakov SP, Beuque MPL, Marcus D, van der Wiel AMA, Zerka F, Oberije CJG, van Timmeren JE, Woodruff HC, Lambin P. Radiomics: from qualitative to quantitative imaging. *Br J Radiol* 2020; **93**: 20190948 [PMID: [32101448](#) DOI: [10.1259/bjr.20190948](#)]
- 10 **Antropova N**, Huynh BQ, Giger ML. A deep feature fusion methodology for breast cancer diagnosis demonstrated on three imaging modality datasets. *Med Phys* 2017; **44**: 5162-5171 [PMID: [28681390](#) DOI: [10.1002/mp.12453](#)]
- 11 **Fusco R**, Sansone M, Sansone C, Petrillo A. Segmentation and classification of breast lesions using dynamic and textural features in Dynamic Contrast Enhanced-Magnetic Resonance Imaging. *IEEE* 2012 [DOI: [10.1109/CBMS.2012.6266312](#)]
- 12 **Nie K**, Chen JH, Yu HJ, Chu Y, Nalcioğlu O, Su MY. Quantitative analysis of lesion morphology and texture features for diagnostic prediction in breast MRI. *Acad Radiol* 2008; **15**: 1513-1525 [PMID: [19000868](#) DOI: [10.1016/j.acra.2008.06.005](#)]
- 13 **Zhang Q**, Peng Y, Liu W, Bai J, Zheng J, Yang X, Zhou L. Radiomics Based on Multimodal MRI for the Differential Diagnosis of Benign and Malignant Breast Lesions. *J Magn Reson Imaging* 2020 [PMID: [32061014](#) DOI: [10.1002/jmri.27098](#)]
- 14 **Waugh SA**, Purdie CA, Jordan LB, Vinnicombe S, Lerski RA, Martin P, Thompson AM. Magnetic resonance imaging texture analysis classification of primary breast cancer. *Eur Radiol* 2016; **26**: 322-330 [PMID: [26065395](#) DOI: [10.1007/s00330-015-3845-6](#)]
- 15 **Kim JH**, Ko ES, Lim Y, Lee KS, Han BK, Ko EY, Hahn SY, Nam SJ. Breast Cancer Heterogeneity: MR Imaging Texture Analysis and Survival Outcomes. *Radiology* 2017; **282**: 665-675 [PMID: [27700229](#) DOI: [10.1148/radiol.2016160261](#)]
- 16 **Gibbs P**, Turnbull LW. Textural analysis of contrast-enhanced MR images of the breast. *Magn Reson Med* 2003; **50**: 92-98 [PMID: [12815683](#) DOI: [10.1002/mrm.10496](#)]
- 17 **Kim SG**, Freed M, Leite APK, Zhang J, Seuss C, Moy L. Separation of benign and malignant breast lesions using dynamic contrast enhanced MRI in a biopsy cohort. *J Magn Reson Imaging* 2017; **45**: 1385-1393 [PMID: [27766710](#) DOI: [10.1002/jmri.25501](#)]
- 18 **Nagarajan MB**, Huber MB, Schlossbauer T, Leinsinger G, Krol A, Wismüller A. Classification of Small Lesions in Breast MRI: Evaluating The Role of Dynamically Extracted Texture Features Through Feature Selection. *J Med Biol Eng* 2013; **33** [PMID: [24223533](#) DOI: [10.5405/jmbe.1183](#)]
- 19 **Gibbs P**, Onishi N, Sadinski M, Gallagher KM, Hughes M, Martinez DF, Morris EA, Sutton EJ. Characterization of Sub-1 cm Breast Lesions Using Radiomics Analysis. *J Magn Reson Imaging* 2019; **50**: 1468-1477 [PMID: [30916835](#) DOI: [10.1002/jmri.26732](#)]
- 20 **Parekh VS**, Jacobs MA. Integrated radiomic framework for breast cancer and tumor biology using advanced machine learning and multiparametric MRI. *NPJ Breast Cancer* 2017; **3**: 43 [PMID: [29152563](#) DOI: [10.1038/s41523-017-0045-3](#)]
- 21 **Bhooshan N**, Giger M, Lan L, Li H, Marquez A, Shimauchi A, Newstead GM. Combined use of T2-weighted MRI and T1-weighted dynamic contrast-enhanced MRI in the automated analysis of breast lesions. *Magn Reson Med* 2011; **66**: 555-564 [PMID: [21523818](#) DOI: [10.1002/mrm.22800](#)]
- 22 **Bickelhaupt S**, Paech D, Kickingeder P, Steudle F, Lederer W, Daniel H, Götz M, Gähler N, Tichy D, Wiesenfarth M, Laun FB, Maier-Hein KH, Schlemmer HP, Bonekamp D. Prediction of malignancy by a radiomic signature from contrast agent-free diffusion MRI in suspicious breast lesions found on screening mammography. *J Magn Reson Imaging* 2017; **46**: 604-616 [PMID: [28152264](#) DOI: [10.1002/jmri.25606](#)]
- 23 **Hu B**, Xu K, Zhang Z, Chai R, Li S, Zhang L. A radiomic nomogram based on an apparent diffusion coefficient map for differential diagnosis of suspicious breast findings. *Chin J Cancer Res* 2018; **30**: 432-438 [PMID: [30210223](#) DOI: [10.21147/j.issn.1000-9604.2018.04.06](#)]
- 24 **Bickelhaupt S**, Jaeger PF, Laun FB, Lederer W, Daniel H, Kuder TA, Wuesthof L, Paech D, Bonekamp D, Radbruch A, Delorme S, Schlemmer HP, Steudle FH, Maier-Hein KH. Radiomics Based on Adapted Diffusion Kurtosis Imaging Helps to Clarify Most Mammographic Findings Suspicious for Cancer. *Radiology* 2018; **287**: 761-770 [PMID: [29461172](#) DOI: [10.1148/radiol.2017170273](#)]
- 25 **Zhou J**, Zhang Y, Chang KT, Lee KE, Wang O, Li J, Lin Y, Pan Z, Chang P, Chow D, Wang M, Su MY. Diagnosis of Benign and Malignant Breast Lesions on DCE-MRI by Using Radiomics and Deep Learning With Consideration of Peritumor Tissue. *J Magn Reson Imaging* 2020; **51**: 798-809 [PMID: [31675151](#) DOI: [10.1002/jmri.26981](#)]
- 26 **Holli K**, Lääperi AL, Harrison L, Luukkaala T, Toivonen T, Ryymin P, Dastidar P, Soimakallio S, Eskola H. Characterization of breast cancer types by texture analysis of magnetic resonance images. *Acad Radiol* 2010; **17**: 135-141 [PMID: [19945302](#) DOI: [10.1016/j.acra.2009.08.012](#)]
- 27 **Chou SS**, Gombos EC, Chikarmane SA, Giess CS, Jayender J. Computer-aided heterogeneity analysis in breast MR imaging assessment of ductal carcinoma in situ: Correlating histologic grade and receptor status. *J Magn Reson Imaging* 2017; **46**: 1748-1759 [PMID: [28371110](#) DOI: [10.1002/jmri.25712](#)]
- 28 **Goldhirsch A**, Wood WC, Coates AS, Gelber RD, Thürlimann B, Senn HJ; Panel members. Strategies for subtypes--dealing with the diversity of breast cancer: highlights of the St. Gallen International Expert Consensus on the Primary Therapy of Early Breast Cancer 2011. *Ann Oncol* 2011; **22**: 1736-1747 [PMID:

- 21709140 DOI: [10.1093/annonc/mdr304](https://doi.org/10.1093/annonc/mdr304)]
- 29 **Goldhirsch A**, Winer EP, Coates AS, Gelber RD, Piccart-Gebhart M, Thürlimann B, Senn HJ; Panel members. Personalizing the treatment of women with early breast cancer: highlights of the St Gallen International Expert Consensus on the Primary Therapy of Early Breast Cancer 2013. *Ann Oncol* 2013; **24**: 2206-2223 [PMID: [23917950](https://pubmed.ncbi.nlm.nih.gov/23917950/) DOI: [10.1093/annonc/mdt303](https://doi.org/10.1093/annonc/mdt303)]
 - 30 **Balic M**, Thomssen C, Würstlein R, Gnant M, Harbeck N. St. Gallen/Vienna 2019: A Brief Summary of the Consensus Discussion on the Optimal Primary Breast Cancer Treatment. *Breast Care (Basel)* 2019; **14**: 103-110 [PMID: [31798382](https://pubmed.ncbi.nlm.nih.gov/31798382/) DOI: [10.1159/000499931](https://doi.org/10.1159/000499931)]
 - 31 **Öztürk VS**, Polat YD, Soyder A, Tanyeri A, Karaman CZ, Taşkın F. The Relationship Between MRI Findings and Molecular Subtypes in Women With Breast Cancer. *Curr Probl Diagn Radiol* 2019 [PMID: [31351695](https://pubmed.ncbi.nlm.nih.gov/31351695/) DOI: [10.1067/j.cpradiol.2019.07.003](https://doi.org/10.1067/j.cpradiol.2019.07.003)]
 - 32 **Guiu S**, Michiels S, André F, Cortes J, Denkert C, Di Leo A, Hennessy BT, Sorlie T, Sotiriou C, Turner N, Van de Vijver M, Viale G, Loi S, Reis-Filho JS. Molecular subclasses of breast cancer: how do we define them? The IMPAKT 2012 Working Group Statement. *Ann Oncol* 2012; **23**: 2997-3006 [PMID: [23166150](https://pubmed.ncbi.nlm.nih.gov/23166150/) DOI: [10.1093/annonc/mds586](https://doi.org/10.1093/annonc/mds586)]
 - 33 **Giuliano AE**, Connolly JL, Edge SB, Mittendorf EA, Rugo HS, Solin LJ, Weaver DL, Winchester DJ, Hortobagyi GN. Breast Cancer-Major changes in the American Joint Committee on Cancer eighth edition cancer staging manual. *CA Cancer J Clin* 2017; **67**: 290-303 [PMID: [28294295](https://pubmed.ncbi.nlm.nih.gov/28294295/) DOI: [10.3322/caac.21393](https://doi.org/10.3322/caac.21393)]
 - 34 **Net JM**, Whitman GJ, Morris E, Brandt KR, Burnside ES, Giger ML, Ganott M, Sutton EJ, Zuley ML, Rao A. Relationships Between Human-Extracted MRI Tumor Phenotypes of Breast Cancer and Clinical Prognostic Indicators Including Receptor Status and Molecular Subtype. *Curr Probl Diagn Radiol* 2019; **48**: 467-472 [PMID: [30270031](https://pubmed.ncbi.nlm.nih.gov/30270031/) DOI: [10.1067/j.cpradiol.2018.08.003](https://doi.org/10.1067/j.cpradiol.2018.08.003)]
 - 35 **Jinguji M**, Kajiya Y, Kamimura K, Nakajo M, Sagara Y, Takahama T, Ando M, Rai Y, Sagara Y, Ohi Y, Yoshida H. Rim enhancement of breast cancers on contrast-enhanced MR imaging: relationship with prognostic factors. *Breast Cancer* 2006; **13**: 64-73 [PMID: [16518064](https://pubmed.ncbi.nlm.nih.gov/16518064/) DOI: [10.2325/jbcs.13.64](https://doi.org/10.2325/jbcs.13.64)]
 - 36 **Blaschke E**, Abe H. MRI phenotype of breast cancer: Kinetic assessment for molecular subtypes. *J Magn Reson Imaging* 2015; **42**: 920-924 [PMID: [25758675](https://pubmed.ncbi.nlm.nih.gov/25758675/) DOI: [10.1002/jmri.24884](https://doi.org/10.1002/jmri.24884)]
 - 37 **Grimm LJ**, Zhang J, Baker JA, Soo MS, Johnson KS, Mazurowski MA. Relationships Between MRI Breast Imaging-Reporting and Data System (BI-RADS) Lexicon Descriptors and Breast Cancer Molecular Subtypes: Internal Enhancement is Associated with Luminal B Subtype. *Breast J* 2017; **23**: 579-582 [PMID: [28295860](https://pubmed.ncbi.nlm.nih.gov/28295860/) DOI: [10.1111/tbj.12799](https://doi.org/10.1111/tbj.12799)]
 - 38 **Martincich L**, Deantoni V, Bertotto I, Redana S, Kubatzki F, Sarotto I, Rossi V, Liotti M, Ponzone R, Aglietta M, Regge D, Montemurro F. Correlations between diffusion-weighted imaging and breast cancer biomarkers. *Eur Radiol* 2012; **22**: 1519-1528 [PMID: [22411304](https://pubmed.ncbi.nlm.nih.gov/22411304/) DOI: [10.1007/s00330-012-2403-8](https://doi.org/10.1007/s00330-012-2403-8)]
 - 39 **Montemezzi S**, Camera L, Giri MG, Pozzetto A, Calìo A, Meliàdò G, Caumo F, Cavedon C. Is there a correlation between 3T multiparametric MRI and molecular subtypes of breast cancer? *Eur J Radiol* 2018; **108**: 120-127 [PMID: [30396643](https://pubmed.ncbi.nlm.nih.gov/30396643/) DOI: [10.1016/j.ejrad.2018.09.024](https://doi.org/10.1016/j.ejrad.2018.09.024)]
 - 40 **Shin HJ**, Baek HM, Cha JH, Kim HH. Evaluation of breast cancer using proton MR spectroscopy: total choline peak integral and signal-to-noise ratio as prognostic indicators. *AJR Am J Roentgenol* 2012; **198**: W488-W497 [PMID: [22528931](https://pubmed.ncbi.nlm.nih.gov/22528931/) DOI: [10.2214/AJR.11.7292](https://doi.org/10.2214/AJR.11.7292)]
 - 41 **Sah RG**, Sharma U, Parshad R, Seenu V, Mathur SR, Jagannathan NR. Association of estrogen receptor, progesterone receptor, and human epidermal growth factor receptor 2 status with total choline concentration and tumor volume in breast cancer patients: an MRI and in vivo proton MRS study. *Magn Reson Med* 2012; **68**: 1039-1047 [PMID: [22213087](https://pubmed.ncbi.nlm.nih.gov/22213087/) DOI: [10.1002/mrm.24117](https://doi.org/10.1002/mrm.24117)]
 - 42 **Sutton EJ**, Dashevsky BZ, Oh JH, Veeraraghavan H, Apte AP, Thakur SB, Morris EA, Deasy JO. Breast cancer molecular subtype classifier that incorporates MRI features. *J Magn Reson Imaging* 2016; **44**: 122-129 [PMID: [26756416](https://pubmed.ncbi.nlm.nih.gov/26756416/) DOI: [10.1002/jmri.25119](https://doi.org/10.1002/jmri.25119)]
 - 43 **Agner SC**, Rosen MA, Englander S, Tomaszewski JE, Feldman MD, Zhang P, Mies C, Schnall MD, Madabhushi A. Computerized image analysis for identifying triple-negative breast cancers and differentiating them from other molecular subtypes of breast cancer on dynamic contrast-enhanced MR images: a feasibility study. *Radiology* 2014; **272**: 91-99 [PMID: [24620909](https://pubmed.ncbi.nlm.nih.gov/24620909/) DOI: [10.1148/radiol.14121031](https://doi.org/10.1148/radiol.14121031)]
 - 44 **Fan M**, Yuan W, Zhao W, Xu M, Wang S, Gao X, Li L. Joint Prediction of Breast Cancer Histological Grade and Ki-67 Expression Level Based on DCE-MRI and DWI Radiomics. *IEEE J Biomed Health Inform* 2020; **24**: 1632-1642 [PMID: [31794406](https://pubmed.ncbi.nlm.nih.gov/31794406/) DOI: [10.1109/JBHI.2019.2956351](https://doi.org/10.1109/JBHI.2019.2956351)]
 - 45 **Wu J**, Sun X, Wang J, Cui Y, Kato F, Shirato H, Ikeda DM, Li R. Identifying relations between imaging phenotypes and molecular subtypes of breast cancer: Model discovery and external validation. *J Magn Reson Imaging* 2017; **46**: 1017-1027 [PMID: [28177554](https://pubmed.ncbi.nlm.nih.gov/28177554/) DOI: [10.1002/jmri.25661](https://doi.org/10.1002/jmri.25661)]
 - 46 **Li H**, Zhu Y, Burnside ES, Huang E, Drukker K, Hoadley KA, Fan C, Conzen SD, Zuley M, Net JM, Sutton E, Whitman GJ, Morris E, Perou CM, Ji Y, Giger ML. Quantitative MRI radiomics in the prediction of molecular classifications of breast cancer subtypes in the TCGA/TCIA data set. *NPJ Breast Cancer* 2016; **2**: 16012 [PMID: [27853751](https://pubmed.ncbi.nlm.nih.gov/27853751/) DOI: [10.1038/npjbcancer.2016.12](https://doi.org/10.1038/npjbcancer.2016.12)]
 - 47 **Chang RF**, Chen HH, Chang YC, Huang CS, Chen JH, Lo CM. Quantification of breast tumor heterogeneity for ER status, HER2 status, and TN molecular subtype evaluation on DCE-MRI. *Magn Reson Imaging* 2016; **34**: 809-819 [PMID: [26968141](https://pubmed.ncbi.nlm.nih.gov/26968141/) DOI: [10.1016/j.mri.2016.03.001](https://doi.org/10.1016/j.mri.2016.03.001)]
 - 48 **Fan M**, Li H, Wang S, Zheng B, Zhang J, Li L. Radiomic analysis reveals DCE-MRI features for prediction of molecular subtypes of breast cancer. *PLoS One* 2017; **12**: e0171683 [PMID: [28166261](https://pubmed.ncbi.nlm.nih.gov/28166261/) DOI: [10.1371/journal.pone.0171683](https://doi.org/10.1371/journal.pone.0171683)]
 - 49 **Wang J**, Kato F, Oyama-Manabe N, Li R, Cui Y, Tha KK, Yamashita H, Kudo K, Shirato H. Identifying Triple-Negative Breast Cancer Using Background Parenchymal Enhancement Heterogeneity on Dynamic Contrast-Enhanced MRI: A Pilot Radiomics Study. *PLoS One* 2015; **10**: e0143308 [PMID: [26600392](https://pubmed.ncbi.nlm.nih.gov/26600392/) DOI: [10.1371/journal.pone.0143308](https://doi.org/10.1371/journal.pone.0143308)]
 - 50 **Braman N**, Prasanna P, Whitney J, Singh S, Beig N, Etesami M, Bates DDB, Gallagher K, Bloch BN, Vulchi M, Turk P, Bera K, Abraham J, Sikov WM, Somlo G, Harris LN, Gilmore H, Plecha D, Varadan V, Madabhushi A. Association of Peritumoral Radiomics With Tumor Biology and Pathologic Response to

- Preoperative Targeted Therapy for HER2 (ERBB2)-Positive Breast Cancer. *JAMA Netw Open* 2019; **2**: e192561 [PMID: 31002322 DOI: 10.1001/jamanetworkopen.2019.2561]
- 51 **Leithner D**, Horvat JV, Marino MA, Bernard-Davila B, Jochelson MS, Ochoa-Albiztegui RE, Martinez DF, Morris EA, Thakur S, Pinker K. Radiomic signatures with contrast-enhanced magnetic resonance imaging for the assessment of breast cancer receptor status and molecular subtypes: initial results. *Breast Cancer Res* 2019; **21**: 106 [PMID: 31514736 DOI: 10.1186/s13058-019-1187-z]
 - 52 **Holli-Helenius K**, Salminen A, Rinta-Kiikka I, Koskivuo I, Brück N, Boström P, Parkkola R. MRI texture analysis in differentiating luminal A and luminal B breast cancer molecular subtypes - a feasibility study. *BMC Med Imaging* 2017; **17**: 69 [PMID: 29284425 DOI: 10.1186/s12880-017-0239-z]
 - 53 **Ma W**, Ji Y, Qi L, Guo X, Jian X, Liu P. Breast cancer Ki67 expression prediction by DCE-MRI radiomics features. *Clin Radiol* 2018; **73**: 909.e1-909.e5 [PMID: 29970244 DOI: 10.1016/j.crad.2018.05.027]
 - 54 **Juan MW**, Yu J, Peng GX, Jun LJ, Feng SP, Fang LP. Correlation between DCE-MRI radiomics features and Ki-67 expression in invasive breast cancer. *Oncol Lett* 2018; **16**: 5084-5090 [PMID: 30250576 DOI: 10.3892/ol.2018.9271]
 - 55 **Liang C**, Cheng Z, Huang Y, He L, Chen X, Ma Z, Huang X, Liang C, Liu Z. An MRI-based Radiomics Classifier for Preoperative Prediction of Ki-67 Status in Breast Cancer. *Acad Radiol* 2018; **25**: 1111-1117 [PMID: 29428211 DOI: 10.1016/j.acra.2018.01.006]
 - 56 **Zhang Y**, Zhu Y, Zhang K, Liu Y, Cui J, Tao J, Wang Y, Wang S. Invasive ductal breast cancer: preoperative predict Ki-67 index based on radiomics of ADC maps. *Radiol Med* 2020; **125**: 109-116 [PMID: 31696388 DOI: 10.1007/s11547-019-01100-1]
 - 57 **Tan H**, Gan F, Wu Y, Zhou J, Tian J, Lin Y, Wang M. Preoperative Prediction of Axillary Lymph Node Metastasis in Breast Carcinoma Using Radiomics Features Based on the Fat-Suppressed T2 Sequence. *Acad Radiol* 2019 [PMID: 31879160 DOI: 10.1016/j.acra.2019.11.004]
 - 58 **Dong Y**, Feng Q, Yang W, Lu Z, Deng C, Zhang L, Lian Z, Liu J, Luo X, Pei S, Mo X, Huang W, Liang C, Zhang B, Zhang S. Preoperative prediction of sentinel lymph node metastasis in breast cancer based on radiomics of T2-weighted fat-suppression and diffusion-weighted MRI. *Eur Radiol* 2018; **28**: 582-591 [PMID: 28828635 DOI: 10.1007/s00330-017-5005-7]
 - 59 **Liu C**, Ding J, Spuhler K, Gao Y, Serrano Sosa M, Moriarty M, Hussain S, He X, Liang C, Huang C. Preoperative prediction of sentinel lymph node metastasis in breast cancer by radiomic signatures from dynamic contrast-enhanced MRI. *J Magn Reson Imaging* 2019; **49**: 131-140 [PMID: 30171822 DOI: 10.1002/jmri.26224]
 - 60 **Liu Z**, Feng B, Li C, Chen Y, Chen Q, Li X, Guan J, Chen X, Cui E, Li R, Li Z, Long W. Preoperative prediction of lymphovascular invasion in invasive breast cancer with dynamic contrast-enhanced-MRI-based radiomics. *J Magn Reson Imaging* 2019; **50**: 847-857 [PMID: 30773770 DOI: 10.1002/jmri.26688]
 - 61 **Liu J**, Sun D, Chen L, Fang Z, Song W, Guo D, Ni T, Liu C, Feng L, Xia Y, Zhang X, Li C. Radiomics Analysis of Dynamic Contrast-Enhanced Magnetic Resonance Imaging for the Prediction of Sentinel Lymph Node Metastasis in Breast Cancer. *Front Oncol* 2019; **9**: 980 [PMID: 31632912 DOI: 10.3389/fonc.2019.00980]
 - 62 **Han L**, Zhu Y, Liu Z, Yu T, He C, Jiang W, Kan Y, Dong D, Tian J, Luo Y. Radiomic nomogram for prediction of axillary lymph node metastasis in breast cancer. *Eur Radiol* 2019; **29**: 3820-3829 [PMID: 30701328 DOI: 10.1007/s00330-018-5981-2]
 - 63 **Cui X**, Wang N, Zhao Y, Chen S, Li S, Xu M, Chai R. Preoperative Prediction of Axillary Lymph Node Metastasis in Breast Cancer using Radiomics Features of DCE-MRI. *Sci Rep* 2019; **9**: 2240 [PMID: 30783148 DOI: 10.1038/s41598-019-38502-0]
 - 64 **Burnside ES**, Drukker K, Li H, Bonaccio E, Zuley M, Ganott M, Net JM, Sutton EJ, Brandt KR, Whitman GJ, Conzen SD, Lan L, Ji Y, Zhu Y, Jaffe CC, Huang EP, Freymann JB, Kirby JS, Morris EA, Giger ML. Using computer-extracted image phenotypes from tumors on breast magnetic resonance imaging to predict breast cancer pathologic stage. *Cancer* 2016; **122**: 748-757 [PMID: 26619259 DOI: 10.1002/cncr.29791]
 - 65 **Reig B**, Heacock L, Geras KJ, Moy L. Machine learning in breast MRI. *J Magn Reson Imaging* 2019 [PMID: 31276247 DOI: 10.1002/jmri.26852]
 - 66 **Schacht DV**, Drukker K, Pak I, Abe H, Giger ML. Using quantitative image analysis to classify axillary lymph nodes on breast MRI: a new application for the Z 0011 Era. *Eur J Radiol* 2015; **84**: 392-397 [PMID: 25547328 DOI: 10.1016/j.ejrad.2014.12.003]
 - 67 **Fusco R**, Sansone M, Granata V, Di Bonito M, Avino F, Catalano O, Botti G, Petrillo A. Use of Quantitative Morphological and Functional Features for Assessment of Axillary Lymph Node in Breast Dynamic Contrast-Enhanced Magnetic Resonance Imaging. *Biomed Res Int* 2018; **2018**: 2610801 [PMID: 30003092 DOI: 10.1155/2018/2610801]
 - 68 **Thompson AM**, Moulder-Thompson SL. Neoadjuvant treatment of breast cancer. *Ann Oncol* 2012; **23** Suppl 10: x231-x236 [PMID: 22987968 DOI: 10.1093/annonc/mds324]
 - 69 **Haque W**, Verma V, Hatch S, Suzanne Klimberg V, Brian Butler E, Teh BS. Response rates and pathologic complete response by breast cancer molecular subtype following neoadjuvant chemotherapy. *Breast Cancer Res Treat* 2018; **170**: 559-567 [PMID: 29693228 DOI: 10.1007/s10549-018-4801-3]
 - 70 **Yuan Y**, Chen XS, Liu SY, Shen KW. Accuracy of MRI in prediction of pathologic complete remission in breast cancer after preoperative therapy: a meta-analysis. *AJR Am J Roentgenol* 2010; **195**: 260-268 [PMID: 20566826 DOI: 10.2214/AJR.09.3908]
 - 71 **Marinovich ML**, Houssami N, Macaskill P, Sardanelli F, Irwig L, Mamounas EP, von Minckwitz G, Brennan ME, Ciatto S. Meta-analysis of magnetic resonance imaging in detecting residual breast cancer after neoadjuvant therapy. *J Natl Cancer Inst* 2013; **105**: 321-333 [PMID: 23297042 DOI: 10.1093/jnci/djs528]
 - 72 **Hylton NM**, Blume JD, Bernreuter WK, Pisano ED, Rosen MA, Morris EA, Weatherall PT, Lehman CD, Newstead GM, Polin S, Marques HS, Esserman LJ, Schnall MD; ACRIN 6657 Trial Team and I-SPY 1 TRIAL Investigators. Locally advanced breast cancer: MR imaging for prediction of response to neoadjuvant chemotherapy--results from ACRIN 6657/I-SPY TRIAL. *Radiology* 2012; **263**: 663-672 [PMID: 22623692 DOI: 10.1148/radiol.12110748]

- 73 **Yu N**, Leung VWY, Meterissian S. MRI Performance in Detecting pCR After Neoadjuvant Chemotherapy by Molecular Subtype of Breast Cancer. *World J Surg* 2019; **43**: 2254-2261 [PMID: [31101952](#) DOI: [10.1007/s00268-019-05032-9](#)]
- 74 **Michoux N**, Van den Broeck S, Lacoste L, Fellah L, Galant C, Berlière M, Leconte I. Texture analysis on MR images helps predicting non-response to NAC in breast cancer. *BMC Cancer* 2015; **15**: 574 [PMID: [26243303](#) DOI: [10.1186/s12885-015-1563-8](#)]
- 75 **Wiechmann L**, Sampson M, Stempel M, Jacks LM, Patil SM, King T, Morrow M. Presenting features of breast cancer differ by molecular subtype. *Ann Surg Oncol* 2009; **16**: 2705-2710 [PMID: [19593632](#) DOI: [10.1245/s10434-009-0606-2](#)]
- 76 **Xiong Q**, Zhou X, Liu Z, Lei C, Yang C, Yang M, Zhang L, Zhu T, Zhuang X, Liang C, Liu Z, Tian J, Wang K. Multiparametric MRI-based radiomics analysis for prediction of breast cancers insensitive to neoadjuvant chemotherapy. *Clin Transl Oncol* 2020; **22**: 50-59 [PMID: [30977048](#) DOI: [10.1007/s12094-019-02109-8](#)]
- 77 **Cain EH**, Saha A, Harowicz MR, Marks JR, Marcom PK, Mazurowski MA. Multivariate machine learning models for prediction of pathologic response to neoadjuvant therapy in breast cancer using MRI features: a study using an independent validation set. *Breast Cancer Res Treat* 2019; **173**: 455-463 [PMID: [30328048](#) DOI: [10.1007/s10549-018-4990-9](#)]
- 78 **Granzier RWY**, van Nijnatten TJA, Woodruff HC, Smidt ML, Lobbes MBI. Exploring breast cancer response prediction to neoadjuvant systemic therapy using MRI-based radiomics: A systematic review. *Eur J Radiol* 2019; **121**: 108736 [PMID: [31734639](#) DOI: [10.1016/j.ejrad.2019.108736](#)]
- 79 **Golden DI**, Lipson JA, Telli ML, Ford JM, Rubin DL. Dynamic contrast-enhanced MRI-based biomarkers of therapeutic response in triple-negative breast cancer. *J Am Med Inform Assoc* 2013; **20**: 1059-1066 [PMID: [23785100](#) DOI: [10.1136/amiainl-2012-001460](#)]
- 80 **Teruel JR**, Heldahl MG, Goa PE, Pickles M, Lundgren S, Bathen TF, Gibbs P. Dynamic contrast-enhanced MRI texture analysis for pretreatment prediction of clinical and pathological response to neoadjuvant chemotherapy in patients with locally advanced breast cancer. *NMR Biomed* 2014; **27**: 887-896 [PMID: [24840393](#) DOI: [10.1002/nbm.3132](#)]
- 81 **Thibault G**, Tudorica A, Afzal A, Chui SY, Naik A, Troxell ML, Kemmer KA, Oh KY, Roy N, Jafarian N, Holtorf ML, Huang W, Song X. DCE-MRI Texture Features for Early Prediction of Breast Cancer Therapy Response. *Tomography* 2017; **3**: 23-32 [PMID: [28691102](#) DOI: [10.18383/j.tom.2016.00241](#)]
- 82 **Parikh J**, Selmi M, Charles-Edwards G, Glendenning J, Ganeshan B, Verma H, Mansi J, Harries M, Tutt A, Goh V. Changes in primary breast cancer heterogeneity may augment midtreatment MR imaging assessment of response to neoadjuvant chemotherapy. *Radiology* 2014; **272**: 100-112 [PMID: [24654970](#) DOI: [10.1148/radiol.14130569](#)]
- 83 **Cao K**, Zhao B, Li XT, Li YL, Sun YS. Texture Analysis of Dynamic Contrast-Enhanced MRI in Evaluating Pathologic Complete Response (pCR) of Mass-Like Breast Cancer after Neoadjuvant Therapy. *J Oncol* 2019; **2019**: 4731532 [PMID: [31949430](#) DOI: [10.1155/2019/4731532](#)]
- 84 **Wu J**, Cao G, Sun X, Lee J, Rubin DL, Napel S, Kurian AW, Daniel BL, Li R. Intratumoral Spatial Heterogeneity at Perfusion MR Imaging Predicts Recurrence-free Survival in Locally Advanced Breast Cancer Treated with Neoadjuvant Chemotherapy. *Radiology* 2018; **288**: 26-35 [PMID: [29714680](#) DOI: [10.1148/radiol.2018172462](#)]
- 85 **Fusco R**, Granata V, Maio F, Sansone M, Petrillo A. Textural radiomic features and time-intensity curve data analysis by dynamic contrast-enhanced MRI for early prediction of breast cancer therapy response: preliminary data. *Eur Radiol Exp* 2020; **4**: 8 [PMID: [32026095](#) DOI: [10.1186/s41747-019-0141-2](#)]
- 86 **Mohammed ZM**, McMillan DC, Edwards J, Mallon E, Doughty JC, Orange C, Going JJ. The relationship between lymphovascular invasion and angiogenesis, hormone receptors, cell proliferation and survival in patients with primary operable invasive ductal breast cancer. *BMC Clin Pathol* 2013; **13**: 31 [PMID: [24274633](#) DOI: [10.1186/1472-6890-13-31](#)]
- 87 **Braman NM**, Etesami M, Prasanna P, Dubchuk C, Gilmore H, Tiwari P, Plecha D, Madabhushi A. Intratumoral and peritumoral radiomics for the pretreatment prediction of pathological complete response to neoadjuvant chemotherapy based on breast DCE-MRI. *Breast Cancer Res* 2017; **19**: 57 [PMID: [28521821](#) DOI: [10.1186/s13058-017-0846-1](#)]
- 88 **Zhou J**, Lu J, Gao C, Zeng J, Zhou C, Lai X, Cai W, Xu M. Predicting the response to neoadjuvant chemotherapy for breast cancer: wavelet transforming radiomics in MRI. *BMC Cancer* 2020; **20**: 100 [PMID: [32024483](#) DOI: [10.1186/s12885-020-6523-2](#)]
- 89 **Liu Z**, Li Z, Qu J, Zhang R, Zhou X, Li L, Sun K, Tang Z, Jiang H, Li H, Xiong Q, Ding Y, Zhao X, Wang K, Liu Z, Tian J. Radiomics of Multiparametric MRI for Pretreatment Prediction of Pathologic Complete Response to Neoadjuvant Chemotherapy in Breast Cancer: A Multicenter Study. *Clin Cancer Res* 2019; **25**: 3538-3547 [PMID: [30842125](#) DOI: [10.1158/1078-0432.CCR-18-3190](#)]
- 90 **Chen X**, Chen X, Yang J, Li Y, Fan W, Yang Z. Combining Dynamic Contrast-Enhanced Magnetic Resonance Imaging and Apparent Diffusion Coefficient Maps for a Radiomics Nomogram to Predict Pathological Complete Response to Neoadjuvant Chemotherapy in Breast Cancer Patients. *J Comput Assist Tomogr* 2020; **44**: 275-283 [PMID: [32004189](#) DOI: [10.1097/RCT.0000000000000978](#)]
- 91 **Hyun SJ**, Kim EK, Moon HJ, Yoon JH, Kim MJ. Preoperative axillary lymph node evaluation in breast cancer patients by breast magnetic resonance imaging (MRI): Can breast MRI exclude advanced nodal disease? *Eur Radiol* 2016; **26**: 3865-3873 [PMID: [26843011](#) DOI: [10.1007/s00330-016-4235-4](#)]
- 92 **Mattingly AE**, Mooney B, Lin HY, Kiluk JV, Khakpour N, Hoover SJ, Laronga C, Lee MC. Magnetic Resonance Imaging for Axillary Breast Cancer Metastasis in the Neoadjuvant Setting: A Prospective Study. *Clin Breast Cancer* 2017; **17**: 180-187 [PMID: [27956116](#) DOI: [10.1016/j.clbc.2016.11.004](#)]
- 93 **Ha SM**, Cha JH, Kim HH, Shin HJ, Chae EY, Choi WJ. Diagnostic performance of breast ultrasonography and MRI in the prediction of lymph node status after neoadjuvant chemotherapy for breast cancer. *Acta Radiol* 2017; **58**: 1198-1205 [PMID: [28350255](#) DOI: [10.1177/0284185117690421](#)]
- 94 **Ha R**, Chang P, Karcich J, Mutasa S, Fardanesh R, Wynn RT, Liu MZ, Jambawalikar S. Axillary Lymph Node Evaluation Utilizing Convolutional Neural Networks Using MRI Dataset. *J Digit Imaging* 2018; **31**:

- 851-856 [PMID: 29696472 DOI: 10.1007/s10278-018-0086-7]
- 95 **Ha R**, Chin C, Karcich J, Liu MZ, Chang P, Mutasa S, Pascual Van Sant E, Wynn RT, Connolly E, Jambawalikar S. Prior to Initiation of Chemotherapy, Can We Predict Breast Tumor Response? Deep Learning Convolutional Neural Networks Approach Using a Breast MRI Tumor Dataset. *J Digit Imaging* 2019; **32**: 693-701 [PMID: 30361936 DOI: 10.1007/s10278-018-0144-1]
- 96 **Ha R**, Chang P, Karcich J, Mutasa S, Van Sant EP, Connolly E, Chin C, Taback B, Liu MZ, Jambawalikar S. Predicting Post Neoadjuvant Axillary Response Using a Novel Convolutional Neural Network Algorithm. *Ann Surg Oncol* 2018; **25**: 3037-3043 [PMID: 29978368 DOI: 10.1245/s10434-018-6613-4]
- 97 **Ashraf AB**, Daye D, Gavenonis S, Mies C, Feldman M, Rosen M, Kontos D. Identification of intrinsic imaging phenotypes for breast cancer tumors: preliminary associations with gene expression profiles. *Radiology* 2014; **272**: 374-384 [PMID: 24702725 DOI: 10.1148/radiol.14131375]
- 98 **Ganeshan B**, Panayiotou E, Burnand K, Dizdarevic S, Miles K. Tumour heterogeneity in non-small cell lung carcinoma assessed by CT texture analysis: a potential marker of survival. *Eur Radiol* 2012; **22**: 796-802 [PMID: 22086561 DOI: 10.1007/s00330-011-2319-8]
- 99 **Li H**, Zhu Y, Burnside ES, Drukker K, Hoadley KA, Fan C, Conzen SD, Whitman GJ, Sutton EJ, Net JM, Ganott M, Huang E, Morris EA, Perou CM, Ji Y, Giger ML. MR Imaging Radiomics Signatures for Predicting the Risk of Breast Cancer Recurrence as Given by Research Versions of MammaPrint, Oncotype DX, and PAM50 Gene Assays. *Radiology* 2016; **281**: 382-391 [PMID: 27144536 DOI: 10.1148/radiol.2016152110]
- 100 **Ha R**, Chang P, Mutasa S, Karcich J, Goodman S, Blum E, Kalinsky K, Liu MZ, Jambawalikar S. Convolutional Neural Network Using a Breast MRI Tumor Dataset Can Predict Oncotype Dx Recurrence Score. *J Magn Reson Imaging* 2019; **49**: 518-524 [PMID: 30129697 DOI: 10.1002/jmri.26244]
- 101 **Harris LN**, Ismaila N, McShane LM, Andre F, Collyar DE, Gonzalez-Angulo AM, Hammond EH, Kuderer NM, Liu MC, Mennel RG, Van Poznak C, Bast RC, Hayes DF; American Society of Clinical Oncology. Use of Biomarkers to Guide Decisions on Adjuvant Systemic Therapy for Women With Early-Stage Invasive Breast Cancer: American Society of Clinical Oncology Clinical Practice Guideline. *J Clin Oncol* 2016; **34**: 1134-1150 [PMID: 26858339 DOI: 10.1200/JCO.2015.65.2289]
- 102 **Saha A**, Harowicz MR, Wang W, Mazurowski MA. A study of association of Oncotype DX recurrence score with DCE-MRI characteristics using multivariate machine learning models. *J Cancer Res Clin Oncol* 2018; **144**: 799-807 [PMID: 29427210 DOI: 10.1007/s00432-018-2595-7]
- 103 **Park H**, Lim Y, Ko ES, Cho HH, Lee JE, Han BK, Ko EY, Choi JS, Park KW. Radiomics Signature on Magnetic Resonance Imaging: Association with Disease-Free Survival in Patients with Invasive Breast Cancer. *Clin Cancer Res* 2018; **24**: 4705-4714 [PMID: 29914892 DOI: 10.1158/1078-0432.CCR-17-3783]
- 104 **Koh J**, Lee E, Han K, Kim S, Kim DK, Kwak JY, Yoon JH, Moon HJ. Three-dimensional radiomics of triple-negative breast cancer: Prediction of systemic recurrence. *Sci Rep* 2020; **10**: 2976 [PMID: 32076078 DOI: 10.1038/s41598-020-59923-2]
- 105 **Kim S**, Kim MJ, Kim EK, Yoon JH, Park VY. MRI Radiomic Features: Association with Disease-Free Survival in Patients with Triple-Negative Breast Cancer. *Sci Rep* 2020; **10**: 3750 [PMID: 32111957 DOI: 10.1038/s41598-020-60822-9]

Artificial intelligence in pancreatic disease

Bang-Bin Chen

ORCID number: Bang-Bin Chen
0000-0001-7058-1427.

Author contributions: Chen BB wrote and revised the manuscript.

Supported by grants from the Ministry of Science and Technology (Taiwan), No. 104-2314-B-002-080-MY3 and No. 107-2314-B-002-102-MY3.

Conflict-of-interest statement: No conflict of interest.

Open-Access: This article is an open-access article that was selected by an in-house editor and fully peer-reviewed by external reviewers. It is distributed in accordance with the Creative Commons Attribution NonCommercial (CC BY-NC 4.0) license, which permits others to distribute, remix, adapt, build upon this work non-commercially, and license their derivative works on different terms, provided the original work is properly cited and the use is non-commercial. See: <http://creativecommons.org/licenses/by-nc/4.0/>

Manuscript source: Invited manuscript

Received: June 9, 2020

Peer-review started: June 9, 2020

First decision: June 15, 2020

Revised: June 18, 2020

Accepted: June 20, 2020

Article in press: June 20, 2020

Bang-Bin Chen, Department of Medical Imaging, National Taiwan University Hospital, Taipei 10016, Taiwan

Bang-Bin Chen, Department of Radiology, College of Medicine, National Taiwan University, Taipei 10016, Taiwan

Corresponding author: Bang-Bin Chen, MD, Associate Professor, Department of Medical Imaging, National Taiwan University College of Medicine and Hospital, No. 7, Chung-Shan South Road, Taipei 10016, Taiwan. bangbin@gmail.com

Abstract

In recent years, the application of artificial intelligence (AI) in radiology has been growing rapidly, fueled by the availability of large datasets, advances in computing power, and newly developed algorithms. Progress in AI applied to medical imaging analyses has transformed these images into quantitative data, termed radiomics. When combined with patients' clinical data, these models, when developed by machine learning, have the potential to improve diagnostic, prognostic, and predictive accuracy. Currently, limited literature is available on the use of radiomics for pancreatic disease. Here, we will review recent studies in the application of AI in a variety of pancreatic diseases, mainly involving lesion detection, tumor characterization, tumor grading, response, and prognosis evaluation. Finally, we will also discuss the challenges and prospects in the field of radiomics for pancreatic disease.

Key words: Artificial intelligence; Machine learning; Deep learning; Radiomics; Texture analysis, Pancreas

©The Author(s) 2020. Published by Baishideng Publishing Group Inc. All rights reserved.

Core tip: The integration of radiomics, clinical data, and advanced machine-learning methodologies will improve diagnostic, prognostic, and predictive accuracy in patients with pancreatic disease, and facilitate clinical decision and management towards precision medicine.

Citation: Chen BB. Artificial intelligence in pancreatic disease. *Artif Intell Med Imaging* 2020; 1(1): 19-30

URL: <https://www.wjgnet.com/2644-3260/full/v1/i1/19.htm>

DOI: <https://dx.doi.org/10.35711/aimi.v1.i1.19>

Published online: June 28, 2020

P-Reviewer: Cimen SG

S-Editor: Wang JL

L-Editor: A

E-Editor: Xing YX



INTRODUCTION

Artificial intelligence (AI) describes the use of computers to simulate performance and critical thinking equivalent to a human being. Its application in radiology has been growing rapidly, powered by the availability of large datasets, advances in computing power, and newly developed algorithms^[1]. The progress in AI of medical imaging analyses has converted these images into quantitative and minable data to facilitate better clinical decisions and management^[2,3]. This comprehensive method, when used to analyze high-dimensional quantitative features from multimodality medical images, is known as radiomics^[4].

To establish robust quantitative image analyses, standardized methodologies are required based on various image modalities, such as those of computed tomography (CT), magnetic resonance imaging (MRI), and positron emission tomography (PET), especially for texture- and filter-based features^[5,6]. After the mining of correlations between these features and diagnosis/prognosis of tumors, tumors can then be decoded into different imaging phenotypes^[7]. These data are then combined with other patients' data to develop models that can potentially enhance diagnostic, prognostic, and predictive accuracy^[8]. Because these analyses are based on the standard of care images, it is imaginable that radiomics analysis will eventually become routine practice^[9,10].

There are three approaches to data-mining for radiomics, including hand-crafted features, deep features, and a hybrid method. Traditional radiomics is done with the computation of agnostic hand-crafted features, which are computed automatically by image analysis algorithms^[5]. For instance, texture analysis has been widely used to quantify intuitive qualities by measuring the spatial variation in pixel intensities on images. In contrast to traditional radiomics, deep-learning extracts deep features from medical images based on the specifications of a pre-defined task, including disease diagnostics, cancer type prediction, or survival prediction. These deep features can be obtained via various architectures, such as a convolutional neural network (CNN), to find the most relevant features related to a pre-defined task^[11]. Thus, they can automatically learn the best features for a given task, without the need for human involvement for feature design. Recent studies have shown better performance by deep learning methods over traditional radiomics^[12,13]. Besides, the hybrid method, which combines hand-crafted and deep features, could provide complementary information for the radiological evaluation in cancer patients^[14-16].

The currently available literature on the use of radiomics for pancreatic disease is limited. Here, we will review recent studies in the application of texture analysis and radiomics in pancreatic malignancy, mainly involving cancer detection, grading, response, and prognosis evaluation. We will also review the performance of radiomics in differentiating between pancreatic cancer and other benign pancreatic lesions, such as autoimmune pancreatitis (AIP) and mass-forming pancreatitis (MFP). Finally, we will discuss the challenges and prospects in the field of radiomics for pancreatic disease. A summary table (Table 1) is also presented based on our review of the recent literature.

PANCREATIC DUCTAL ADENOCARCINOMA

Pancreatic ductal adenocarcinoma (PDAC) is the third leading cause of cancer-related deaths in the USA. The 5-year survival for PDAC is only 8%, due to its aggressive nature and late-stage presentation when discovered in most patients^[17]. Therefore, early detection of PDAC is critical, because surgical resection is the only method to cure this disease. In patients receiving a surgical intervention, the involvement of regional lymph nodes and residual tumor at the surgical margin are also important issues related to survival outcome. In patients with metastatic disease receiving chemotherapy or radiotherapy, the use of radiomics to predict treatment response is being investigated.

Early detection of pancreatic ductal adenocarcinoma

Radiomics might offer an advantage over other techniques in the early detection of PDAC. This is because the subtle difference of the texture patterns between early cancer and normal pancreas might be discernable using radiomic features prior to visual detection.

Chu *et al*^[18] used 3D CT radiomic features to differentiate PDAC and normal pancreas by manually segmented features of the pancreas. The dataset included 190

Table 1 Recent publications using artificial intelligence and radiomics in pancreatic disease

Ref.	Year	Disease	Number	Training/testing	Modality	Design	Feature selection	Results
PADC detection								
Chu <i>et al</i> ^[18]	2019	PDAC <i>vs</i> normal	190:190	255/125	CT	Retrospective	RF	Accuracy: 99.2%; AUC: 0.99
Liu <i>et al</i> ^[19]	2020	PDAC <i>vs</i> normal	370:320	PDAC: 295/256; Normal: 75/64	CT	Retrospective	CNN	Accuracy: 98.6-98.9%; AUC: 0.997-0.999
Li <i>et al</i> ^[21]	2020	LN metastasis	159	118/41	CT	Retrospective	LASSO	Combined model; AUC: Training/test = 0.944/0.912
Bian <i>et al</i> ^[22]	2019	LN metastasis	225	-	CT	Retrospective	LASSO	The arterial rad-score is associated with the risk of LN metastasis.
Hui <i>et al</i> ^[25]	2020	R0 <i>vs</i> R1 after PD	34:52	-	CT	Retrospective	SVM	AUC: 0.8614 Accuracy: 84.88%
Bian <i>et al</i> ^[26]	2020	SMV margin (R0 <i>vs</i> R1) after PD	127:54	-	CT	Retrospective	LASSO	AUC: 0.75
Zhang <i>et al</i> ^[28]	2018	POPF after PD	117	80/37	CT	Retrospective	LASSO	AUC: Training/test = 0.8248/0.7609
Xie <i>et al</i> ^[32]	2020	PFS and OS	220	147/73	CT	Retrospective	LASSO	Rad-score is better than clinical model and TNM system
Cozzi <i>et al</i> ^[33]	2019	OS and local control after SBRT	100	60/40	CT	Retrospective	Elastic net regularization, Cox regression models	Identify low and high-risk groups
IPMN								
Chakraborty <i>et al</i> ^[41]	2018	Low risk <i>vs</i> high risk	103	-	CT	Retrospective	RF, SVM	AUC: 0.77
Corral <i>et al</i> ^[42]	2019	Normal pancreas, low-grade dysplasia, high-grade dysplasia, and adenocarcinoma	139 (31:48:20:40)	-	MRI	Retrospective	Deep learning	AUC: 0.78
PNET								
Liang <i>et al</i> ^[49]	2019	Grade 1 <i>vs</i> 2/3	137	86/51	CT	Retrospective	LASSO	AUC: Training/test = 0.907/0.891
Gu <i>et al</i> ^[50]	2019	Grade 1 <i>vs</i> 2/3	138	104/34	CT	Retrospective	MRMR, RF	AUC: Training/test = 0.974/0.902
Bian <i>et al</i> ^[51]	2020	Grade 1 <i>vs</i> 2/3 (non-functional)	139	97/42	MRI	Retrospective	LASSO and LDA	AUC: Training/test = 0.851/0.736
Other pancreatic lesions								
Park <i>et al</i> ^[54]	2020	AIP <i>vs</i> PDAC	85: 93	60/29: 60/33	CT	Retrospective	RF	Accuracy: 95.2%; AUC: 0.975
Zhang <i>et al</i> ^[55]	2019	AIP <i>vs</i> PDAC	45: 66	-	PET/CT	Retrospective	RF, adaptive boosting, SVM	Accuracy: 85%; AUC: 0.93
Ren <i>et al</i> ^[56]	2019	MFP <i>vs</i> PDAC	79: 30	69/40	CT	Retrospective	Mann-Whitney U test, MRMR	AUC: 0.98

Mashayekhi <i>et al</i> ^[57]	2020	Functional abdominal pain, recurrent acute pancreatitis, chronic pancreatitis	20:19:17	-	CT	Retrospective	Isomap and SVM	Accuracy: 82.1%
Yang <i>et al</i> ^[58]	2019	Serous <i>vs</i> mucinous cystadenoma	53: 25	4:1	CT	Retrospective	RF	Accuracy: 83%; AUC: 0.75

AIP: Autoimmune pancreatitis; AUC: Area under receiver operating characteristic curve; CNN: Convolutional neural network; DFS: Disease-free survival; IPMN: Intraductal papillary mucinous neoplasms; LASSO: Least absolute shrinkage and selection operator; LDA: Linear discriminative analysis; LN: Lymph node; MFP: Mass-forming pancreatitis; MRMR: Minimum redundancy maximum relevance; OS: Overall survival; PD: Pancreaticoduodenectomy; PDAC: Pancreatic ductal adenocarcinoma; PET: Positron emission tomography; PFS: Progression-free survival; PNET: Pancreatic neuroendocrine tumor; POPF: Postoperative pancreatic fistula; RF: Random forest; SBRT: Stereotactic body radiation therapy; SVM: Support vector machine; SMV: Superior mesenteric vein.

patients with PDAC and 190 healthy controls, and was divided into 255 training and 125 validation cases. A total of 478 features was extracted, and 40 features were selected for analysis by a random forest (RF) classifier. The overall accuracy was 99.2%, and the area under the curve (AUC) was 99.9%. The results were encouraging for using radiomics in the early detection of PDAC, but a limitation of this study was that the manual segmentation of pancreas boundaries was a labor-intensive work and required expert knowledge of radiologists.

To overcome this limitation, Liu *et al*^[19] used CNN to distinguish 370 patients with pancreatic cancer and 320 normal controls. CT images were preprocessed into patches to classify as cancerous or non-cancerous. In local test sets, CNN-based analysis had an accuracy of 0.986–0.989 and AUC of 0.997–0.999. In the test set (281 pancreatic cancers and 82 controls) of a different country, the accuracy was 0.832 and AUC was 0.920. The sensitivity for tumors smaller than 2 cm was 92.1% in the local test sets and 63.1% in the other country test set. When compared with radiologists' interpretation, CNN-based analysis achieved higher sensitivity than radiologists. Therefore, this method could be incorporated into the development of computer-aided detection software for pancreatic cancer detection. In clinical practice, other benign lesions, such as MFP or AIP, might mimic PDAC. Whether CNNs can distinguish between PDAC and other pancreatic pathologies, such as pancreatitis and other pancreatic tumors, must also be further studied. Besides, about 11%–27% of pancreatic cancer is enhancing the pancreatic parenchyma and not visible on contrast-enhanced CT^[20]. It is interesting to see whether radiomics can detect this particular type of PDAC.

Predicting lymph node metastasis

Accurate identification of the extent of lymph node (LN) metastasis is critical for the determination of surgical methods in resectable PDAC.

Li *et al*^[21] developed a model integrating clinical data and imaging features extracted from venous phase CT to predict LN metastasis. Their study included 159 patients with PDAC (118 in the primary cohort and 41 in the validation cohort). A total of 2041 radiomics features were extracted, and 15 features were selected for constructing the radiomics signature in the primary cohort. A combined prediction model was built by integrating the radiomics signature and clinical characteristics selected by using multivariable logistic regression. The combined prediction model reached a better discrimination power than the clinical prediction model, with an AUC of 0.944 *vs* 0.666 in the primary cohort, and 0.912 *vs* 0.713 in the validation cohort.

Bian *et al*^[22] used arterial phase CT images to predict LN metastasis in 225 patients. A total of 1029 radiomics features of the arterial phase were extracted and then reduced using the least absolute shrinkage and selection operator logistic regression (LASSO) algorithm. Multivariate logistic regression models were used to analyze the association. The radiomics score (rad-score), which consisted of 12 selected features, was significantly associated with LN status, both in univariate and multivariate analyses. Higher arterial rad-score was also associated with LN metastasis. In the future, it is necessary to establish a one-to-one correlation between the imaging findings and the pathological evidence of LN metastasis.

Predicting surgical margin and postoperative pancreatic fistula after pancreaticoduodenectomy

In a pathological examination after pancreaticoduodenectomy (PD), a resection margin

without cancer cells in 1 mm is considered as R0; a resection margin with cancer cells in 1 mm is considered as R1. The preoperative identification of R0 and R1 is a determining factor for surgical decisions and prognosis^[23,24].

Hui *et al*^[25] retrospectively analyzed CT images of 86 patients (34 cases of R0 and 52 cases of R1) with pancreatic head PDAC and that underwent PD. The radiomics features were reduced using principal component analysis. The support vector machine (SVM) with a linear kernel was used to classify the resection margins with leave-one-out cross-validation. The results achieved an AUC of 0.8614 and an accuracy of 84.88%. Two features of the run-length matrix, which are derived from diagonal sub-bands in wavelet decomposition, showed significant differences between R0 and R1.

Similarly, Yun *et al*^[26] used a portal rad-score to predict pathologic superior mesenteric vein (SMV) resection margin in 181 patients. For each patient, 1029 radiomics features of the portal phase were extracted, which were reduced using the LASSO logistic regression algorithm. The rad-score was significantly associated with the SMV resection margin status. The portal rad-score had an accuracy of 71.3% and AUC of 0.750. Although radiomics seem promising in predicting SMV section margin, assessment of all pancreatic resection margins is needed to predict patients' outcomes. Furthermore, the radiomic features of mesopancreas (located between the superior mesenteric artery and the uncinate process) are more likely to predict the status of the section margin than those of a primary tumor, because it is regarded as the primary site of cancer cell infiltration^[27].

Zhang *et al*^[28] used radiomic features extracted from the portal venous phase CT for the preoperative prediction of postoperative pancreatic fistula (POPF) in 117 patients receiving PD. The rad-score was constructed by LASSO, and its performance was compared with standard pancreatic Fistula Risk Score. Their rad-score could predict POPF with an AUC of 0.8248 in the training cohort (80 patients) and of 0.7609 in the validation cohort (39 patients). In addition, the AUC of the rad-score was statistically higher than the Fistula Risk Score for predicting POPF in both cohorts.

Predicting therapy response

Many researchers have utilized radiomic features derived from pretreatment CT to identify imaging phenotypes that might predict the treatment response in patients with PDAC.

Chen *et al*^[29] assessed the response of pancreatic head cancer during chemoradiation therapy in 20 patients. They found that significant changes in CT radiomic features were observed during therapy based on quantitative analysis of daily CT. In cases of good response, patients tend to have large reductions in mean histograms of CT number and skewness, and large increases in standard deviation and kurtosis. Thus, a high reduction of these features might suggest early treatment response and could be used to identify patients that need therapeutic intensification.

Borazanci *et al*^[30] used texture analysis to predict treatment response to poly adenosine diphosphate-ribose polymerase (PARP) inhibitors. In 13 patients with PDAC who have deoxyribonucleic acid damage repair deficiency mutations, exploratory analysis of index lesions revealed correlations between lesion texture features with overall survival (OS), and also with time on PARP inhibitors.

Yue *et al*^[31] stratified patients into low and high-risk groups using pre- and post-radiotherapy 18F-FDG-PET/CT images from 26 patients. A total of 48 texture and clinical variables were identified, and the prognostic heterogeneity features were selected using LASSO/elastic net regression and multivariate Cox analysis. After radiotherapy, the metabolic activity in the primary tumor was suppressed, and underlying tissue heterogeneity was reduced. The authors identified five significant variables: Age, node stage, variations of homogeneity, variance, and cluster tendency. These patients could be stratified into two risk groups: A low-risk group ($n = 11$) with a longer mean OS and higher texture variation ($> 30\%$), and a high-risk group ($n = 15$) with a shorter mean OS and lower texture variation ($< 15\%$). The authors concluded that locoregional metabolic texture response might predict clinical outcomes following radiotherapy.

Predicting prognosis

Recent studies have suggested that radiomic features extracted from CT and PET were predictive of the survival outcome of PDAC patients.

Xie *et al*^[32] developed a CT-based radiomics nomogram for survival prediction in patients with resected PDAC in 220 patients (training = 147; validation = 73). A total of 300 radiomic features were extracted, followed by LASSO with multivariate regression analysis. The rad-score was significantly associated with disease-free survival (DFS)

and OS. Radiomics nomogram could better predict survival than the clinical model, and the TNM staging system could. However, there was no association between the rad-score and recurrence patterns.

Cozzi *et al*^[33] used CT radiomics signature to predict clinical outcomes after stereotactic body radiation therapy in 100 patients (training = 60; validation = 40) and found a clinical-radiomics signature was associated with OS and local control.

The value of texture features to predict prognosis and help clinical management in PDAC patients has been evaluated in several studies. In patients undergoing surgical resection, Kim *et al*^[34] found that high grey-level non-uniformity values suggested shorter recurrence-free survival in 116 patients, suggesting that high tumor heterogeneity was a poor prognostic indicator. However, Yun *et al*^[35] found that lower average values with homogeneous features (lower standard deviation and contrast and higher correlation) were significantly associated with poorer DFS in 18 patients. They conjectured that homogeneous texture features could represent more aggressive tumor nature, resulting from higher cellular density or dense desmoplasia. Besides, Eilaghi *et al*^[36] found that high tumor dissimilarity (high heterogeneity) and low inverse difference normalized (low heterogeneity) were associated with better OS in 30 patients. Therefore, the results of correlations between tumor heterogeneity with surgical outcome were contradictory and need further investigation.

In patients with unresectable PDAC treated with chemotherapy, Cheng *et al*^[37] found pretreatment CT texture analysis was associated with PFS and OS in 41 patients. Besides, a combination of pretreatment standard deviation (spatial scaling factor = 3) with tumor size in the survival model performed better than the standard deviation alone. Similarly, Sandrasegaran *et al*^[38] found that texture features of the mean value of positive pixels and kurtosis at medium spatial filters had a significant correlation with OS in 60 patients.

Hyun *et al*^[39] evaluated intratumoral heterogeneity measured by 18F-FDG PET texture analysis in 137 patients. The best imaging biomarker for OS prediction was first-order entropy (AUC = 0.720), followed by total lesion glycolysis (AUC = 0.697), metabolic tumor volume (AUC = 0.692), and maximum standard uptake value (AUC = 0.625). Multivariable Cox analysis demonstrated that higher entropy was independently associated with worse survival. Thus, first-order entropy is a better quantitative imaging biomarker of prognosis than conventional PET parameters.

INTRADUCTAL PAPILLARY MUCINOUS NEOPLASMS GRADE AND RISK

Intraductal papillary mucinous neoplasms (IPMN) represents 15%–30% of cystic lesions of the pancreas. They are premalignant tumors that can progress from low-grade dysplasia to high-grade dysplasia to invasive cancer, accounting for 20%–30% of pancreatic cancer^[40]. The ability to identify IPMNs with low or high risk and malignant transformation into invasive cancer would optimize treatment strategy and improve surgical decision-making.

Chakraborty *et al*^[41] retrospectively analyzed pancreatic cyst and parenchyma regions on preoperative CT in 103 patients with pathologically proven branch duct-IPMN to predict IPMN risk. Expert pathologists categorized IPMNs as low or high risk following resection. A total of 131 texture features were derived from each cyst and pancreas regions. Five clinical variables were combined with imaging features to design prediction models. Their results of CT features achieved an AUC of 0.77, and the combination model obtained an AUC of 0.81.

Corral *et al*^[42] developed a new deep learning protocol on MRI to identify neoplasia for IPMN in 139 cases. A computer-aided framework was designed using CNN to classify IPMN. Their cases included normal pancreas (20%), low-grade dysplasia (34%), high-grade dysplasia (14%), and adenocarcinoma (29%). The sensitivity and specificity of the deep learning protocol to detect dysplasia were 92% and 52%, and to detect high-grade dysplasia or cancer were 75% and 78%, respectively. The deep learning protocol showed accuracy (AUC = 0.78) comparable to current radiographic criteria (American Gastroenterology Association, AUC = 0.76; Fukuoka, AUC = 0.77). Their computer-aided frameworks could assist in identifying high-risk IPMN.

Hanania *et al*^[43] investigated 360 texture features on CT images in 53 patients with IPMN (34 high-grade and 19 low-grade). These authors identified 14 imaging features within the gray-level co-occurrence matrix that predicted histopathological grade. The most predictive feature differentiated low-grade and high-grade lesions with an AUC of 0.82 (sensitivity 85%, specificity 68%). Using a cross-validated design, the best logistic regression yielded an AUC of 0.96 (sensitivity 97%, specificity of 88%).

Permuth *et al*^[44] evaluated 38 IPMNs (20 benign, 18 malignant) with preoperative CT radiomic data and matched plasma-based miRNA genomic classifier data. The miRNA classifier, high-risk, and worrisome radiologic features had AUC values of 0.83, 0.84, and 0.54, respectively. Fourteen CT radiomic features differentiated malignant from benign IPMNs with an AUC of 0.77. Combining radiomic features with the miRNA classifier revealed an AUC of 0.92 and superior predictive performance than other models. This study suggested that radiogenomic approach might more accurately predict IPMN pathology than radiologic features in consensus guidelines.

PANCREATIC NEUROENDOCRINE TUMOR GRADES

Recent updates of the World Health Organization classification separate pancreatic neuroendocrine tumor (PNET) into two broad categories, including the Ki-67 proliferative index and mitotic counts: Well-differentiated PNET and poorly differentiated pancreatic neuroendocrine carcinoma (PNEC). The classification also incorporates a new subcategory of well-differentiated grade 3 (G3) PNET^[45]. The assessment of tumor grade is essential for the prediction of prognosis and choice of the proper treatment strategy.

D'Onofrio *et al*^[46] evaluated 3D CT-texture analysis in 100 patients with NET [grade 1 (G1) in 31, grade 2 (G2) in 52, and G3 in 17 cases]. Their results showed kurtosis was significantly different among the three groups, and entropy was significantly different between the G1 and G3 groups and between the G2 and G3 groups.

Guo *et al*^[47] evaluated CT images of 37 patients (G1 in 13, G2 in 11, and G3 in 13 cases). Arterial enhancement ratio and portal enhancement ratio showed the best sensitivity (0.86–0.94) and specificity (0.92–1.0) for differentiating G3 from G1/G2, while the mean grey-level intensity, entropy, and uniformity showed acceptable sensitivity (0.73–0.91) and specificity (0.85–1.0). Mean grey-level intensity also showed acceptable sensitivity (91% to 100%) and specificity (82% to 91%) in differentiating G1 from G2.

Canellas *et al*^[48] evaluated CT images of 101 patients (G1 in 63, G2 in 35, and G3 in 3 cases). The CT features predictive of G2/3 were size larger than 2.0 cm, presence of vascular involvement, pancreatic ductal dilatation, and lymphadenopathy. The texture parameter entropy was also predictive of more aggressive tumors. Tumors with high grade (G2/3), vascular invasion, and high entropy had shorter PFS after surgical resection.

Liang *et al*^[49] used arterial phase CT to preoperatively differentiate grade 1 and grade 2/3 NET of 137 patients (training = 86, validation = 51). The Mann-Whitney U test and LASSO were applied for feature selection, and an eight-feature-combined radiomics signature was constructed. The nomogram model combining the radiomics signature with the clinical stage had the best performance (training AUC = 0.907; validation AUC = 0.891). A significant correlation was found between the nomogram model and the Ki-67 index and the rate of nuclear mitosis. The survivals of predicted grade 1 and grade 2/3 groups were significantly different.

Gu *et al*^[50] used arterial and portal venous phase CT images for preoperatively predicting grade 1 and grade 2/3 NET in 138 patients (training = 104, validation = 34). A total of 853 radiomic features were extracted. Minimum redundancy, maximum relevance, and RF methods were adopted for the feature selection. The radiomics signature had a significant association with histologic grade. The nomogram incorporating independent clinical risk factor, tumor margin, and fusion radiomics signature showed strong discrimination in the training cohort (AUC = 0.974) and validation cohort (AUC = 0.902) with good calibration.

Bian *et al*^[51] used 3T MRI for the preoperative prediction of nonfunctional PNET grade in 139 cases (training = 97, validation = 42). The LASSO and linear discriminative analysis were used to select the features and to construct a radiomics model. The clinical model revealed an AUC of 0.769 in the training cohort and 0.729 in the validation cohort. The mixed model, which combined the radiomics signature and 14 imaging features, yielded AUC values of 0.870 and 0.701. Thus, the noncontrast MRI could be used as a screening tool to help differentiate G1 and G2/3 tumors.

Currently, most studies have attempted to differentiate between G1 and G2/3 PNETs. However, the 5-year survival rates were 75%, 62%, and 7% for G1, G2, and G3, respectively^[52]. It would be more valuable to show the diagnostic values of the nomogram model in differentiating G1/G2 and G3. Furthermore, the G3 tumors are divided into two subgroups: Well-differentiated PNETs G3 and PNEC^[53]. The prognosis of the two subgroups is also different. Further studies are now needed to

differentiate well-differentiated PNET G3 and PNEC, and between PNETs G1/G2 and G3.

PANCREATIC TUMOR CHARACTERIZATION

Autoimmune pancreatitis vs pancreatic ductal adenocarcinoma

AIP has similar clinical and radiological presentations to PDAC, but the treatments of these two entities are different. Patients with AIP might be treated with oral corticosteroids, but patients with PDAC need surgical resection and chemotherapy. Thus, the differentiation of these two entities is imperative to avoid unnecessary surgical resections in patients with AIP or delayed treatment in patients with PDAC.

Park *et al*^[54] used CT-based machine learning of radiomic features to distinguish AIP from PDAC. Eighty-nine patients with AIP and 93 patients with PDAC were retrospectively included. Four-hundred-thirty-one radiomic features were extracted, and a RF method was used to discriminate AIP from PDAC. The radiomic features help differentiate AIP from PDAC with a sensitivity of 89.7%, specificity of 100%, accuracy of 95.2%, and AUC of 0.975.

Zhang *et al*^[55] used 18F FDG PET/CT to distinguish AIP from PDAC in 111 patients (AIP = 45, PDAC = 66). They extracted 251 features from 2D and 3D images and recombined these features into five feature sets according to their modalities and dimensions. Four machine learning classifiers were evaluated. CT features and 3D features performed better than PET features and 2D features, respectively. Multidomain features were superior to single domain features. In addition, the combination of the SVM-recursive feature elimination feature selection strategy and linear SVM classifier had the best performance (AUC = 0.93, accuracy = 0.85). The radiomics model was significantly superior to both human doctors and clinical factors-based prediction models.

The results of these studies are encouraging. For future work, combined features extracted from CNNs and more clinical factors to differentiate these two diseases would be an interesting direction to pursue.

Mass-forming pancreatitis vs pancreatic ductal adenocarcinoma

Ren *et al*^[56] used arterial and portal phase CT texture analysis to differentiate 30 patients with MFP and 79 patients with PDAC. Arterial CT attenuation, arterial, and portal enhancement ratios of MFP were higher than PDAC. Arterial CT attenuation and pancreatic duct penetrating sign were independent predictors in multivariate analysis. AUC of imaging feature-based, texture feature-based in arterial and portal phases, and the combined models were 0.84, 0.96, 0.93, and 0.98, respectively. Thus, CT texture analysis holds great potential to differentiate MFP from PDAC.

Mashayekhi *et al*^[57] used CT radiomics to differentiate 56 patients with recurrent acute pancreatitis ($n = 20$), functional abdominal pain ($n = 19$), or chronic pancreatitis ($n = 17$). In 54 radiomic features extracted by one-vs-one Isomap SVM classifier, 11 radiomic features were significantly different between the patient groups with an overall accuracy of 82.1%.

Serous and mucinous cystadenomas

Yang *et al*^[58] used CT textural features in the differential diagnosis of pancreatic serous cystadenomas ($n = 53$) and mucinous cystadenomas ($n = 25$). Textural parameters were analyzed using RF and LASSO methods. Patients were divided into training and validation sets with a ratio of 4:1. Radiomic features were able to separate serous from mucinous cystadenomas in both the training group (slice thickness of 5 mm, AUC 0.72, accuracy 0.86) and the validation group (AUC 0.75, accuracy 0.83). These results might provide a noninvasive approach to determine whether surgery or imaging follow up is suitable for these patients.

CHALLENGES AND PROSPECTS OF ARTIFICIAL INTELLIGENCE IN THE PANCREAS

There are three main challenges for the application of AI in the pancreas. First, the image analysis methods are diverse and variable, so many study results are inconsistent and contradictory. To ensure the availability of accurate and reproducible radiomics data, the initiatives to standardize the development of quantitative imaging

biomarkers have recently been developed^[59]. Second, the public data of pancreatic imaging available for machine-learning is insufficient, because most early pancreatic lesions are small and occult, and require labor-intensive work from experienced radiologists to label the target lesion. Automatic detection and segmentation of these pancreatic lesions, either with or without the aid of a radiologist, is needed to solve this issue. Third, most studies are retrospective, with limited clinical, laboratory, and outcome data. Previous studies have shown that combined models of radiomic and clinical factors achieve better performance than each individual model. Upcoming prospective studies that combined radiomics and clinical data, even with genomic data, are warranted. Ultimately, it is only with the availability of robust integrated radiomics and comprehensive clinical data that we can proceed to deploy AI in daily practice to improve the care of our patients.

CONCLUSION

The pancreas has both an endocrine and an exocrine digestive function, and its imaging presentations are diverse and frequently pose a diagnostic dilemma in clinical settings. The use of AI will greatly facilitate accurate pancreatic lesion detection, characterization, treatment response evaluation, and prognosis prediction in these patients. Currently, radiomics is under rigorous investigation in various pancreatic diseases, and recent study results are promising. With the growth of advanced AI technology and the availability of standardized imaging data, it seems likely that we will accomplish the goal of precision medicine and increase patients' outcomes in the near future.

REFERENCES

- 1 **Hosny A**, Parmar C, Quackenbush J, Schwartz LH, Aerts HJWL. Artificial intelligence in radiology. *Nat Rev Cancer* 2018; **18**: 500-510 [PMID: 29777175 DOI: 10.1038/s41568-018-0016-5]
- 2 **Thrall JH**, Li X, Li Q, Cruz C, Do S, Dreyer K, Brink J. Artificial Intelligence and Machine Learning in Radiology: Opportunities, Challenges, Pitfalls, and Criteria for Success. *J Am Coll Radiol* 2018; **15**: 504-508 [PMID: 29402533 DOI: 10.1016/j.jacr.2017.12.026]
- 3 **Savadjiev P**, Chong J, Dohan A, Vakalopoulou M, Reinhold C, Paragios N, Gallix B. Demystification of AI-driven medical image interpretation: past, present and future. *Eur Radiol* 2019; **29**: 1616-1624 [PMID: 30105410 DOI: 10.1007/s00330-018-5674-x]
- 4 **Larue RT**, Defraene G, De Ruysscher D, Lambin P, van Elmpt W. Quantitative radiomics studies for tissue characterization: a review of technology and methodological procedures. *Br J Radiol* 2017; **90**: 20160665 [PMID: 27936886 DOI: 10.1259/bjr.20160665]
- 5 **Savadjiev P**, Chong J, Dohan A, Agnus V, Forghani R, Reinhold C, Gallix B. Image-based biomarkers for solid tumor quantification. *Eur Radiol* 2019; **29**: 5431-5440 [PMID: 30963275 DOI: 10.1007/s00330-019-06169-w]
- 6 **Aerts HJ**, Velazquez ER, Leijenaar RT, Parmar C, Grossmann P, Carvalho S, Bussink J, Monshouwer R, Haibe-Kains B, Rietveld D, Hoebers F, Rietbergen MM, Leemans CR, Dekker A, Quackenbush J, Gillies RJ, Lambin P. Decoding tumour phenotype by noninvasive imaging using a quantitative radiomics approach. *Nat Commun* 2014; **5**: 4006 [PMID: 24892406 DOI: 10.1038/ncomms5006]
- 7 **Aerts HJ**. The Potential of Radiomic-Based Phenotyping in Precision Medicine: A Review. *JAMA Oncol* 2016; **2**: 1636-1642 [PMID: 27541161 DOI: 10.1001/jamaoncol.2016.2631]
- 8 **Liu Z**, Wang S, Dong D, Wei J, Fang C, Zhou X, Sun K, Li L, Li B, Wang M, Tian J. The Applications of Radiomics in Precision Diagnosis and Treatment of Oncology: Opportunities and Challenges. *Theranostics* 2019; **9**: 1303-1322 [PMID: 30867832 DOI: 10.7150/thno.30309]
- 9 **Verma V**, Simone CB 2nd, Krishnan S, Lin SH, Yang J, Hahn SM. The Rise of Radiomics and Implications for Oncologic Management. *J Natl Cancer Inst* 2017; **109**: dx055 [PMID: 28423406 DOI: 10.1093/jnci/djx055]
- 10 **Gillies RJ**, Kinahan PE, Hricak H. Radiomics: Images Are More than Pictures, They Are Data. *Radiology* 2016; **278**: 563-577 [PMID: 26579733 DOI: 10.1148/radiol.2015151169]
- 11 **Afshar P**, Mohammadi A, Plataniotis KN, Oikonomou A, Benali H. From Handcrafted to Deep-Learning-Based Cancer Radiomics Challenges and opportunities. *IEEE Signal Process Mag* 2019; **36**: 132-160 [DOI: 10.1109/Msp.2019.2900993]
- 12 **Truhn D**, Schradang S, Haarbuerger C, Schneider H, Merhof D, Kuhl C. Radiomic versus Convolutional Neural Networks Analysis for Classification of Contrast-enhancing Lesions at Multiparametric Breast MRI. *Radiology* 2019; **290**: 290-297 [PMID: 30422086 DOI: 10.1148/radiol.2018181352]
- 13 **Zhu Y**, Man C, Gong L, Dong D, Yu X, Wang S, Fang M, Wang S, Fang X, Chen X, Tian J. A deep learning radiomics model for preoperative grading in meningioma. *Eur J Radiol* 2019; **116**: 128-134 [PMID: 31153553 DOI: 10.1016/j.ejrad.2019.04.022]
- 14 **Yang X**, Wu L, Zhao K, Ye W, Liu W, Wang Y, Li J, Li H, Huang X, Zhang W, Huang Y, Chen X, Yao S, Liu Z, Liang C. Evaluation of human epidermal growth factor receptor 2 status of breast cancer using preoperative multidetector computed tomography with deep learning and handcrafted radiomics features.

- Chin J Cancer Res* 2020; **32**: 175-185 [PMID: [32410795](#) DOI: [10.21147/j.issn.1000-9604.2020.02.05](#)]
- 15 **Wu X**, Li Y, Chen X, Huang Y, He L, Zhao K, Huang X, Zhang W, Huang Y, Li Y, Dong M, Huang J, Xia T, Liang C, Liu Z. Deep Learning Features Improve the Performance of a Radiomics Signature for Predicting KRAS Status in Patients with Colorectal Cancer. *Acad Radiol* 2020 [PMID: [31982342](#) DOI: [10.1016/j.acra.2019.12.007](#)]
- 16 **Hasan AM**, Jalab HA, Meziane F, Kahtan H, Al-Ahmad AS. Combining Deep and Handcrafted Image Features for MRI Brain Scan Classification. *IEEE Access* 2019; **7**: 79959-79967 [DOI: [10.1109/Access.2019.2922691](#)]
- 17 **Rawla P**, Sunkara T, Gaduputi V. Epidemiology of Pancreatic Cancer: Global Trends, Etiology and Risk Factors. *World J Oncol* 2019; **10**: 10-27 [PMID: [30834048](#) DOI: [10.14740/wjon1166](#)]
- 18 **Chu LC**, Park S, Kawamoto S, Fouladi DF, Shayesteh S, Zinreich ES, Graves JS, Horton KM, Hruban RH, Yuille AL, Kinzler KW, Vogelstein B, Fishman EK. Utility of CT Radiomics Features in Differentiation of Pancreatic Ductal Adenocarcinoma From Normal Pancreatic Tissue. *AJR Am J Roentgenol* 2019; **213**: 349-357 [PMID: [31012758](#) DOI: [10.2214/AJR.18.20901](#)]
- 19 **Liu KL**, Wu TH, Chen PT, Tsai YM, Roth H, Wu MS, Liao WC, Wang WC. Deep learning to distinguish pancreatic cancer tissue from non-cancerous pancreatic tissue: a retrospective study with cross-racial external validation. *Lancet Digit Health* 2020; **2**: E303-E313 [DOI: [10.1016/S2589-7500\(20\)30078-9](#)]
- 20 **Pietryga JA**, Morgan DE. Imaging preoperatively for pancreatic adenocarcinoma. *J Gastrointest Oncol* 2015; **6**: 343-357 [PMID: [26261722](#) DOI: [10.3978/j.issn.2078-6891.2015.024](#)]
- 21 **Li K**, Yao Q, Xiao J, Li M, Yang J, Hou W, Du M, Chen K, Qu Y, Li L, Li J, Wang X, Luo H, Yang J, Zhang Z, Chen W. Contrast-enhanced CT radiomics for predicting lymph node metastasis in pancreatic ductal adenocarcinoma: a pilot study. *Cancer Imaging* 2020; **20**: 12 [PMID: [32000852](#) DOI: [10.1186/s40644-020-0288-3](#)]
- 22 **Bian Y**, Guo S, Jiang H, Gao S, Shao C, Cao K, Fang X, Li J, Wang L, Hua W, Zheng J, Jin G, Lu J. Relationship Between Radiomics and Risk of Lymph Node Metastasis in Pancreatic Ductal Adenocarcinoma. *Pancreas* 2019; **48**: 1195-1203 [PMID: [31593021](#) DOI: [10.1097/MPA.0000000000001404](#)]
- 23 **Tummers WS**, Groen JV, Sibinga Mulder BG, Farina-Sarasqueta A, Morreau J, Putter H, van de Velde CJ, Vahrmeijer AL, Bonsing BA, Mieog JS, Swijnenburg RJ. Impact of resection margin status on recurrence and survival in pancreatic cancer surgery. *Br J Surg* 2019; **106**: 1055-1065 [PMID: [30883699](#) DOI: [10.1002/bjs.11115](#)]
- 24 **Strobel O**, Hank T, Hinz U, Bergmann F, Schneider L, Springfield C, Jäger D, Schirmacher P, Hackert T, Büchler MW. Pancreatic Cancer Surgery: The New R-status Counts. *Ann Surg* 2017; **265**: 565-573 [PMID: [27918310](#) DOI: [10.1097/SLA.0000000000001731](#)]
- 25 **Hui B**, Qiu JJ, Liu JH, Ke NW. Identification of Pancreaticoduodenectomy Resection for Pancreatic Head Adenocarcinoma: A Preliminary Study of Radiomics. *Comput Math Methods Med* 2020; **2020**: 2761627 [PMID: [32377222](#) DOI: [10.1155/2020/2761627](#)]
- 26 **Bian Y**, Jiang H, Ma C, Cao K, Fang X, Li J, Wang L, Zheng J, Lu J. Performance of CT-based radiomics in diagnosis of superior mesenteric vein resection margin in patients with pancreatic head cancer. *Abdom Radiol (NY)* 2020; **45**: 759-773 [PMID: [31932878](#) DOI: [10.1007/s00261-019-02401-9](#)]
- 27 **Terakawa H**, Kitagawa H, Makino I, Hayashi H, Oyama K, Nakagawara H, Miyashita T, Tajima H, Takamura H, Fushida S, Ozaki N, Ohta T. Location of the meso-pancreatoduodenum as a regional lymphatic basin for pancreatic head carcinoma. *Oncol Lett* 2017; **14**: 397-403 [PMID: [28693182](#) DOI: [10.3892/ol.2017.6138](#)]
- 28 **Zhang W**, Cai W, He B, Xiang N, Fang C, Jia F. A radiomics-based formula for the preoperative prediction of postoperative pancreatic fistula in patients with pancreaticoduodenectomy. *Cancer Manag Res* 2018; **10**: 6469-6478 [PMID: [30568506](#) DOI: [10.2147/CMAR.S185865](#)]
- 29 **Chen X**, Oshima K, Schott D, Wu H, Hall W, Song Y, Tao Y, Li D, Zheng C, Knechtges P, Erickson B, Li XA. Assessment of treatment response during chemoradiation therapy for pancreatic cancer based on quantitative radiomic analysis of daily CTs: An exploratory study. *PLoS One* 2017; **12**: e0178961 [PMID: [28575105](#) DOI: [10.1371/journal.pone.0178961](#)]
- 30 **Borazanci E**, Korn R, Liang WS, Guarnieri C, Haag S, Snyder C, Hendrickson K, Caldwell L, Von Hoff D, Jameson G. An Analysis of Patients with DNA Repair Pathway Mutations Treated with a PARP Inhibitor. *Oncologist* 2020; **25**: e60-e67 [PMID: [31391296](#) DOI: [10.1634/theoncologist.2018-0905](#)]
- 31 **Yue Y**, Osipov A, Fraass B, Sandler H, Zhang X, Nissen N, Hendifar A, Tuli R. Identifying prognostic intratumor heterogeneity using pre- and post-radiotherapy 18F-FDG PET images for pancreatic cancer patients. *J Gastrointest Oncol* 2017; **8**: 127-138 [PMID: [28280617](#) DOI: [10.21037/jgo.2016.12.04](#)]
- 32 **Xie T**, Wang X, Li M, Tong T, Yu X, Zhou Z. Pancreatic ductal adenocarcinoma: a radiomics nomogram outperforms clinical model and TNM staging for survival estimation after curative resection. *Eur Radiol* 2020; **30**: 2513-2524 [PMID: [32006171](#) DOI: [10.1007/s00330-019-06600-2](#)]
- 33 **Cozzi L**, Comito T, Fogliata A, Franzese C, Franceschini D, Bonifacio C, Tozzi A, Di Brina L, Clerici E, Tomatis S, Reggiori G, Lobefalo F, Stravato A, Mancosu P, Zerbi A, Sollini M, Kirienco M, Chiti A, Scorsetti M. Computed tomography based radiomic signature as predictive of survival and local control after stereotactic body radiation therapy in pancreatic carcinoma. *PLoS One* 2019; **14**: e0210758 [PMID: [30657785](#) DOI: [10.1371/journal.pone.0210758](#)]
- 34 **Kim HS**, Kim YJ, Kim KG, Park JS. Preoperative CT texture features predict prognosis after curative resection in pancreatic cancer. *Sci Rep* 2019; **9**: 17389 [PMID: [31757989](#) DOI: [10.1038/s41598-019-53831-w](#)]
- 35 **Yun G**, Kim YH, Lee YJ, Kim B, Hwang JH, Choi DJ. Tumor heterogeneity of pancreas head cancer assessed by CT texture analysis: association with survival outcomes after curative resection. *Sci Rep* 2018; **8**: 7226 [PMID: [29740111](#) DOI: [10.1038/s41598-018-25627-x](#)]
- 36 **Eilaghi A**, Baig S, Zhang Y, Zhang J, Karanicolas P, Gallinger S, Khalvati F, Haider MA. CT texture features are associated with overall survival in pancreatic ductal adenocarcinoma - a quantitative analysis. *BMC Med Imaging* 2017; **17**: 38 [PMID: [28629416](#) DOI: [10.1186/s12880-017-0209-5](#)]

- 37 **Cheng SH**, Cheng YJ, Jin ZY, Xue HD. Unresectable pancreatic ductal adenocarcinoma: Role of CT quantitative imaging biomarkers for predicting outcomes of patients treated with chemotherapy. *Eur J Radiol* 2019; **113**: 188-197 [PMID: [30927946](#) DOI: [10.1016/j.ejrad.2019.02.009](#)]
- 38 **Sandrasegaran K**, Lin Y, Asare-Sawiri M, Taiyini T, Tann M. CT texture analysis of pancreatic cancer. *Eur Radiol* 2019; **29**: 1067-1073 [PMID: [30116961](#) DOI: [10.1007/s00330-018-5662-1](#)]
- 39 **Hyun SH**, Kim HS, Choi SH, Choi DW, Lee JK, Lee KH, Park JO, Lee KH, Kim BT, Choi JY. Intratumoral heterogeneity of (18)F-FDG uptake predicts survival in patients with pancreatic ductal adenocarcinoma. *Eur J Nucl Med Mol Imaging* 2016; **43**: 1461-1468 [PMID: [26872788](#) DOI: [10.1007/s00259-016-3316-6](#)]
- 40 **Lim J**, Allen PJ. The diagnosis and management of intraductal papillary mucinous neoplasms of the pancreas: has progress been made? *Updates Surg* 2019; **71**: 209-216 [PMID: [31175628](#) DOI: [10.1007/s13304-019-00661-0](#)]
- 41 **Chakraborty J**, Midya A, Gazit L, Attiyeh M, Langdon-Embry L, Allen PJ, Do RKG, Simpson AL. CT radiomics to predict high-risk intraductal papillary mucinous neoplasms of the pancreas. *Med Phys* 2018; **45**: 5019-5029 [PMID: [30176047](#) DOI: [10.1002/mp.13159](#)]
- 42 **Corral JE**, Hussein S, Kandel P, Bolan CW, Bagci U, Wallace MB. Deep Learning to Classify Intraductal Papillary Mucinous Neoplasms Using Magnetic Resonance Imaging. *Pancreas* 2019; **48**: 805-810 [PMID: [31210661](#) DOI: [10.1097/MPA.0000000000001327](#)]
- 43 **Hanania AN**, Bantis LE, Feng Z, Wang H, Tamm EP, Katz MH, Maitra A, Koay EJ. Quantitative imaging to evaluate malignant potential of IPMNs. *Oncotarget* 2016; **7**: 85776-85784 [PMID: [27588410](#) DOI: [10.18632/oncotarget.11769](#)]
- 44 **Permuth JB**, Choi J, Balarunathan Y, Kim J, Chen DT, Chen L, Orcutt S, Doepker MP, Gage K, Zhang G, Latifi K, Hoffe S, Jiang K, Coppola D, Centeno BA, Magliocco A, Li Q, Trevino J, Merchant N, Gillies R, Malafa M; Florida Pancreas Collaborative. Combining radiomic features with a miRNA classifier may improve prediction of malignant pathology for pancreatic intraductal papillary mucinous neoplasms. *Oncotarget* 2016; **7**: 85785-85797 [PMID: [27589689](#) DOI: [10.18632/oncotarget.11768](#)]
- 45 **Guilmette JM**, Nosé V. Neoplasms of the Neuroendocrine Pancreas: An Update in the Classification, Definition, and Molecular Genetic Advances. *Adv Anat Pathol* 2019; **26**: 13-30 [PMID: [29912000](#) DOI: [10.1097/PAP.0000000000000201](#)]
- 46 **D'Onofrio M**, Ciaravino V, Cardobi N, De Robertis R, Cingarlini S, Landoni L, Capelli P, Bassi C, Scarpa A. CT Enhancement and 3D Texture Analysis of Pancreatic Neuroendocrine Neoplasms. *Sci Rep* 2019; **9**: 2176 [PMID: [30778137](#) DOI: [10.1038/s41598-018-38459-6](#)]
- 47 **Guo C**, Zhuge X, Wang Z, Wang Q, Sun K, Feng Z, Chen X. Textural analysis on contrast-enhanced CT in pancreatic neuroendocrine neoplasms: association with WHO grade. *Abdom Radiol (NY)* 2019; **44**: 576-585 [PMID: [30182253](#) DOI: [10.1007/s00261-018-1763-1](#)]
- 48 **Canellas R**, Burk KS, Parakh A, Sahani DV. Prediction of Pancreatic Neuroendocrine Tumor Grade Based on CT Features and Texture Analysis. *AJR Am J Roentgenol* 2018; **210**: 341-346 [PMID: [29140113](#) DOI: [10.2214/AJR.17.18417](#)]
- 49 **Liang W**, Yang P, Huang R, Xu L, Wang J, Liu W, Zhang L, Wan D, Huang Q, Lu Y, Kuang Y, Niu T. A Combined Nomogram Model to Preoperatively Predict Histologic Grade in Pancreatic Neuroendocrine Tumors. *Clin Cancer Res* 2019; **25**: 584-594 [PMID: [30397175](#) DOI: [10.1158/1078-0432.CCR-18-1305](#)]
- 50 **Gu D**, Hu Y, Ding H, Wei J, Chen K, Liu H, Zeng M, Tian J. CT radiomics may predict the grade of pancreatic neuroendocrine tumors: a multicenter study. *Eur Radiol* 2019; **29**: 6880-6890 [PMID: [31227882](#) DOI: [10.1007/s00330-019-06176-x](#)]
- 51 **Bian Y**, Zhao Z, Jiang H, Fang X, Li J, Cao K, Ma C, Guo S, Wang L, Jin G, Lu J, Xu J. Noncontrast Radiomics Approach for Predicting Grades of Nonfunctional Pancreatic Neuroendocrine Tumors. *J Magn Reson Imaging* 2020 [PMID: [32343872](#) DOI: [10.1002/jmri.27176](#)]
- 52 **Strosberg JR**, Weber JM, Feldman M, Coppola D, Meredith K, Kvols LK. Prognostic validity of the American Joint Committee on Cancer staging classification for midgut neuroendocrine tumors. *J Clin Oncol* 2013; **31**: 420-425 [PMID: [23248248](#) DOI: [10.1200/JCO.2012.44.5924](#)]
- 53 **Lee L**, Ito T, Jensen RT. Prognostic and predictive factors on overall survival and surgical outcomes in pancreatic neuroendocrine tumors: recent advances and controversies. *Expert Rev Anticancer Ther* 2019; **19**: 1029-1050 [PMID: [31738624](#) DOI: [10.1080/14737140.2019.1693893](#)]
- 54 **Park S**, Chu LC, Hruban RH, Vogelstein B, Kinzler KW, Yuille AL, Fouladi DF, Shayesteh S, Ghandili S, Wolfgang CL, Burkhart R, He J, Fishman EK, Kawamoto S. Differentiating autoimmune pancreatitis from pancreatic ductal adenocarcinoma with CT radiomics features. *Diagn Interv Imaging* 2020 [PMID: [32278586](#) DOI: [10.1016/j.diii.2020.03.002](#)]
- 55 **Zhang Y**, Cheng C, Liu Z, Wang L, Pan G, Sun G, Chang Y, Zuo C, Yang X. Radiomics analysis for the differentiation of autoimmune pancreatitis and pancreatic ductal adenocarcinoma in ¹⁸F-FDG PET/CT. *Med Phys* 2019; **46**: 4520-4530 [PMID: [31348535](#) DOI: [10.1002/mp.13733](#)]
- 56 **Ren S**, Zhang J, Chen J, Cui W, Zhao R, Qiu W, Duan S, Chen R, Chen X, Wang Z. Evaluation of Texture Analysis for the Differential Diagnosis of Mass-Forming Pancreatitis From Pancreatic Ductal Adenocarcinoma on Contrast-Enhanced CT Images. *Front Oncol* 2019; **9**: 1171 [PMID: [31750254](#) DOI: [10.3389/fonc.2019.01171](#)]
- 57 **Mashayekhi R**, Parekh VS, Faghih M, Singh VK, Jacobs MA, Zaheer A. Radiomic features of the pancreas on CT imaging accurately differentiate functional abdominal pain, recurrent acute pancreatitis, and chronic pancreatitis. *Eur J Radiol* 2020; **123**: 108778 [PMID: [31846864](#) DOI: [10.1016/j.ejrad.2019.108778](#)]
- 58 **Yang J**, Guo X, Ou X, Zhang W, Ma X. Discrimination of Pancreatic Serous Cystadenomas From Mucinous Cystadenomas With CT Textural Features: Based on Machine Learning. *Front Oncol* 2019; **9**: 494 [PMID: [31245294](#) DOI: [10.3389/fonc.2019.00494](#)]
- 59 **Zwanenburg A**, Vallières M, Abdalah MA, Aerts HJWL, Andrearczyk V, Apte A, Ashrafinia S, Bakas S, Beukinga RJ, Boellaard R, Bogowicz M, Boldrini L, Buvat I, Cook GJR, Davatzikos C, Depeursinge A, Desseroit MC, Dinapoli N, Dinh CV, Echegaray S, El Naqa I, Fedorov AY, Gatta R, Gillies RJ, Goh V, Götz M, Guckenberger M, Ha SM, Hatt M, Isensee F, Lambin P, Leger S, Leijenaar RTH, Lenkiewicz J,

Lippert F, Losnegård A, Maier-Hein KH, Morin O, Müller H, Napel S, Nioche C, Orlhac F, Pati S, Pfahler EAG, Rahmim A, Rao AUK, Scherer J, Siddique MM, Sijtsma NM, Socarras Fernandez J, Spezi E, Steenbakkens RJHM, Tanadini-Lang S, Thorwarth D, Troost EGC, Upadhaya T, Valentini V, van Dijk LV, van Griethuysen J, van Velden FHP, Whybra P, Richter C, Löck S. The Image Biomarker Standardization Initiative: Standardized Quantitative Radiomics for High-Throughput Image-based Phenotyping. *Radiology* 2020; **295**: 328-338 [PMID: [32154773](#) DOI: [10.1148/radiol.2020191145](#)]

Machine learning for diagnosis of coronary artery disease in computed tomography angiography: A survey

Feng-Jun Zhao, Si-Qi Fan, Jing-Fang Ren, Karen M von Deneen, Xiao-Wei He, Xue-Li Chen

ORCID number: Feng-Jun Zhao 0000-0001-8658-8412; Si-Qi Fan 0000-0002-8805-7962; Jing-Fang Ren 0000-0002-8070-1282; Karen M von Deneen 0000-0002-5310-1003; Xiao-Wei He 0000-0003-2126-178X; Xue-Li Chen 0000-0002-3898-9892.

Author contributions: Zhao FJ performed the majority of the writing and the investigation of articles; Fan SQ performed writing for coronary plaque detection; Ren JF performed writing for coronary artery extraction; He XW and von Deneen KM polished the language and expression of the paper; Chen XL checked the organization and revised the writing of the paper.

Supported by the National Natural Science Foundation of China, Nos. 61971350, 81627807 and 11727813; the National Key R&D Program of China, No. 2016YFC1300300; the China Postdoctoral Science Foundation, No. 2019M653717; Shaanxi Science Funds for Distinguished Young Scholars, No. 2020JC-27; Fok Ying Tung Education Foundation, No. 161104; and Program for the Young Top-notch Talent of Shaanxi Province.

Conflict-of-interest statement: The authors declare they have no conflicts of interest.

Open-Access: This article is an open-access article that was

Feng-Jun Zhao, Si-Qi Fan, Jing-Fang Ren, Xiao-Wei He, School of Information Science and Technology, Northwest University, Xi'an 710069, Shaanxi Province, China

Feng-Jun Zhao, Si-Qi Fan, Jing-Fang Ren, Xiao-Wei He, Xi'an Key Lab of Radiomics and Intelligent Perception, Northwest University, Xi'an 710069, Shaanxi Province, China

Karen M von Deneen, Xue-Li Chen, Engineering Research Center of Molecular and Neuro Imaging, Ministry of Education, School of Life Science and Technology, Xidian University, Xi'an 710126, Shaanxi Province, China

Corresponding author: Xue-Li Chen, PhD, Professor, Engineering Research Center of Molecular and Neuro Imaging, Ministry of Education, School of Life Science and Technology, Xidian University, No. 266, Xinglong Section of Xifeng Road, Xi'an 710126, Shaanxi Province, China. xlchen@xidian.edu.cn

Abstract

Coronary artery disease (CAD) has become a major illness endangering human health. It mainly manifests as atherosclerotic plaques, especially vulnerable plaques without obvious symptoms in the early stage. Once a rupture occurs, it will lead to severe coronary stenosis, which in turn may trigger a major adverse cardiovascular event. Computed tomography angiography (CTA) has become a standard diagnostic tool for early screening of coronary plaque and stenosis due to its advantages in high resolution, noninvasiveness, and three-dimensional imaging. However, manual examination of CTA images by radiologists has been proven to be tedious and time-consuming, which might also lead to intra- and interobserver errors. Nowadays, many machine learning algorithms have enabled the (semi-)automatic diagnosis of CAD by extracting quantitative features from CTA images. This paper provides a survey of these machine learning algorithms for the diagnosis of CAD in CTA images, including coronary artery extraction, coronary plaque detection, vulnerable plaque identification, and coronary stenosis assessment. Most included articles were published within this decade and are found in the Web of Science. We wish to give readers a glimpse of the current status, challenges, and perspectives of these machine learning-based analysis methods for automatic CAD diagnosis.

Key words: Machine learning; Deep learning; Coronary artery disease; Atherosclerotic plaque; Vulnerability; Stenosis; Segmentation; Computed tomography angiography

selected by an in-house editor and fully peer-reviewed by external reviewers. It is distributed in accordance with the Creative Commons Attribution NonCommercial (CC BY-NC 4.0) license, which permits others to distribute, remix, adapt, build upon this work non-commercially, and license their derivative works on different terms, provided the original work is properly cited and the use is non-commercial. See: <http://creativecommons.org/licenses/by-nc/4.0/>

Manuscript source: Invited manuscript

Received: May 7, 2020

Peer-review started: May 7, 2020

First decision: June 4, 2020

Revised: June 12, 2020

Accepted: June 17, 2020

Article in press: June 17, 2020

Published online: June 28, 2020

P-Reviewer: Chello M, Dai X, Korosoglou G

S-Editor: Wang JL

L-Editor: Filipodia

E-Editor: Xing YX



©The Author(s) 2020. Published by Baishideng Publishing Group Inc. All rights reserved.

Core tip: There are reviews that contributed to the segmentation of the coronary artery, detection of calcified plaques, and calculation of fractional flow reserve. To the best of our knowledge, this is the first paper to survey the machine learning algorithms for the diagnosis of coronary artery disease in computed tomography angiography images, including extraction of coronary arteries, detection of calcified, soft and mixed plaques, identification of plaque vulnerability features including low density plaque, positive remodeling, spot calcification, and napkin ring sign, assessment of both anatomically and hemodynamically significant stenosis, and the challenges and perspectives of these machine learning-based analysis methods.

Citation: Zhao FJ, Fan SQ, Ren JF, von Deneen KM, He XW, Chen XL. Machine learning for diagnosis of coronary artery disease in computed tomography angiography: A survey. *Artif Intell Med Imaging* 2020; 1(1): 31-39

URL: <https://www.wjgnet.com/2644-3260/full/v1/i1/31.htm>

DOI: <https://dx.doi.org/10.35711/aimi.v1.i1.31>

INTRODUCTION

Coronary artery disease (CAD) has become a major illness endangering human health, which caused more than 17.6 million deaths worldwide in 2016^[1]. Atherosclerotic plaque is the pathological basis of CAD, especially vulnerable plaques without obvious symptoms in the early stage. Once a rupture occurs, it will lead to severe coronary stenosis, which in turn may trigger a major adverse cardiovascular event^[2]. Therefore in CAD diagnosis, it is urgent to accurately detect coronary plaques, identify their vulnerable features, and assess the resulting stenosis. Computed tomography angiography (CTA) has become a standard diagnostic tool for early screening of CAD due to its advantages in high resolution, noninvasiveness, and three-dimensional (3D) imaging^[3]. However, manual examination of CTA images by radiologists has been proven to be tedious and time-consuming, which might also lead to intra- and interobserver errors^[4].

To date, many state-of-the-art machine learning (ML) algorithms have enabled the (semi-)automatic diagnosis of CAD by extracting quantitative features from CTA images. These ML algorithms can be grouped into: (1) Conventional ML algorithms that are typically based on the predefined or hand-crafted features, such as linear regression, support vector machine (SVM), and random forests; and (2) Deep learning (DL) algorithms that can directly learn features from original medical images, such as the convolutional neural network (CNN) and recurrent neural network.

There are some reviews that contributed to the segmentation of the coronary artery^[5], detection of calcified plaques^[6], and calculation of fractional flow reserve (FFR) with both the rule-based (non-ML) and ML-based methods^[7]. This paper provides a survey of the above two groups of ML methods in (semi-)automatic diagnosis of CAD, including coronary artery extraction, coronary plaque detection, vulnerable plaque identification, and coronary stenosis assessment (Figure 1 and Table 1). Most included articles were published within this decade and appear in the Web of Science. Instead of exhaustively listing all of the ML methods of coronary plaque diagnosis, we focus on typical ML-based methods with CTA images in recent years and summarize the challenges regarding these methods.

CORONARY ARTERY EXTRACTION

Due to the tortuous structure of the coronary arteries, it is necessary to perform multiplanar reconstruction or curved planar reconstruction visualization of CTA images before CAD diagnosis^[8]. The reconstruction of both multiplanar reconstruction and curved planar reconstruction images relies on the extraction of coronary artery trees. In addition, some studies have directly carried out a plaque analysis along the cross-section perpendicular to the coronary artery^[9,10]. It can be seen that the accurate extraction of coronary arteries plays an indispensable role in CAD diagnosis. Manual

Table 1 Summary of different machine learning-based methods used in coronary artery disease diagnosis

CAD diagnosis	Method	Task	Category
Coronary artery extraction			
Schaap <i>et al</i> ^[14]	Linear and nonlinear regression	Artery	ML
Huang <i>et al</i> ^[15]	3D U-net	Artery	DL
Kong <i>et al</i> ^[16]	ConvRNN + ConvGRU	Artery	DL
Shen <i>et al</i> ^[17]	3D FCN + level set	Artery	DL
Wu <i>et al</i> ^[18]	CNN + nearest neighbor search	Artery	DL
Wolterink <i>et al</i> ^[19]	3D dilated CNN	Centerline	DL
Coronary plaque detection			
Mittal <i>et al</i> ^[20]	PBT, RF	Calcified	ML
Kurkure <i>et al</i> ^[21]	SVM	Calcified	ML
Wei <i>et al</i> ^[22]	Linear discriminant analysis	Soft	ML
Jawaid <i>et al</i> ^[23]	SVM	Soft	ML
Tessmann <i>et al</i> ^[24]	AdaBoost	Multiple	ML
Kelm <i>et al</i> ^[25]	PBT, RF	Multiple	ML
Zhao <i>et al</i> ^[26]	SVM	Multiple	ML
Zreik <i>et al</i> ^[27]	CNN + RNN	Multiple	DL
Huo <i>et al</i> ^[28]	Attention recognition dual network	Calcified	DL
Vulnerable plaque identification			
Kolossváry <i>et al</i> ^[33]	Radiomics	NRS	ML
Kolossváry <i>et al</i> ^[2]	Radiomics	LAP & NRS	ML
Kolossváry <i>et al</i> ^[34]	Logistic regression, K-nearest neighbors, RF, least angle regression, naive Bayes, Gaussian process classifier, decision trees, DNN	Advanced lesion	ML, DL
Coronary stenosis assessment			
Zuluaga <i>et al</i> ^[36]	SVM	ASS	ML
Kang <i>et al</i> ^[37]	SVM + formula-based analytical method	ASS	ML
Zreik <i>et al</i> ^[27]	CNN + RNN	ASS	DL
Itu <i>et al</i> ^[41]	DNN	HSS	DL
Wang <i>et al</i> ^[42]	DeepVessel-FFR	HSS	DL
Dey <i>et al</i> ^[43]	Boosted ensemble algorithm	HSS	ML
Kumamaru <i>et al</i> ^[44]	2D conditional generative adversarial network + 3D convolutional ladder network	HSS	DL

ASS: Anatomically significant stenosis; CAD: Coronary artery disease; CNN: Convolutional neural network; ConvGRU: Convolutional gated recurrent unit; ConvRNN: Convolutional recurrent neural network; DL: Deep learning method; DNN: Deep neural network; FCN: Fully convolutional network; FFR: Fractional flow reserve; HSS: Hemodynamically significant stenosis; LAP: Low density plaque; ML: Conventional machine learning method; NRS: Napkin ring sign; PBT: Probability boosting tree; RF: Random forest; RNN: Recurrent neural network; SVM: Support vector machine.

extraction of the coronary arteries is labor intensive and observer dependent. Therefore, automatic/semi-automatic extraction methods have been adopted, such as the Hessian matrix method, mathematical morphology, and minimal cost path^[5,11]. These traditional methods discriminate coronary arteries from the background based on intuitively and exquisitely designed models^[12].

ML methods transfer the segmentation into the problem of pixel classification by assigning each pixel as the coronary artery or background^[13]. Specifically, Schaap *et al*^[14] employed both linear regression and nonlinear regression to learn the arterial geometry and appearance from annotated CTA images, and then made full use of the

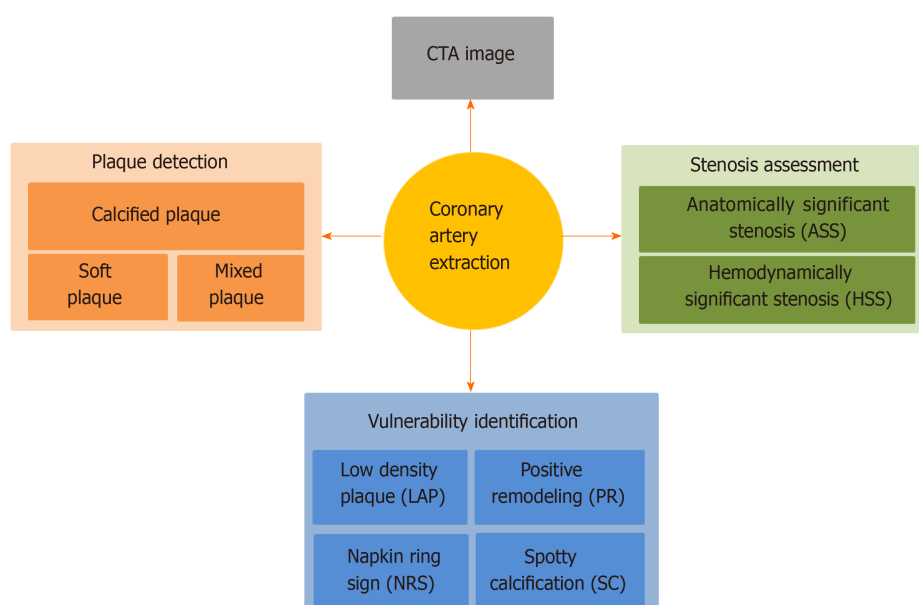


Figure 1 Main topics of this survey, including coronary artery extraction, coronary plaque detection, vulnerable plaque identification, and coronary stenosis assessment. CTA: Computed tomography angiography.

learned knowledge to segment coronary arteries in unseen CTA images. Huang *et al*^[15] introduced the 3D U-net, a typical fully convolutional network (FCN), to segment the coronary artery, which densely performed the pixel-wise classification *via* directly extracting features from CTA images. Alternatively, Kong *et al*^[16] employed a convolutional recurrent neural network and a tree-structured convolutional gated recurrent unit to learn the anatomical structure of the coronary artery, and hereby they achieved accurate segmentation of coronary arteries. Recently, the combination of traditional methods (such as level set and nearest neighbor search) and DL methods (such as fully convolutional network and CNN) were also devised for coronary artery segmentation^[17,18]. Moreover, Wolterink *et al*^[19] trained a 3D dilated CNN to iteratively track the centerline points in CTA images in which the coronary artery could be reconstructed based on the extracted centerline and the radius of each centerline point.

CORONARY PLAQUE DETECTION

Depending on the degree of calcification, coronary plaques can be divided into calcified plaques (full calcification), soft plaques (no calcification), and mixed plaques (partial calcification). Mittal *et al*^[20] used probability boosting trees and random forests to detect coronary calcified plaques with the designed rotation invariant features along the coronary centerline. Kurkure *et al*^[21] adopted an SVM-based method to detect the calcification positions in the aorta and coronary arteries, amongst which they selected coronary calcified plaques. Wei *et al*^[22] proposed a topological soft gradient pre-screening method to obtain candidate soft plaques and then detected soft plaques from the candidate set by a linear discriminant analysis. Jawaid *et al*^[23] divided the coronary cross-section into eight concentric circles. Then they constructed an SVM to identify abnormal coronary segments caused by soft plaques based on the difference in strength stability and localized and identified soft plaques. However, due to large morphological differences between different types of plaques, it is challenging to simultaneously detect multiple types of coronary plaques.

Thus, Tessmann *et al*^[24] performed feature extraction on a cylindrical coronary region of interest and introduced the AdaBoost algorithm to identify calcified plaques and soft plaques. Kelm *et al*^[25] regressed the vessel radius based on the pre-acquired centerline to evaluate stenosis and then constructed a classifier (similar to^[20]) to determine the type of coronary plaques that caused the stenosis, so as to realize the classification of multiple types of plaques. Zhao *et al*^[26] designed a random radial symmetric feature vector and augmented the training data by rotating the cross-section with random angles. Then they trained an SVM to detect and classify

multiclass coronary plaques. With the advantages in representing the complex texture of medical images, DL methods have been brought to the domain of plaque image analysis. Zreik *et al*^[27] constructed a CNN model to extract the image features of coronary artery sections, and then used a recurrent neural network to fuse the features extracted by multiple CNNs. Finally, they realized the detection and classification of different coronary plaques. Huo *et al*^[28] proposed a weak supervised attention recognition dual network to perform the detection of calcified plaques, which required only scan-level labels instead of pixel-level labels.

VULNERABLE PLAQUE IDENTIFICATION

CTA imaging can evaluate plaque components in coronary arteries with the diameter greater than 1.5 mm^[29]. Studies found that the plaque vulnerability in CTA images was closely related to low density plaque, positive remodeling, spotty calcification, and napkin ring sign (NRS)^[30,31]. If a coronary plaque contains two or more of the above four vulnerable features, the plaque is more likely to be a vulnerable plaque^[32]. Traditionally, visual inspection performed by radiologists is used to determine whether a coronary plaque contains the above vulnerable features. However, different patients have large individual differences in CTA imaging, resulting in the visual inspection relying heavily on experienced radiologists.

ML-based radiomics can extract a large number of quantitative features from the image to describe the complex texture and spatial structure of the lesion area, providing an automated solution for plaque vulnerability analysis. Kolossváry *et al*^[33] applied radiomics to the identification of NRS in coronary CTA images, and the results showed that radiomic features were superior to traditional imaging parameters in distinguishing NRS and non-NRS plaques. Afterwards, they identified the low density plaque, NRS, and Na¹⁸F-positive vulnerable features in CTA images^[2]. The results demonstrated that noninvasive CTA diagnosis could accurately distinguish high risk plaques that were previously diagnosed by intravascular ultrasound, optical coherence tomography, and positron emission tomography. In addition, they also collaborated with researchers from the Massachusetts General Hospital to identify advanced coronary atherosclerotic lesions through an ML-based radiomics analysis of *ex vivo* coronary CTA imaging^[34]. The identification results on the cross-section were better than the visual inspection and histogram evaluation.

CORONARY STENOSIS ASSESSMENT

Various types of plaques are the main causes of coronary stenosis, *i.e.* narrowing of the coronary artery lumen, which will restrain blood flow to the myocardium and potentially lead to myocardial ischemia^[35]. Therefore, the assessment of coronary stenosis is also an important aspect in the diagnosis of CAD. Taking physiology into account, coronary stenotic lesions are generally categorized as anatomically significant stenosis and hemodynamically significant stenosis, both of which can be noninvasively assessed by CTA imaging. Anatomically significant stenosis refers to the narrowing of the coronary lumen of at least 50%, which acts as the early assessment for the severity of stenosis in CAD patients. Zuluaga *et al*^[36] employed SVM to detect coronary stenosis and arterial bifurcation based on the features of concentric circles in two-dimensional cross-sectional images. Kang *et al*^[37] developed a structured learning algorithm based on SVM and a formula-based analytical method to detect both obstructive (with over 50% stenosis) and non-obstructive (with stenosis between 25% and 50%) lesions. Furthermore, Zreik *et al*^[27] applied a recurrent CNN on coronary artery multiplanar reconstruction images to detect different grades of anatomically significant stenosis, including no stenosis, nonsignificant stenosis (with less than 50% narrowing), and significant stenosis (with over 50% narrowing). However, the detected anatomically significant stenosis from CTA images has only moderate specificity for predicting hemodynamically significant stenosis (HSS) that causes myocardial ischemia^[38].

Currently, FFR is the standard examination for diagnosis of HSS, which invasively measures the ratio of distal blood flow to the proximal blood flow of the stenosis by inserting a special catheter. FFR estimation based on CTA images (FFTC_T) provides a noninvasive alternative for evaluating HSS based on computational fluid dynamics^[39,40], which is accurate but computationally demanding due to the complex iterative computation. To improve the computation efficiency, Itu *et al*^[41] proposed an

artificial neural network to predict the FFR value of each coronary artery segment based on the geometry and global features extracted from the most severe stenosis. Wang *et al*^[42] developed a DL method (DEEPVESSEL-FFR) to calculate the FFR value from CTA images and predicted the ischemic risk of HSS. Both of the above ML-based FFR prediction methods only rely on the geometry of the coronary artery, leading to their susceptibility to the errors of coronary artery segmentation. Therefore, Dey *et al*^[43] performed the HSS identification with a boosted ensemble algorithm, which combined the geometric features of stenosis with the volumes of plaques, the contrast density difference, and the plaque length. Moreover, Kumamaru *et al*^[44] proposed a 3D DL model to identify patients with at least one HSS, where the model could automatically extract the representative features from the CTA dataset without segmentation or other data manipulation.

CHALLENGES AND PERSPECTIVES

ML algorithms have been widely used in the analysis of CTA images for CAD diagnosis, including the extraction of coronary arteries, diagnosis of plaques, and assessment of stenotic lesions. In particular, DL methods can directly extract task-specific features from input CTA images, which have partially replaced conventional ML methods that depend on the hand-crafted features (or engineered features). Nevertheless, there are some merits and challenges for both the conventional ML methods and DL-based methods. (1) Conventional ML methods are more often involved in plaque and stenosis diagnosis, where the used hand-crafted features were designed according to the visual and clinical experience of radiologists. For this reason, the diagnostic results of these ML methods are inherently explainable, which means they can explicitly show task-relevant quantitative features. Moreover, these ML models are relatively simple and easy to train with only a small number of CTA images. However, the quantitative features used in the ML methods heavily depend on the careful designing by computer vision experts. How to develop or select task-specific quantitative features requires extensive experience accumulation; and (2) DL-based methods are sometimes applied in both coronary artery extraction, and stenosis and plaque diagnosis. DL methods can integrate the whole ML-based analysis workflow including (hand-crafted) feature extraction, feature selection, and classifier training into only one DL model, whose performance would be continuously improved *via* end-to-end learning as long as enough training samples are provided^[45]. However, DL methods generally require a large number of training samples. As is known, manual labeling of coronary data is time-consuming and laborious, so the number of labeled samples is still very limited, even though there are large amounts of patient data in the clinics. Moreover, difficulty in interpretability may also prevent using the DL methods in clinical diagnosis of CAD.

Nevertheless, the DL method has become an important branch in the family of ML algorithms, especially for coronary artery segmentation and coronary stenosis assessment. It is foreseeable that most tasks in CAD diagnosis may start using DL methods or at least the combination of DL and conventional ML methods. For the latter, the DL method functions like a feature extractor, and the classifier from the conventional ML method carries out the subsequent classification. There are some solutions that may address the shortcomings of DL methods. For example, semi-supervised DL methods in natural image processing can potentially solve the classification with only small labeled data. It is reported the prediction error of semi-supervised methods using only 4000 labeled samples in the CIFAR-10 dataset was approximated to supervised learning with 50000 labeled samples^[46,47]. Moreover, some studies tried to explain the decision made by a DL model by double-checking the results with an expert^[48], generating a heat-map to highlight the input regions responsible for a specific task^[49], or projecting the high-dimensional feature space to a bi-dimensional plane^[50].

CONCLUSION

In conclusion, we have surveyed the ML-based CAD diagnostic methods in CTA images in recent years and highlighted the most typical application of both conventional ML and DL methods. We wish to give the readers a glimpse of the current status, challenges, and perspectives of these ML-based analysis methods for automatic CAD diagnosis.

REFERENCES

- 1 **Benjamin EJ**, Muntner P, Alonso A, Bittencourt MS, Callaway CW, Carson AP, Chamberlain AM, Chang AR, Cheng S, Das SR, Delling FN, Djousse L, Elkind MSV, Ferguson JF, Fornage M, Jordan LC, Khan SS, Kissela BM, Knutson KL, Kwan TW, Lackland DT, Lewis TT, Lichtman JH, Longenecker CT, Loop MS, Lutsey PL, Martin SS, Matsushita K, Moran AE, Mussolino ME, O'Flaherty M, Pandey A, Perak AM, Rosamond WD, Roth GA, Sampson UKA, Satou GM, Schroeder EB, Shah SH, Spartano NL, Stokes A, Tirschwell DL, Tsao CW, Turakhia MP, VanWagner LB, Wilkins JT, Wong SS, Virani SS; American Heart Association Council on Epidemiology and Prevention Statistics Committee and Stroke Statistics Subcommittee. Heart Disease and Stroke Statistics-2019 Update: A Report From the American Heart Association. *Circulation* 2019; **139**: e56-e528 [PMID: [30700139](#) DOI: [10.1161/CIR.0000000000000659](#)]
- 2 **Kolossváry M**, Park J, Bang JI, Zhang J, Lee JM, Paeng JC, Merkely B, Narula J, Kubo T, Akasaka T, Koo BK, Maurovich-Horvat P. Identification of invasive and radionuclide imaging markers of coronary plaque vulnerability using radiomic analysis of coronary computed tomography angiography. *Eur Heart J Cardiovasc Imaging* 2019; **20**: 1250-1258 [PMID: [30838375](#) DOI: [10.1093/ehjci/jez033](#)]
- 3 **Hampe N**, Wolterink JM, van Velzen SGM, Leiner T, Išgum I. Machine Learning for Assessment of Coronary Artery Disease in Cardiac CT: A Survey. *Front Cardiovasc Med* 2019; **6**: 172 [PMID: [32039237](#) DOI: [10.3389/fcvm.2019.00172](#)]
- 4 **Litjens G**, Kooi T, Bejnordi BE, Setio AAA, Ciompi F, Ghafoorian M, van der Laak JAWM, van Ginneken B, Sánchez CI. A survey on deep learning in medical image analysis. *Med Image Anal* 2017; **42**: 60-88 [PMID: [28778026](#) DOI: [10.1016/j.media.2017.07.005](#)]
- 5 **Lesage D**, Angelini ED, Bloch I, Funka-Lea G. A review of 3D vessel lumen segmentation techniques: models, features and extraction schemes. *Med Image Anal* 2009; **13**: 819-845 [PMID: [19818675](#) DOI: [10.1016/j.media.2009.07.011](#)]
- 6 **Al'Aref SJ**, Anchouche K, Singh G, Slomka PJ, Kolli KK, Kumar A, Pandey M, Maliakal G, van Rosendaal AR, Beecy AN, Berman DS, Leipsic J, Nieman K, Andreini D, Pontone G, Schoepf UJ, Shaw LJ, Chang HJ, Narula J, Bax JJ, Guan Y, Min JK. Clinical applications of machine learning in cardiovascular disease and its relevance to cardiac imaging. *Eur Heart J* 2019; **40**: 1975-1986 [PMID: [30060039](#) DOI: [10.1093/eurheartj/ehy404](#)]
- 7 **Cook CM**, Petraco R, Shun-Shin MJ, Ahmad Y, Nijjer S, Al-Lamee R, Kikuta Y, Shiono Y, Mayet J, Francis DP, Sen S, Davies JE. Diagnostic Accuracy of Computed Tomography-Derived Fractional Flow Reserve : A Systematic Review. *JAMA Cardiol* 2017; **2**: 803-810 [PMID: [28538960](#) DOI: [10.1001/jamacardio.2017.1314](#)]
- 8 **Cademartiri F**, La Grutta L, Palumbo A, Malagutti P, Pugliese F, Meijboom WB, Baks T, Mollet NR, Bruining N, Hamers R, de Feyter PJ. Non-invasive visualization of coronary atherosclerosis: state-of-art. *J Cardiovasc Med (Hagerstown)* 2007; **8**: 129-137 [PMID: [17312429](#) DOI: [10.2459/01.JCM.0000260820.40145.a8](#)]
- 9 **Sankaran S**, Schaap M, Hunley SC, Min JK, Taylor CA, Grady L. In: Ourselin S, Joskowicz L, Sabuncu M, Unal G, Wells W, editors. Medical Image Computing and Computer-Assisted Intervention - MICCAI 2016. MICCAI 2016. Lecture Notes in Computer Science, vol 9902. Cham: Springer 2016; 380-387 [DOI: [10.1007/978-3-319-46726-9_44](#)]
- 10 **Zuluaga MA**, Hernandez Hoyos M, Orkisz M. Feature selection based on empirical-risk function to detect lesions in vascular computed tomography. *Irbm* 2014; **35**: 244-254 [DOI: [10.1016/j.irbm.2014.07.003](#)]
- 11 **Kirbas C**, Quek F. A review of vessel extraction techniques and algorithms. *ACM Comput Surv* 2004; **36**: 81-121 [DOI: [10.1145/1031120.1031121](#)]
- 12 **Zhao F**, Chen Y, Hou Y, He X. Segmentation of blood vessels using rule-based and machine-learning-based methods: a review. *Multimed Syst* 2019; **25**: 109-118 [DOI: [10.1007/s00530-017-0580-7](#)]
- 13 **Tetteh G**, Efremov V, Forkert ND, Schneider M, Kirschke J, Weber B, Zimmer C, Piraud M, Menze BH. DeepVesselNet: Vessel Segmentation, Centerline Prediction, and Bifurcation Detection in 3-D Angiographic Volumes. 2018 Preprint. Available from: [arXiv:1803.09340](#)
- 14 **Schaap M**, van Walsum T, Neefjes L, Metz C, Capuano E, de Bruijne M, Niessen W. Robust shape regression for supervised vessel segmentation and its application to coronary segmentation in CTA. *IEEE Trans Med Imaging* 2011; **30**: 1974-1986 [PMID: [21708497](#) DOI: [10.1109/TMI.2011.2160556](#)]
- 15 **Huang W**, Huang L, Lin Z, Huang S, Chi Y, Zhou J, Zhang J, Tan RS, Zhong L. Coronary Artery Segmentation by Deep Learning Neural Networks on Computed Tomographic Coronary Angiographic Images. *Conf Proc IEEE Eng Med Biol Soc* 2018; **2018**: 608-611 [PMID: [30440470](#) DOI: [10.1109/EMBC.2018.8512328](#)]
- 16 **Kong B**, Wang X, Bai J, Lu Y, Gao F, Cao K, Xia J, Song Q, Yin Y. Learning tree-structured representation for 3D coronary artery segmentation. *Comput Med Imaging Graph* 2020; **80**: 101688 [PMID: [31926366](#) DOI: [10.1016/j.compmedimag.2019.101688](#)]
- 17 **Shen Y**, Fang Z, Gao Y, Xiong N, Zhong C, Tang X. Coronary Arteries Segmentation Based on 3D FCN With Attention Gate and Level Set Function. *IEEE Access* 2019; **7**: 42826-42835 [DOI: [10.1109/ACCESS.2019.2908039](#)]
- 18 **Wu A**, Xu Z, Gao M, Buty M, Mollura DJ. Deep vessel tracking: A generalized probabilistic approach via deep learning. In: 2016 IEEE 13th International Symposium on Biomedical Imaging (ISBI). IEEE, 2016: 1363-1367 [DOI: [10.1109/ISBI.2016.7493520](#)]
- 19 **Wolterink JM**, van Hamersvelt RW, Viergever MA, Leiner T, Išgum I. Coronary artery centerline extraction in cardiac CT angiography using a CNN-based orientation classifier. *Med Image Anal* 2019; **51**: 46-60 [PMID: [30388501](#) DOI: [10.1016/j.media.2018.10.005](#)]
- 20 **Mittal S**, Zheng Y, Georgescu B, Vega-Higuera F, Zhou SK, Meer P, Comaniciu D. Fast Automatic Detection of Calcified Coronary Lesions in 3D Cardiac CT Images. In: Wang F, Yan P, Suzuki K, Shen D, editors. Machine Learning in Medical Imaging. MLMI 2010. Lecture Notes in Computer Science, vol 6357. Berlin, Heidelberg: Springer 2010; 1-9 [DOI: [10.1007/978-3-642-15948-0_1](#)]
- 21 **Kurkure U**, Chittajallu DR, Brunner G, Le YH, Kakadiaris IA. A supervised classification-based method

- for coronary calcium detection in non-contrast CT. *Int J Cardiovasc Imaging* 2010; **26**: 817-828 [PMID: 20229312 DOI: 10.1007/s10554-010-9607-2]
- 22 **Wei J**, Zhou C, Chan HP, Chughtai A, Agarwal P, Kuriakose J, Hadjiiski L, Patel S, Kazerooni E. Computerized detection of noncalcified plaques in coronary CT angiography: evaluation of topological soft gradient prescreening method and luminal analysis. *Med Phys* 2014; **41**: 081901 [PMID: 25086532 DOI: 10.1118/1.4885958]
 - 23 **Jawaid MM**, Riaz A, Rajani R, Reyes-Aldasoro CC, Slabaugh G. Framework for detection and localization of coronary non-calcified plaques in cardiac CTA using mean radial profiles. *Comput Biol Med* 2017; **89**: 84-95 [PMID: 28797740 DOI: 10.1016/j.compbiomed.2017.07.021]
 - 24 **Tessmann M**, Vega-Higuera F, Fritz D, Scheuering M, Greiner G. Multi-scale feature extraction for learning-based classification of coronary artery stenosis. *SPIE* 2009; 726002
 - 25 **Kelm BM**, Mittal S, Zheng Y, Tsymbal A, Bernhardt D, Vega-Higuera F, Zhou SK, Meer P, Comaniciu D. Detection, grading and classification of coronary stenoses in computed tomography angiography. *Med Image Comput Comput Assist Interv* 2011; **14**: 25-32 [PMID: 22003680 DOI: 10.1007/978-3-642-23626-6_4]
 - 26 **Zhao F**, Wu B, Chen F, Cao X, Yi H, Hou Y, He X, Liang J. An automatic multi-class coronary atherosclerosis plaque detection and classification framework. *Med Biol Eng Comput* 2019; **57**: 245-257 [PMID: 30088125 DOI: 10.1007/s11517-018-1880-6]
 - 27 **Zreik M**, van Hamersvelt RW, Wolterink JM, Leiner T, Viergever MA, Isgum I. A Recurrent CNN for Automatic Detection and Classification of Coronary Artery Plaque and Stenosis in Coronary CT Angiography. *IEEE Trans Med Imaging* 2019; **38**: 1588-1598 [PMID: 30507498 DOI: 10.1109/TMI.2018.2883807]
 - 28 **Huo Y**, Terry JG, Wang J, Nath V, Bermudez C, Bao S, Parvathaneni P, Carr JJ, Landman BA. Coronary Calcium Detection using 3D Attention Identical Dual Deep Network Based on Weakly Supervised Learning. *Proc SPIE Int Soc Opt Eng* 2019; **10949**: 1094917 [PMID: 31762534 DOI: 10.1117/12.2512541]
 - 29 **Kolossváry M**, Szilveszter B, Merkely B, Maurovich-Horvat P. Plaque imaging with CT-a comprehensive review on coronary CT angiography based risk assessment. *Cardiovasc Diagn Ther* 2017; **7**: 489-506 [PMID: 29255692 DOI: 10.21037/cdt.2016.11.06]
 - 30 **Rodriguez-Granillo GA**, Carrascosa P, Bruining N, Waksman R, Garcia-Garcia HM. Defining the non-vulnerable and vulnerable patients with computed tomography coronary angiography: evaluation of atherosclerotic plaque burden and composition. *Eur Heart J Cardiovasc Imaging* 2016; **17**: 481-491 [PMID: 26903599 DOI: 10.1093/ehjci/jew012]
 - 31 **Motoyama S**, Sarai M, Narula J, Ozaki Y. Coronary CT angiography and high-risk plaque morphology. *Cardiovasc Interv Ther* 2013; **28**: 1-8 [PMID: 23108779 DOI: 10.1007/s12928-012-0140-1]
 - 32 **Lee JM**, Bang JJ, Koo BK, Hwang D, Park J, Zhang J, Yaliang T, Suh M, Paeng JC, Shiono Y, Kubo T, Akasaka T. Clinical Relevance of ¹⁸F-Sodium Fluoride Positron-Emission Tomography in Noninvasive Identification of High-Risk Plaque in Patients With Coronary Artery Disease. *Circ Cardiovasc Imaging* 2017; **10**: e006704 [PMID: 29133478 DOI: 10.1161/CIRCIMAGING.117.006704]
 - 33 **Kolossváry M**, Karády J, Szilveszter B, Kitslaar P, Hoffmann U, Merkely B, Maurovich-Horvat P. Radiomic Features Are Superior to Conventional Quantitative Computed Tomographic Metrics to Identify Coronary Plaques With Napkin-Ring Sign. *Circ Cardiovasc Imaging* 2017; **10**: e006843 [PMID: 29233836 DOI: 10.1161/CIRCIMAGING.117.006843]
 - 34 **Kolossváry M**, Karády J, Kikuchi Y, Ivanov A, Schlett CL, Lu MT, Foldyna B, Merkely B, Aerts HJ, Hoffmann U, Maurovich-Horvat P. Radiomics versus Visual and Histogram-based Assessment to Identify Atheromatous Lesions at Coronary CT Angiography: An ex Vivo Study. *Radiology* 2019; **293**: 89-96 [PMID: 31385755 DOI: 10.1148/radiol.2019190407]
 - 35 **Fuchs TA**, Fiechter M, Gebhard C, Stehli J, Ghadri JR, Kazakauskaitė E, Herzog BA, Husmann L, Gaemperli O, Kaufmann PA. CT coronary angiography: impact of adapted statistical iterative reconstruction (ASIR) on coronary stenosis and plaque composition analysis. *Int J Cardiovasc Imaging* 2013; **29**: 719-724 [PMID: 23053859 DOI: 10.1007/s10554-012-0134-1]
 - 36 **Zuluaga MA**, Magnin IE, Hernández Hoyos M, Delgado Leyton EJ, Lozano F, Orkisz M. Automatic detection of abnormal vascular cross-sections based on density level detection and support vector machines. *Int J Comput Assist Radiol Surg* 2011; **6**: 163-174 [PMID: 20549375 DOI: 10.1007/s11548-010-0494-8]
 - 37 **Kang D**, Dey D, Slomka PJ, Arsanjani R, Nakazato R, Ko H, Berman DS, Li D, Kuo CC. Structured learning algorithm for detection of nonobstructive and obstructive coronary plaque lesions from computed tomography angiography. *J Med Imaging (Bellingham)* 2015; **2**: 014003 [PMID: 26158081 DOI: 10.1117/1.JMI.2.1.014003]
 - 38 **Meijboom WB**, Van Mieghem CA, van Pelt N, Weustink A, Pugliese F, Mollet NR, Boersma E, Regar E, van Geuns RJ, de Jaegere PJ, Serruys PW, Krestin GP, de Feyter PJ. Comprehensive assessment of coronary artery stenoses: computed tomography coronary angiography versus conventional coronary angiography and correlation with fractional flow reserve in patients with stable angina. *J Am Coll Cardiol* 2008; **52**: 636-643 [PMID: 18702967 DOI: 10.1016/j.jacc.2008.05.024]
 - 39 **Taylor CA**, Fonte TA, Min JK. Computational fluid dynamics applied to cardiac computed tomography for noninvasive quantification of fractional flow reserve: scientific basis. *J Am Coll Cardiol* 2013; **61**: 2233-2241 [PMID: 23562923 DOI: 10.1016/j.jacc.2012.11.083]
 - 40 **Tesche C**, Vliegenthart R, Duguay TM, De Cecco CN, Albrecht MH, De Santis D, Langenbach MC, Varga-Szemes A, Jacobs BE, Jochheim D, Baquet M, Bayer RR Nd, Litwin SE, Hoffmann E, Steinberg DH, Schoepf UJ. Coronary Computed Tomographic Angiography-Derived Fractional Flow Reserve for Therapeutic Decision Making. *Am J Cardiol* 2017; **120**: 2121-2127 [PMID: 29102036 DOI: 10.1016/j.amjcard.2017.08.034]
 - 41 **Itu L**, Rapaka S, Passerini T, Georgescu B, Schwemmer C, Schoebinger M, Flohr T, Sharma P, Comaniciu D. A machine-learning approach for computation of fractional flow reserve from coronary computed tomography. *J Appl Physiol (1985)* 2016; **121**: 42-52 [PMID: 27079692 DOI: 10.1152/japplphysiol.00752.2015]

- 42 **Wang ZQ**, Zhou YJ, Zhao YX, Shi DM, Liu YY, Liu W, Liu XL, Li YP. Diagnostic accuracy of a deep learning approach to calculate FFR from coronary CT angiography. *J Geriatr Cardiol* 2019; **16**: 42-48 [PMID: 30800150 DOI: 10.11909/j.issn.1671-5411.2019.01.010]
- 43 **Dey D**, Gaur S, Ovrehus KA, Slomka PJ, Betancur J, Goeller M, Hell MM, Gransar H, Berman DS, Achenbach S, Botker HE, Jensen JM, Lassen JF, Norgaard BL. Integrated prediction of lesion-specific ischaemia from quantitative coronary CT angiography using machine learning: a multicentre study. *Eur Radiol* 2018; **28**: 2655-2664 [PMID: 29352380 DOI: 10.1007/s00330-017-5223-z]
- 44 **Kumamaru KK**, Fujimoto S, Otsuka Y, Kawasaki T, Kawaguchi Y, Kato E, Takamura K, Aoshima C, Kamo Y, Kogure Y, Inage H, Daida H, Aoki S. Diagnostic accuracy of 3D deep-learning-based fully automated estimation of patient-level minimum fractional flow reserve from coronary computed tomography angiography. *Eur Heart J Cardiovasc Imaging* 2020; **21**: 437-445 [PMID: 31230076 DOI: 10.1093/ehjci/jez160]
- 45 **Afshar P**, Mohammadi A, Plataniotis KN, Oikonomou A, Benali H. From Handcrafted to Deep-Learning-Based Cancer Radiomics: Challenges and Opportunities. *IEEE Signal Process Mag* 2019; **36**: 132-160 [DOI: 10.1109/MSP.2019.2900993]
- 46 **Berthelot D**, Carlini N, Goodfellow I, Papernot N, Oliver A, Raffel C. MixMatch: a holistic approach to semi-supervised learning. 2019 Preprint. Available from: [arXiv:1905.02249](https://arxiv.org/abs/1905.02249)
- 47 **Qizhe X**, Dai Z, Hovy E, Luong MT, Le QV. Unsupervised Data Augmentation for Consistency Training. 2019 Preprint. Available from: [arXiv:1904.12848v1](https://arxiv.org/abs/1904.12848v1)
- 48 **Oakden-Rayner L**, Carneiro G, Bessen T, Nascimento JC, Bradley AP, Palmer LJ. Precision Radiology: Predicting longevity using feature engineering and deep learning methods in a radiomics framework. *Sci Rep* 2017; **7**: 1648 [PMID: 28490744 DOI: 10.1038/s41598-017-01931-w]
- 49 **Jamaludin A**, Kadir T, Zisserman A. SpineNet: Automated classification and evidence visualization in spinal MRIs. *Med Image Anal* 2017; **41**: 63-73 [PMID: 28756059 DOI: 10.1016/j.media.2017.07.002]
- 50 **Ciampi F**, Chung K, van Riel SJ, Setio AAA, Gerke PK, Jacobs C, Scholten ET, Schaefer-Prokop C, Wille MMW, Marchianò A, Pastorino U, Prokop M, van Ginneken B. Towards automatic pulmonary nodule management in lung cancer screening with deep learning. *Sci Rep* 2017; **7**: 46479 [PMID: 28422152 DOI: 10.1038/srep46479]

Acute pancreatitis: A pictorial review of early pancreatic fluid collections

Bo Xiao

ORCID number: Bo Xiao 0000-0001-5862-974X.

Author contributions: Xiao B wrote and revised this manuscript.

Conflict-of-interest statement: There is no conflict of interest.

Open-Access: This article is an open-access article that was selected by an in-house editor and fully peer-reviewed by external reviewers. It is distributed in accordance with the Creative Commons Attribution NonCommercial (CC BY-NC 4.0) license, which permits others to distribute, remix, adapt, build upon this work non-commercially, and license their derivative works on different terms, provided the original work is properly cited and the use is non-commercial. See: <http://creativecommons.org/licenses/by-nc/4.0/>

Manuscript source: Invited manuscript

Received: May 28, 2020

Peer-review started: May 28, 2020

First decision: June 5, 2020

Revised: June 8, 2020

Accepted: June 12, 2020

Article in press: June 12, 2020

Published online: June 28, 2020

P-Reviewer: Gokce E

Bo Xiao, Sichuan Key Laboratory of Medical Imaging, Department of Radiology, Affiliated Hospital of North Sichuan Medical College, Nanchong 637000, Sichuan Province, China

Bo Xiao, North Sichuan Medical College, Nanchong 637000, Sichuan Province, China

Corresponding author: Bo Xiao, MD, PhD, Associate Professor, Sichuan Key Laboratory of Medical Imaging, Department of Radiology, Affiliated Hospital of North Sichuan Medical College, No. 63, Wenhua Road, Nanchong 637000, Sichuan Province, China.
xiaoboimaging@163.com

Abstract

Acute pancreatitis is a common acute inflammatory disease involving the pancreas and peripancreatic tissues or remote organs. The revised Atlanta classification 2012 of acute pancreatitis divides patients into mild, moderately severe and severe groups. Major changes of the classification include acute fluid collection terminology. However, some inappropriate terms of the radiological diagnosis reports in the daily clinical work or available literature may still be found. The aim of this review article is: to present an image-rich overview of different morphologic characteristics of the early-stage (within 4 wk after symptom onset) local complications associated with acute pancreatitis by computed tomography or magnetic resonance imaging; to clarify confusing imaging concepts for pancreatic fluid collections and underline standardised reporting nomenclature; to assist communication among treating physicians; and to facilitate the implications for clinical management decision-making.

Key words: Acute pancreatitis; Computed tomography; Magnetic resonance imaging; Acute peripancreatic fluid collection; Acute necrotic collection; Complication

©The Author(s) 2020. Published by Baishideng Publishing Group Inc. All rights reserved.

Core tip: To our best of knowledge, this is the first pictorial review that determines the spectrum of magnetic resonance imaging features in patients with acute pancreatitis of distinct early acute necrotic collection compared with acute peripancreatic fluid collection.

Citation: Xiao B. Acute pancreatitis: A pictorial review of early pancreatic fluid collections. *Artif Intell Med Imaging* 2020; 1(1): 40-49

S-Editor: Wang JL
L-Editor: Filipodia
E-Editor: Xing YX



URL: <https://www.wjgnet.com/2644-3260/full/v1/i1/40.htm>
DOI: <https://dx.doi.org/10.35711/aimi.v1.i1.40>

INTRODUCTION

Acute pancreatitis is a common digestive disease, which is related to an acute onset of epigastric pain with/without nausea and vomiting. Cholelithiasis, alcoholism and hyperlipidaemia are the most widely recognised etiological factors in acute pancreatitis patients^[1]. Clinically, physicians often make the accurate diagnosis based on clinical manifestations and biochemical parameters (sufficiently elevated serum lipase or amylase) for the majority of patients with acute pancreatitis^[1]. Indeed, the routine medical imaging for this disease is unwarranted. However, the natural history and consequences of critically ill patients (particularly moderately severe or severe acute pancreatitis) can result in a variety of local complications^[2]. These developments thus prompt imaging to detect clinical complications.

Imaging approaches, especially computed tomography (CT) and magnetic resonance imaging (MRI), are valuable in detecting local complications associated with acute pancreatitis in both the early-phase and the late-phase of disease. With the increasing application of the revised Atlanta classification criteria 2012^[2], radiologists play a crucial role in relevant imaging diagnosis, scientific research and multidisciplinary team communication. Although this classification updates the definitions of acute pancreatitis and many pancreatitis-associated complications, some inappropriate terms of the radiological diagnosis reports in the daily clinical work or available literature may still be found.

Therefore, the purpose of this pictorial article is: To serve as an image-rich overview of different morphologic characteristics of the early-stage (within 4 wk after symptom onset) local complications associated with acute pancreatitis by CT or MR; to clarify confusing imaging concepts and enable standardised reporting nomenclature; to assist communication among treating physicians; and to facilitate the implications for treatments.

DEFINITION AND DIAGNOSIS OF EARLY-STAGE COLLECTIONS ASSOCIATED WITH ACUTE PANCREATITIS

In general, acute pancreatitis is classically divided into two types: Interstitial oedematous pancreatitis and necrotising pancreatitis. Clinically, the majority of patients with acute pancreatitis are present as interstitial oedematous pancreatitis. They have diffuse or localised enlargement of the pancreas owing to inflammatory oedema. On the other hand, necrotising pancreatitis accounts for 20%-30% of acute pancreatitis patients^[3-5], and it is subdivided into three subtypes on the basis of contrast-enhanced CT according to the new Atlanta classification^[2]: (1) Combined pancreatic necrosis and peripancreatic necrosis (most common, approximately 75% of all necrotising pancreatitis); (2) Peripancreatic tissue necrosis alone (less common, with an incidence of approximately 20%)^[6]; and (3) Pancreatic parenchymal necrosis alone (rare, with an incidence of only 5%)^[7-9]. For radiologists, it is crucial to make a distinction between interstitial oedematous pancreatitis and necrotising pancreatitis in diagnosing acute pancreatitis. The correct diagnosis of imaging type can assist in the recognition of subsequent pancreatitis-related complications and application of the proper terminology.

Currently, there are two diagnostic terms for local complications in the early stage of acute pancreatitis: Acute peripancreatic fluid collections (APFCs) and acute necrotic collections (ANCs)^[2]. On the one hand, the characteristics of acute peripancreatic fluid collections include: (1) Arising from interstitial oedematous pancreatitis; (2) Nonencapsulated collections (lack of a well-defined capsule/definable wall); (3) Collection age within the initial 4 wk after symptom onset; (4) Peripancreatic location (surrounding or adjacent to pancreas); and (5) A homogeneous or simple fluid appearance (containing purely fluid) (Figure 1)^[7-9].

On the other hand, the characteristics of acute necrotic collections include: (1) Occurring only in the setting of necrotising pancreatitis; (2) Collections without an encapsulating capsule or over time with poorly organised wall, (3) Collection age within the first 4 wk of this disease; (4) Peripancreatic and pancreatic different

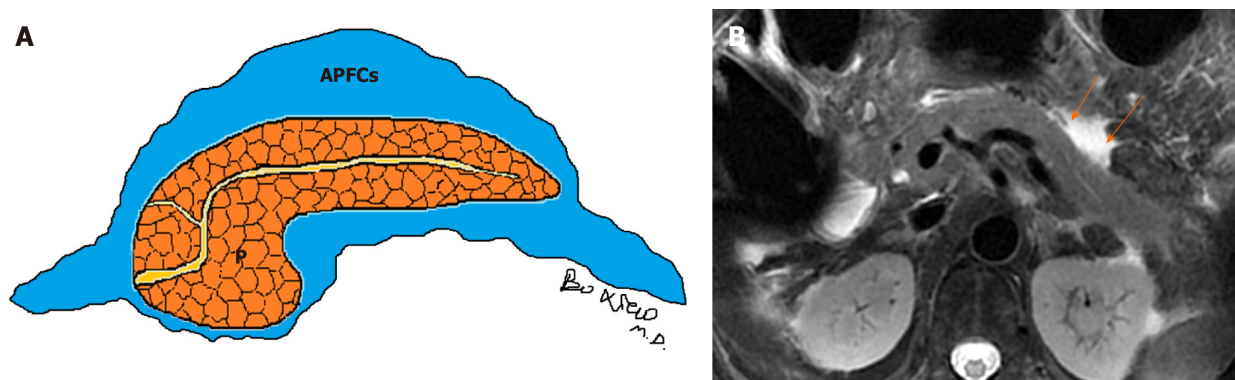


Figure 1 Schematic diagram of acute peripancreatic fluid collections and magnetic resonance imaging of a patient. A: Schematic diagram of acute peripancreatic fluid collections within 4 wk of onset of interstitial oedematous pancreatitis. The term "acute peripancreatic fluid collections" applies only to interstitial oedematous pancreatitis patients; B: A 66-year-old woman with interstitial oedematous pancreatitis. Magnetic resonance imaging axial T2WI image shows a homogeneous fluid finding (arrows) around the pancreas. APFCs: Acute peripancreatic fluid collections; P: Pancreas.

locations (surrounding the pancreas or intrapancreatic extension or both); and (5) A heterogeneous appearance due to containing variable amounts of inflammatory fluid and liquefied or nonliquefied necrotic debris (Figure 2)^[7-10].

LOCATION, SHAPE, SIZE OF APFCs/ANCs

On CT/MRI, acute peripancreatic fluid collections are predominantly localised in peripancreatic areas (*e.g.*, the lesser sac) and the retroperitoneal spaces (*e.g.*, left anterior pararenal space) or peripancreatic fascial planes. They exhibit variable shape and size but mostly present as a uniform linear or strip-shaped liquid appearance^[3-6]. In addition, the volume of APFCs is relatively smaller due to fluid generally confined by a simple retroperitoneum space and/or normal peripancreatic fascial planes (Figure 3).

On the other side, acute necrotic collections often break through the limitation of the interfascial planes and can affect multiple retroperitoneal spaces, interfascial planes, subperitoneal spaces and other abdominal spaces. In fact, they are most frequently situated in the lesser sac and the anterior pararenal spaces, followed by transverse mesocolon, mesenteric root, and thereafter, gastrohepatic, gastrosplenic and gastrocolic ligaments^[11]. Furthermore, these collections may additionally involve the remote regions, such as the pelvic sidewalls and mediastinum. Thus, acute necrotic collections are generally numerous (multiple), irregular and loculated, and the volume of effusion often appears larger than that of acute peripancreatic fluid collections (Figure 4)^[9-11].

DENSITY/SIGNAL INTENSITY, ENHANCEMENT CHARACTERISTICS OF APFCs/ANCs

Acute peripancreatic fluid collections have homogeneous fluid appearances. They are uniformly hypoattenuating on CT and T1 hypointense and T2 hyperintense on MRI. After intravenous contrast-material administration, acute peripancreatic fluid collections are not enhancing owing to the pure fluid nature^[8-10].

In contrast, acute necrotic collections are heterogeneous (Figure 5). There are relatively hyperdense materials (necrotic fragments of pancreas) and/or markedly hypodense fat globules (peripancreatic fat) among hypodense fluid on CT^[6-8]. Similarly, there are varying degrees of round, patchy, strip-shaped T2-hypointense components (adipose fragments or necrotic pancreatic tissue) among T2-hyperintense fluid on MR images^[3-6]. During contrast-enhanced CT/MRI, the internal necrotic debris or trapped fat within acute necrotic collections often does not show enhancement (Figure 5), while the immature, fibrous granulation tissue wall of these collections may be detectable as slight to confluent enhancement (Figure 6).

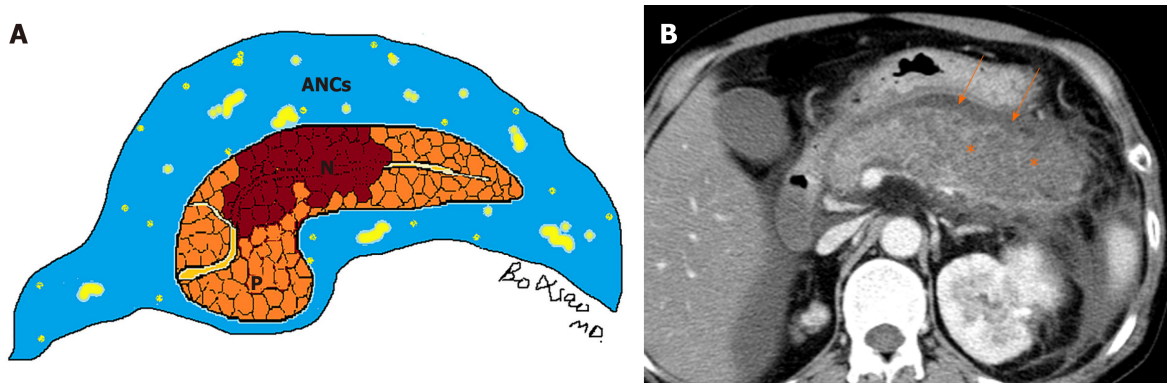


Figure 2 Schematic diagram of acute necrotic collections and computed tomography of a patient. A: Schematic diagram of acute necrotic collections within 4 wk of onset of necrotizing pancreatitis. The term "acute necrotic collections" is diagnosed only in necrotizing pancreatitis patients; B: A 56-year-old man with necrotizing pancreatitis. Axial contrast-enhanced computed tomography image in the venous phase shows a large area of necrosis (asterisks) in the pancreatic body and tail; therefore, a lesser omental sac collection (arrows) should be diagnosed as acute necrotic collections. ANCs: Acute necrotic collections; P: Pancreas; N: Necrosis.

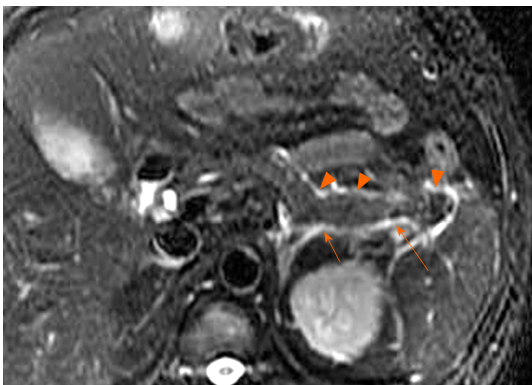


Figure 3 A 40-year-old woman with interstitial oedematous pancreatitis. Magnetic resonance imaging axial T2WI image shows uniform linear liquid hyperintense (acute peripancreatic fluid collections) in the left pararenal anterior spaces (arrowheads) and retromesenteric plane (arrows).

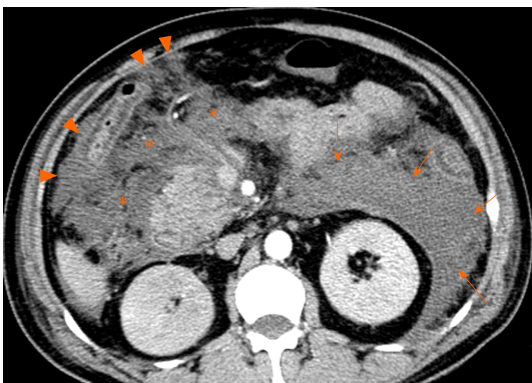


Figure 4 A 53-year-old man with necrotizing pancreatitis. Axial contrast-enhanced computed tomography image in the venous phase shows extensive heterogeneous collections (acute necrotic collections) in the left pararenal anterior spaces (arrows) and the subperitoneal spaces/transverse mesentery areas (asterisks) as well as greater omentum zones (arrowheads).

SECONDARY OR CONCOMITANT CT/MRI FINDINGS OF APFCs/ANCs

In general, (peri)pancreatic fluid collections may also be associated with a variety of complications, which can make the clinical condition more complex. After conservative treatments, acute peripancreatic fluid collections are often absorbed quickly with rare follow-up complications. Most of these patients are discharged within 1-2 wk after admission^[7-9].

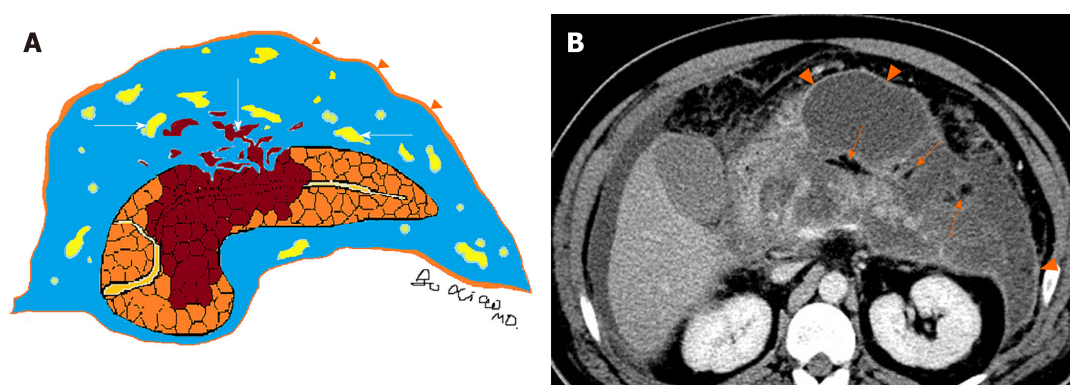


Figure 5 Schematic diagram of heterogeneous collections and computed tomography image of a patient. A: Schematic diagram of heterogeneous collections (acute necrotic collections) secondary to necrotizing pancreatitis. With the prolongation of the disease course, immature poorly organized walls (arrowheads) can gradually form. There are two components within necrotic collections: fat fragments and necrotic parenchymal fragments (arrows); B: A 60-year-old man with necrotizing pancreatitis. Axial contrast-enhanced computed tomography image in the venous phase shows markedly hypodense fat globules (arrows) within acute necrotic collections as well as slight enhancement of capsule (arrowheads) of collections. P: Pancreas; N: Necrosis.

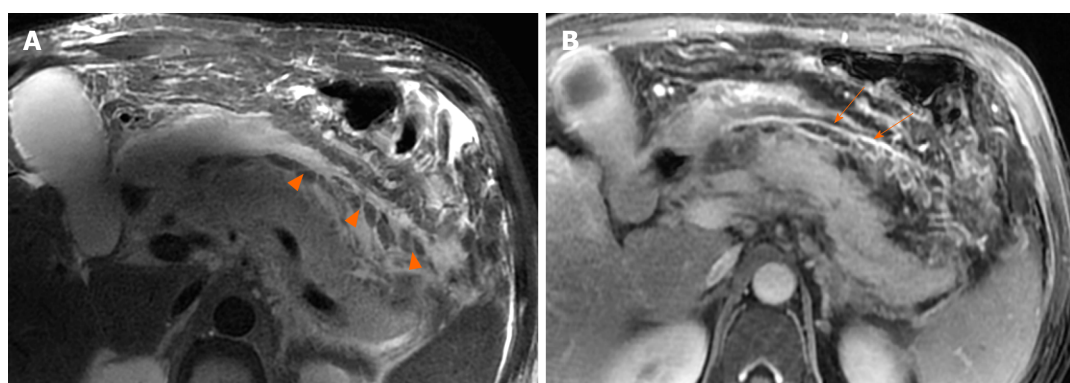


Figure 6 A 46-year-old man with necrotizing pancreatitis. A: Magnetic resonance imaging axial T2WI image shows a number of patchy, strip-shaped T2-hypointense components (necrotic adipose fragments) (arrowheads) among T2-hyperintense fluid; B: Axial contrast-enhanced magnetic resonance imaging shows viable capsule enhancement (arrows).

Clinically, necrotising pancreatitis with acute necrotic collection is mainly seen in patients with moderate severe acute pancreatitis and severe acute pancreatitis, with a longer disease course (lasting several weeks or months). Consequently, secondary infectious complications are more likely to occur in acute necrotic collections, compared with acute peripancreatic fluid collections^[9-11]. Infection should be suspected when there are secondary clinical signs of sepsis, such as a new occurrence of fever and leucocytosis^[8-10]. On CT images, the sign of multiple extraluminal gas or a gas-fluid level in the peripancreatic zones and retroperitoneal spaces is highly suggestive of acute necrotic collections complicated by infection (Figure 7). If clinical manifestations are concordant or needle-guided aspiration confirms the development of infection, then these collections should be classified as infected acute necrotic collections^[9-11]. In this setting, percutaneous aspiration or drain insertion can be performed for the treatment of an infected collection^[11-13].

Moreover, when necrotising pancreatitis affects a large area of intrapancreatic pancreas, it involves the main pancreatic duct (necrosis of the pancreatic duct). Over time, the pancreatic duct rupture or disrupted integrity of the pancreatic duct accompanied with the intrapancreatic acute necrotic collections (liquefied pancreatic tissue) can result in the formation of “disconnected duct syndrome” (Figure 8)^[11,14]. As for this condition, a collection communication with main pancreatic duct is usually evident on MRI and MR cholangiopancreatography (Figure 8). This syndrome may alter treatment but does not affect acute necrotic collection classification, and these patients often require surgical management for a complete recovery^[12-15].

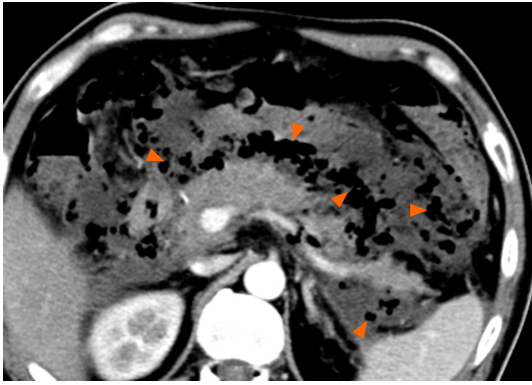


Figure 7 A 59-year-old man with necrotizing pancreatitis complicating infection. Axial contrast-enhanced computed tomography image in the venous phase shows multiple extraluminal gas bubbles (arrowheads) in the peripancreatic and the retroperitoneal spaces, consistent with a pathognomonic sign of the infected necrosis.

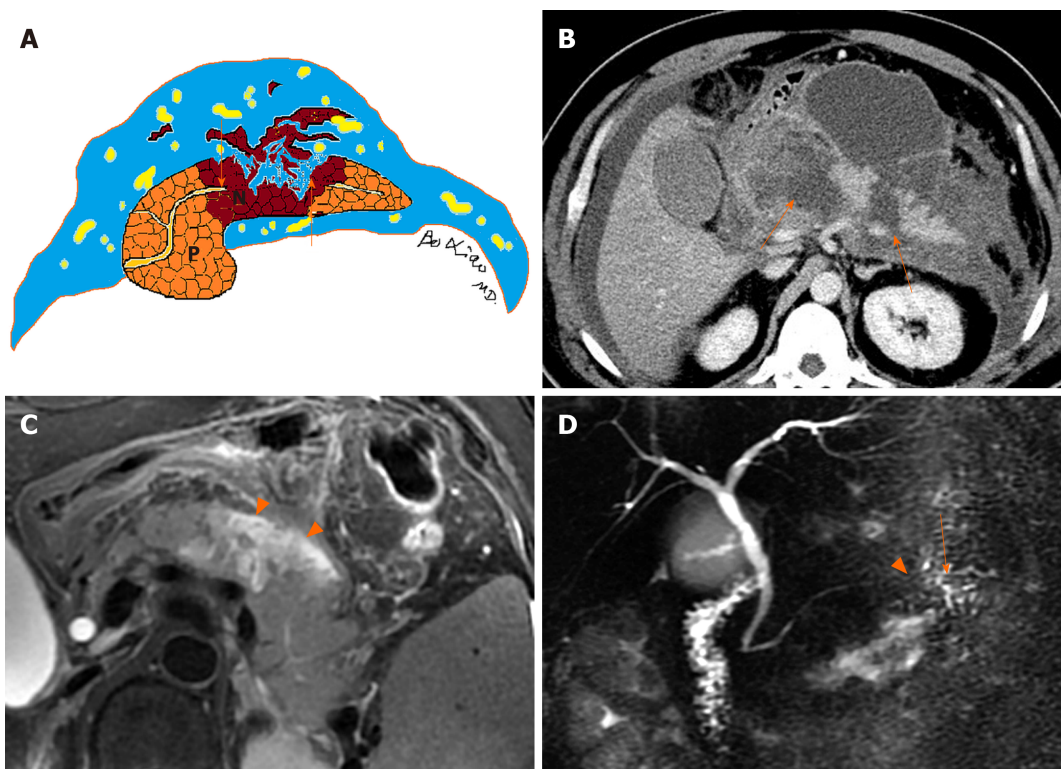


Figure 8 Schematic diagram of disconnected pancreatic duct syndrome and medical images of patients. A: Schematic diagram of disconnected pancreatic duct syndrome. The pancreatic duct rupture and interruption (arrows) resulting from a wide range of liquefied pancreatic body tissue is seen; B: A 60-year-old man with necrotizing pancreatitis. Axial contrast-enhanced computed tomography image in the venous phase shows extensive parenchymal transmural necrosis (arrows) in the region of neck and body of the pancreas. Disconnected main pancreatic duct was proved at surgery; C: A 57-year-old woman with necrotizing pancreatitis. Magnetic resonance imaging axial T2WI image shows a majority of liquefied necroses (arrowheads) in the pancreatic body; D: The main pancreatic duct (arrow) of the tail of pancreas is interrupted (arrowhead) by the mentioned-above lesion. P: Pancreas; N: Necrosis.

TERMINOLOGY MISUSE IN IMAGING REPORTS OF APFCs/ANCs

Depending on the revised Atlanta classification and our clinical practice, common terminology misuse conditions in the daily imaging reports are summarised as follows: (1) On CT/MRI, no necrosis finding was observed in the pancreatic parenchyma, which was assumed to be “interstitial oedematous pancreatitis.” Then the accumulation of fluid in the peripancreatic regions may be misinterpreted as “acute peripancreatic fluid collection.” However, a pitfall is probably present because we may ignore the presence of small “adipose tissue debris” in peripancreatic collections (Figure 9). At this point, it should be diagnosed as “necrotising pancreatitis (peripancreatic necrotic type),” due to necrotic adipose fragments around the pancreas. Therefore, the nomenclature of the collection is referred to as an “acute

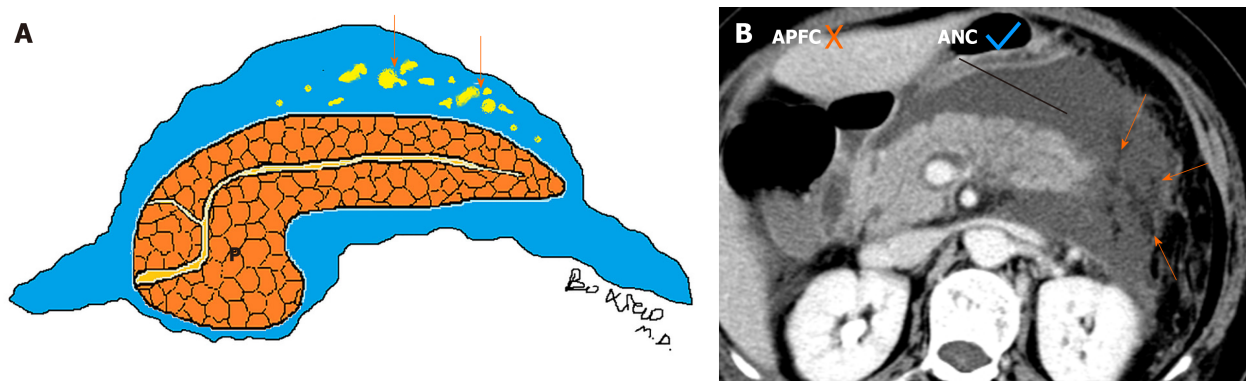


Figure 9 Schematic diagram of necrotizing pancreatitis and computed tomography image of a patient. A: Schematic diagram of necrotizing pancreatitis (peripancreatic necrotic type). Acute necrotic collection involving peripancreatic fat only (arrows) is seen; B: A 58-year-old woman with necrotizing pancreatitis (peripancreatic necrosis only). Axial contrast-enhanced computed tomography image in the venous phase shows normal pancreatic parenchymal enhancement without definite necrosis. A peripancreatic collection may be misdiagnosed as “acute peripancreatic fluid collection.” However, multiple heterogeneous, nonliquid adipose components (arrows) are revealed among the collection. For this reason, it should be considered as acute necrotic collection. P: Pancreas; APFC: Acute peripancreatic fluid collection; ANC: Acute necrotic collection.

necrotic collection” (Figure 9)^[8-11]; (2) On CT/MRI images, when a peripancreatic or retroperitoneal homogeneous collection with uniform fluid density or signal intensity was seen, it may be misinterpreted as an “acute peripancreatic fluid collection.” Instead, if a peripancreatic collection was secondary to known pancreatic parenchymal necrosis and/or haemorrhage, the correct diagnosis term for the collection should be “acute necrotic collection,” even if it is radiologically homogeneous and contains no nonliquefied component (Figure 10)^[4-8]; and (3) As aforementioned content, it may be easier to diagnose a peripancreatic homogeneous collection as “acute peripancreatic fluid collection.” However, if a collection is involving the pancreas parenchyma, a correct term for the surrounding fluid should be diagnosed as “acute necrotic collection” (Figure 11), regardless of the nature of fluid density or signal intensity. In another word, any collection involving the pancreas parenchyma should be determined as necrotising pancreatitis^[8-12].

EXISTING PROBLEMS AND PROSPECTS

Although there are many differences between acute peripancreatic fluid collections and acute necrotic collections, in the clinical practice it is sometimes difficult to accurately distinguish acute peripancreatic fluid collections from acute necrotic collections on CT at the early stage of acute pancreatitis (especially within 2 d of symptom onset). The reasons may be related to the following factors: (1) It may allow sufficient time for completed necrosis of the pancreas and/or peripancreatic fat (findings of solid necrotic materials to liquefy over several days). Thus, heterogeneous contents may not be found within the early-phase fluid. This also explains why an early contrast-enhanced CT may underestimate the eventual degree of (peri)pancreatic necrosis. In this setting, further CT studies after an interval of between 5 d and 7 d should be performed^[2-5]; and (2) Due to the low contrast resolution of CT, it is difficult to detect a small amount of heterogeneous contents. For this purpose, MRI may be required for this distinction because it is very sensitive to the detection of internal architecture of collections (even a small area of heterogeneous debris)^[6-9]. Moreover, MRI diffusion weighted imaging combined with ADC value measurement is helpful for the differential diagnosis of interstitial oedematous pancreatitis and necrotising pancreatitis^[4-6]. Whether diffusion weighted imaging is also valuable for the early differential diagnosis of acute peripancreatic fluid collection and acute necrotic collection may become a direction of future research.

CONCLUSION

To sum up, the natural history and consequences of different pancreatic and peripancreatic collections are now better described and understood. The differential

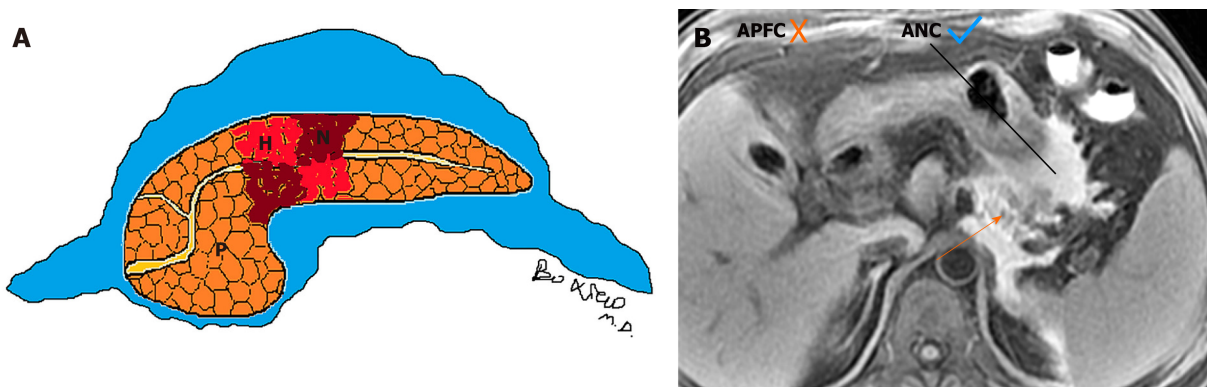


Figure 10 Schematic diagram of necrotizing pancreatitis and magnetic resonance imaging of a patient. A: Schematic diagram of necrotizing pancreatitis (pancreatic parenchymal necrosis alone). The peripancreatic collections are homogeneous; B: A 47-year-old man with necrotizing pancreatitis complicated with haemorrhage. Magnetic resonance imaging axial T1WI image shows peripancreatic homogeneous fluid with greater hyperintense signal. For this reason, it may be misdiagnosed as “acute peripancreatic fluid collection.” However, the necrosis and haemorrhage (arrow) of the body and tail of the pancreas can be indicated. Therefore, the collection should be diagnosed as acute necrotic collection. P: Pancreas, N: Necrosis, H: Haemorrhage; APFC: Acute peripancreatic fluid collection; ANC: Acute necrotic collection.

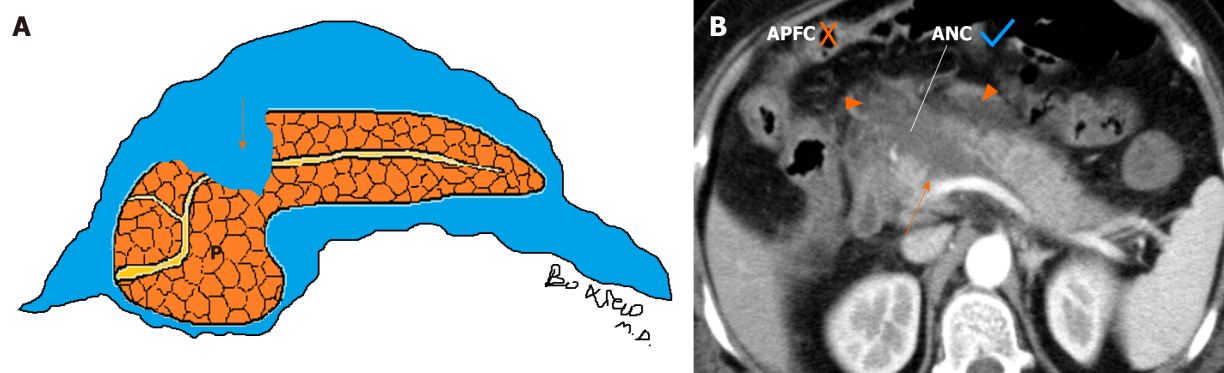


Figure 11 Schematic diagram of acute necrotizing pancreatitis, and extrapancreatic fluid and computed tomography of a patient. A: Schematic diagram of acute necrotizing pancreatitis and extrapancreatic fluid with extension within the pancreatic parenchyma (arrow); B: A 56-year-old woman with acute necrotizing pancreatitis. Axial contrast-enhanced computed tomography image in the late arterial phase shows a peripancreatic homogeneous collection (arrowheads). It may be misinterpreted as “acute peripancreatic fluid collection.” However, note the peripancreatic fluid extends into the parenchyma of the head and neck of the pancreas (arrow). Therefore, it should be diagnosed as an “acute necrotic collection.” P: Pancreas; APFC: Acute peripancreatic fluid collection; ANC: Acute necrotic collection.

diagnosis of these collections within 4 wk of symptom onset is succinctly summarised in Table 1. The accurate description of pancreatitis-associated collections, including location (pancreatic, peripancreatic, others), the presence of contents (liquid, solid, gas), the thickness of collection wall (thin, thick) and the presence or absence of infectious findings will facilitate the radiologic reports in daily practice. Finally, radiologists should be fully aware of the standardised imaging nomenclature on the basis of associated morphologic descriptions. It is necessary for accurate documentation and reporting of academic research, and it is also important to direct implications of care plans for patients with acute pancreatitis.

Table 1 Key points of clinical and imaging differential diagnosis between acute peripancreatic fluid collection and acute necrotic collection

Key points	Acute peripancreatic fluid collection	Acute necrotic collection
Clinical severity	Mostly mild acute pancreatitis	Moderately severe acute pancreatitis or severe acute pancreatitis
Management algorithm	Conservative treatment (usually resolves spontaneously without intervention)	Likely increased morbidity and intervention rates (drainage or surgical treatment)
Course and prognosis	The hospital stay is usually about one week after onset; a good prognosis	Hospitalization often lasts from weeks to months; increased infection and mortality rates
CT/MRI imaging pattern	Occurs only in the setting of interstitial oedematous pancreatitis	Occurs in the setting of acute necrotising pancreatitis (including peripancreatic necrosis only)
Location and number of collections on CT/MRI	Mostly confined to simple retroperitoneal space or interfascial plane	Mostly in transabdominal-pelvic cavities and multiple spaces or interfascial planes
Shape, size, edge	Linear/strip-shaped, a small amount of collections, clear edge	Large patchy-shaped, a large amount of collections, unclear or irregular edge
Density/intense, enhancement characteristics	Homogeneous low density/hypointense T1 hyperintense T2 signal; no enhancement	Mixed features, mainly low density/hypointense T1 /hyperintense T2 signal, containing low density fat/fat signal intensity and low density or hypointense pancreas fragments; fragments are not enhancing
Secondary or concomitant signs	Rare	Frequent secondary infection with “bubble sign” (caused by infection itself or intestinal fistula with adjacent intestine); when a large area of intrapancreatic collections is present, “pancreatic duct disruption syndrome” may occur (further invasive operation is often required)

CT: Computed tomography; MRI: Magnetic resonance imaging.

REFERENCES

- 1 **Yadav D**, Lowenfels AB. The epidemiology of pancreatitis and pancreatic cancer. *Gastroenterology* 2013; **144**: 1252-1261 [PMID: [23622135](#) DOI: [10.1053/j.gastro.2013.01.068](#)]
- 2 **Banks PA**, Bollen TL, Dervenis C, Gooszen HG, Johnson CD, Sarr MG, Tsotos GG, Vege SS; Acute Pancreatitis Classification Working Group. Classification of acute pancreatitis--2012: revision of the Atlanta classification and definitions by international consensus. *Gut* 2013; **62**: 102-111 [PMID: [23100216](#) DOI: [10.1136/gutjnl-2012-302779](#)]
- 3 **Thoeni RF**. The revised Atlanta classification of acute pancreatitis: its importance for the radiologist and its effect on treatment. *Radiology* 2012; **262**: 751-764 [PMID: [22357880](#) DOI: [10.1148/radiol.11110947](#)]
- 4 **Xiao B**, Xu HB, Jiang ZQ, Zhang J, Zhang XM. Current concepts for the diagnosis of acute pancreatitis by multiparametric magnetic resonance imaging. *Quant Imaging Med Surg* 2019; **9**: 1973-1985 [PMID: [31929970](#) DOI: [10.21037/qims.2019.11.10](#)]
- 5 **Sun H**, Zuo HD, Lin Q, Yang DD, Zhou T, Tang MY, Wang YXJ, Zhang XM. MR imaging for acute pancreatitis: the current status of clinical applications. *Ann Transl Med* 2019; **7**: 269 [PMID: [31355236](#) DOI: [10.21037/atm.2019.05.37](#)]
- 6 **Meyrignac O**, Lagarde S, Bournet B, Mokrane FZ, Buscail L, Rousseau H, Otal P. Acute Pancreatitis: Extrapaneatic Necrosis Volume as Early Predictor of Severity. *Radiology* 2015; **276**: 119-128 [PMID: [25642743](#) DOI: [10.1148/radiol.15141494](#)]
- 7 **Zhao K**, Adam SZ, Keswani RN, Horowitz JM, Miller FH. Acute Pancreatitis: Revised Atlanta Classification and the Role of Cross-Sectional Imaging. *AJR Am J Roentgenol* 2015; **205**: W32-W41 [PMID: [26102416](#) DOI: [10.2214/AJR.14.14056](#)]
- 8 **Murphy KP**, O'Connor OJ, Maher MM. Updated imaging nomenclature for acute pancreatitis. *AJR Am J Roentgenol* 2014; **203**: W464-W469 [PMID: [25341160](#) DOI: [10.2214/AJR.13.12222](#)]
- 9 **Türkvtan A**, Erden A, Türkoğlu MA, Seçil M, Yüce G. Imaging of acute pancreatitis and its complications. Part 2: complications of acute pancreatitis. *Diagn Interv Imaging* 2015; **96**: 161-169 [PMID: [24703377](#) DOI: [10.1016/j.diii.2013.12.018](#)]
- 10 **Bollen TL**. Acute pancreatitis: international classification and nomenclature. *Clin Radiol* 2016; **71**: 121-133 [PMID: [26602933](#) DOI: [10.1016/j.crad.2015.09.013](#)]
- 11 **Foster BR**, Jensen KK, Bakis G, Shaaban AM, Coakley FV. Revised Atlanta Classification for Acute Pancreatitis: A Pictorial Essay. *Radiographics* 2016; **36**: 675-687 [PMID: [27163588](#) DOI: [10.1148/rg.2016150097](#)]
- 12 **Sarathi Patra P**, Das K, Bhattacharyya A, Ray S, Hembram J, Sanyal S, Dhali GK. Natural resolution or intervention for fluid collections in acute severe pancreatitis. *Br J Surg* 2014; **101**: 1721-1728 [PMID: [25329330](#) DOI: [10.1002/bjs.9666](#)]
- 13 **Holleman RA**, Bakker OJ, Boermeester MA, Bollen TL, Bosscha K, Bruno MJ, Buskens E, Dejong CH, van Duijvendijk P, van Eijck CH, Fockens P, van Goor H, van Grevenstein WM, van der Harst E, Heisterkamp J, Hesselink EJ, Hofker S, Houdijk AP, Karsten T, Kruij PM, van Laarhoven CJ, Laméris JS, van Leeuwen MS, Manusama ER, Molenaar IQ, Nieuwenhuijs VB, van Ramshorst B, Roos D, Rosman C,

- Schaapherder AF, van der Schelling GP, Timmer R, Verdonk RC, de Wit RJ, Gooszen HG, Besselink MG, van Santvoort HC; Dutch Pancreatitis Study Group. Superiority of Step-up Approach vs Open Necrosectomy in Long-term Follow-up of Patients With Necrotizing Pancreatitis. *Gastroenterology* 2019; **156**: 1016-1026 [PMID: [30391468](#) DOI: [10.1053/j.gastro.2018.10.045](#)]
- 14 **Fischer TD**, Gutman DS, Hughes SJ, Trevino JG, Behrns KE. Disconnected pancreatic duct syndrome: disease classification and management strategies. *J Am Coll Surg* 2014; **219**: 704-712 [PMID: [25065360](#) DOI: [10.1016/j.jamcollsurg.2014.03.055](#)]
- 15 **van Brunschot S**, van Grinsven J, van Santvoort HC, Bakker OJ, Besselink MG, Boermesteer MA, Bollen TL, Bosscha K, Bouwense SA, Bruno MJ, Cappendijk VC, Consten EC, Dejong CH, van Eijck CH, Erkelens WG, van Goor H, van Grevenstein WMU, Haveman JW, Hofker SH, Jansen JM, Laméris JS, van Lienden KP, Meijssen MA, Mulder CJ, Nieuwenhuijs VB, Poley JW, Quispel R, de Ridder RJ, Römkens TE, Scheepers JJ, Schepers NJ, Schwartz MP, Seerden T, Spanier BWM, Straathof JWA, Strijker M, Timmer R, Venneman NG, Vleggaar FP, Voermans RP, Witteman BJ, Gooszen HG, Dijkgraaf MG, Fockens P; Dutch Pancreatitis Study Group. Endoscopic or surgical step-up approach for infected necrotising pancreatitis: a multicentre randomised trial. *Lancet* 2018; **391**: 51-58 [PMID: [29108721](#) DOI: [10.1016/S0140-6736\(17\)32404-2](#)]



Basic Study

Acoustic concept based on an autonomous capsule and a wideband concentric ring resonator for pathophysiological prevention

Amina Medjdoub, Fabrice Lefebvre, Nadine Saad, Saïd Soudani, Georges Nassar

ORCID number: Amina Medjdoub 0000-0002-7312-6478; Fabrice Lefebvre 0000-0001-8274-0464; Nadine Saad 0000-0001-9091-0793; Saïd Soudani 0000-0002-1934-3615; Georges Nassar 0000-0002-8413-3307

Author contributions: Nassar G was responsible for overall study concept; Medjdoub A and Lefebvre F were responsible for the quantification of the physical and electrical characteristics of sensors; Saad N and Soudani S were responsible of sensor/biological tissue interfaces behavior and signal processing analysis component; Nassar G, Medjdoub A and Lefebvre F were responsible for the experimental concept design and application; all authors reviewed, edited, and approved the final manuscript.

Institutional review board statement: No human and/or animal subjects are involved in this study.

Conflict-of-interest statement: Nothing to disclose.

Data sharing statement: No additional data are available.

Open-Access: This article is an open-access article that was selected by an in-house editor and

Amina Medjdoub, Fabrice Lefebvre, Georges Nassar, Institute of Electronic, Microelectronic and Nanotechnology, Department of Opto-Acousto-Electronic, Université Polytechnique Hauts-de-France, Villeneuve d'Ascq 59652, France

Nadine Saad, Department of Physics, Université Libanaise-Faculté des Sciences, Beyrouth 1000, Lebanon

Saïd Soudani, Signal Processing Department, Université des Sciences et de la Technologie d'Oran, Oran 31000, Algeria

Corresponding author: Georges Nassar, PhD, Professor, Institute of Electronic, Microelectronic and Nanotechnology, Department of Opto-Acousto-Electronic, Université Polytechnique Hauts-de-France, Avenue Henri Poincaré, Cité Scientifique CS 60069, Villeneuve d'Ascq 59652, France. gnassar@uphf.fr

Abstract

BACKGROUND

Research on the performance of elements constituting our modern environment is constantly evolving, both on a daily basis and on technological basis. But to date, the response of the system to the expectations of the population remains too modest.

AIM

To elaborate an ultrasonic technique to scan and evaluate *in-vivo* physiological properties by coupling sensors and multilayer biological tissues model.

METHODS

A low-frequency ultrasonic method (around a frequency of 32 KHz) based on the use of an innovative autonomous ultrasonic capsule as a miniaturized elementary spherical sensor (1 cm of diameter) and micro-rings resonators were examined.

RESULTS

Other their functions as passive listeners for the prevention and diagnosis in physiopathology of the respiratory and laryngeal apparatus, these micro-resonators coupled to the ultrasonic capsule through biological tissues (the body) are capable of evaluating the effects of aggression of the environment on human metabolism.

fully peer-reviewed by external reviewers. It is distributed in accordance with the Creative Commons Attribution NonCommercial (CC BY-NC 4.0) license, which permits others to distribute, remix, adapt, build upon this work non-commercially, and license their derivative works on different terms, provided the original work is properly cited and the use is non-commercial. See: <http://creativecommons.org/licenses/by-nc/4.0/>

Manuscript source: Invited manuscript

Received: May 28, 2020

Peer-review started: May 28, 2020

First decision: June 19, 2020

Revised: June 22, 2020

Accepted: June 25, 2020

Article in press: June 25, 2020

Published online: June 28, 2020

P-Reviewer: Mohammed RHA

S-Editor: Wang JL

L-Editor: A

E-Editor: Wang LL



CONCLUSION

This would allow consequently the detection of some potential diseases at an early stage, even in people who still represent no symptoms, which would permit an early treatment and a higher chance of cure.

Key words: Sensor; Capsule; Acoustics; Ring resonators; Biological tissues

©The Author(s) 2020. Published by Baishideng Publishing Group Inc. All rights reserved.

Core tip: Research on the performance of elements constituting our modern environment is constantly evolving, both on a daily basis and on technological basis. But to date, the response of the system to the expectations of the population remains too modest. The current trend lies in the very definition of performance, seen mainly from the point of view of optimizing the service provided to the users. Estimating it, is putting first the medico-technological coherence that will be measured by its capacity to respond to a certain number of needs of both care and comfort.

Citation: Medjdoub A, Lefebvre F, Saad N, Soudani S, Nassar G. Acoustic concept based on an autonomous capsule and a wideband concentric ring resonator for pathophysiological prevention. *Artif Intell Med Imaging* 2020; 1(1): 50-64

URL: <https://www.wjgnet.com/2644-3260/full/v1/i1/50.htm>

DOI: <https://dx.doi.org/10.35711/aimi.v1.i1.50>

INTRODUCTION

Studying interactions between acoustic and living fields goes far beyond biological and health impact studies. Within the context of the development or application of treatments, we intend to explore potential innovations motivated by the wide variety of medical challenges.

Obtaining continuous measurements is often more difficult and only a few constraining devices (rectal, esophageal probes, *etc.*) allow continuous monitoring of the physiological properties of an individual.

Many of the studies have addressed endoscopic ultrasound applications, the majority of which used wired systems. As an example, Lay *et al*^[1] developed a wired ultrasonic imaging capsule for gastrointestinal disorders combining the imaging capabilities of endoscopic ultrasound. The work of Peng *et al*^[2] focuses more on ultrasonic ablation of cancer cells and He *et al*^[3] combines' optoacoustic interference for these endoscopic characterizations. To this end, de Groen^[4] presents a panoramic view of endoscopic features and associated applications.

The evaluations of the quantities concerned are based on significant parameter uncertainty, which constitutes an undeniable field of application for statistical approaches. In this context and taking into account the limitations and the difficulty of some applications (morphology, age, *etc.*), our work focused on the development of an autonomous information system able to collect data on physiological variations or body composition using vibratory waves. This means of exploration combines endoscopy and ultrasound.

The layout of a sensor network embedded in the body is at the heart of concerns in terms of wave propagation, wave/tissue interactions, and biocompatibility of the radiating elements.

The objective of this work was partly to contribute to the development of innovative radiating structures close to the body (sensors radiating inside the body and through multilayer tissues). The development of a new autonomous ultrasound capsule-based scanning method associated with multilayer models represents a very important challenge given the difficulty of experimental implementation in the low frequency band. This work aimed to obtain conclusive results to assess exposure compared to the thresholds tolerated normatively and to propose an alternative method in order to set a better soft diagnosis to avoid in the limit of possible exposure regarding the harmful radiation [Magnetic resonance imaging (MRI), X-rays, *etc.*]. This device makes it possible to monitor continuously the physiological evolution (mechanical stress, *etc.*) and consequently reduce, by alert, the risks in situations considered as extreme.

To improve understanding and quantify the interaction process of evolving tissue characteristics in real conditions, a new low-frequency ultrasonic technique with a miniaturized elementary spherical sensor that behaves as a point source (capsule) was examined. This source was coupled through tissues to receivers spatially identified on the body and adapted, by their concentric ring shapes, to the central vibration frequency of the transmitter. The use of a dedicated algorithm allowed data logging and triggering of alerts if the threshold of a critical value was exceeded.

Using an embedded electrical control architecture, this “capsule” can simultaneously manage tasks such as acoustic transmission/reception, remote data storage and/or telecommunication, as well as provide extended autonomy, which is currently not available for discrete elements.

Given the technical characteristics of such resonators, the randomly distributed capsule network will be able to deliver useful information regarding the evolution of the mechanical state of a dynamic system. A threshold regarding the desired state set by the user must be included in the device in order to reach optimal decisions.

Figure 1 shows the global concept and the potential application in the biological domain. However, for legislative and regulatory reasons, the concept studied in this paper was validated using biological tissues of animal origin and agar as a coupling medium because its physical properties are close to those of human physiological fluid.

MATERIALS AND METHODS

Resonator devices

Integrated emitter capsule sensor: Contrary to most ultrasonic transmission techniques, our goal was to obtain a low-frequency acoustic point source to generate a spherical wave in the medium. To do this, we used a piezo element for which the frequency was optimized to bring the entire mechanical structure of a small sphere into resonance. The radius of the sphere is smaller than the acoustic wavelength generated in the medium so it can be considered as an acoustic point source.

The resonator is a closed spherical shell composed of two hemispheres made of a biocompatible material. Its inner radius is about 8 mm and it is about 2 mm thick^[5]. Resonance of the overall structure occurs as a result of the vibrations produced by a piezoelectric ring (0.5 mm thick) clamped between the two hemispheres (Figure 1A). This configuration offers a good compromise between a frequency of around 32 kHz suitable for the “ultrasonic” exploration of complex dispersive media and easy decoupling of the mechanical vibration frequency from the process (background noise) “until then considered as an undesirable parameter”.

Fundamental acoustic vibrational mode: Spherical motion

Relatively few studies have investigated miniaturized spherical resonators. The most recent studies concern an ultrasonic capsule device measuring 1 cm × 2.5 cm developed by Wang *et al*^[6] and Memon *et al*^[7] dedicated to scanning the gastrointestinal tract using ultrasound with an external emission provided by active elements positioned around the capsule. In the same context, Cox *et al*^[8] conducted studies regarding the feasibility of a wired ultrasound capsule endoscopy. Walker^[9] and Nasedkin *et al*^[10] developed a theoretical and finite element model of an ultrasonic transducer incorporating spherical resonators. However, a number have been developed over the past decades, especially for studying the properties of gasses and liquids. Mehl *et al*^[11] used a spherical resonator in a frequency range of 4 to 13 kHz to measure the velocity and attenuation of sound in C₂H₄ between 0 and 100 °C and 0.15 to 1.0 MPa. The resonator is made of two aluminum hemispheres with an inner diameter of 127 mm and a thickness of 12.1 mm. He *et al*^[12] developed another spherical resonator to measure sound velocity in the gas phase (argon). The resonator comprises two stainless steel (00Cr17Ni14Mo2 type) hemispheres with an inner radius of 61.77 mm and a working frequency between 1 and 15 kHz. The resonator was placed in a pressurized container that was immersed in a thermos-regulated bath.

Analytical approach

Many studies have been conducted in the field of mechanical vibration of spherical shells for axisymmetric modes. Baker^[13], Wilkinson^[14], Kalnins^[15] and Duffey *et al*^[16], for example, studied the vibration of a macro spherical shell under the effect of transverse shear and rotational inertia.

In what follows, to establish the equations of motion of a spherical shell we

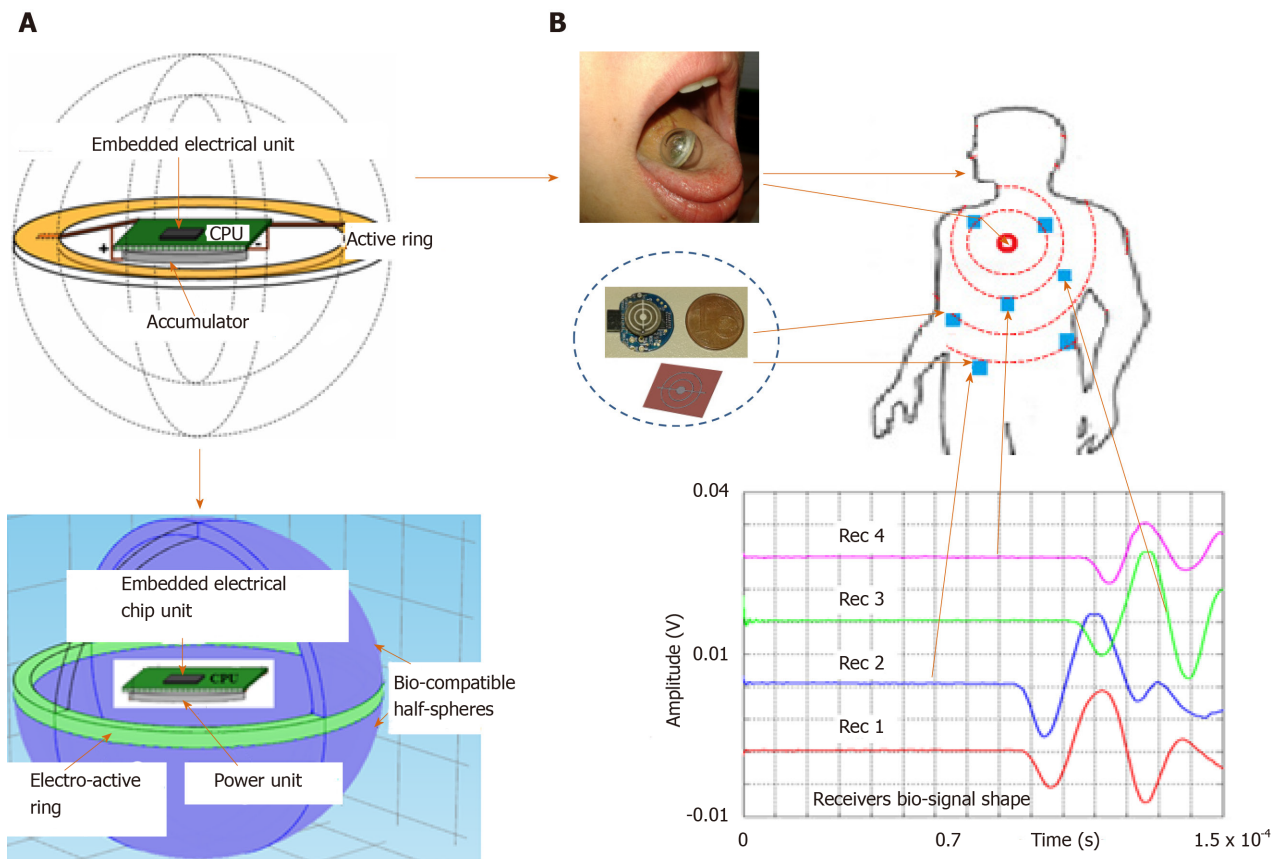


Figure 1 Illustration of the global concept based on a mobile ultrasonic capsule resonator as an emitter and a thin layer concentric rings resonators playing the role of receivers. A: The global concept based on a mobile ultrasonic capsule resonator; B: An emitter and a thin layer concentric rings resonators playing the role of receivers.

considered the fundamental theory of Love based on the Lagrangian formulation. In the case of an undamped system, the Lagrangian “L” is defined as the difference between kinetic “T” and potential “U” energy: $L = T - U$.

For a dynamic system undergoing a continuously free vibratory motion ($t_1 \leq t \leq t_2$), the equation of motion can be expressed using the Hamilton principle that satisfies the following condition (Formula 1).

For a spherical shape, the kinetic energy is given by Formula 2.

Where h is the thickness of the sphere, ρ is the material density, and (u, v, w) are the deformation of the sphere in spherical coordinates. Based on this model, Wilkinson^[14] established, for a thin spherical shell, a cubic polynomial in λ^2 (frequency parameter) whose solution expresses the vibration modes governing the spherical axisymmetric vibration (without torsion): $\alpha\lambda^6 - \beta\lambda^6 + \beta\lambda^6 - \lambda = 0$. Where α , β and δ are the dimensional characteristics of the sphere.

The solution of the polynomial of Eq. 4 governs the motion of the spherical structure and can be expressed analytically by the “axisymmetric fundamental resonance mode” which is given by Formula 3, and provides the natural radial frequencies of both the breathing and n th mode of closed spherical shells.

Where R is the radius of the mid-surface of the spherical shell, ρ is the density, E is Young’s modulus, ν is Poisson’s ratio, n is the mode number, and λ_n is a frequency parameter for the vibration mode n given by Formula 4.

Figure 2A shows the natural frequencies of the membrane modes with the following properties: Elastic modulus $E = 3300$ Mpa, mass density $\rho = 1190$ kg/m³, Poisson’s ratio $\nu = 0.39$, radius $R = 6.7$ mm, and thickness $h = 2.6$ mm.

For each value of $n \geq 1$, there are three distinct frequencies (three branches or three mode shapes), but only two branches are presented in this part of the study. These two lower and upper branches correspond to the membrane and bending modes, respectively. The mode associated with $n = 0$ on the membrane branch is called the “fundamental mode”, a pure breathing (elongation) mode of the spherical shell. The results are in good agreement with those of Soedel^[17] and Husson^[18] and those given by applying the modal analysis to determine the first resonance frequency of the sensor

$$\delta \int_{t_1}^{t_2} L dt = \delta \int_{t_1}^{t_2} (T - U) dt = 0$$

$$T = \frac{1}{2} \rho h \iint [u^2 + v^2 + w^2] R^2 \sin \varphi d\varphi d\theta$$

$$f_n = \frac{\lambda_n}{2\pi R} \left[\frac{E}{\rho(1 - \nu^2)} \right]^{1/2}$$

$$f_n = \frac{\lambda_n}{2\pi R} \left[\frac{E}{\rho(1 - \nu^2)} \right]^{1/2}$$

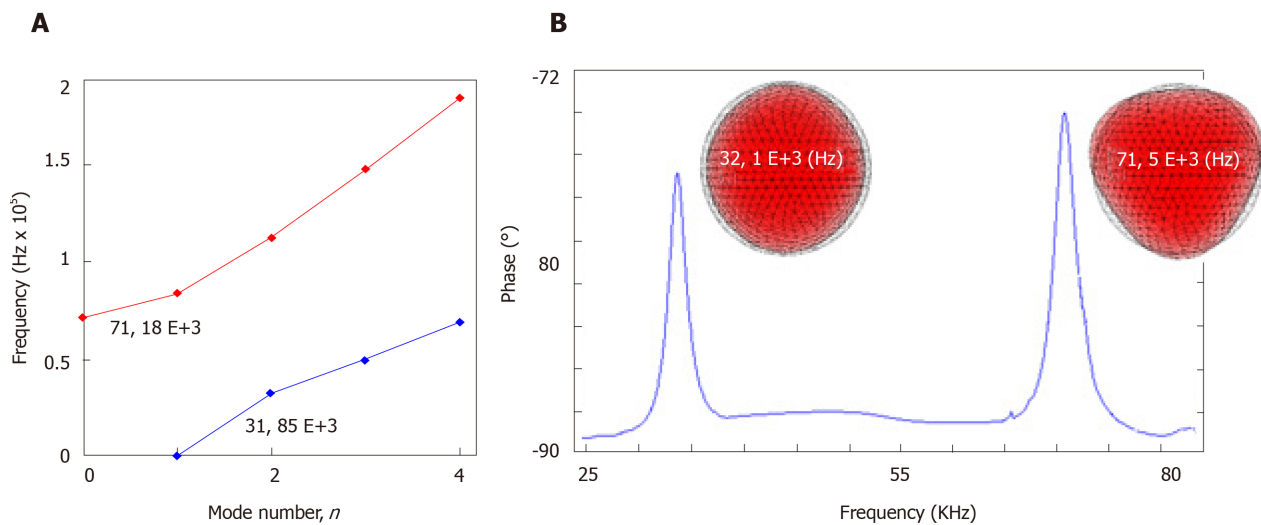


Figure 2 Natural frequencies of torsionless modes for the sensor and frequency response mode of impedance measurement and finite element analysis. A: Natural frequencies of torsionless modes; B: Frequency response mode of impedance measurement and finite element analysis.

considered (Figure 2B).

Physical concept

Embedded electrical scheduling unit: An electronic module is inserted into the hollow part of the sphere (Figure 3) to ensure the following tasks of the sensor simultaneously: (1) Structure resonance; (2) Emission-reception control; (3) Encoding algorithm; and (4) Signal processing and data storage.

The electronics are integrated into a chip system that includes a central processing unit (CPU), a digital oscillator (DCO), a task scheduler (IT), a coded ultrasonic generator (PWMG), a power management unit (PMU), an output amplifier (OB), and an accumulator (BAT).

The device was made from a SoC of the MSP430 family from “Texas Instruments”. The MSP430F2012 was chosen for its small size and minimal hardware resources.

The DCO produces three clock sources: A low-frequency clock (TB) set to 12 kHz to produce a stable time base for the task scheduler (IT), a high-frequency clock (MCLK) set to 16 MHz for timing the CPU, and an average frequency clock (USCLK) set to 32 kHz, which is the frequency of the vibrations emitted by the capsule.

At regular intervals (60 ms), the task scheduler (IT) sends an interrupted signal (INT) to the CPU that produces a sequence of width-modulated bit pulses (CP). This bit sequence is both the interrogation signal and the medium identifier of the device. This sequence is modulated by the all or nothing width modulation generator (PWMG) based on the carrier frequency (USCLK). These coded pulses are amplified by the output amplifier (OB) before being applied to the piezoelectric element. A 3V accumulator (BAT) powers the unit. A PMU provides an economical supply for the various elements of the chain to ensure minimum energy consumption and maximum autonomy of the device.

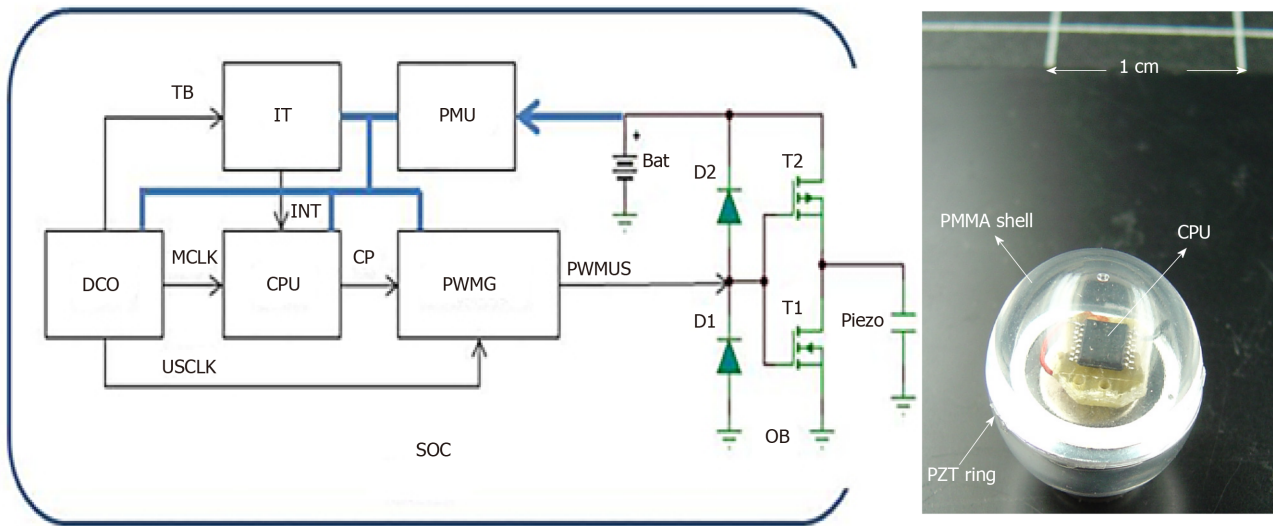


Figure 3 Architecture of the real-time electrical control system embedded in the physical concept (ultrasonic capsule). DCO: A digital oscillator; CPU: Central processing unit; PMU: Power management unit; PWMG: A coded ultrasonic generator; IT: A task scheduler; OB: An output amplifier.

Autonomies and energy balance: One of the goals was to design a sensor with a broad operating range that could be injected into a process (mixer, tank, *etc.*) for monitoring purposes, so we carried out measurements on power consumption during active sensor emissions. Electrical consumption was determined using a 10-Ohm shunt placed in series in the battery. The battery voltage and the voltage across the shunt were measured using differential isolation amplifiers. Both signals were recorded on a digital oscilloscope (Figure 4), which was also used to calculate the instantaneous power consumption of the device.

Outside the frame of bits, the consumption was insignificant except for the low-frequency clock (TB) and the task scheduler (IT). The CPU, PWMG generator, output amplifier, and other clocks were stopped.

For the transmission of the frame of bits, all the elements were “in operation” and the consumption was maximal. This consumption is due mainly to the central unit that works even during the spaces between bits as these spaces are managed by software. Minor overconsumption occurs when the PWMG generator is turned on transmitting a 0 or 1 level, but this consumption is marginal.

Based on different recordings, we can see that the average consumption of the system for a bit frame is relatively independent of the code transmitted: $I_{\text{frame}} \approx 4.5$ mA.

The average current consumed over a time frame $T_{\text{frame}} = 15$ ms repeated periodically every $T = 1.5$ s is then Formula 5.

Another possibility could be a more sophisticated IT task management scheduler that can turn the system unit “off” during these spaces. In this case, the emission of code 15 (1111 and maximum power requirement) would produce an average current drain between two frames (Formula 6).

Thin layer concentric ring receiver sensor

The usual ultrasonic concept is generally based on the use of a resonant piezoelectric transducer vibrating in thickness mode. As the resonant frequency of a transducer is inversely proportional to its size, it becomes greater and greater for low frequencies around 100 kHz.

Our aim was to obtain miniaturized low-frequency acoustic broadband receivers with a frequency component of the same order as the resonance frequency of the capsule. To do this, a different procedure from the classic sensor design was used. The new technique was based on the principle of setting in resonance small, thin concentric rings (Figure 5).

To validate the approach, the mechanical behavior (Figure 6) was assessed and the study was completed with a numerical step using the finite elements method to characterize the resonator vibration modes and visualize the corresponding distortions when the structure was excited. The concordance enabled the use of the experimental device to receive waves coupled with the body or tissues.

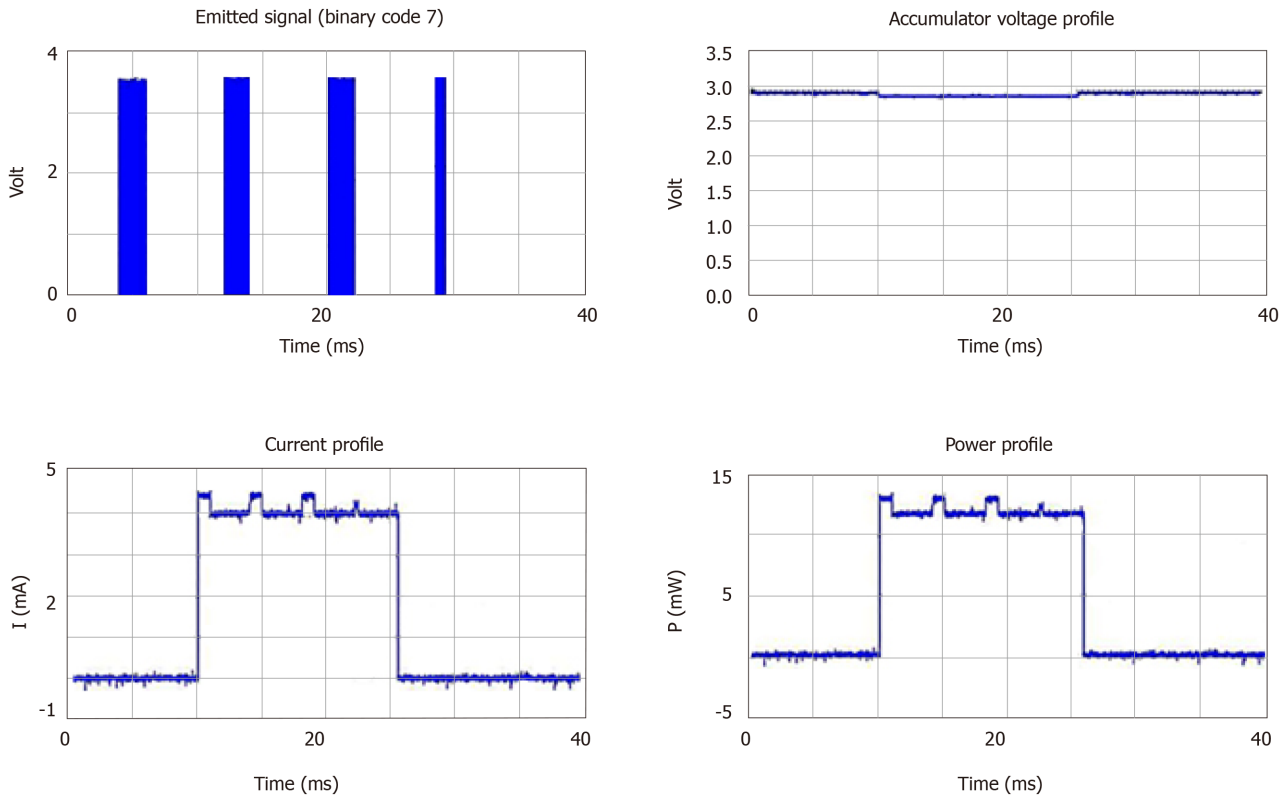


Figure 4 Power consumption during a 0111 frame emission (code 7).

$$I_{\text{average}} = \frac{I_{\text{frame}} \times T_{\text{frame}}}{T} \approx \frac{4.5 \text{ mA} \times 15 \times 10^{-2}}{1.5 \text{ s}} = 0.045 \text{ mA}$$

$$I_{\text{average}} = \frac{I_{\text{frame}} \times T_{\text{frame}}}{T} \approx \frac{4.8 \text{ mA} \times (4 \times 2 \text{ ms})}{1.5 \text{ s}} = 0.026 \text{ mA}$$

From a mechanical point of view, eigenvalues of following equation express the dynamics frequencies of the system: $-\omega^6 + 15.107j\omega^5 + 4.1015\omega^4 - 33.1020j\omega^3 + 1.1027\omega^2 + 2.1032j\omega + 25.1036 = 0$. So, $f_0 = 35 \text{ KHz}$, $f_1 = 56 \text{ KHz}$ and $f_2 = 5.25 \text{ MHz}$. Numerical values: $k = 18.104 \text{ N/m}$, $c = 0.5$, $m_1 = 4835.10^{-6} \text{ kg}$, $m_2 = 1088.10^{-8} \text{ kg}$, $m_3 = 1813.10^{-8} \text{ kg}$.

The physical concept of the micro-receiver is elaborated on the basis of a piezoelectric disk of diameter at the base 10 mm and thickness of 0.25 mm. The central concentric rings are made through an assisted laser engraving system. Other than the physical maintenance of the rings, the central rod allows both electrical polarization and electrical continuity with the central control unit (Figure 5).

RESULTS

Metrological approach

System stability: Before using the composite sensor to characterize a medium reflecting real biological tissues, its performance was validated in a medium with well-known, stable physical properties. For this purpose, we used water as a coupling medium.

At a frequency of 32 kHz, the first mode of vibration emitted by the spherical structure produced the echo diagram presented in Figure 7.

Based on the resonance frequency mode, the experiment was conducted in thermostated water ($25 \text{ }^\circ\text{C} \pm 0.3 \text{ }^\circ\text{C}$) in which a network of resonators (one transmitter and some receivers) was placed.

Knowing *in-situ* information about the state of *in-vivo* tissues requires the instantaneous position of the receivers to be known. The spatial identification of the

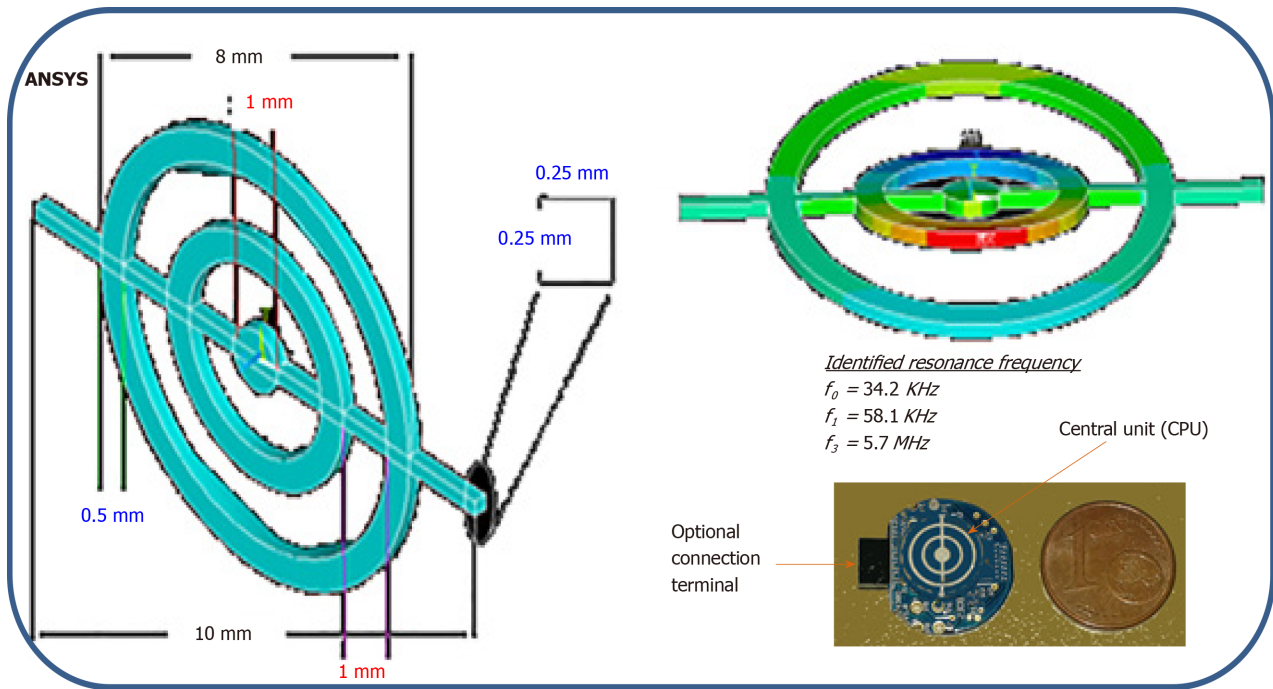


Figure 5 Numerical and physical concept of a micro acoustic sensor based on the use of the vibrational motion of a resonator comprised of concentric rings.

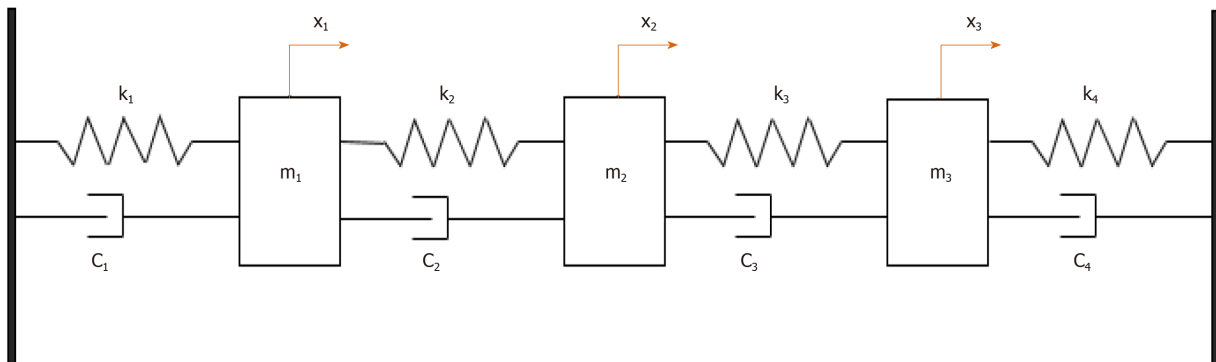


Figure 6 Mechanical equivalent of the micro acoustic sensor consisting of an assembly of masses (x_i) interposed between systems of springs (k_i) and dampers (C_i). k and c reflect the spring and dashpot characteristics.

transmitter at all times gives access to the history of the latter and consequently provides access to the desired physical state or properties of the environment.

The principle of trilateration makes it possible to know the distance between the transmitter and a given receiver by instantaneously locating the source in motion and consequently determining the relative position of the transmitter with respect to a reference point. Measurements are made by exploiting the relative time of flight of the wave (using zero-crossing protocol) between the mobile transmitter and each receiver in the space considered.

These transducers were coupled to the medium to be characterized and totally submerged. The emitter plays the role of a point source; this phenomenon generates a divergent ultrasonic wave, part of which was measured by receivers located at a regular distance from the transmitter. Figure 8 shows a schematic diagram of the measuring system and the stability plot of the variation in the compressional wave velocity measured at different reception points in the given space. A velocity of around 1545 ± 7 m/s in the Agar used as a coupling medium at 25°C is always linked to a longitudinal vibration mode.

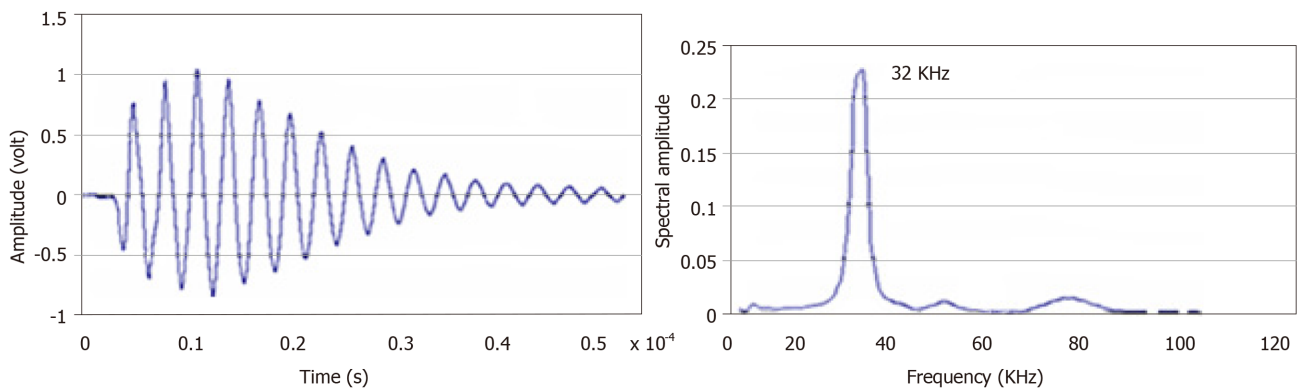


Figure 7 Time and frequency response of the sensor resulting from a short electrical pulse.

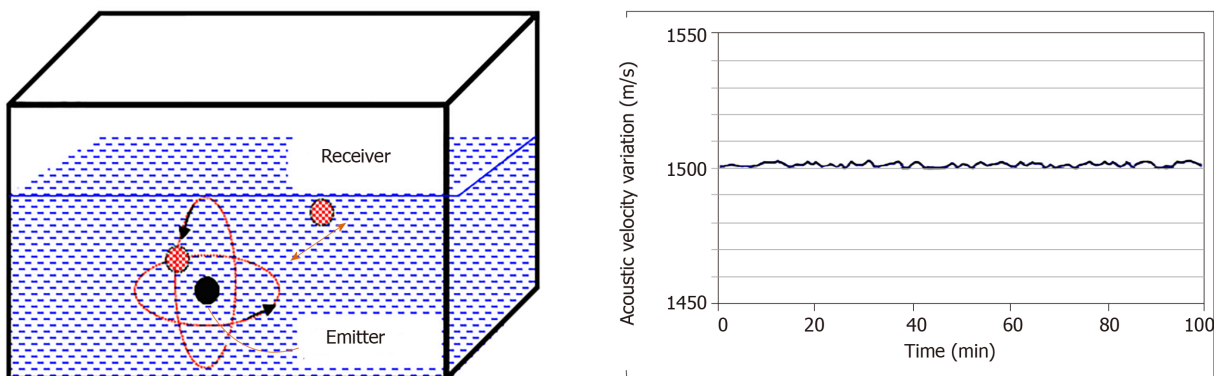


Figure 8 Schematic illustration of the metrological calibration of the capsule.

In-situ applications

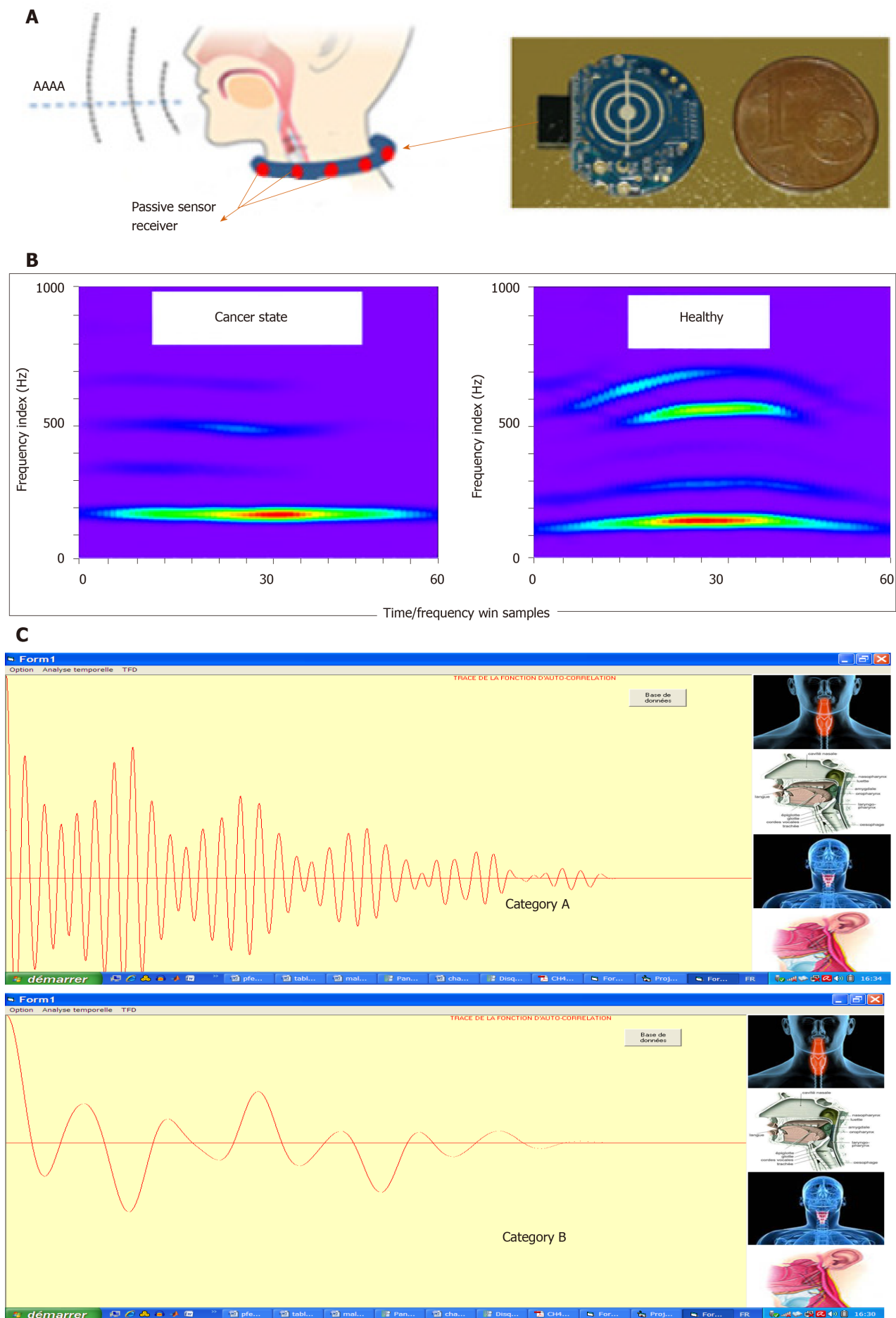
To validate this concept experimentally, we proceeded by two approaches in order to show the field of application and the potential of such system in medical domain. (1) Passive listening approach using concentric micro-sensors for the pathophysiological prevention of the respiratory and vocal apparatus; and (2) Coupling approach (by transmission mode) Capsule/ μ -Resonators to estimate the bio-physical evolution properties of multilayers biological tissues resulting from environmental aggression (electromagnetic waves radiation, stress, *etc.*).

Passive listening approach: This part of study aims to evaluate some larynx physical properties variation through a non-intrusive passive smart listening collar (Figure 9A). The vibratory signal was acquired after each person pronounced the vowel / a /, which reflects the greatest number of vocal cord vibrations modes^[19,20]. The latter can provide systematic and *in-vivo* screening for some laryngeal diseases, including laryngeal cancer, by spectro-temporal analysis of the voice signal resonance. This would allow consequently the detection of these diseases at an early stage, even in people who still represent no symptoms, which would permit an early treatment and a higher chance of cure.

For that, micro resonators collar is implemented and is used to carry a detailed examination on four different categories of people: Healthy cases, subjects with laryngeal cancer, those suffering from inflammatory polypus, and the ones having chronic laryngitis. Figure 9B shows the spectrograms of the two extreme physiological cases: A healthy state versus a cancerous one. In our application, one hundred patients with an average age of 53 years of whom 20% were women were diagnosed in the same context but separately.

Figure 9C gives an idea about the display of data and the classification of categories in a real environment. It shows an example of the graphical interface implemented providing the time signature of the signals for each of the above-mentioned patient categories:

The ENT examination shows that in a healthy subject the laryngeal pathway is normal with good mobility of the vocal cords (A). The autocorrelation function (of the



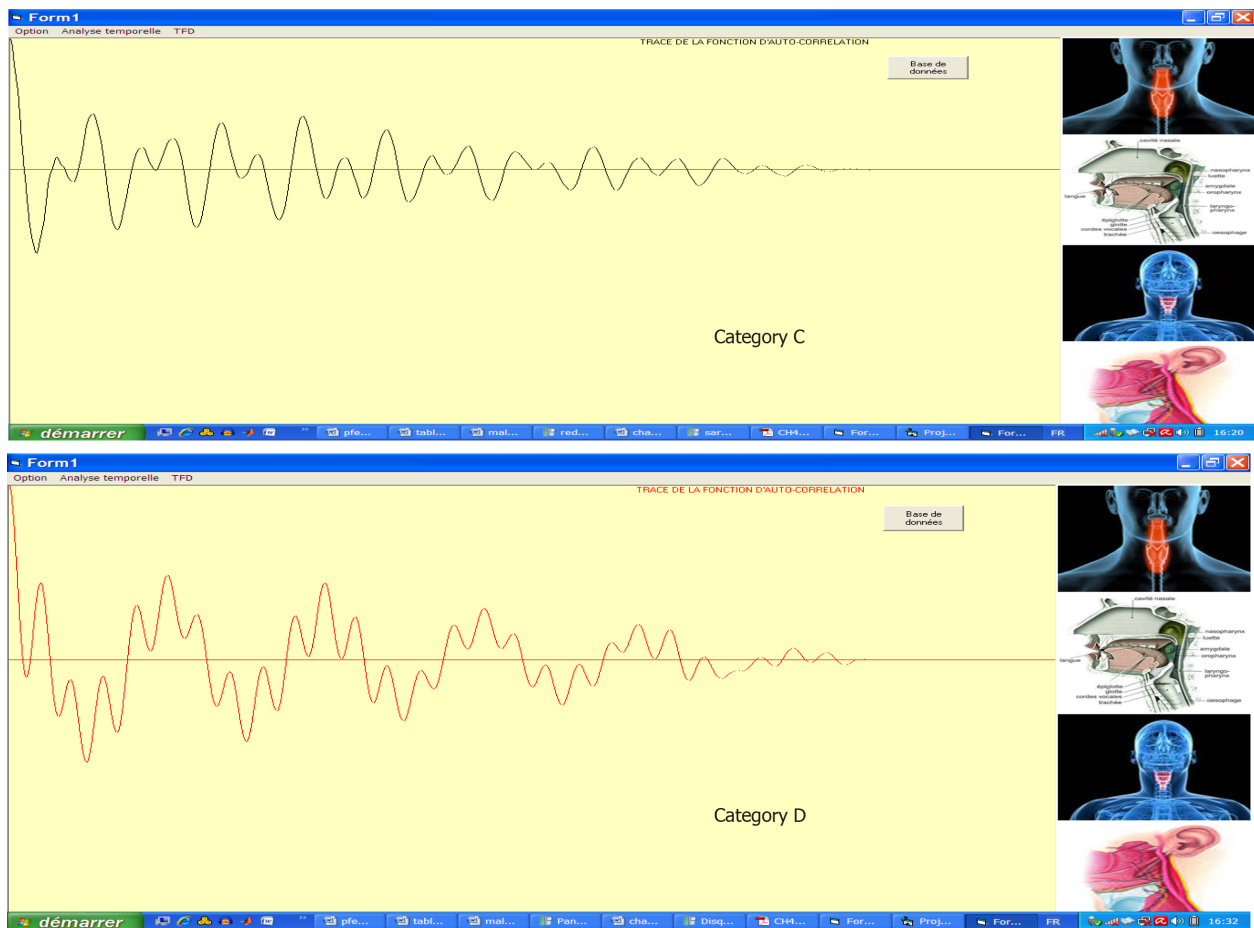


Figure 9 Passive listening approach. A: Physical concept of the micro-resonator acoustic prevention system; B: Spectrograms showing the different frequency components weights for two extreme physiological states: a healthy case and a cancerous state; C: Graphical interface of connected system showing the morphological diagram of signal issued from each category.

time signal) is a sin function; it is maximal at the intercept and contains several secondary periodic lobes resulting from the periodicity of the vibration of the vocal cords.

For a person with cancer (B), the temporal plot is irregular (random) and the spectrum is limited to low frequencies due to a significant decrease in and even total absence of vibration of the vocal cords.

As for subjects with inflammatory polyps or chronic laryngitis (C and D), the temporal plot contains some irregularities but also shows some similarities with the temporal plot of healthy patients. Additionally, the spectrum contains high frequencies but with lower values than healthy subjects.

Coupling capsule/ μ -resonators approach: This approach was carried out on the variation of the wave properties such as velocity and energy absorption of the acoustic wave at reception. Reason of ethical consideration, the parameters were measured through a composite medium made from biological tissues of animal origin embedded in a coupling medium, in this case, "Agar" (Figure 10).

To measure the evolution over time of the physical state of the biological tissues, we considered four samples of animal origin placed at equal distance (10 cm) from the diagonal crossing where the transmitter was located. The samples were embedded in the agar.

The receivers (R_i ; $i = 1, 2, 3, 4$) in the measurement space, close to the samples, were distributed as follows: R1 - Skin sample 3 mm thick; R2 - Composite sample; skin + muscle (3 mm + 7 mm); R3 - Muscle sample 10 mm thick; and R4 - Reference point (coupling without tissue).

Table 1 summarizes the averages of the physical properties of the different samples. These values were considered as starting values at time (t_0) in the measurement process based on the "LabView" acquisition system.

Given the dependence of the ultrasonic velocities on the physical properties of the samples (*e.g.*, compression and shear modulus), the curves on Figure 11 shows the

Table 1 Averages of the physical properties of the different samples

	Agar (0.5%)	Skin	Muscle
E	25 kPa	30 MPa	480 MPa
G	148 kPa	0.58 MPa	0.14 MPa
kg/m ³	□ 1	1.3	1.57
	0.5	0.3	0.31


Figure 10 Illustration of the measurement cell showing the spatial distribution of the emitter capsule embedded in the volume of agar at controlled distance of the different bio-tissue samples equipped with micro-resonators receivers.

decrease in the compression elastic and shear modulus (E and G) of the samples over time under the effect of aging (applied as physical stress).

E and G were measured every two days over a period of 10 d (D) starting from the time of origin t_0 at 25°C.

As the agar is primarily a water incompressible fluid, its Poisson's ratio is near 0.50 and slight deviations do not significantly affect the results.

To consolidate this variation, the ultrasonic quantification based on matrix stiffness formalism^[21] was reported for each measurement showing the response of each layer and the multilayers taking into account the effects of the interfaces and boundary conditions between the layers (agar-muscle-epidermis). Indeed, the multi-layered structure being merged into a single layer, the reflection and transmission coefficients were calculated considering that the whole structure is bounded by fluids. Then, a back-recursive algorithm was applied to compute the displacement vectors amplitudes in each layer, which allows the calculation of acoustic field in every layer based on the angular spectrum approach.

DISCUSSION

The study and design of an autonomous embedded ultrasonic system able to meet a medical need was the main objective of this work. We have proposed a concept of measuring elements based on miniaturized spherical capsule sensors coupled with concentric ring receivers.

A detailed description of the proposed resonator and its vibratory mechanical behavior has been consolidated with a mechanical approach and a numerical approach using finite element analysis.

The physical implementation of the capsule led us to an autonomous vibratory element. The power analysis (impedance and phase) of the overall structure showed very good agreement between the numerical and analytical results.

However, the analysis of the effect of aging factors of tissues on the variation of the acoustic properties gave a coherent view of the mechanical behavior of both the

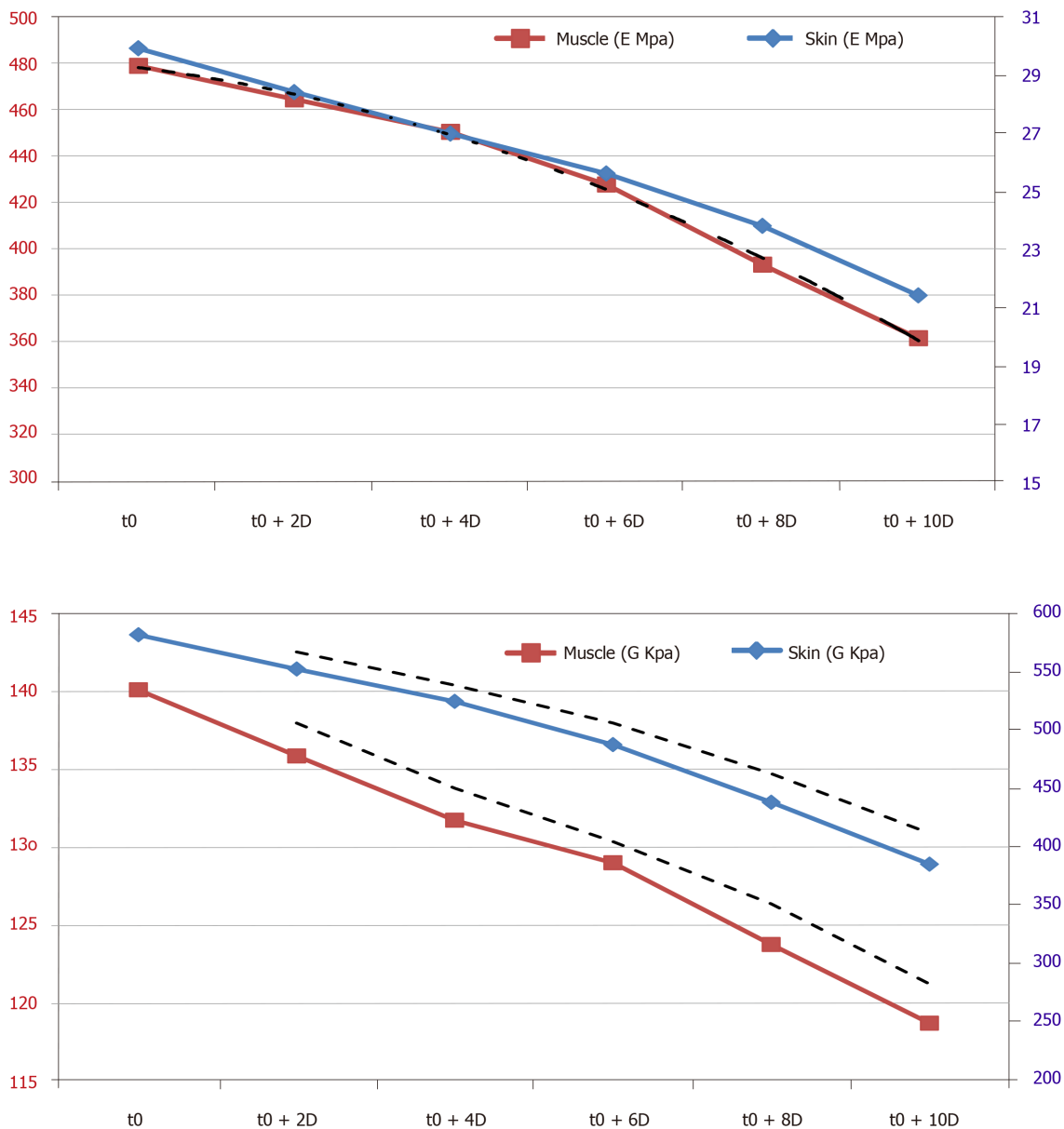


Figure 11 Curves showing the evolution of the stress and shear components measured by the experimental approach and compared to the calculated displacement-stress vector (dashed lines) for an incident plane wave in the three-layer medium (agar, skin and muscle).

measuring system and the dynamic medium considered. The curves show all the critical phases in a complex evolutionary environment, knowing that there are few techniques, which, under similar conditions, give access to the local physical properties sought.

As a result, this work presents a "soft" and reliable diagnostic system based on the vibratory mechanical behavior of the vocal apparatus. A double interest results in the prospects of such application.

Clinically, this system has been studied and designed to implement an alternative screening method for laryngeal pathologies to save patients from frequent exposure to harmful radiation as RX, MRI, *etc.*

In terms of prevention, the connected feature of this system offers a means of continuous information on the evolution of a state of health, continuously viewable by a "smart phone" interface, which could lead to a possible early detection of severe laryngeal diseases, especially cancer, giving the subject a higher chance of cure.

ARTICLE HIGHLIGHTS

Research background

Studying interactions between acoustic and living fields goes far beyond biological and health impact studies.

Research motivation

The present manuscript is one of the first reports on a potentially connected "real-time" diagnostic technique, optimizing interactions between acoustic and live fields, providing an autonomous information system capable of collecting data on physiological variations using a soft vibratory wave.

Research objectives

The objective of this work was partly to contribute to the development of innovative radiating structures close to the body (sensors radiating inside the body and through multilayer tissues).

Research methods

A low-frequency ultrasonic method based on the use of an innovative autonomous ultrasonic capsule as a miniaturized elementary spherical sensor and micro-rings resonators were examined.

Research results

Other their functions as passive listeners for the prevention and diagnosis in physiopathology of the respiratory and laryngeal apparatus, these micro-resonators coupled to the ultrasonic capsule through biological tissues are capable of evaluating the effects of aggression of the environment on human metabolism.

Research conclusions

This work presents a "soft" and reliable diagnostic system based on the vibratory mechanical behavior of the vocal apparatus. A double interest results in the prospects of such application.

REFERENCES

- 1 **Lay HS**, Cox BF, Seetohul V, Demore CEM, Cochran S. Design and Simulation of a Ring-Shaped Linear Array for Microultrasound Capsule Endoscopy. *IEEE Trans Ultrason Ferroelectr Freq Control* 2018; **65**: 589-599 [PMID: 29610089 DOI: 10.1109/TUFFC.2018.2794220]
- 2 **Peng C**, Sun T, Vykhotseva N, Power C, Zhang Y, McDannold N, Porter T. Intracranial Non-thermal Ablation Mediated by Transcranial Focused Ultrasound and Phase-Shift Nanoemulsions. *Ultrasound Med Biol* 2019; **45**: 2104-2117 [PMID: 31101446 DOI: 10.1016/j.ultrasmedbio.2019.04.010]
- 3 **He H**, Stylogiannis A, Afshari P, Wiedemann T, Steiger K, Buehler A, Zakian C, Ntziachristos V. Capsule optoacoustic endoscopy for esophageal imaging. *J Biophotonics* 2019; **12**: e201800439 [PMID: 31034135 DOI: 10.1002/jbio.201800439]
- 4 **de Groen P**. From propofol to midazolam/fentanyl to nosedation during colonoscopy: can the propofol trend be reversed? *Gastrointest Endosc* 2018; **87**: AB149 [DOI: 10.1016/j.gie.2018.04.1378]
- 5 **Diab D**, Lefebvre F, Nassar G, Smagin N, Isber S, El Omar F, Naja A. An autonomous low-power management system for energy harvesting from a miniaturized spherical piezoelectric transducer. *Rev Sci Instrum* 2019; **90**: 075004 [PMID: 31370448 DOI: 10.1063/1.5084267]
- 6 **Wang J**, Memon F, Touma G, Baltsavias S, Jang JH, Chang C, Rasmussen MF, Olcott E, Jeffrey RB, Arbabian A, Khuri-Yakub BT. Capsule Ultrasound Device: Characterization and Testing Results. 2017 IEEE International Ultrasonics Symposium (IUS); 2017 Sep 6-9; Washington, USA. IEEE, 2017: 1-4 [DOI: 10.1109/ULTSYM.2017.8092071]
- 7 **Memon F**, Touma G, Wang J, Baltsavias S, Moini A, Chang C, Rasmussen MF, Nikoozadeh A, Choe JW, Olcott E, Jeffrey RB, Arbabian A, Khuri-Yakub BT. Capsule Ultrasound Device: Further Developments. 2016 IEEE International Ultrasonics Symposium (IUS); 2016 Sep 18-21; Tours, France. IEEE, 2016: 1-4 [DOI: 10.1109/ULTSYM.2016.7728851]
- 8 **Cox BF**, Stewart F, Lay H, Cummins G, Newton IP, Desmulliez MPY, Steele RJC, Nätke I, Cochran S. Ultrasound capsule endoscopy: sounding out the future. *Ann Transl Med* 2017; **5**: 201 [PMID: 28567381 DOI: 10.21037/atm.2017.04.21]
- 9 **Walker AJ**. A theoretical model of an ultrasonic transducer incorporating spherical resonators. *IMA J Appl Math* 2016; **81**: 1-25 [DOI: 10.1093/imamat/hxv023]
- 10 **Nasedkin K**, Rybyanets A. Finite element analysis of ultrasonic spherical piezoelectric phased array with split electrodes. 2016 Joint IEEE International Symposium on the Applications of Ferroelectrics, European Conference on Application of Polar Dielectrics, and Piezoelectric Force Microscopy Workshop (ISAF/ECAPD/PFM); 2016 Aug 21-25; Darmstadt, Germany. IEEE, 2016 [DOI: 10.1109/ISAF/ECAPD/PFM.2016.7728851]

- 10.1109/ISAF.2016.7578074]
- 11 **Mehl JB**, Moldover MR. Precision acoustic measurements with a spherical resonator: Ar and C₂H₄. *J Chem Phys* 1981; **74**: 4062-4077 [DOI: [10.1063/1.441587](https://doi.org/10.1063/1.441587)]
- 12 **He MG**, Liu ZG, Yin JM. Measurement of speed of sound with a spherical resonator: HCFC-22, HFC-152a, HFC-143a, and Propane. *Int J Thermophys* 2002; **23**: 1599-1615 [DOI: [10.1023/A:1020742018220](https://doi.org/10.1023/A:1020742018220)]
- 13 **Baker WE**. Axisymmetric Modes of Vibration of Thin Spherical Shell. *J Acoust Soc Am* 1961; **33**: 1749 [DOI: [10.1121/1.1908562](https://doi.org/10.1121/1.1908562)]
- 14 **Wilkinson JP**. Natural Frequencies of Closed Spherical Shells. *J Acoust Soc Am* 1965; **38**: 367-368 [DOI: [10.1121/1.1909687](https://doi.org/10.1121/1.1909687)]
- 15 **Kalnins A**. Effect of Bending on Vibrations of Spherical Shells. *J Acoust Soc Am* 1964; **36**: 74-81 [DOI: [10.1121/1.1918916](https://doi.org/10.1121/1.1918916)]
- 16 **Duffey TA**, Romero C. Strain growth in spherical explosive chambers subjected to internal blast loading. *Int J Impact Eng* 2003; **28**: 967-983 [DOI: [10.1016/S0734-743X\(02\)00169-0](https://doi.org/10.1016/S0734-743X(02)00169-0)]
- 17 **Soedel W**. Vibrations of Shells and Plates (Mechanical Engineering). 3rd Edition. Boca Raton: CRC Press, 2004 [DOI: [10.4324/9780203026304](https://doi.org/10.4324/9780203026304)]
- 18 **Husson D**. A perturbation theory for the acoustoelastic effect of surface waves. *J Appl Phys* 1985; **57**: 1562 [DOI: [10.1063/1.334471](https://doi.org/10.1063/1.334471)]
- 19 **Story H**. An overview of the physiology, physics and modeling of the sound source for vowels. *Acoust Sci Technol* 2002; **23**: 195 [DOI: [10.1250/ast.23.195](https://doi.org/10.1250/ast.23.195)]
- 20 **Gramming P**. Vocal loudness and frequency capabilities of the voice. *J Voice* 1991; **5**: 144 [DOI: [10.1016/S0892-1997\(05\)80178-X](https://doi.org/10.1016/S0892-1997(05)80178-X)]
- 21 **Matta S**. Acoustic wave propagation in a multilayer composed of fluid, solid, and porous viscoelastic layers. PhD Thesis, Université de Valenciennes et du Hainaut-Cambresis. 2018. Available from: <https://hal.inria.fr/tel-02398764/>

Cerebral amyloid angiopathy vs Alzheimer's dementia: Diagnostic conundrum

Jamie Arberry, Sarneet Singh, Ruth Akiyo Mizoguchi

ORCID number: Jamie Arberry 0000-0001-9485-5576; Sarneet Singh 0000-0003-1279-4760; Ruth Akiyo Mizoguchi 0000-0001-8938-5477.

Author contributions: Arberry J and Mizoguchi RA were the patient's physicians, Arberry J and Singh S reviewed the literature and drafted the manuscript; all authors were responsible for the revision of the manuscript and issued final approval for the version to be submitted.

Informed consent statement:

Informed written consent was obtained from the patient.

Conflict-of-interest statement: No conflict of interest.

CARE Checklist (2016) statement:

The authors have read the CARE Checklist (2016), and the manuscript was prepared and revised according to the CARE Checklist (2016).

Open-Access: This article is an open-access article that was selected by an in-house editor and fully peer-reviewed by external reviewers. It is distributed in accordance with the Creative Commons Attribution NonCommercial (CC BY-NC 4.0) license, which permits others to distribute, remix, adapt, build upon this work non-commercially,

Jamie Arberry, Sarneet Singh, Ruth Akiyo Mizoguchi, Chelsea and Westminster Hospital, London SW10 9NH, United Kingdom

Corresponding author: Jamie Arberry, BM BCh, Doctor, Chelsea and Westminster Hospital, 369 Fulham Palace Road, London SW10 9NH, United Kingdom. jamie.arberry@doctors.org.uk

Abstract

BACKGROUND

Diagnosis of a dementia subtype can be complex and often requires comprehensive cognitive assessment and dedicated neuroimaging. Clinicians are prone to cognitive biases when reviewing such images. We present a case of cognitive impairment and demonstrate that initial imaging may have resulted in misleading the diagnosis due to such cognitive biases.

CASE SUMMARY

A 76-year-old man with no cognitive impairment presented with acute onset word finding difficulty with unremarkable blood tests and neurological examination. Magnetic resonance imaging (MRI) demonstrated multiple foci of periventricular and subcortical microhaemorrhage, consistent with cerebral amyloid angiopathy (CAA). Cognitive assessment of this patient demonstrated marked impairment mainly in verbal fluency and memory. However, processing speed and executive function are most affected in CAA, whereas episodic memory is relatively preserved, unlike in other causes of cognitive impairment, such as Alzheimer's dementia (AD). This raised the question of an underlying diagnosis of dementia. Repeat MRI with dedicated coronal views demonstrated mesial temporal lobe atrophy which is consistent with AD.

CONCLUSION

MRI brain can occasionally result in diagnostic overshadowing, and the application of artificial intelligence to medical imaging may overcome such cognitive biases.

Key words: Alzheimer's dementia; Cerebral amyloid angiopathy; Cognitive impairment; Microhaemorrhages; Artificial intelligence; Case report

©The Author(s) 2020. Published by Baishideng Publishing Group Inc. All rights reserved.

and license their derivative works on different terms, provided the original work is properly cited and the use is non-commercial. See: <http://creativecommons.org/licenses/by-nc/4.0/>

Manuscript source: Invited manuscript

Received: March 17, 2020

Peer-review started: March 17, 2020

First decision: June 5, 2020

Revised: June 15, 2020

Accepted: June 18, 2020

Article in press: June 18, 2020

Published online: June 28, 2020

P-Reviewer: Chen TL, Nassar G

S-Editor: Wang JL

L-Editor: A

E-Editor: Ma YJ



Core tip: This case represents the complexities of diagnosing dementia subtypes with an unusual presentation for what is likely Alzheimer's dementia, rather than cerebral amyloid angiopathy as per initial magnetic resonance imaging brain. In such cases, imaging can potentially influence the diagnostic accuracy, which might ultimately result in misdiagnosis and hence alter the management plan. We argue that artificial intelligence and image automation could avoid such diagnostic oversights.

Citation: Arberry J, Singh S, Mizoguchi RA. Cerebral amyloid angiopathy vs Alzheimer's dementia: Diagnostic conundrum. *Artif Intell Med Imaging* 2020; 1(1): 65-69

URL: <https://www.wjgnet.com/2644-3260/full/v1/i1/65.htm>

DOI: <https://dx.doi.org/10.35711/aimi.v1.i1.65>

INTRODUCTION

Cerebral β -amyloid angiopathy (CAA) occurs when β -amyloid is deposited in the vascular media and adventitia. It is a common pathology in the brains of older individuals and is known to co-exist with other causes of cognitive decline. CAA has been shown to contribute to changes in early Alzheimer's dementia (AD) pathogenesis^[1,2]; CAA is present in 2%-3% of the AD brains of which half of them have a severe form. Therefore, it is possible that vascular change and neuritic plaque deposition are not just parallel processes but reflect additive pathological cascades.

CAA also predisposes one to cerebral infarction and cerebral haemorrhage, though the clinical effects of CAA in AD are mostly silent, or at least are "masked" by the greater degree of neuronal dysfunction induced by senile plaque formation and neurofibrillary degeneration. However major haemorrhagic episodes can still occur in patients with AD and CAA appears to be the underlying cause of these.

There can be diagnostic uncertainties in patients with CAA and underlying dementia. In this case report, we discuss an unusual presentation of AD. Through this we aim to emphasise the importance of robust cognitive assessment and dedicated neuroimaging in patients presenting with cognitive impairment, to investigate and consider all causes of dementia, and in order to ensure an accurate diagnosis in such patients.

CASE PRESENTATION

Chief complaints

A 76-year-old man presented to our hospital with acute onset word finding difficulty and "confused" speech.

History of presenting illness

He had returned from work and could not remember the events that followed. A collateral history from his wife reveals that on his return to the house, he was delirious and had difficulty word finding. There was no obvious history of trauma reported.

In the years leading up to this episode, he had small problems remembering complex instructions and would be a little more repetitive.

History of past illness

He had a background of hypertension, hypercholesterolaemia, gout and alcohol excess, with no known cognitive impairment. He had recently had a mesenteric aneurysm repaired. He was a non-smoker.

Social and family history

There was no family history of note. He worked as an advisor on multiple boards and lived with his wife, both fully independent.

Physical examination upon admission

On general examination, there was no evidence of alcohol intoxication or alcohol withdrawal. A Glasgow Coma Scale score, which is used to review levels of consciousness, was 13 (15 is the highest score and the patient scored 2 points less due

to his “confused” speech). An Abbreviated Mental Test Score (AMTS) used to assess cognition at the bedside was low at 2/10 (a score of less than 7 would prompt more sensitive cognitive testing). His neurological examination was intact aside from his speech disturbance: There was evidence of an expressive dysphasia, perseveration and confabulation. As prompted by the low AMTS, further detailed cognitive tests were carried out: (1) Montreal Cognitive Assessment, he scored 10/30 (a score of 26 or over is normal); and (2) Addenbrookes Cognitive Examination 3 (ACE3), he scored 62/100, affecting mainly memory and fluency domains (a score of 88 and above is normal; below 83 is abnormal; and between 83 and 87 is inconclusive).

Laboratory examinations

All initial blood tests including full blood count, renal profile, liver function tests, ammonia, clotting screen, inflammatory markers were normal. Chest X-ray and urinalysis were normal. Electrocardiogram revealed normal sinus rhythm.

Imaging examinations

Both computed tomography (CT) brain and CT angiogram revealed bilateral hygromas without mass effect, but no other abnormality. Diffusion-weighted magnetic resonance imaging (MRI) demonstrated bilateral infarcts, with haemorrhagic transformation. Susceptibility weighted MRI (SWI) demonstrated multiple foci of periventricular and subcortical microhaemorrhages, consistent with CAA.

FINAL DIAGNOSIS

On this presentation, the patient was treated as having CAA due to the MRI changes. Further diagnostic evaluation (see below), later questioned this diagnosis and raised the possibility of AD.

TREATMENT

Given the presence of the haemorrhages on initial imaging, this patient did not receive antiplatelet or anticoagulant therapy. His vascular risk factors were optimised by commencing atorvastatin and amlodipine. He was also commenced on vitamin B and thiamine tablets with his previous medications (lansoprazole, allopurinol, ferrous fumarate). He was discharged with memory clinic follow-up.

OUTCOME AND FOLLOW-UP

Prior to his attendance at the memory clinic, his condition was complicated by another episode of delirium and dysphasia – CT brain on this occasion demonstrated bilateral subdural haematomas, which were operated on the following day.

At the memory clinic, his repeat ACE3 reflected some degree of improvement from 62/100 to 73/100. Despite fluent speech and extensive description of historic events, the main deficits were seen again in the domains of working memory and semantic language function; he only scored 10/26 on memory domain and 5/14 on verbal fluency. This pattern of cognitive decline is consistent with AD, which is contrary to the initial diagnosis of CAA.

DISCUSSION

In this case, we are faced with multiple potential causes of cognitive decline, including AD, CAA^[3,4] and intracerebral haemorrhage^[4]. Gold standard diagnostic testing for AD is still post-mortem assessment of brain tissue, therefore dementia diagnosis is made based upon a combination of history, cognitive assessment and neuroimaging to provide a probable diagnosis.

Our patient demonstrated significant decline in episodic memory and verbal fluency, as per the ACE3. In recent studies^[5,6], CAA has been shown to be associated with deficits in executive function and processing speed, while working memory is usually relatively preserved. Patients with AD demonstrate deficits in all domains,

especially working memory. This suggests that the cognitive impairment here could represent an underlying diagnosis of AD.

Despite this, the initial MRI brain focused significantly on features of CAA rather than mesial temporal lobe (MTL) atrophy, the latter of which correlates more with the findings on cognitive assessment. These features of CAA (microhaemorrhages) are shown more clearly on the SWI (Figure 1A), which is more sensitive at detecting CAA compared with conventional gradient-echo imaging.

Given the diagnostic overshadowing from the CAA, we proceeded to dedicated T1 coronal views of his hippocampi (Figure 1B), which demonstrated MTL atrophy. In this case, the initial MRI may have masked the potential for an alternative diagnosis of the much more likely AD. The next step would be amyloid PET scanning to add more evidence to our final diagnosis of AD.

This case highlights the perils of diagnostic oversight while reviewing imaging, resulting in the potential for misdiagnosis. It is known that the workload of radiologists has massively increased over the past decade^[7], meaning they have less time to review each image. When uncertainty arises, as it did in our case, radiologists are under temporal pressure to commit to a diagnosis using their visual perception. Artificial intelligence (AI) in imaging not only removes this time pressure, but also allows image automation to remove cognitive biases that clinicians might face when reviewing imaging. Deep learning algorithms in AI allow for machines to learn how to review imaging data without the need for pre-defined human input. This increases accuracy and efficiency of image acquisition, providing objective assessment of disease and removing radiologist subjectivity. Such an approach would have assisted in the case here, and indeed would assist in all cases of cognitive impairment, by comparing imaging to a database of other age and sex matched images. Data has already demonstrated the increased sensitivity and specificity of AI techniques in diagnosis of AD with MRI^[8].

CONCLUSION

There are clear diagnostic uncertainties in patients presenting with evidence of cognitive impairment and CAA. CAA has been shown to contribute to changes in early AD pathogenesis, therefore, in order to correctly diagnose the dementia subtype, robust cognitive assessment and dedicated neuroimaging is required to actively search for other causes of cognitive impairment. AI in imaging may offer a step towards accurate diagnosis in such cases using deep learning methods to provide accurate and early diagnosis of dementia subtypes.

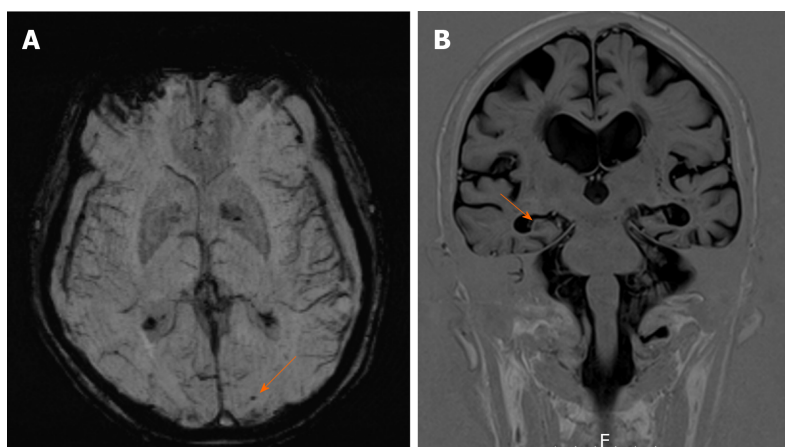


Figure 1 Magnetic resonance imaging of the patient. A: Susceptibility weighted magnetic resonance imaging (MRI) showing left occipital microhaemorrhage (arrow), suggestive of cerebral amyloid angiopathy; B: Coronal view T1-weighted MRI showing bilateral mesial temporal atrophy (arrow).

REFERENCES

- 1 **Vidoni ED**, Yeh HW, Morris JK, Newell KL, Alqahtani A, Burns NC, Burns JM, Billinger SA. Cerebral β -Amyloid Angiopathy Is Associated with Earlier Dementia Onset in Alzheimer's Disease. *Neurodegener Dis* 2016; **16**: 218-224 [PMID: [26756746](#) DOI: [10.1159/000441919](#)]
- 2 **De Reuck J**. The Impact of Cerebral Amyloid Angiopathy in Various Neurodegenerative Dementia Syndromes: A Neuropathological Study. *Neurol Res Int* 2019; **2019**: 7247325 [PMID: [30792924](#) DOI: [10.1155/2019/7247325](#)]
- 3 **Boyle PA**, Yu L, Nag S, Leurgans S, Wilson RS, Bennett DA, Schneider JA. Cerebral amyloid angiopathy and cognitive outcomes in community-based older persons. *Neurology* 2015; **85**: 1930-1936 [PMID: [26537052](#) DOI: [10.1212/WNL.0000000000002175](#)]
- 4 **Banerjee G**, Wilson D, Ambler G, Osei-Bonsu Appiah K, Shakeshaft C, Lunawat S, Cohen H, Yousry T Dr, Lip GYH, Muir KW, Brown MM, Al-Shahi Salman R, Jäger HR, Werring DJ; CROMIS-2 Collaborators. Cognitive Impairment Before Intracerebral Hemorrhage Is Associated With Cerebral Amyloid Angiopathy. *Stroke* 2018; **49**: 40-45 [PMID: [29247143](#) DOI: [10.1161/STROKEAHA.117.019409](#)]
- 5 **Case NF**, Charlton A, Zwiers A, Batool S, McCreary CR, Hogan DB, Ismail Z, Zerna C, Coutts SB, Frayne R, Goodyear B, Haffenden A, Smith EE. Cerebral Amyloid Angiopathy Is Associated With Executive Dysfunction and Mild Cognitive Impairment. *Stroke* 2016; **47**: 2010-2016 [PMID: [27338926](#) DOI: [10.1161/STROKEAHA.116.012999](#)]
- 6 **Xiong L**, Davidsdottir S, Reijmer YD, Shoamanesh A, Roongpiboonsopit D, Thanprasertsuk S, Martinez-Ramirez S, Charidimou A, Ayres AM, Fotiadis P, Gurol E, Blacker DL, Greenberg SM, Viswanathan A. Cognitive Profile and its Association with Neuroimaging Markers of Non-Demented Cerebral Amyloid Angiopathy Patients in a Stroke Unit. *J Alzheimers Dis* 2016; **52**: 171-178 [PMID: [27060947](#) DOI: [10.3233/JAD-150890](#)]
- 7 **McDonald RJ**, Schwartz KM, Eckel LJ, Diehn FE, Hunt CH, Bartholmai BJ, Erickson BJ, Kallmes DF. The effects of changes in utilization and technological advancements of cross-sectional imaging on radiologist workload. *Acad Radiol* 2015; **22**: 1191-1198 [PMID: [26210525](#) DOI: [10.1016/j.acra.2015.05.007](#)]
- 8 **Salvatore C**, Cerasa A, Castiglioni I. MRI Characterizes the Progressive Course of AD and Predicts Conversion to Alzheimer's Dementia 24 Months Before Probable Diagnosis. *Front Aging Neurosci* 2018; **10**: 135 [PMID: [29881340](#) DOI: [10.3389/fnagi.2018.00135](#)]



Published by **Baishideng Publishing Group Inc**
7041 Koll Center Parkway, Suite 160, Pleasanton, CA 94566, USA

Telephone: +1-925-3991568

E-mail: bpgoffice@wjgnet.com

Help Desk: <https://www.f6publishing.com/helpdesk>

<https://www.wjgnet.com>



Artificial Intelligence in *Medical Imaging*

Artif Intell Med Imaging 2020 August 28; 1(2): 70-86





Artificial Intelligence in Medical Imaging

Contents

Bimonthly Volume 1 Number 2 August 28, 2020

MINIREVIEWS

- 70 Artificial intelligence and pituitary adenomas: A review
Guerriero E, Ugga L, Cuocolo R
- 78 Development of tomographic reconstruction for three-dimensional optical imaging: From the inversion of light propagation to artificial intelligence
Cao X, Li K, Xu XL, Deneen KMV, Geng GH, Chen XL

ABOUT COVER

Co-Editor-in-Chief of *Artificial Intelligence in Medical Imaging*, Dr Ahmed Abdel Khalek Abdel Razek, MD is Professor and Head of the Diagnostic Radiology Department, Faculty of Medicine, Mansoura University (Egypt). He has published more than 200 papers as lead author in peer-reviewed, high-impact journals. He has written four book chapters and presented more than 400 papers at national and international congresses. He serves as reviewer for more than 100 high-impact journals and as an editorial board member of 7 peer-reviewed journals. He has supervised more than 100 PhD and MD thesis students. His research involves head and neck imaging, neuroradiology and advanced magnetic resonance imaging techniques, such as diffusion, perfusion, and magnetic resonance spectroscopy, including studies on artificial intelligence and deep learning in the field of medical imaging. He has won scientific awards from Scopus, Publons, the Radiological Society of North America, and the European Society of Radiology. (L-Editor: Filipodia)

AIMS AND SCOPE

The primary aim of *Artificial Intelligence in Medical Imaging* (AIMI, *Artif Intell Med Imaging*) is to provide scholars and readers from various fields of artificial intelligence in medical imaging with a platform to publish high-quality basic and clinical research articles and communicate their research findings online.

AIMI mainly publishes articles reporting research results obtained in the field of artificial intelligence in medical imaging and covering a wide range of topics, including artificial intelligence in radiology, pathology image analysis, endoscopy, molecular imaging, and ultrasonography.

INDEXING/ABSTRACTING

There is currently no indexing.

RESPONSIBLE EDITORS FOR THIS ISSUE

Production Editor: Yan-Xia Xing; Production Department Director: Yun-Xiaojuan Wu; Editorial Office Director: Jin-Lai Wang.

NAME OF JOURNAL

Artificial Intelligence in Medical Imaging

ISSN

ISSN 2644-3260 (online)

LAUNCH DATE

June 28, 2020

FREQUENCY

Bimonthly

EDITORS-IN-CHIEF

Xue-Li Chen, Caroline Chung, Ahmed Abdel Khalek Abdel Razek, Jun Shen

EDITORIAL BOARD MEMBERS

<https://www.wjnet.com/2644-3260/editorialboard.htm>

PUBLICATION DATE

August 28, 2020

COPYRIGHT

© 2020 Baishideng Publishing Group Inc

INSTRUCTIONS TO AUTHORS

<https://www.wjnet.com/bpg/gerinfo/204>

GUIDELINES FOR ETHICS DOCUMENTS

<https://www.wjnet.com/bpg/GerInfo/287>

GUIDELINES FOR NON-NATIVE SPEAKERS OF ENGLISH

<https://www.wjnet.com/bpg/gerinfo/240>

PUBLICATION ETHICS

<https://www.wjnet.com/bpg/GerInfo/288>

PUBLICATION MISCONDUCT

<https://www.wjnet.com/bpg/gerinfo/208>

ARTICLE PROCESSING CHARGE

<https://www.wjnet.com/bpg/gerinfo/242>

STEPS FOR SUBMITTING MANUSCRIPTS

<https://www.wjnet.com/bpg/GerInfo/239>

ONLINE SUBMISSION

<https://www.f6publishing.com>

Artificial intelligence and pituitary adenomas: A review

Elvira Guerriero, Lorenzo Ugga, Renato Cuocolo

ORCID number: Elvira Guerriero 0000-0003-3853-721X; Lorenzo Ugga 0000-0001-7811-4612; Renato Cuocolo 0000-0002-1452-1574.

Author contributions: Guerriero E collected the data and wrote the paper; Ugga L collected the data and edited the paper; Cuocolo R collected the data and edited the paper.

Conflict-of-interest statement: No conflict of interest.

Open-Access: This article is an open-access article that was selected by an in-house editor and fully peer-reviewed by external reviewers. It is distributed in accordance with the Creative Commons Attribution NonCommercial (CC BY-NC 4.0) license, which permits others to distribute, remix, adapt, build upon this work non-commercially, and license their derivative works on different terms, provided the original work is properly cited and the use is non-commercial. See: <http://creativecommons.org/licenses/by-nc/4.0/>

Manuscript source: Invited manuscript

Received: May 25, 2020

Peer-review started: May 25, 2020

First decision: July 4, 2020

Revised: July 15, 2020

Accepted: August 22, 2020

Article in press: August 22, 2020

Elvira Guerriero, Lorenzo Ugga, Renato Cuocolo, Department of Advanced Biomedical Sciences, University of Naples “Federico II”, Naples 80131, Italy

Corresponding author: Renato Cuocolo, MD, PhD, Department of Advanced Biomedical Sciences, University of Naples “Federico II”, via Pansini 5, Naples 80131, Italy. renato.cuocolo@unina.it

Abstract

The aim of this review was to provide an overview of the main concepts in machine learning (ML) and to analyze the ML applications in the imaging of pituitary adenomas. After describing the clinical, pathological and imaging features of pituitary tumors, we defined the difference between ML and classical rule-based algorithms, we illustrated the fundamental ML techniques: supervised, unsupervised and reinforcement learning and explained the characteristic of deep learning, a ML approach employing networks inspired by brain's structure. Pre-treatment assessment and neurosurgical outcome prediction were the potential ML applications using magnetic resonance imaging. Regarding pre-treatment assessment, ML methods were used to have information about tumor consistency, predict cavernous sinus invasion and high proliferative index, discriminate null cell adenomas, which respond to neo-adjuvant radiotherapy from other subtypes, predict somatostatin analogues response and visual pathway injury. Regarding neurosurgical outcome prediction, the following applications were discussed: Gross total resection prediction, evaluation of Cushing disease recurrence after transsphenoidal surgery and prediction of cerebrospinal fluid fistula's formation after surgery. Although clinical applicability requires more replicability, generalizability and validation, results are promising, and ML software can be a potential power to facilitate better clinical decision making in pituitary tumor patients.

Key Words: Pituitary adenoma; Machine learning; Deep learning; Radiomics; Texture analysis; Magnetic resonance imaging

©The Author(s) 2020. Published by Baishideng Publishing Group Inc. All rights reserved.

Core Tip: Machine learning (ML) has seen an explosion of interest in medical imaging because of its capability of analyzing large amounts of data. Recent studies applied ML techniques to the imaging of pituitary adenomas. The purpose of our review was to describe the main concepts in ML and its current and potential applications in imaging

Published online: August 28, 2020

P-Reviewer: Wang RF

S-Editor: Wang JL

L-Editor: A

P-Editor: Xing YX



analysis of pituitary tumors.

Citation: Guerriero E, Ugga L, Cuocolo R. Artificial intelligence and pituitary adenomas: A review. *Artif Intell Med Imaging* 2020; 1(2): 70-77

URL: <https://www.wjgnet.com/2644-3260/full/v1/i2/70.htm>

DOI: <https://dx.doi.org/10.35711/aimi.v1.i2.70>

INTRODUCTION

Pituitary adenomas are benign tumors accounting for 15%-20% of all intracranial neoplasms, with an incidence of 80-90 cases per 100000 population^[1,2]. Microadenomas are defined as tumors < 10 mm in maximum diameter, whereas larger adenomas are considered macroadenomas. Their peak age of presentation is between the fourth and seventh decades. Almost two-thirds of pituitary adenomas are hormone-secreting, prolactin most commonly, followed by growth hormone, corticotropin and thyrotropin, and cause typical hypersecretion syndromes. Non-functioning, small intrasellar tumors can be clinically silent and diagnosed only as incidental magnetic resonance findings, while bulky pituitary macroadenomas typically present with mass effect signs, such as headache, visual disturbances, and hypopituitarism^[3,4]. The 2017 World Health Organization (WHO) classification adopted pituitary adenohypophyseal cell lineage as the main principle guiding the classification of adenomas. According to this principle we distinguish the acidophilic lineage (in which the involved transcription factor is PIT1), the corticotrope lineage (TPIT transcription factor), and the gonadotroph lineage (SF1 transcription factor). Null-cell adenomas (NCAs) are now defined as tumors that have no immunohistochemical evidence of cell-type-specific differentiation considering both pituitary hormones and transcription factors. Furthermore, in the new WHO classification the term "atypical adenoma" has been abandoned and replaced by "high risk adenoma", in reference to tumors with high proliferation index and tendency to invasion. In particular, emphasis is placed on the evaluation of tumor proliferation (mitotic count and Ki-67 index), tumor invasion, and on special adenomas variants for which clinical behavior has been shown to be more aggressive due to their intrinsic histological features: lactotroph adenoma in men, sparsely granulated somatotroph adenoma, the silent corticotroph adenoma, the Crooke's cell adenoma and the plurihormonal PIT1-positive adenoma^[5]. Magnetic resonance imaging (MRI) is the investigation of choice for a complete evaluation of pituitary adenomas^[6]. Various parameters regarding the extent, consistency, and contrast enhancement can be analyzed in order to help neurosurgeons in planning an appropriate surgical approach and long-term follow-up^[7].

Attempting to predict invasion (cavernous and/or sphenoid sinus involvement) based on imaging is an important challenge. The Knosp classification is one of the more commonly used systems to determine the likelihood of cavernous sinus invasion by pituitary macroadenomas, but the highest accuracy of this grading system is observed in extreme cases of overt invasion or non-invasion, while sensitivity and specificity are low in intermediate cases^[8,9].

Tumor consistency in pituitary macroadenomas has been known to be one of the main factors that determine the success rate of the transsphenoidal approach. The role of MRI in predicting the consistency of pituitary macroadenomas is controversial. Several studies suggested that relative signal intensity or signal intensity ratio on T2-weighted MRI correlates with the tumor consistency, while some others concluded that they have no predictive value^[10-12]. A similar controversy has been reported in several studies which investigated the usefulness of diffusion-weighted imaging in tumor consistency prediction^[13-15].

Considering the above, it is still difficult to achieve an early identification of clinical and radiological features suggestive of an aggressive behavior, characterized by rapid growth, local invasion, and high ki-67 proliferation index.

In this setting, artificial intelligence (AI) has proved promising in recently published papers. Machine learning (ML) is a subfield of AI that employs algorithms to allow computers to learn directly from the data and subsequently perform predictions without explicit prior programming. The potential impact of ML on medicine, and particularly medical imaging, is relative to its ability to analyze large datasets including gray level textural features that humans do not consciously assess. Unlike

classical rule-based algorithms, machine learning can take advantage of increased exposure to new data and learn over time^[16]. ML techniques can be further divided into supervised, unsupervised learning and reinforcement learning^[17-20]. In supervised learning there is a ground truth which is directly used to guide the algorithm training process. The goal of the resulting model is usually to learn a general rule that maps inputs to outputs and is applicable to new, unseen cases. In unsupervised learning there is no preliminary labeling and therefore its goal is to cluster the given inputs based solely on the underlying data structure. Finally, reinforcement learning consists of a computer program performing an assigned task in a dynamic environment and consequently receiving feedback as a positive or negative reinforcement. To improve algorithm's performance, these approaches can be combined, some examples are semi-supervised, self-supervised and multi-instance learning.

Deep learning (DL) is an ML approach employing networks inspired by brain's structure, with a large number of simple interconnected units performing complicated tasks. The DL algorithms most applied to medical imaging are convolutional neural networks. Lower level information inputs, derived from imaging data transformed in feature vectors, form connections to the next level or "layer" of neurons. Each neuron in this second layer can combine the inputs from lower level neurons to form a newer, more complex output. As the number of intermediate or hidden layers increases, the final output from the highest layer becomes richer and more complex.

ML tasks are not limited to tumor property prediction but include many possible applications in other medical imaging and daily workflow fields, such as image acquisition, segmentation, image quality analytics, automated dose estimation and radiology reporting^[21-23]. Despite the high number of recent ML successes, there are still many limitations in its clinical use^[24-27]. First of all, an obstacle to AI adoption in the clinical setting is identifiable in its limited interpretability, especially true for DL. Clinicians are consequently reluctant to trust and to adopt something whose decision process is not fully understood. Secondly, ML research has to deal with issues due to the nature of the health domain, including the lack of large amounts of data, necessary during the training phase, the need for algorithm frequent updating and potential model overfitting.

This review aims to give an overview of the current applications of ML methods in pituitary adenomas evaluation.

PRETREATMENT ASSESSMENT

Tumor consistency is one of the main factors that determine the success-rate of transsphenoidal adenomectomy. For this reason, pre-operative information about tumor consistency would help neurosurgeons in planning the most appropriate surgical approach. Zeynalova *et al*^[28] demonstrated the utility of ML-based histogram analysis (from 55 pituitary adenoma patients) to predict tumor consistency and compared it with a conventional signal intensity ratio (SIR) evaluation. Histogram features were extracted from coronal T2-weighted original, filtered and transformed MRI images by manual segmentation. The high dimensionality of the histogram texture features was reduced with reproducibility analysis, collinearity analysis and wrapper-based feature selection. They employed the artificial neural network (ANN) as ML classifier. The reference-standard was consensual evaluations of neurosurgeons and pathologists. For histogram analysis, the ANN correctly classified 72.5% of pituitary macroadenomas with an area under the receiver operating characteristic (ROC) curve (AUC) value of 0.710. As for SIR evaluation, accuracy and AUC values were 74.5% and 0.551, respectively. Considering AUC values, ML-based histogram analysis performed better than SIR evaluation^[28].

Fan *et al*^[29] demonstrated how a radiomics model can assist neurosurgeons in predicting tumor consistency in patients with acromegaly before surgery and facilitate the determination of an appropriate therapeutic approach. 158 patients (training group $n = 100$, validation group $n = 58$) were included in this retrospective study, while 30 were enrolled in a prospective multi-center study for model validation. The consistency of the tumor was classified as soft or firm according to the neurosurgeon's evaluation. All patients underwent MRI examination which included T1-, T2- and contrast-enhanced T1-weighted sequences in the coronal plane, used for feature extraction. The radiomics features were collected based on the regions of interest drawn by an expert neuroradiologist and verified by a second expert. Total 1561 quantitative features were collected for every sequence. The radiomics features were determined using the elastic net feature selection algorithm, and the radiomics

signature was constructed. Next, a radiomics model was developed using the radiomics signature and clinical characteristics, which were further screened according to the Akaike information criterion. Then, 30 patients with acromegaly from three hospitals were enrolled for multicenter validation of the model. The prediction accuracy was then evaluated through ROC analyses and associated classification measures. The radiomics model constructed in this study showed an AUC of 0.83 and 0.81 in the primary and validation cohorts, respectively. In conclusion, this model was convenient to use and could accurately predict the tumor consistency in a multicenter prospective validation before surgery^[29].

The pre-operative prediction of cavernous sinus (CS) invasion by pituitary adenomas (Knosp grade 2-3) can help neurosurgeons in planning the surgical approach, follow-up, and long-term management. Niu *et al*^[30] used a radiomics method to predict CS invasion, enrolling 194 patients with Knosp grade 2-3 (training set $n = 97$; test set $n = 97$) and extracting 2553 quantitative imaging texture features from contrast-enhanced T1- and T2-weighted MR images. A linear support vector machine (SVM) was used to fit the predictive model, then a nomogram was constructed incorporating radiomics signature and clinico-radiological risk factors. Radiomics model yielded an AUC of 0.852 and 0.826 for the training and test set, respectively. The nomogram yielded an AUC of 0.899 in the training test and 0.871 in the test set^[30].

According to the 2017 WHO classification, “high risk” pituitary adenomas are tumors with rapid growth, radiological invasion, and high Ki-67 proliferation index. MRI had already proved promising in proliferative index prediction, using diffusion-weighted imaging. Indeed, Tamrazi *et al*^[31] performed a retrospective review of diffusion imaging and immunohistochemical characteristics of 17 with pituitary macroadenomas and demonstrated an inverse relationship between apparent diffusion coefficient values and Ki-67. In this context, machine learning can be effective for the early identification of “high risk” adenomas and could allow making a more accurate pre-operative assessment and long-term follow-up. Regarding the last, a recent study by Uggas *et al*^[32] employed ML analysis of texture-derived parameters from pre-operative coronal T2-weighted MR images. A total of 89 patients that underwent endoscopic endonasal procedure were included. Pituitary adenomas were classified in high versus low Ki-67 proliferation index according to pathological data. Total 1128 features were extracted, and different supervised feature selection methods were employed to select the most informative features. A k-nearest neighbors (k-NN) classifier was used to predict the proliferative index, then algorithm validation was performed with a train-test approach. The accuracy of k-NN in the test group was 91.67% of correctly classified patients.

Non-functioning pituitary adenomas are a huge group of adenomas and can be divided in NCAs, oncocyomas and gonadotrophic adenomas. Patients with NCAs are more likely to respond to neo-adjuvant radiotherapy, so radiomics could play a role in discriminating preoperatively NCAs from other subtypes. Zhang *et al*^[33] enrolled 112 patients (training set $n = 75$; test set $n = 37$) with non-functioning pituitary adenomas who underwent MR examination. In their retrospective study a SVM trained a predictive model that was validated using a ROC analysis on an independent test set. Then, a nomogram was constructed incorporating clinical characteristics and the radiomics signature for a more individualized predictive model. T1-weighted image features yielded an AUC value of 0.83 and 0.80 for the training and test sets, respectively. The nomogram incorporating sex and the T1 radiomics signature yielded good calibration in the training and test sets (concordance index of 0.854 and 0.857, respectively)^[33].

Somatostatin analogues (SAs) response prediction is an essential information in acromegalic patient medical treatment in the presence of GH-secreting pituitary adenomas. Indeed, this medical treatment can improve the surgical outcome, but it is burdened by high costs. Heck *et al*^[34] showed how quantitative analysis of T2-weighted MR images could predict response to SAs in patients with acromegaly. However, they verified that conventional visual T2 intensity assessment achieved similar results. This retrospective cohort study included 58 newly diagnosed patients. Parameters from the T2 histogram analyses (T2 intensity ratio and T2 homogeneity ratio) were correlated to visually assessed T2 intensity (hypo-, iso- or hyperintense), baseline characteristics, response to SA treatment, and histological granulation pattern (anti-Cam5.2). T2 intensity ratio was lowest in the hypointense tumors and highest in the hyperintense tumors. T2 intensity at baseline correlated with reduction in GH ($r = -0.67$) and IGF-1 ($r = -0.36$) after primary SA treatment ($n = 34$). The T2 homogeneity ratio correlated with adenoma size reduction ($r = -0.45$). Sparsely granulated adenomas, which are typically associated to resistance to SAs, had a higher T2 intensity than densely or intermediately granulated adenomas. In conclusion, using T2 histogram analyses the

authors found that high T2 intensity correlated with more aggressive adenoma subtypes, larger adenoma size, lower GH and IGF-1 production, and blunted response to an octreotide test dose at baseline. Moreover, a better biochemical response to SA therapy was observed in adenomas with low T2 intensity. In their retrospective study, Kocak *et al*^[35] demonstrated the potential role of ML-based high-dimensional quantitative texture analysis (qTA) in predicting SAs response in acromegalic patients with a GH-secreting pituitary adenoma. They showed how ML performs better than relative signal intensity (rSI) evaluation or immunohistochemical granulation pattern evaluation. Coronal T2-weighted images of 47 patients (24 SA responsive and 23 SA resistant patients) were used for qTA and quantitative and qualitative rSI evaluation, while the immunohistochemical evaluation was based on the granulation pattern of the adenomas. ML classifiers were k-NN and C4.5 algorithm. The reference standard was the biochemical response status (6 months post-therapy). Predictive performance of qTA was compared with that of the quantitative and qualitative rSI and immunohistochemical evaluation. For the qTA, k-NN correctly classified 85.1% macroadenomas with an AUC of 0.847. The accuracy and AUC ranges of the other methods were lower, equal to 57.4/70.2% and 0.575/0.704, respectively^[35].

Pituitary tumor growth can lead to compression of the anterior visual pathways, leading to visual impairment, which is the most common and earliest symptom in this pathology. In their retrospective study Lilja *et al*^[36] demonstrated that diffusion Tensor imaging (DTI) and a prediction model may be an additional diagnostic tool that provides objective data about visual pathway injury, guiding treatment decisions. Total 23 patients with pituitary adenomas and 20 healthy patients underwent a complete neuro-ophthalmological examination and an MRI study, which included 3D T1-weighted and DTI sequences. A prediction model using logistic regression was constructed to test the capability of DTI parameters to correctly classify a subject as a patient (before surgery) or a control. Total 12 features quantifying mean DTI parameters from the optic tract regions were included. Based on the axial diffusivity and fractional anisotropy, the prediction model could separate patients from controls with high sensitivity. The prediction model correctly classified all patients with visual field defects (sensitivity = 1.0), 9 of 12 patients without visual field defects (sensitivity = 0.75), and 17 of 20 controls (specificity = 0.85)^[36].

NEUROSURGICAL OUTCOME PREDICTION

Gross total resection (GTR) is the main surgical goal in transsphenoidal surgery for most pituitary adenomas. Predictive analytics for GTR may help in surgical decision-making, especially in intermediate cases (Knops grade 2-3A). In their retrospective study, Staartjes *et al*^[37] investigated the potential value of deep neural network for predicting GTR in comparison with the Knops classification and logistic regression. They enrolled a total of 140 patients who underwent endoscopic transsphenoidal surgery and trained a deep neural network to predict GTR from 16 preoperatively available neuro-radiological and procedural variables. Their DL model (AUC = 0.96; accuracy = 91%; sensitivity = 94%; specificity = 89%) outperformed both the Knops classification (AUC = 0.87; accuracy = 81%; sensitivity = 92%; specificity = 70%) and logistic regression (AUC = 0.86; accuracy = 82%; sensitivity = 81%; specificity = 83%)^[37].

In their retrospective study, Liu *et al*^[38] aimed to develop machine learning-based predictive models to evaluate Cushing disease recurrence after initial transsphenoidal surgery and to investigate their performance. Seventeen radiomic features including tumor volume computed from pre-operative MRI (contrast-enhanced T1-weighted MRI) and other pre/post-operative clinical variables were evaluated. Five supervised ML algorithms, including decision tree, gradient boosting decision tree, random forest (RF), adaptive boosting, and extreme gradient boost and 2 conventional models (Logistic regression, Naïve Bayes) were applied. Models were evaluated based on their AUC. The study demonstrated that ML-based predictive models for neurosurgical outcomes performed well, better than some conventional models such as logistic regression. Using 17 variables, several ML-based predictive models for recurrence were developed, and most of them (4/5) maintained high performance, with AUCs ranging from 0.694 to 0.781 which were much higher than that of conventional statistics. The best performance (AUC = 0.781) was obtained introducing 8 variables to RF algorithm, which was much better than that of logistic regression (AUC = 0.684) and that of using only postoperative morning serum cortisol (AUC = 0.635). According to the feature selection algorithms, the top predictors were age, postoperative serum cortisol, and postoperative ACTH^[38].

Cerebrospinal fluid (CSF) fistulas remain a major complication of transnasal transsphenoidal surgery for pituitary adenoma. Staartjes *et al.*^[39] developed a neural network-based model with the aim of classifying pituitary surgeries in having high versus low-risk of CSF leak. From a prospective registry, 154 patients who underwent endoscopic transnasal transsphenoidal surgery for pituitary adenoma were identified and underwent an MRI study. Moreover, risk factors for intraoperative CSF leaks were identified using conventional statistical methods. Selected features included both imaging features from inter-carotid distances and other clinical pre/post-operative variables. The authors built a predictive model for intraoperative CSF leaks based on a deep multilayer perceptron with 5 hidden layers. The deep neural network-based prediction model could identify patients at high risk for intraoperative CSF leak. It correctly classified 88% of patients in the test set, with an AUC of 0.84. Sensitivity and specificity were high, of 83% and 89% respectively. The positive predictive value was 71%, negative predictive value was 94%, and F1 score was 0.77^[39].

CONCLUSION

We reviewed a set of articles related to ML applications in pituitary adenomas. These studies showed that ML has a certain potential to improve the diagnostic performance of MRI in pre-treatment assessment and neurosurgical outcome prediction. In current studies there is not a standardized procedure, ML methodologies vary a lot, different types of classifiers are applied and only a few models are validated on an external set. The major limits of these studies are the replicability and generalizability. Publicly available datasets are needed, and clinical applicability still requires more robust validation across different sites, scanner vendors and field intensity. However, the research in the years is growing rapidly and ML software can be a potential power to facilitate better clinical decision making in pituitary tumor patients.

REFERENCES

- 1 **McDowell BD**, Wallace RB, Carnahan RM, Chrischilles EA, Lynch CF, Schlechte JA. Demographic differences in incidence for pituitary adenoma. *Pituitary* 2011; **14**: 23-30 [PMID: [20809113](#) DOI: [10.1007/s11102-010-0253-4](#)]
- 2 **Fernandez A**, Karavitaki N, Wass JA. Prevalence of pituitary adenomas: a community-based, cross-sectional study in Banbury (Oxfordshire, UK). *Clin Endocrinol (Oxf)* 2010; **72**: 377-382 [PMID: [19650784](#) DOI: [10.1111/j.1365-2265.2009.03667.x](#)]
- 3 **Chen L**, White WL, Spetzler RF, Xu B. A prospective study of nonfunctioning pituitary adenomas: presentation, management, and clinical outcome. *J Neurooncol* 2011; **102**: 129-138 [PMID: [20730474](#) DOI: [10.1007/s11060-010-0302-x](#)]
- 4 **Asa SL**, Ezzat S. The pathogenesis of pituitary tumors. *Annu Rev Pathol* 2009; **4**: 97-126 [PMID: [19400692](#) DOI: [10.1146/annurev.pathol.4.110807.092259](#)]
- 5 **Inoshita N**, Nishioka H. The 2017 WHO classification of pituitary adenoma: overview and comments. *Brain Tumor Pathol* 2018; **35**: 51-56 [PMID: [29687298](#) DOI: [10.1007/s10014-018-0314-3](#)]
- 6 **Gupta K**, Sahni S, Saggar K, Vashisht G. Evaluation of Clinical and Magnetic Resonance Imaging Profile of Pituitary Macroadenoma: A Prospective Study. *J Nat Sci Biol Med* 2018; **9**: 34-38 [PMID: [29456390](#) DOI: [10.4103/jnsbm.JNSBM_111_17](#)]
- 7 **Boxerman JL**, Rogg JM, Donahue JE, Machan JT, Goldman MA, Doberstein CE. Preoperative MRI evaluation of pituitary macroadenoma: imaging features predictive of successful transsphenoidal surgery. *AJR Am J Roentgenol* 2010; **195**: 720-728 [PMID: [20729452](#) DOI: [10.2214/AJR.09.4128](#)]
- 8 **Knosp E**, Steiner E, Kitz K, Matula C. Pituitary adenomas with invasion of the cavernous sinus space: a magnetic resonance imaging classification compared with surgical findings. *Neurosurgery* 1993; **33**: 610-7; discussion 617-8 [PMID: [8232800](#) DOI: [10.1227/00006123-199310000-00008](#)]
- 9 **Micko AS**, Wöhrer A, Wolfsberger S, Knosp E. Invasion of the cavernous sinus space in pituitary adenomas: endoscopic verification and its correlation with an MRI-based classification. *J Neurosurg* 2015; **122**: 803-811 [PMID: [25658782](#) DOI: [10.3171/2014.12.JNS141083](#)]
- 10 **Bahuleyan B**, Raghuram L, Rajshekhar V, Chacko AG. To assess the ability of MRI to predict consistency of pituitary macroadenomas. *Br J Neurosurg* 2006; **20**: 324-326 [PMID: [17129884](#) DOI: [10.1080/02688690601000717](#)]
- 11 **Hagiwara A**, Inoue Y, Wakasa K, Haba T, Tashiro T, Miyamoto T. Comparison of growth hormone-producing and non-growth hormone-producing pituitary adenomas: imaging characteristics and pathologic correlation. *Radiology* 2003; **228**: 533-538 [PMID: [12819334](#) DOI: [10.1148/radiol.2282020695](#)]
- 12 **Snow RB**, Johnson CE, Morgello S, Lavyne MH, Patterson RH Jr. Is magnetic resonance imaging useful in guiding the operative approach to large pituitary tumors? *Neurosurgery* 1990; **26**: 801-803 [PMID: [2352598](#) DOI: [10.1097/00006123-199005000-00011](#)]
- 13 **Pierallini A**, Caramia F, Falcone C, Tinelli E, Paonessa A, Ciddio AB, Fiorelli M, Bianco F, Natalizi S, Ferrante L, Bozzao L. Pituitary macroadenomas: preoperative evaluation of consistency with diffusion-weighted MR imaging--initial experience. *Radiology* 2006; **239**: 223-231 [PMID: [16452397](#) DOI: [10.1148/radiol.2392060001](#)]

- 10.1148/radiol.2383042204]
- 14 **Mohamed FF**, Abouhasheem S. Diagnostic value of apparent diffusion coefficient (ADC) in assessment of pituitary macroadenoma consistency. *Egypt J Radiol Nucl Med* 2013; **44**: 617–24 [DOI: 10.1016/j.ejnm.2013.05.012]
- 15 **Suzuki C**, Maeda M, Hori K, Kozuka Y, Sakuma H, Taki W, Takeda K. Apparent diffusion coefficient of pituitary macroadenoma evaluated with line-scan diffusion-weighted imaging. *J Neuroradiol* 2007; **34**: 228–235 [PMID: 17719632 DOI: 10.1016/j.neurad.2007.06.007]
- 16 **Erickson BJ**, Korfiatis P, Akkus Z, Kline TL. Machine Learning for Medical Imaging. *Radiographics* 2017; **37**: 505–515 [PMID: 28212054 DOI: 10.1148/rg.2017160130]
- 17 **Choy G**, Khalilzadeh O, Michalski M, Do S, Samir AE, Panykh OS, Geis JR, Pandharipande PV, Brink JA, Dreyer KJ. Current Applications and Future Impact of Machine Learning in Radiology. *Radiology* 2018; **288**: 318–328 [PMID: 29944078 DOI: 10.1148/radiol.2018171820]
- 18 **Wang S**, Summers RM. Machine learning and radiology. *Med Image Anal* 2012; **16**: 933–951 [PMID: 22465077 DOI: 10.1016/j.media.2012.02.005]
- 19 **Gillies RJ**, Kinahan PE, Hricak H. Radiomics: Images Are More than Pictures, They Are Data. *Radiology* 2016; **278**: 563–577 [PMID: 26579733 DOI: 10.1148/radiol.2015151169]
- 20 **Schmidt J**, Marques MRG, Botti S, Marques MAL. Recent advances and applications of machine learning in solid-state materials science. *NPJ Comput Mater* 2019; **5**: 83 [DOI: 10.1038/s41524-019-0221-0]
- 21 **Zaharchuk G**, Gong E, Wintermark M, Rubin D, Langlotz CP. Deep Learning in Neuroradiology. *AJNR Am J Neuroradiol* 2018; **39**: 1776–1784 [PMID: 29419402 DOI: 10.3174/ajnr.A5543]
- 22 **Mazurowski MA**, Buda M, Saha A, Bashir MR. Deep learning in radiology: An overview of the concepts and a survey of the state of the art with focus on MRI. *J Magn Reson Imaging* 2019; **49**: 939–954 [PMID: 30575178 DOI: 10.1002/jmri.26534]
- 23 **McBee MP**, Awan OA, Colucci AT, Ghobadi CW, Kadom N, Kansagra AP, Tridandapani S, Auffermann WF. Deep Learning in Radiology. *Acad Radiol* 2018; **25**: 1472–1480 [PMID: 29606338 DOI: 10.1016/j.acra.2018.02.018]
- 24 **Romeo V**, Ricciardi C, Cuocolo R, Stanzione A, Verde F, Sarno L, Improta G, Mainenti PP, D'Armiento M, Brunetti A, Maurea S. Machine learning analysis of MRI-derived texture features to predict placenta accreta spectrum in patients with placenta previa. *Magn Reson Imaging* 2019; **64**: 71–76 [PMID: 31102613 DOI: 10.1016/j.mri.2019.05.017]
- 25 **Ciampi F**, Chung K, van Riel SJ, Setio AAA, Gerke PK, Jacobs C, Scholten ET, Schaefer-Prokop C, Wille MMW, Marchianò A, Pastorino U, Prokop M, van Ginneken B. Towards automatic pulmonary nodule management in lung cancer screening with deep learning. *Sci Rep* 2017; **7**: 46479 [PMID: 28422152 DOI: 10.1038/srep46479]
- 26 **Cuocolo R**, Perillo T, De Rosa E, Ugga L, Petretta M. Current applications of big data and machine learning in cardiology. *J Geriatr Cardiol* 2019; **16**: 601–607 [PMID: 31555327 DOI: 10.11909/j.issn.1671-5411.2019.08.002]
- 27 **Islam MM**, Nasrin T, Walther BA, Wu CC, Yang HC, Li YC. Prediction of sepsis patients using machine learning approach: A meta-analysis. *Comput Methods Programs Biomed* 2019; **170**: 1–9 [PMID: 30712598 DOI: 10.1016/j.cmpb.2018.12.027]
- 28 **Zeynalova A**, Kocak B, Durmaz ES, Comunoglu N, Ozcan K, Ozcan G, Turk O, Tanriover N, Kocer N, Kizilkilic O, Islak C. Preoperative evaluation of tumour consistency in pituitary macroadenomas: a machine learning-based histogram analysis on conventional T2-weighted MRI. *Neuroradiology* 2019; **61**: 767–774 [PMID: 31011772 DOI: 10.1007/s00234-019-02211-2]
- 29 **Fan Y**, Hua M, Mou A, Wu M, Liu X, Bao X, Wang R, Feng M. Preoperative Noninvasive Radiomics Approach Predicts Tumor Consistency in Patients With Acromegaly: Development and Multicenter Prospective Validation. *Front Endocrinol (Lausanne)* 2019; **10**: 403 [PMID: 31316464 DOI: 10.3389/fendo.2019.00403]
- 30 **Niu J**, Zhang S, Ma S, Diao J, Zhou W, Tian J, Zang Y, Jia W. Preoperative prediction of cavernous sinus invasion by pituitary adenomas using a radiomics method based on magnetic resonance images. *Eur Radiol* 2019; **29**: 1625–1634 [PMID: 30255254 DOI: 10.1007/s00330-018-5725-3]
- 31 **Tamrazi B**, Pekmezci M, Aboian M, Tihan T, Glastonbury CM. Apparent diffusion coefficient and pituitary macroadenomas: pre-operative assessment of tumor atypia. *Pituitary* 2017; **20**: 195–200 [PMID: 27734275 DOI: 10.1007/s11102-016-0759-5]
- 32 **Ugga L**, Cuocolo R, Solari D, Guadagno E, D'Amico A, Somma T, Cappabianca P, Del Basso de Caro ML, Cavallo LM, Brunetti A. Prediction of high proliferative index in pituitary macroadenomas using MRI-based radiomics and machine learning. *Neuroradiology* 2019; **61**: 1365–1373 [PMID: 31375883 DOI: 10.1007/s00234-019-02266-1]
- 33 **Zhang S**, Song G, Zang Y, Jia J, Wang C, Li C, Tian J, Dong D, Zhang Y. Non-invasive radiomics approach potentially predicts non-functioning pituitary adenomas subtypes before surgery. *Eur Radiol* 2018; **28**: 3692–3701 [PMID: 29572634 DOI: 10.1007/s00330-017-5180-6]
- 34 **Heck A**, Emblem KE, Casar-Borota O, Bollerslev J, Ringstad G. Quantitative analyses of T2-weighted MRI as a potential marker for response to somatostatin analogs in newly diagnosed acromegaly. *Endocrine* 2016; **52**: 333–343 [PMID: 26475495 DOI: 10.1007/s12020-015-0766-8]
- 35 **Kocak B**, Durmaz ES, Kadioglu P, Polat Korkmaz O, Comunoglu N, Tanriover N, Kocer N, Islak C, Kizilkilic O. Predicting response to somatostatin analogues in acromegaly: machine learning-based high-dimensional quantitative texture analysis on T2-weighted MRI. *Eur Radiol* 2019; **29**: 2731–2739 [PMID: 30506213 DOI: 10.1007/s00330-018-5876-2]
- 36 **Lilja Y**, Gustafsson O, Ljungberg M, Starck G, Lindblom B, Skoglund T, Bergquist H, Jakobsson KE, Nilsson D. Visual pathway impairment by pituitary adenomas: quantitative diagnostics by diffusion tensor imaging. *J Neurosurg* 2017; **127**: 569–579 [PMID: 27885957 DOI: 10.3171/2016.8.JNS161290]
- 37 **Staatjes VE**, Serra C, Muscas G, Maldaner N, Akeret K, van Niftrik CHB, Fierstra J, Holzmans D, Regli L. Utility of deep neural networks in predicting gross-total resection after transsphenoidal surgery for pituitary adenoma: a pilot study. *Neurosurg Focus* 2018; **45**: E12 [PMID: 30453454 DOI: 10.3171/2018.8.FOCUS18243]

- 38 **Liu Y**, Liu X, Hong X, Liu P, Bao X, Yao Y, Xing B, Li Y, Huang Y, Zhu H, Lu L, Wang R, Feng M. Prediction of Recurrence after Transsphenoidal Surgery for Cushing's Disease: The Use of Machine Learning Algorithms. *Neuroendocrinology* 2019; **108**: 201-210 [PMID: [30630181](#) DOI: [10.1159/000496753](#)]
- 39 **Staartjes VE**, Zatra CM, Akeret K, Maldaner N, Muscas G, Bas van Niftrik CH, Fierstra J, Regli L, Serra C. Neural network-based identification of patients at high risk for intraoperative cerebrospinal fluid leaks in endoscopic pituitary surgery. *J Neurosurg* 2019; 1-7 [PMID: [31226693](#) DOI: [10.3171/2019.4.JNS19477](#)]

Development of tomographic reconstruction for three-dimensional optical imaging: From the inversion of light propagation to artificial intelligence

Xin Cao, Kang Li, Xue-Li Xu, Karen M von Deneen, Guo-Hua Geng, Xue-Li Chen

ORCID number: Xin Cao 0000-0001-8658-8412; Kang Li 0000-0001-6218-5715; Xue-Li Xu 0000-0001-7518-376X; Karen M von Deneen 0000-0002-5310-1003; Guo-Hua Geng 0000-0003-2563-4029; Xue-Li Chen 0000-0002-3898-9892.

Author contributions: Cao X performed the majority of the writing and the investigation of articles; Li K and Xu XL performed the literature search and writing for the light propagation model-based OMT algorithm; Geng GH performed writing for the machine learning-based OMT algorithm; von Deneen KM polished the language and expression of the paper; Chen XL checked the organization and revised the writing of the paper.

Supported by the National Natural Science Foundation of China, No. 61701403; the Project Funded by China Post-doctoral Science Foundation, No. 2018M643719; the Young Talent Support Program of the Shaanxi Association for Science and Technology, No. 20190107; the Scientific Research Program Funded by Shaanxi Provincial Education Department, No. 18JK0767; and the Natural Science Research Plan Program in Shaanxi Province of China, No. 2017JQ6006.

Xin Cao, Kang Li, Xue-Li Xu, Guo-Hua Geng, School of Information Science and Technology, Northwest University, Xi'an 710069, Shaanxi Province, China

Karen M von Deneen, Xue-Li Chen, Engineering Research Center of Molecular and Neuro Imaging, Ministry of Education, and School of Life Science and Technology, Xidian University, Xi'an 710126, Shaanxi Province, China

Corresponding author: Xue-Li Chen, PhD, Professor, Engineering Research Center of Molecular and Neuro Imaging, Ministry of Education, and School of Life Science and Technology, Xidian University, No. 266 Xinglong Section of Xifeng Road, Xi'an 710126, Shaanxi Province, China. xlchen@xidian.edu.cn

Abstract

Optical molecular tomography (OMT) is an imaging modality which uses an optical signal, especially near-infrared light, to reconstruct the three-dimensional information of the light source in biological tissue. With the advantages of being low-cost, noninvasive and having high sensitivity, OMT has been applied in preclinical and clinical research. However, due to its serious ill-posedness and ill-condition, the solution of OMT requires heavy data analysis and the reconstruction quality is limited. Recently, the artificial intelligence (commonly known as AI)-based methods have been proposed to provide a different tool to solve the OMT problem. In this paper, we review the progress on OMT algorithms, from conventional methods to AI-based methods, and we also give a prospective towards future developments in this domain.

Key Words: Optical molecular tomography; Deep learning; Artificial intelligence; Light propagation based algorithm; Tomographic reconstruction

©The Author(s) 2020. Published by Baishideng Publishing Group Inc. All rights reserved.

Core Tip: Most of the existing review articles about optical molecular tomography (OMT) focus on the traditional light propagation model-based algorithm, which possesses ill-posedness and ill-condition and the reconstruction result is unsatisfactory. The emergence of deep learning has brought OMT into the era of artificial intelligence, which can obtain a

Conflict-of-interest statement: The authors confirm having no conflict of interest in relation to this article's content.

Open-Access: This article is an open-access article that was selected by an in-house editor and fully peer-reviewed by external reviewers. It is distributed in accordance with the Creative Commons Attribution NonCommercial (CC BY-NC 4.0) license, which permits others to distribute, remix, adapt, build upon this work non-commercially, and license their derivative works on different terms, provided the original work is properly cited and the use is non-commercial. See: <http://creativecommons.org/licenses/by-nc/4.0/>

Manuscript source: Invited manuscript

Received: June 5, 2020

Peer-review started: June 5, 2020

First decision: June 4, 2020

Revised: August 1, 2020

Accepted: August 22, 2020

Article in press: August 22, 2020

Published online: August 28, 2020

P-Reviewer: Nassar G, Ogino S

S-Editor: Wang JL

L-Editor: Filipodia

P-Editor: Xing YX



highly accurate reconstruction result. This article systematically reviews the development of tomographic reconstruction for OMT, which involves the light propagation model-based OMT algorithm and machine learning-based OMT algorithm. The challenges and perspectives of these machine learning-based algorithms are given at the end of the article.

Citation: Cao X, Li K, Xu XL, Deneen KMV, Geng GH, Chen XL. Development of tomographic reconstruction for three-dimensional optical imaging: From the inversion of light propagation to artificial intelligence. *Artif Intell Med Imaging* 2020; 1(2): 78-86

URL: <https://www.wjgnet.com/2644-3260/full/v1/i2/78.htm>

DOI: <https://dx.doi.org/10.35711/aimi.v1.i2.78>

INTRODUCTION

Optical molecular imaging (OMI) is the technology of using optical imaging instruments to detect biological tissues in organisms. In the time since Roger Yonchien Tsien reported that the tumor of a mouse could be resected under the guidance of fluorescence microscopy, winning the Nobel Prize in 2008, OMI has achieved rapid development, especially in recent years. With the advantages of high imaging sensitivity, tissue specificity, relatively short acquisition time and low cost, OMI has been successfully applied to many research fields, including - but not limited to - gene expression, tumor detection, drug development, and therapy evaluation^[1-12]. However, OMI can only provide a two-dimensional image, which lacks deeper information and cannot describe the 3D distribution of the optical signal in an imaging object. Thus, researchers have proposed a series of 3D imaging methods, which can be named as optical molecular tomography (OMT).

In fact, OMT can be further divided into several subtypes, such as bioluminescence tomography, Cerenkov luminescence tomography (CLT), fluorescence molecular tomography (FMT), diffuse optical tomography, X-ray luminescence computed tomography (commonly referred to as XLCT), and so on^[13-18]. The main difference between them is the means of producing the optical signal. For example, in CLT, the optical signal is emitted during the decay of a radionuclide probe, and in XLCT, high energy X-ray photons are used to excite X-ray excitable nanophosphors which emit the optical signal. Although the way of producing light signal varies, the reconstruction methods for these modalities can be concluded as one unified framework, as shown in **Figure 1**. It should be noted that anatomical information is essential for OMT, and in most cases, it is provided by X-ray computed tomography or magnetic resonance imaging^[19-21]. Finally, the 3D distribution of the optical signal in the imaging object can be obtained, and the light source can then be located based on the reconstruction result. It is obvious that the core component of the framework is the OMT algorithm, which can determine the quality of the final reconstruction result.

In this review, we summarize recent progress on the OMT algorithm in two aspects: the traditional light propagation model-based way and machine learning-based way. Subsequently, we will provide a prospect towards future developments in a machine learning-based way for OMT.

LIGHT PROPAGATION MODEL-BASED OMT ALGORITHM

The accuracy of the traditional OMT algorithm is dependent on the description of photon propagation in biological tissue. The most popular light transfer model for OMT is the radiative transfer equation (RTE) from Maxwell's equations^[22-25]. Although RTE can accurately depict photon propagation in diffusive media, it is a complicated integro-differential equation, and the computational time and memory requirements are extremely expensive. As a result, RTE is commonly simplified as the diffusion equation (DE, the lower-order approximation of the RTE)^[26-28] and Nrd order is a simplified spherical harmonics function (SP₃, the high-order approximation of RTE, and in most cases, N equals 3)^[29-31]. After introducing the boundary condition, the simplified RTE can be solved using the finite element method^[32-34] and the OMT problem can be linearized as the following weight matrix equation^[28,25-37]: $AX = \Phi^{\text{measure}}$, where $X \geq 0$ (Eq. 1) "where A" denotes the optical transport system matrix, X is the unknown distribution of the optical source and Φ^{measure} represents the luminous flux of

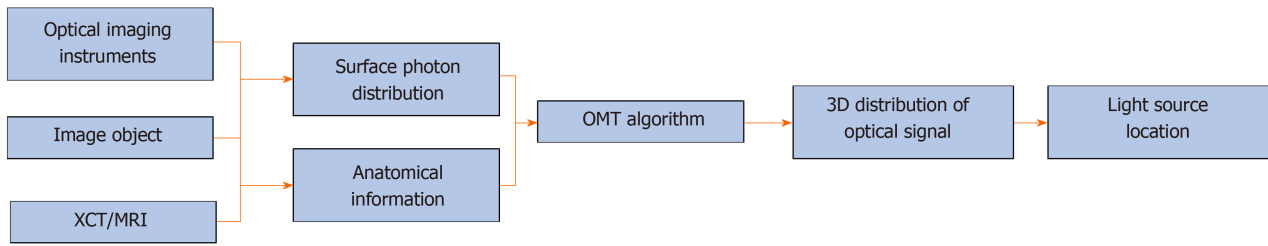


Figure 1 Main flowchart of optical molecular tomography. 3D: Three-dimensional; MRI: Magnetic resonance imaging; OMT: Optical molecular tomography; XCT: X-ray computed tomography.

the vertices. As Φ^{measure} can only be collected on the surface of an imaging object, the goal of OMT can be regarded as the determination of the 3D luminescence source distribution X from boundary measurements Φ^{measure} based on the formulation of Eq. 1, and this is a typically inverse problem. It should be noted that the number of measurements is often substantially less than the number of unknowns, making the inverse reconstruction an ill-conditioned problem.

Up until now, many methods have been developed to address the limitation mentioned above to make the OMT algorithm strong and robust. These methods can be roughly divided into two categories. The first one is the priori information-based method. In these methods, *a priori* information is first inferred according to the surface light power distribution and the heterogeneous structure of the imaging object, and then is used as the permissible source region. The aim of using *a priori* information is to constrain the unknown sources in the region where the sources may exist, resulting in the reduction of the amount of unknown source locations. Many numerical and *in vivo* experiments have been conducted, and the results indicate that the size of the permissible source region can significantly affect the reconstruction quality^[37-46]. It is obvious that the smaller the permissible source region, the more stable the reconstruction results. The main obstacle of the priori information-based methods is that the prior information about the permissible source region cannot always be obtained in advance, especially for the early diseased tissue which cannot be distinguished from anatomical information. Figure 2 shows the reconstruction results with *a priori* information^[47].

The second one is the posteriori information-based method. In these methods, the whole object is used as the initial permissible source region, and the permissible region is updated by selecting the elements where the reconstructed energy is relatively higher than others^[48-53]. As the posteriori information-based method avoids the segmentation of the permissible source region from anatomical information, it has superior generalization performance than the priori information-based method, and most of the recent studies are focused on optimizing it^[54-58]. Besides the above methods for OMT, the reconstruction accuracy can also be improved by increasing the number of detectable measurements^[46,59-66]. For example, in FMT, the quality of the reconstructed results can be improved with the increasing number of measurement data. In CLT, multispectral images can be acquired using a group of filters and the result can be improved significantly. The drawback of this method is that the more optical signal data are acquired, the more time is consumed. However, these traditional light propagation model-based methods are still limited to their reconstruction accuracy, and the main reason is that the simplified RTE cannot accurately describe the process of photon propagation. Thus, more effective methods to improve the reconstruction quality of OMT are still required. Figure 3 shows the reconstruction results with posteriori information^[62,67].

MACHINE LEARNING-BASED OMT ALGORITHM

With the development of artificial intelligence (AI), machine learning algorithms, especially deep learning-based technologies, have gained stunning successes at solving difficult and previously unsolved computational problems in many fields, such as computer vision, natural language processing, speech recognition, and so on^[68-71]. The great success of AI has also attracted the attention of researchers in the field of OMT. Based on multilayer perceptrons (commonly known as MLPs), Gao *et al*^[72] proposed a data-driven-based strategy for OMT. As the machine learning-based method requires

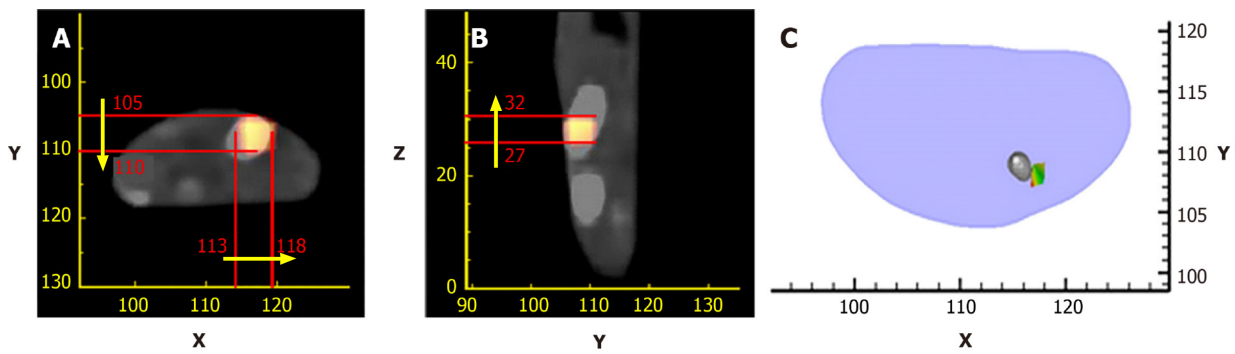


Figure 2 Reconstruction results with *a priori* information. A and B: The axial and sagittal views of single photon emission computed tomography/computed tomography imaging, and an implanted light source is inserted into a mouse; C: The axial-view result of the reconstructed source. These images are reproduced from^[47].

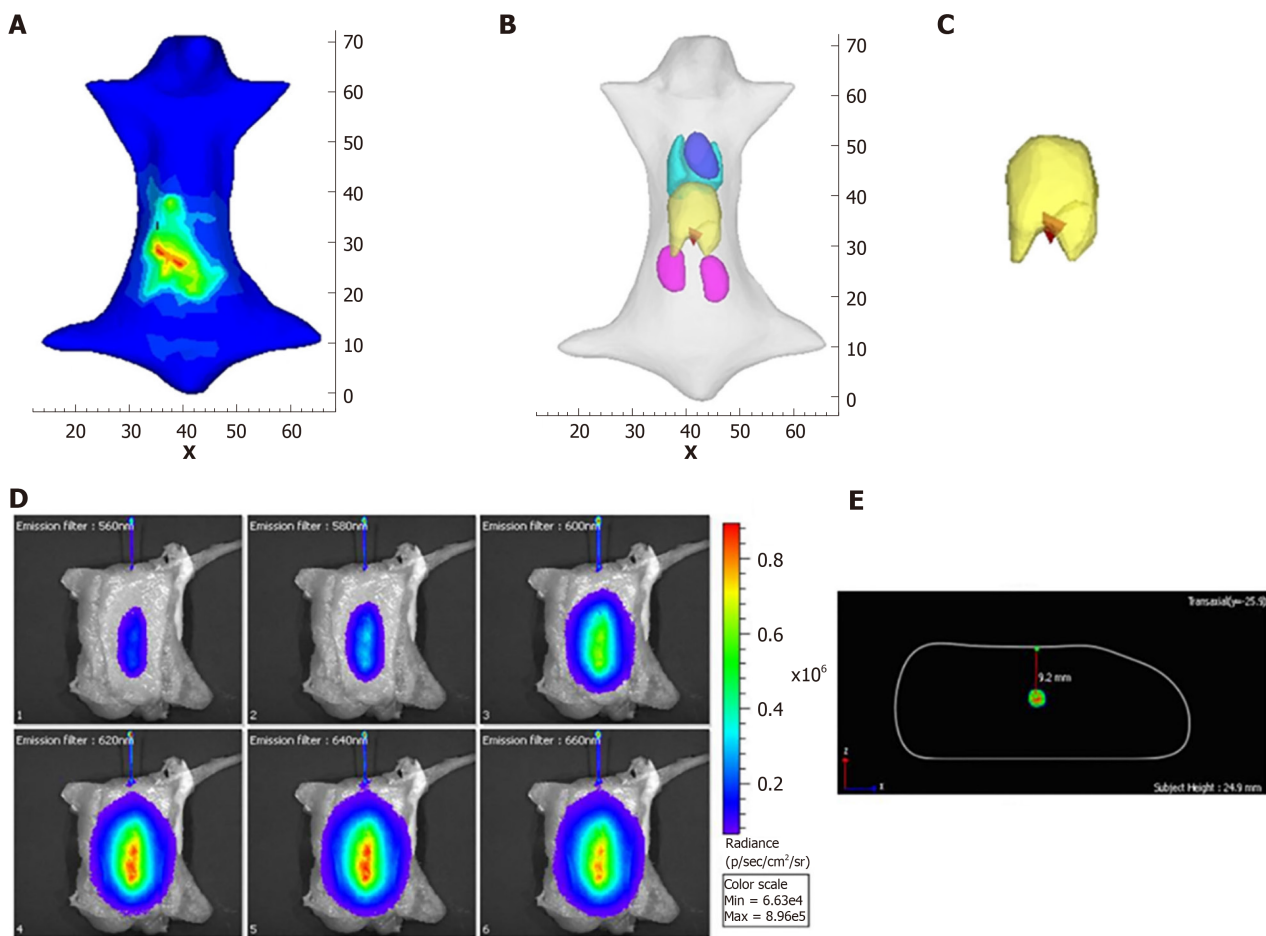


Figure 3 Reconstruction results with *posteriori* information. A: The luminescence distribution in the body; B and C: The three-dimensional results and the results of the local enlarged image in the local area of the liver; C: The images of the capillary acquired using six filters; D, E: The trans-axial multispectral-Cerenkov luminescence tomography reconstructed image of the capillary filled with ³²P-ATP at a 9 mm depth. A and B are reproduced from^[67], while C and D are reproduced from^[62].

large amounts of data to train the network, Molecular Optical Simulation Environment software^[73] is adopted to produce the simulation data. The experimental results showed the proposed method can greatly improve the reconstruction quality compared with conventional approaches. Subsequently, based on the convolutional neural network and recurrent neural network, Guo *et al*^[74] proposed a framework for FMT reconstruction. The input of this method is two-dimensional fluorescent images, which can avoid errors caused by mesh registration in conventional methods. Zhang *et al*^[75] used MLPs to solve the CLT problem, and the complex relationship between the

surface optical signal and the true photon source has been learned by the network. Meng *et al*^[76] constructed a K-nearest neighbor-based locally connected network (KNN-LCN) for FMT. In their work, KNN-LCN cascades a fully connected (referred to as FC) sub-network with a locally connected (referred to as LC) sub-network, where the FC part provides a coarse reconstruction result and the LC part fine-tunes the morphological quality of the reconstructed result. Compared to the traditional light propagation model-based methods, the biggest advantage of the machine learning-based method is that it can directly fit the nonlinear relationship between an object surface optical density and its internal luminescence source. Figure 4 shows the structure of the networks used in OMT reconstruction^[72,74-76].

CONCLUSION

Although the machine learning-based OMT algorithm can obtain a more accurate reconstruction result than the traditional light propagation model-based algorithm, further application is still limited and requires more theoretical research. One reason is that the network trained for one object cannot be used for others, and if the object is changed, another network with different parameters should be built and its training will cost a lot of time. Another reason is that there is no ideal method that can explain the mechanism of such a neural network. The solution to the above two limitations is the development direction for future research. In addition, there are many environmental, dietary, and other factors that influence the microbiome, immune system, and pathogenic mechanisms. The recent studies on molecular pathological epidemiology have provided a powerful tool which can pathologically, epidemiologically investigate those factors in relation to molecular pathologies, immunity, and clinical outcomes^[77], and it is believed that the molecular pathological epidemiology research can be a promising direction and in which OMT can take a big role.

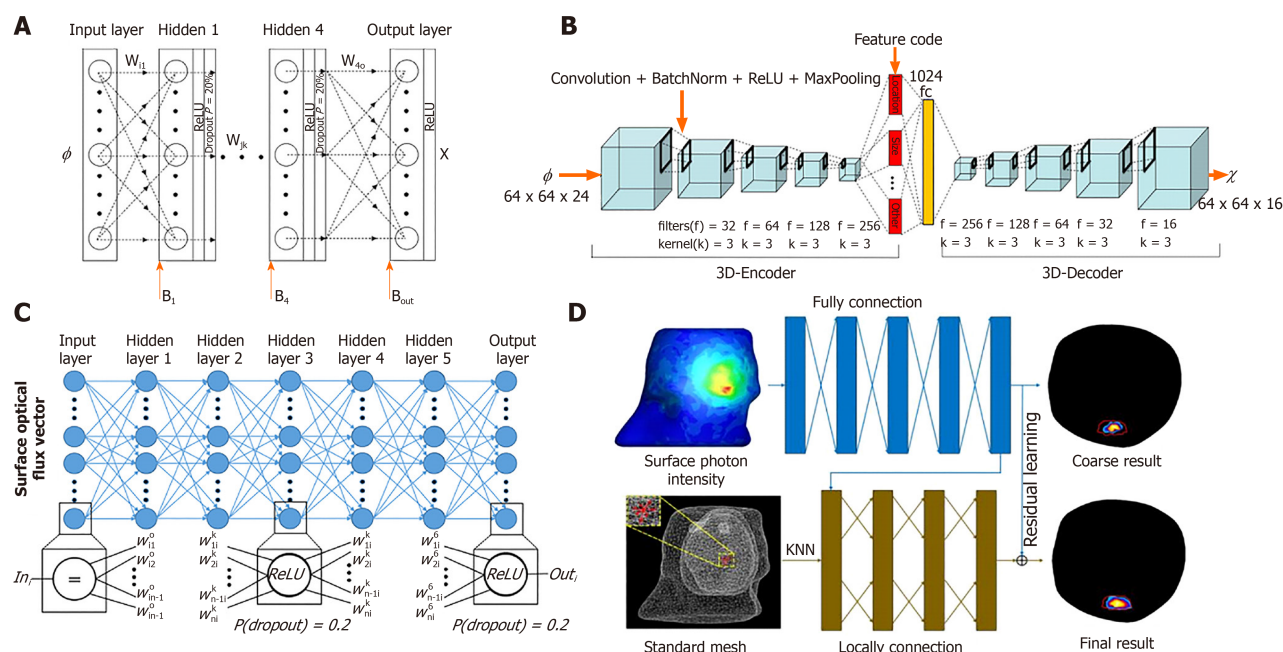


Figure 4 Structure of the networks used in optical molecular tomography reconstruction. A: Multilayer perceptron-based bioluminescence tomography reconstruction network reproduced from^[72]; B: Convolutional neural network-recurrent neural network-based fluorescence molecular tomography (FMT) reconstruction framework reproduced from^[74]; C: Multilayer fully-connected neural network based on Cerenkov luminescence tomography reproduced from^[75]; D: K-nearest neighbor-based locally connected network based on FMT reproduced from^[76].

REFERENCES

- 1 Weissleder R, Pittet MJ. Imaging in the era of molecular oncology. *Nature* 2008; **452**: 580-589 [PMID: 18385732 DOI: 10.1038/nature06917]
- 2 Nguyen QT, Tsien RY. Fluorescence-guided surgery with live molecular navigation--a new cutting edge. *Nat Rev Cancer* 2013; **13**: 653-662 [PMID: 23924645 DOI: 10.1038/nrc3566]
- 3 Hu Z, Qu Y, Wang K, Zhang X, Zha J, Song T, Bao C, Liu H, Wang Z, Wang J, Liu Z, Liu H, Tian J. In vivo nanoparticle-mediated radiopharmaceutical-excited fluorescence molecular imaging. *Nat Commun* 2015; **6**: 7560 [PMID: 26123615 DOI: 10.1038/ncomms8560]
- 4 Klose AD, Paragas N. Automated quantification of bioluminescence images. *Nat Commun* 2018; **9**: 4262 [PMID: 30323260 DOI: 10.1038/s41467-018-06288-w]
- 5 Thorek DL, Ogirala A, Beattie BJ, Grimm J. Quantitative imaging of disease signatures through radioactive decay signal conversion. *Nat Med* 2013; **19**: 1345-1350 [PMID: 24013701 DOI: 10.1038/nm.3323]
- 6 Zhang Z, Cai M, Bao C, Hu Z, Tian J. Endoscopic Cerenkov luminescence imaging and image-guided tumor resection on hepatocellular carcinoma-bearing mouse models. *Nanomedicine* 2019; **17**: 62-70 [PMID: 30654183 DOI: 10.1016/j.nano.2018.12.017]
- 7 Mitchell GS, Lloyd PNT, Cherry SR. Cerenkov luminescence and PET imaging of ⁹⁰Y: capabilities and limitations in small animal applications. *Phys Med Biol* 2020; **65**: 065006 [PMID: 32045899 DOI: 10.1088/1361-6560/ab7502]
- 8 Cao X, Zhan Y, Cao X, Liang J, Chen X. Harnessing the Power of Cerenkov Luminescence Imaging for Gastroenterology: Cerenkov Luminescence Endoscopy. *Curr Med Imaging Rev* 2017; **13**: 50-57 [DOI: 10.2174/1573405612666160607094334]
- 9 Cao X, Chen X, Kang F, Zhan Y, Cao X, Wang J, Liang J, Tian J. Intensity Enhanced Cerenkov Luminescence Imaging Using Terbium-Doped Gd₂O₃S Microparticles. *ACS Appl Mater Interfaces* 2015; **7**: 11775-11782 [PMID: 25992597 DOI: 10.1021/acsami.5b00432]
- 10 Cao X, Chen X, Kang F, Cao X, Zhan Y, Wang J, Wu K, Liang J. Sensitivity improvement of Cerenkov luminescence endoscope with terbium doped Gd₂O₃S nanoparticles. *Appl Phys Lett* 2015; **106**: 4 [DOI: 10.1063/1.4921858]
- 11 Cao X, Chen X, Kang F, Lin Y, Liu M, Hu H, Nie Y, Wu K, Wang J, Liang J, Tian J. Performance evaluation of endoscopic Cerenkov luminescence imaging system: in vitro and pseudotumor studies. *Biomed Opt Express* 2014; **5**: 3660-3670 [PMID: 25360380 DOI: 10.1364/BOE.5.003660]
- 12 Fan D, Zhang X, Zhong L, Liu X, Sun Y, Zhao H, Jia B, Liu Z, Zhu Z, Shi J, Wang F. (68)Ga-labeled 3PRGD2 for dual PET and Cerenkov luminescence imaging of orthotopic human glioblastoma. *Bioconjug Chem* 2015; **26**: 1054-1060 [PMID: 25853280 DOI: 10.1021/acs.bioconjchem.5b00169]
- 13 Gao Y, Wang K, Jiang S, Liu Y, Ai T, Tian J. Corrections to "Bioluminescence Tomography Based on Gaussian Weighted Laplace Prior Regularization for Morphological Imaging of Glioma". *IEEE Trans Med Imaging* 2018; **37**: 1733 [PMID: 29969423 DOI: 10.1109/TMI.2018.2845038]
- 14 Zhong J, Qin C, Yang X, Zhu S, Zhang X, Tian J. Cerenkov luminescence tomography for in vivo radiopharmaceutical imaging. *Int J Biomed Imaging* 2011; **2011**: 641618 [PMID: 21747821 DOI: 10.1155/2011/641618]
- 15 Zhang B, Liu S, Cao X, Liu F, Wang X, Luo J, Shan B, Bai J. Fluorescence Tomography Reconstruction

- With Simultaneous Positron Emission Tomography Priors. *IEEE Trans Multimedia* 2013; **15**: 1031-1038 [DOI: [10.1109/TMM.2013.2244205](https://doi.org/10.1109/TMM.2013.2244205)]
- 16 **Baritau JC**, Hassler K, Bucher M, Sanyal S, Unser M. Sparsity-driven reconstruction for FDOT with anatomical priors. *IEEE Trans Med Imaging* 2011; **30**: 1143-1153 [PMID: [21507771](https://pubmed.ncbi.nlm.nih.gov/21507771/)] DOI: [10.1109/TMI.2011.2136438](https://doi.org/10.1109/TMI.2011.2136438)]
 - 17 **Lewis MA**, Kodibagkar VD, Öz OK, Mason RP. On the potential for molecular imaging with Cerenkov luminescence. *Opt Lett* 2010; **35**: 3889-3891 [PMID: [21124555](https://pubmed.ncbi.nlm.nih.gov/21124555/)] DOI: [10.1364/OL.35.003889](https://doi.org/10.1364/OL.35.003889)]
 - 18 **Contag CH**, Bachmann MH. Advances in in vivo bioluminescence imaging of gene expression. *Annu Rev Biomed Eng* 2002; **4**: 235-260 [PMID: [12117758](https://pubmed.ncbi.nlm.nih.gov/12117758/)] DOI: [10.1146/annurev.bioeng.4.111901.093336](https://doi.org/10.1146/annurev.bioeng.4.111901.093336)]
 - 19 **Meng H**, Wang K, Gao Y, Jin Y, Ma X, Tian J. Adaptive Gaussian Weighted Laplace Prior Regularization Enables Accurate Morphological Reconstruction in Fluorescence Molecular Tomography. *IEEE Trans Med Imaging* 2019; **38**: 2726-2734 [PMID: [31021763](https://pubmed.ncbi.nlm.nih.gov/31021763/)] DOI: [10.1109/TMI.2019.2912222](https://doi.org/10.1109/TMI.2019.2912222)]
 - 20 **Guo H**, Hou Y, He X, Yu J, Cheng J, Pu X. Adaptive hp finite element method for fluorescence molecular tomography with simplified spherical harmonics approximation. *J Innov Opt Health Sci* 2014; **7**: 12 [DOI: [10.1142/S1793545813500570](https://doi.org/10.1142/S1793545813500570)]
 - 21 **Yi H**, Wei H, Peng J, Hou Y, He X. Adaptive threshold method for recovered images of FMT. *J Opt Soc Am A Opt Image Sci Vis* 2018; **35**: 256-261 [PMID: [29400892](https://pubmed.ncbi.nlm.nih.gov/29400892/)] DOI: [10.1364/JOSAA.35.000256](https://doi.org/10.1364/JOSAA.35.000256)]
 - 22 **Cai W**, Xu M, Alfano R. Three-dimensional radiative transfer tomography for turbid media. *IEEE J Sel Top Quantum Electron* 2003; **9**: 189-198 [DOI: [10.1109/JSTQE.2003.813312](https://doi.org/10.1109/JSTQE.2003.813312)]
 - 23 **Joshi A**, Rasmussen JC, Sevic-Muraca EM, Wareing TA, McGhee J. Radiative transport-based frequency-domain fluorescence tomography. *Phys Med Biol* 2008; **53**: 2069-2088 [PMID: [18364555](https://pubmed.ncbi.nlm.nih.gov/18364555/)] DOI: [10.1088/0031-9155/53/8/005](https://doi.org/10.1088/0031-9155/53/8/005)]
 - 24 **Gao H**, Zhao H. Multilevel bioluminescence tomography based on radiative transfer equation Part 1: 11 regularization. *Opt Express* 2010; **18**: 1854-1871 [PMID: [20174013](https://pubmed.ncbi.nlm.nih.gov/20174013/)] DOI: [10.1364/OE.18.001854](https://doi.org/10.1364/OE.18.001854)]
 - 25 **Klose AD**. The forward and inverse problem in tissue optics based on the radiative transfer equation: a brief review. *J Quant Spectrosc Radiat Transf* 2010; **111**: 1852-1853 [PMID: [20607145](https://pubmed.ncbi.nlm.nih.gov/20607145/)] DOI: [10.1016/j.jqsrt.2010.01.020](https://doi.org/10.1016/j.jqsrt.2010.01.020)]
 - 26 **Wang G**, Cong W, Durairaj K, Qian X, Shen H, Sinn P, Hoffman E, McLennan G, Henry M. In vivo mouse studies with bioluminescence tomography. *Opt Express* 2006; **14**: 7801-7809 [PMID: [19529149](https://pubmed.ncbi.nlm.nih.gov/19529149/)] DOI: [10.1364/OE.14.007801](https://doi.org/10.1364/OE.14.007801)]
 - 27 **Cong W**, Wang G, Kumar D, Liu Y, Jiang M, Wang L, Hoffman E, McLennan G, McCray P, Zabner J, Cong A. Practical reconstruction method for bioluminescence tomography. *Opt Express* 2005; **13**: 6756-6771 [PMID: [19498692](https://pubmed.ncbi.nlm.nih.gov/19498692/)] DOI: [10.1364/OPEX.13.006756](https://doi.org/10.1364/OPEX.13.006756)]
 - 28 **Li C**, Mitchell GS, Cherry SR. Cerenkov luminescence tomography for small-animal imaging. *Opt Lett* 2010; **35**: 1109-1111 [PMID: [20364233](https://pubmed.ncbi.nlm.nih.gov/20364233/)] DOI: [10.1364/OL.35.001109](https://doi.org/10.1364/OL.35.001109)]
 - 29 **Yang D**, Chen X, Cao X, Wang J, Liang J, Tian J. Performance investigation of SP3 and diffusion approximation for three-dimensional whole-body optical imaging of small animals. *Med Biol Eng Comput* 2015; **53**: 805-814 [PMID: [25850985](https://pubmed.ncbi.nlm.nih.gov/25850985/)] DOI: [10.1007/s11517-015-1293-8](https://doi.org/10.1007/s11517-015-1293-8)]
 - 30 **Zhong J**, Tian J, Yang X, Qin C. Whole-body Cerenkov luminescence tomography with the finite element SP(3) method. *Ann Biomed Eng* 2011; **39**: 1728-1735 [PMID: [21301961](https://pubmed.ncbi.nlm.nih.gov/21301961/)] DOI: [10.1007/s10439-011-0261-1](https://doi.org/10.1007/s10439-011-0261-1)]
 - 31 **Zhong J**, Tian J, Yang X, Qin C. L1-regularized Cerenkov luminescence tomography with a SP3 method and CT fusion. *Conf Proc IEEE Eng Med Biol Soc* 2011; **2011**: 6158-6161 [PMID: [22255745](https://pubmed.ncbi.nlm.nih.gov/22255745/)] DOI: [10.1109/IEMBS.2011.6091521](https://doi.org/10.1109/IEMBS.2011.6091521)]
 - 32 **Han D**, Tian J, Zhu S, Feng J, Qin C, Zhang B, Yang X. A fast reconstruction algorithm for fluorescence molecular tomography with sparsity regularization. *Opt Express* 2010; **18**: 8630-8646 [PMID: [20588707](https://pubmed.ncbi.nlm.nih.gov/20588707/)] DOI: [10.1364/OE.18.008630](https://doi.org/10.1364/OE.18.008630)]
 - 33 **Chen X**, Gao X, Chen D, Ma X, Zhao X, Shen M, Li X, Qu X, Liang J, Ripoll J, Tian J. 3D reconstruction of light flux distribution on arbitrary surfaces from 2D multi-photographic images. *Opt Express* 2010; **18**: 19876-19893 [PMID: [20940879](https://pubmed.ncbi.nlm.nih.gov/20940879/)] DOI: [10.1364/OE.18.019876](https://doi.org/10.1364/OE.18.019876)]
 - 34 **Han R**, Liang J, Qu X, Hou Y, Ren N, Mao J, Tian J. A source reconstruction algorithm based on adaptive hp-FEM for bioluminescence tomography. *Opt Express* 2009; **17**: 14481-14494 [PMID: [19687926](https://pubmed.ncbi.nlm.nih.gov/19687926/)] DOI: [10.1364/OE.17.014481](https://doi.org/10.1364/OE.17.014481)]
 - 35 **Lu Y**, Zhu B, Shen H, Rasmussen JC, Wang G, Sevic-Muraca EM. A parallel adaptive finite element simplified spherical harmonics approximation solver for frequency domain fluorescence molecular imaging. *Phys Med Biol* 2010; **55**: 4625-4645 [PMID: [20671350](https://pubmed.ncbi.nlm.nih.gov/20671350/)] DOI: [10.1088/0031-9155/55/16/002](https://doi.org/10.1088/0031-9155/55/16/002)]
 - 36 **Liu K**, Lu Y, Tian J, Qin C, Yang X, Zhu S, Yang X, Gao Q, Han D. Evaluation of the simplified spherical harmonics approximation in bioluminescence tomography through heterogeneous mouse models. *Opt Express* 2010; **18**: 20988-21002 [PMID: [20940994](https://pubmed.ncbi.nlm.nih.gov/20940994/)] DOI: [10.1364/OE.18.020988](https://doi.org/10.1364/OE.18.020988)]
 - 37 **Liu J**, Wang Y, Qu X, Li X, Ma X, Han R, Hu Z, Chen X, Sun D, Zhang R, Chen D, Chen D, Chen X, Liang J, Cao F, Tian J. In vivo quantitative bioluminescence tomography using heterogeneous and homogeneous mouse models. *Opt Express* 2010; **18**: 13102-13113 [PMID: [20588440](https://pubmed.ncbi.nlm.nih.gov/20588440/)] DOI: [10.1364/OE.18.013102](https://doi.org/10.1364/OE.18.013102)]
 - 38 **Baikejiang R**, Zhao Y, Fite BZ, Ferrara KW, Li C. Anatomical image-guided fluorescence molecular tomography reconstruction using kernel method. *J Biomed Opt* 2017; **22**: 55001 [PMID: [28464120](https://pubmed.ncbi.nlm.nih.gov/28464120/)] DOI: [10.1117/1.JBO.22.5.055001](https://doi.org/10.1117/1.JBO.22.5.055001)]
 - 39 **Holt RW**, Demers JL, Sexton KJ, Gunn JR, Davis SC, Samkoe KS, Pogue BW. Tomography of epidermal growth factor receptor binding to fluorescent Affibody in vivo studied with magnetic resonance guided fluorescence recovery in varying orthotopic glioma sizes. *J Biomed Opt* 2015; **20**: 26001 [PMID: [25652703](https://pubmed.ncbi.nlm.nih.gov/25652703/)] DOI: [10.1117/1.JBO.20.2.026001](https://doi.org/10.1117/1.JBO.20.2.026001)]
 - 40 **Davis SC**, Samkoe KS, Tichauer KM, Sexton KJ, Gunn JR, Deharvenst SJ, Hasan T, Pogue BW. Dynamic dual-tracer MRI-guided fluorescence tomography to quantify receptor density in vivo. *Proc Natl Acad Sci U S A* 2013; **110**: 9025-9030 [PMID: [23671066](https://pubmed.ncbi.nlm.nih.gov/23671066/)] DOI: [10.1073/pnas.1213490110](https://doi.org/10.1073/pnas.1213490110)]
 - 41 **Qin C**, Zhu S, Feng J, Zhong J, Ma X, Wu P, Tian J. Comparison of permissible source region and multispectral data using efficient bioluminescence tomography method. *J Biophotonics* 2011; **4**: 824-839 [PMID: [21987294](https://pubmed.ncbi.nlm.nih.gov/21987294/)] DOI: [10.1002/jbio.201100049](https://doi.org/10.1002/jbio.201100049)]
 - 42 **Ma X**, Tian J, Qin C, Yang X, Zhang B, Xue Z, Zhang X, Han D, Dong D, Liu X. Early detection of liver

- cancer based on bioluminescence tomography. *Appl Opt* 2011; **50**: 1389-1395 [PMID: [21460905](#) DOI: [10.1364/AO.50.001389](#)]
- 43 **Huang H**, Qu X, Liang J, He X, Chen X, Yang D, Tian J. A multi-phase level set framework for source reconstruction in bioluminescence tomography. *J Comput Phys* 2010; **229**: 5246-5256 [DOI: [10.1016/j.jcp.2010.03.041](#)]
 - 44 **Davis SC**, Samkoe KS, O'Hara JA, Gibbs-Strauss SL, Paulsen KD, Pogue BW. Comparing implementations of magnetic-resonance-guided fluorescence molecular tomography for diagnostic classification of brain tumors. *J Biomed Opt* 2010; **15**: 051602 [PMID: [21054076](#) DOI: [10.1117/1.3483902](#)]
 - 45 **Schulz RB**, Ale A, Sarantopoulos A, Freyer M, Soehngen E, Zientkowska M, Ntziachristos V. Hybrid system for simultaneous fluorescence and x-ray computed tomography. *IEEE Trans Med Imaging* 2010; **29**: 465-473 [PMID: [19906585](#) DOI: [10.1109/TMI.2009.2035310](#)]
 - 46 **Feng J**, Jia K, Yan G, Zhu S, Qin C, Lv Y, Tian J. An optimal permissible source region strategy for multispectral bioluminescence tomography. *Opt Express* 2008; **16**: 15640-15654 [PMID: [18825203](#) DOI: [10.1364/OE.16.015640](#)]
 - 47 **Hu Z**, Chen X, Liang J, Qu X, Chen D, Yang W, Wang J, Cao F, Tian J. Single photon emission computed tomography-guided Cerenkov luminescence tomography. *J Appl Phys* 2012; **112**: 024703 [DOI: [10.1063/1.4739266](#)]
 - 48 **Chehade M**, Srivastava AK, Bulte JW. Co-Registration of Bioluminescence Tomography, Computed Tomography, and Magnetic Resonance Imaging for Multimodal *In Vivo* Stem Cell Tracking. *Tomography* 2016; **2**: 159-165 [PMID: [27478872](#) DOI: [10.18383/j.tom.2016.00160](#)]
 - 49 **Zhang X**, Lu Y, Chan T. A novel sparsity reconstruction method from Poisson data for 3D bioluminescence tomography. *J Sci Comput* 2012; **50**: 519-535 [DOI: [10.1007/s10915-011-9533-z](#)]
 - 50 **Dutta J**, Ahn S, Li C, Cherry SR, Leahy RM. Joint L1 and total variation regularization for fluorescence molecular tomography. *Phys Med Biol* 2012; **57**: 1459-1476 [PMID: [22390906](#) DOI: [10.1088/0031-9155/57/6/1459](#)]
 - 51 **Liu K**, Tian J, Qin C, Yang X, Zhu S, Han D, Wu P. Tomographic bioluminescence imaging reconstruction via a dynamically sparse regularized global method in mouse models. *J Biomed Opt* 2011; **16**: 046016 [PMID: [21529085](#) DOI: [10.1117/1.3570828](#)]
 - 52 **Lu Y**, Zhang X, Douraghy A, Stout D, Tian J, Chan TF, Chatzioannou AF. Source reconstruction for spectrally-resolved bioluminescence tomography with sparse a priori information. *Opt Express* 2009; **17**: 8062-8080 [PMID: [19434138](#) DOI: [10.1364/OE.17.008062](#)]
 - 53 **Xu X**, Deng Z, Iordachita I, Wong J, Wang K. A Novel Multi-Projection Bioluminescence Tomography for Small Animal Radiation Research Platform (SARRP). *Med Phys* 2018; **45**: E393-E393
 - 54 **Guo H**, Gao L, Yu J, He X, Wang H, Zheng J, Yang X. Sparse-graph manifold learning method for bioluminescence tomography. *J Biophotonics* 2020; **13**: e201960218 [PMID: [31990430](#) DOI: [10.1002/jbio.201960218](#)]
 - 55 **Cai M**, Zhang Z, Shi X, Yang J, Hu Z, Tian J. Non-negative Iterative Convex Refinement Approach for Accurate and Robust Reconstruction in Cerenkov Luminescence Tomography. *IEEE Trans Med Imaging* 2020 [PMID: [32324543](#) DOI: [10.1109/TMI.2020.2987640](#)]
 - 56 **Wang L**, Cao H, Cao X, Ren S, Li K, Zhan Y, Chen X, He X. Adaptively Hybrid 3 Simplified Spherical Harmonics With Diffusion Equation-Based Multispectral Cerenkov Luminescence Tomography. *IEEE Access* 2019; **7**: 160779-160785 [DOI: [10.1109/ACCESS.2019.2950265](#)]
 - 57 **Pu H**, Gao P, Liu Y, Rong J, Shi F, Lu H. Principal Component Analysis Based Dynamic Cone Beam X-Ray Luminescence Computed Tomography: A Feasibility Study. *IEEE Trans Med Imaging* 2019; **38**: 2891-2902 [PMID: [31095480](#) DOI: [10.1109/TMI.2019.2917026](#)]
 - 58 **Liu X**, Tang X, Shu Y, Zhao L, Liu Y, Zhou T. Single-view cone-beam x-ray luminescence optical tomography based on Group_YALL1 method. *Phys Med Biol* 2019; **64**: 105004 [PMID: [30970336](#) DOI: [10.1088/1361-6560/ab1819](#)]
 - 59 **He X**, Xiang W, Yu J, Li Q. Penalty method for source reconstruction of multispectral bioluminescence tomography. *Opt Eng* 2018; **57**: 083104 [DOI: [10.1117/1.OE.57.8.083104](#)]
 - 60 **Guo H**, He X, Liu M, Zhang Z, Hu Z, Tian J. Weight Multispectral Reconstruction Strategy for Enhanced Reconstruction Accuracy and Stability With Cerenkov Luminescence Tomography. *IEEE Trans Med Imaging* 2017; **36**: 1337-1346 [PMID: [28182554](#) DOI: [10.1109/TMI.2017.2658661](#)]
 - 61 **Liu H**, Yang X, Song T, Bao C, Shi L, Hu Z, Wang K, Tian J. Multispectral hybrid Cerenkov luminescence tomography based on the finite element SPn method. *J Biomed Opt* 2015; **20**: 86007 [PMID: [26271053](#) DOI: [10.1117/1.JBO.20.8.086007](#)]
 - 62 **Spinelli AE**, Kuo C, Rice BW, Calandrino R, Marzola P, Sbarbati A, Boschi F. Multispectral Cerenkov luminescence tomography for small animal optical imaging. *Opt Express* 2011; **19**: 12605-12618 [PMID: [21716501](#) DOI: [10.1364/OE.19.012605](#)]
 - 63 **Li C**, Yang Y, Mitchell GS, Cherry SR. Simultaneous PET and multispectral 3-dimensional fluorescence optical tomography imaging system. *J Nucl Med* 2011; **52**: 1268-1275 [PMID: [21810591](#) DOI: [10.2967/jnumed.110.082859](#)]
 - 64 **Crane LM**, Themelis G, Pleijhuis RG, Harlaar NJ, Sarantopoulos A, Arts HJ, van der Zee AG, Ntziachristos V, van Dam GM. Intraoperative multispectral fluorescence imaging for the detection of the sentinel lymph node in cervical cancer: a novel concept. *Mol Imaging Biol* 2011; **13**: 1043-1049 [PMID: [20835767](#) DOI: [10.1007/s11307-010-0425-7](#)]
 - 65 **Chaudhari AJ**, Darvas F, Bading JR, Moats RA, Conti PS, Smith DJ, Cherry SR, Leahy RM. Hyperspectral and multispectral bioluminescence optical tomography for small animal imaging. *Phys Med Biol* 2005; **50**: 5421-5441 [PMID: [16306643](#) DOI: [10.1088/0031-9155/50/23/001](#)]
 - 66 **Tong S**, Han B, Chen Y, Tang J, Bi B, Gu R. RTE-based parameter reconstruction with TV+L1 regularization. *J Comput Appl Math* 2018; **337**: 256-273 [DOI: [10.1016/j.cam.2018.01.011](#)]
 - 67 **Yang D**, Wang L, Chen D, Yan C, He X, Liang J, Chen X. Filtered maximum likelihood expectation maximization based global reconstruction for bioluminescence tomography. *Med Biol Eng Comput* 2018; **56**: 2067-2081 [PMID: [29770920](#) DOI: [10.1007/s11517-018-1842-z](#)]
 - 68 **Gurovich Y**, Hanani Y, Bar O, Nadav G, Fleischer N, Gelbman D, Basel-Salmon L, Krawitz PM,

- Kamphausen SB, Zenker M, Bird LM, Gripp KW. Identifying facial phenotypes of genetic disorders using deep learning. *Nat Med* 2019; **25**: 60-64 [PMID: [30617323](#) DOI: [10.1038/s41591-018-0279-0](#)]
- 69 **Hannun AY**, Rajpurkar P, Haghighpanahi M, Tison GH, Bourn C, Turakhia MP, Ng AY. Cardiologist-level arrhythmia detection and classification in ambulatory electrocardiograms using a deep neural network. *Nat Med* 2019; **25**: 65-69 [PMID: [30617320](#) DOI: [10.1038/s41591-018-0268-3](#)]
- 70 **Moen E**, Bannon D, Kudo T, Graf W, Covert M, Van Valen D. Deep learning for cellular image analysis. *Nat Methods* 2019; **16**: 1233-1246 [PMID: [31133758](#) DOI: [10.1038/s41592-019-0403-1](#)]
- 71 **LeCun Y**, Bengio Y, Hinton G. Deep learning. *Nature* 2015; **521**: 436-444 [PMID: [26017442](#) DOI: [10.1038/nature14539](#)]
- 72 **Gao Y**, Wang K, An Y, Jiang S, Meng H, Tian J. Nonmodel-based bioluminescence tomography using a machine-learning reconstruction strategy. *Optica* 2018; **5**: 1451-1454 [DOI: [10.1364/OPTICA.5.001451](#)]
- 73 **Ren S**, Chen X, Wang H, Qu X, Wang G, Liang J, Tian J. Molecular Optical Simulation Environment (MOSE): a platform for the simulation of light propagation in turbid media. *PLoS One* 2013; **8**: e61304 [PMID: [23577215](#) DOI: [10.1371/journal.pone.0061304](#)]
- 74 **Guo L**, Liu F, Cai C, Liu J, Zhang G. 3D deep encoder-decoder network for fluorescence molecular tomography. *Opt Lett* 2019; **44**: 1892-1895 [PMID: [30985768](#) DOI: [10.1364/OL.44.001892](#)]
- 75 **Zhang Z**, Cai M, Gao Y, Shi X, Zhang X, Hu Z, Tian J. A novel Cerenkov luminescence tomography approach using multilayer fully connected neural network. *Phys Med Biol* 2019; **64**: 245010 [PMID: [31770734](#) DOI: [10.1088/1361-6560/ab5bb4](#)]
- 76 **Meng H**, Gao Y, Yang X, Wang K, Tian J. K-nearest Neighbor Based Locally Connected Network for Fast Morphological Reconstruction in Fluorescence Molecular Tomography. *IEEE Trans Med Imaging* 2020 [PMID: [32286961](#) DOI: [10.1109/TMI.2020.2984557](#)]
- 77 **Ogino S**, Lochhead P, Chan AT, Nishihara R, Cho E, Wolpin BM, Meyerhardt JA, Meissner A, Schernhammer ES, Fuchs CS, Giovannucci E. Molecular pathological epidemiology of epigenetics: emerging integrative science to analyze environment, host, and disease. *Mod Pathol* 2013; **26**: 465-484 [PMID: [23307060](#) DOI: [10.1038/modpathol.2012.214](#)]



Published by **Baishideng Publishing Group Inc**
7041 Koll Center Parkway, Suite 160, Pleasanton, CA 94566, USA

Telephone: +1-925-3991568

E-mail: bpgoffice@wjgnet.com

Help Desk: <https://www.f6publishing.com/helpdesk>

<https://www.wjgnet.com>



Artificial Intelligence in *Medical Imaging*

Artif Intell Med Imaging 2020 September 28; 1(3): 87-107





Artificial Intelligence in Medical Imaging

Contents

Bimonthly Volume 1 Number 3 September 28, 2020

EDITORIAL

- 87 Current trends of artificial intelligence in cancer imaging
Verde F, Romeo V, Stanzione A, Maurea S

ORIGINAL ARTICLE

Basic Study

- 94 Predicting a live birth by artificial intelligence incorporating both the blastocyst image and conventional embryo evaluation parameters
Miyagi Y, Habara T, Hirata R, Hayashi N

ABOUT COVER

Editorial board member of *Artificial Intelligence in Medical Imaging*, Ying-Kun Guo, MD is a Professor and Deputy Director of the Department of Radiology, West China Second University Hospital, Sichuan University (China). His career research has focused on cardiovascular imaging, pediatric radiology, and molecular and metabolic imaging. As an experienced radiologist, Dr. Guo's research achievements have been published in international professional journals, such as *JACC*, *Radiology*, *International Journal of Cardiology*, *Neuroimage*, and *Journal of Cardiac Magnetic Resonance*. Also, Professor Guo serves as PI of the Molecular Imaging Lab, which was established in 2015 and aims to develop novel molecular imaging in vivo, targeted nano-molecular probe, radiogenomics, and imaging contrast mechanisms, to evaluate emerging MRI sequences in animal models of human diseases, and to translate and apply innovative diagnostic imaging in clinic. (L-Editor: Filipodia)

AIMS AND SCOPE

The primary aim of *Artificial Intelligence in Medical Imaging* (AIMI, *Artif Intell Med Imaging*) is to provide scholars and readers from various fields of artificial intelligence in medical imaging with a platform to publish high-quality basic and clinical research articles and communicate their research findings online.

AIMI mainly publishes articles reporting research results obtained in the field of artificial intelligence in medical imaging and covering a wide range of topics, including artificial intelligence in radiology, pathology image analysis, endoscopy, molecular imaging, and ultrasonography.

INDEXING/ABSTRACTING

There is currently no indexing.

RESPONSIBLE EDITORS FOR THIS ISSUE

Production Editor: Jia-Hui Li; Production Department Director: Yun-Xiaojuan Wu; Editorial Office Director: Jin-Lei Wang.

NAME OF JOURNAL

Artificial Intelligence in Medical Imaging

ISSN

ISSN 2644-3260 (online)

LAUNCH DATE

June 28, 2020

FREQUENCY

Bimonthly

EDITORS-IN-CHIEF

Xue-Li Chen, Caroline Chung, Ahmed Abdel Khalek Abdel Razek, Jun Shen

EDITORIAL BOARD MEMBERS

<https://www.wjnet.com/2644-3260/editorialboard.htm>

PUBLICATION DATE

September 28, 2020

COPYRIGHT

© 2020 Baishideng Publishing Group Inc

INSTRUCTIONS TO AUTHORS

<https://www.wjnet.com/bpg/gerinfo/204>

GUIDELINES FOR ETHICS DOCUMENTS

<https://www.wjnet.com/bpg/GerInfo/287>

GUIDELINES FOR NON-NATIVE SPEAKERS OF ENGLISH

<https://www.wjnet.com/bpg/gerinfo/240>

PUBLICATION ETHICS

<https://www.wjnet.com/bpg/GerInfo/288>

PUBLICATION MISCONDUCT

<https://www.wjnet.com/bpg/gerinfo/208>

ARTICLE PROCESSING CHARGE

<https://www.wjnet.com/bpg/gerinfo/242>

STEPS FOR SUBMITTING MANUSCRIPTS

<https://www.wjnet.com/bpg/GerInfo/239>

ONLINE SUBMISSION

<https://www.f6publishing.com>

Current trends of artificial intelligence in cancer imaging

Francesco Verde, Valeria Romeo, Arnaldo Stanzione, Simone Maurea

ORCID number: Francesco Verde 0000-0002-9823-4678; Valeria Romeo 0000-0002-1603-6396; Arnaldo Stanzione 0000-0002-7905-5789; Simone Maurea 0000-0002-8269-3765.

Author contributions: Verde F drafted the manuscript; Romeo V conceptualized and drafted the manuscript; Stanzione A and Maurea S performed critical revision and approved the final manuscript.

Conflict-of-interest statement: The authors declare no conflicts of interest.

Open-Access: This article is an open-access article that was selected by an in-house editor and fully peer-reviewed by external reviewers. It is distributed in accordance with the Creative Commons Attribution NonCommercial (CC BY-NC 4.0) license, which permits others to distribute, remix, adapt, build upon this work non-commercially, and license their derivative works on different terms, provided the original work is properly cited and the use is non-commercial. See: <http://creativecommons.org/licenses/by-nc/4.0/>

Manuscript source: Invited manuscript

Received: August 23, 2020

Peer-review started: August 23,

Francesco Verde, Valeria Romeo, Arnaldo Stanzione, Simone Maurea, Department of Advanced Biomedical Sciences, University of Naples "Federico II", Napoli 80131, Italy

Corresponding author: Valeria Romeo, MD, PhD, Academic Research, Doctor, Research Fellow, Department of Advanced Biomedical Sciences, University of Naples "Federico II", Via S. Pansini 5, Napoli 80131, Italy. valeria.romeo@unina.it

Abstract

In this editorial, we discussed the current research status of artificial intelligence (AI) in Oncology, reviewing the basics of machine learning (ML) and deep learning (DL) techniques and their emerging applications on clinical and imaging cancer workflow. The growing amounts of available "big data" coupled to the increasing computational power have enabled the development of computer-based systems capable to perform advanced tasks in many areas of clinical care, especially in medical imaging. ML is a branch of data science that allows the creation of computer algorithms that can learn and make predictions without prior instructions. DL is a subgroup of artificial neural network algorithms configured to automatically extract features and perform high-level tasks; convolutional neural networks are the most common DL models used in medical image analysis. AI methods have been proposed in many areas of oncology granting promising results in radiology-based clinical applications. In detail, we explored the emerging applications of AI in oncological risk assessment, lesion detection, characterization, staging, and therapy response. Critical issues such as the lack of reproducibility and generalizability need to be addressed to fully implement AI systems in clinical practice. Nevertheless, AI impact on cancer imaging has been driving the shift of oncology towards a precision diagnostics and personalized cancer treatment.

Key Words: Artificial intelligence; Machine learning; Deep learning; Oncology; Medical imaging; Cancer imaging

©The Author(s) 2020. Published by Baishideng Publishing Group Inc. All rights reserved.

Core Tip: Advanced computational systems and availability of multi-dimensional data have led the possibility of artificial intelligence (AI) consisting of machine learning (ML) and deep learning (DL) algorithms to be implemented in healthcare data analysis, with reliable results in the oncology field and particularly in diagnostic imaging tasks. Supervised algorithms are the most common ML models used in medical image analysis, while

2020

First decision: September 13, 2020**Revised:** September 22, 2020**Accepted:** September 23, 2020**Article in press:** September 23, 2020**Published online:** September 28, 2020**P-Reviewer:** Abdel Razek AAK,
Ogino S, Ren J, Wang RF**S-Editor:** Wang JL**L-Editor:** A**P-Editor:** Li JH

convolutional neural networks are the main DL approach. AI-based models have demonstrated outperforming results in oncological risk assessment, lesion detection, segmentation, characterization, staging, and therapy response. Growing emerging evidence supports the leading role of AI in all cancer imaging pathways from screening programs to diagnostic and prognostic tasks, boosting the paradigm of precision medicine.

Citation: Verde F, Romeo V, Stanzione A, Maurea S. Current trends of artificial intelligence in cancer imaging. *Artif Intell Med Imaging* 2020; 1(3): 87-93

URL: <https://www.wjgnet.com/2644-3260/full/v1/i3/87.htm>

DOI: <https://dx.doi.org/10.35711/aimi.v1.i3.87>

INTRODUCTION

In this new era of health-related technology and medical advances, artificial intelligence (AI) has put down roots making it possible to teach computers to do an intelligence human task, thus emerging as a problem-solving tool in data analysis and improving many aspects of clinical care^[1,2].

Machine learning (ML) is a subset of AI that develops computer algorithms to make predictions or decision tasks without prior explicit programmed rules. ML algorithms use iterative static methods learning from “training” data to progressively improve the model performance over time. Based on the type of learning, ML is generally divided in (1) supervised learning, which uses labelled training data to map the expected outputs; (2) unsupervised learning, which deploys unlabelled data to learn new patterns; and (3) reinforcement learning, considered as a subfield of ML using reinforcement tools in a dynamic setting^[3] (Figure 1). The supervised method is the most used ML technique in medical imaging applications and, relying on the relationship between input features and expected outcomes, the ML algorithms are grouped into three broad categories: Linear, Nonlinear and Ensemble, as described in Table 1. Furthermore, based on the data features exploited by the algorithms, ML can be applied to handcrafted features as predefined features in the data set, or to non-handcrafted features, involving raw data as part of the learning process^[4]. Deep learning (DL), is a subgroup of ML techniques using non-handcrafted features and it is composed of artificial neural networks (ANN) modelled as neuron multi-layered networks allowing to automatically extract features without prior labelling and perform high-level tasks^[5]. The most common ANN used in medical image analysis is based on convolutional architecture [convolutional neural networks (CNN)], consisting of hidden multi-layers that compute and filter high dimensional data to obtain the correct outputs, such as detection and characterization of tumoral lesions on imaging examinations^[6].

AI-based approaches have been investigated in many fields of oncology, from imaging to histopathological and molecular diagnosis. Indeed, encouraging results have been obtained in cancer imaging, especially in screening environments. Among the different available imaging modalities, computed tomography (CT) and magnetic resonance imaging (MRI) are the most widely employed due to their prominent role in oncologic patients for staging, treatment monitoring and follow-up. Moreover, the introduction of advanced imaging techniques such as perfusion CT, MRI and MRI-diffusion-weighted imaging could provide the addition of functional over morphological data to further characterize tumor phenotype and behavior. Of note, radiology and oncology share the need for precision diagnosis and prediction models, by using cross-valuable multiple parameters from medical images and clinical data. The current applications of AI in cancer imaging include the optimization of the clinical-radiological workflow (patient screening, image acquisition) and also more specific image-based tasks (cancer detection, characterization, and treatment monitoring).

In the next sections we introduce the possible applications of AI in oncology imaging (Table 2).

Clinical-radiological workflow empowerment

AI techniques can enable the aggregation of clinical and imaging data to improve screening programs' efficiency, due to the possibility to analyse a large volume of different types of data including clinical risk factors, genetic data, and imaging

Table 1 Most commonly adopted algorithms in supervised machine learning

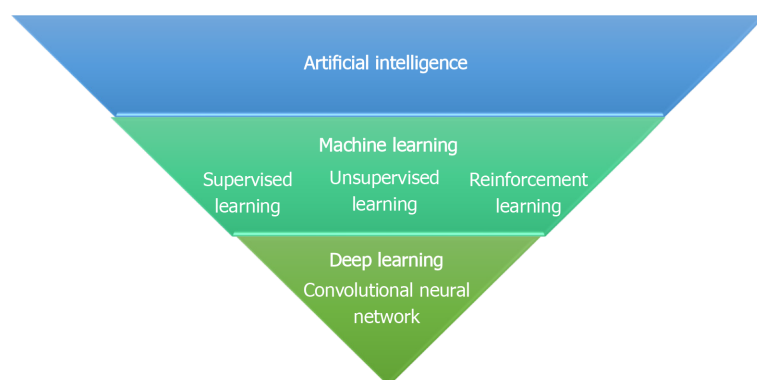
ML technique	ML algorithms	Description
Linear	(1) Linear regression; and (2) Logistic regression	Linear methods are used to modelling the relationship between the dependent variable and one or more independent variables
Nonlinear	(1) Naive Bayes; (2) Decision tree; (3) k-Nearest Neighbors; (4) Support vector machines; and (5) Neural network	Nonlinear approaches are used to produce predictive insights depending on nonlinear relationships in experimental data
Ensemble	(1) Random forest; (2) Bootstrap aggregation; and (3) Stacked generalization	Ensemble techniques stack multiple models in order to improve prediction robustness and provide more accurate predictions than any individual model

ML: Machine learning.

Table 2 Possible clinical applications of artificial intelligence in oncological imaging

Clinical application	Oncologic field	Imaging modality	AI technique
Clinical-radiological workflow	Breast cancer ^[9]	Mammography	ML
	Image acquisition ^[10,11]	CT, MRI	DL
Cancer detection	Breast cancer ^[12,13]	Mammography	DL
	Lung cancer ^[14]	X-Ray, CT	DL
Tumor segmentation	Breast Cancer ^[17,18]	MRI	DL
Tumor characterization	Adrenal cancer ^[20]	MRI	ML
	Renal cancer ^[21]	MRI	ML
	Lung cancer ^[22]	CT	ML
Tumor staging	Head and neck cancer ^[23]	CT	ML
	Endometrial cancer ^[24]	MRI	ML
Treatment monitoring	Breast cancer ^[26]	MRI	ML

CT: Computed tomography; MRI: Magnetic resonance imaging; AI: Artificial intelligence; ML: Machine learning; DL: Deep learning.

**Figure 1 Diagram showing different categories of artificial intelligence.**

examinations. Breast cancer surely represents a leading area of AI development, in particular in screening practices as demonstrated by recent studies that explored the impact on clinical practice of ML model in identifying individuals at increased risk of breast cancer^[7,8]. Indeed, a recent study of Ming *et al*^[9] investigated the performance of different ML-based techniques in predicting breast cancer risk using clinical and genetic risk factors in comparison to the Breast and Ovarian Analysis of Disease Incidence and Carrier Estimation Algorithm (BOADICEA) risk prediction model; decision ML-based models yielded better results in classifying cancer from non-cancer cases and increased the predictive accuracy by 20%-25% including equal risk factors

used in the BOADICEA model. Moreover, considerable differences between the BOADICEA and risk-based ML models were observed in terms of classification for mammography surveillance according to the Swiss Surveillance Protocol, confirming the feasibility of ML prediction models in the clinical-imaging decision workflow^[9].

Regarding imaging acquisition and pre-processing, DL methods have shown an important impact on the reduction of radiation dose in CT examinations^[10] and have been used for improving magnetic resonance imaging quality with the potential to decrease acquisition time^[11].

Cancer detection

Recent evidences of AI applications include breast cancer detection in mammography, tomosynthesis, and MRI as well as identification of CT lung nodes, brain tumors, and prostate cancer on MRI.

Among these, mammographic detection of breast cancer represents a challenging image analysis task because breast cancer could be masked by healthy breast tissue. In a recent study^[12], a DL AI system provided by Google Health company outperformed the radiologists involved in the mammographic screening from multiple centres in the United Kingdom (UK) and United States (US). The AI system yielded absolute reductions of 1.2% and 2.7% in false-positive and false-negative rates, respectively, in the UK test set and 5.7% and 9.4% in the US dataset. Moreover, the AI system exceeded the average performance of six expert radiologists who interpreted a sample of 500 randomly selected cases in a controlled study^[12]. Similarly, Rodríguez-Ruiz *et al*^[13] demonstrated that radiologists improved their diagnostic performance in detecting breast cancer on screening mammography examinations with the use of a DL-based AI system. In detail, the authors observed that radiologists improved their average area under the receiver operating characteristic curve (AUC) from 0.87 to 0.89 ($P = 0.002$).

In the field of lung cancer, recent research showed that a DL automatic detection algorithm achieved higher performance than the radiologist group in the detection of malignant pulmonary nodules on chest radiographs; moreover, radiologists' performance improved when DL algorithm was used as a second reader^[14].

Tumor segmentation, characterization and staging

Segmentation represents one of the most challenging tasks of oncological image analysis and AI algorithms have allowed the development of systems that can enable automatic tumor segmentation. Recently, DL networks, such as CNN, have been applied in segmentation tasks gaining accurate results regarding radiotherapy treatment planning, volume measurements and, monitoring disease progression^[15,16]. Indeed, increasing evidence in recent literature has highlighted the high performance of DL models in performing fully automated whole-breast segmentation to obtain reliable and robust methods for quantitative imaging analysis^[17,18].

High-performance levels of AI algorithms in handling multi-dimensional data have allowed extracting and analyzing radiomic biomarkers reflecting image tumor heterogeneity thus empowering precision diagnosis and staging in cancer imaging^[19] (Figure 2). For instance, with our research group, we used a combined model of MRI radiomic features and ML analysis to differentiate typical and atypical adenomas from non-adenoma adrenal lesions, which showed a better performance than the radiologist assessment^[20]. Further, our group assessed the usefulness of an ML-based radiomic approach applied to MR imaging to differentiate high- from low-grade clear cell renal cell carcinoma achieving accuracy greater than 90%^[21]. Reliable results and robust evidence have been providing in lung cancer diagnosis as showed in a recent work of Beig *et al*^[22], which proposed a radiomic-based ML algorithm using non-contrast lung CT to distinguish non-small cell lung cancer adenocarcinomas from benign granuloma, resulting with outperforming results of AI system in comparison to the radiologists' evaluation (accuracy = 75% *vs* 61%).

Staging represents a crucial point of the oncological workflow to delineate the most appropriate treatment in a personalized and precision way. In this view, recent pilot studies have been carried out on the staging of primary tumor size, lymph nodes involvement, and distant metastasis^[23]. For example, our group investigated the clinical feasibility of a combined approach of radiomics and ML-based on MR images for the identification of deep myometrial invasion in endometrial cancer in a clinical context; indeed, the integration of the developed ML algorithm improved radiologist accuracy from 82% to 100%^[24].

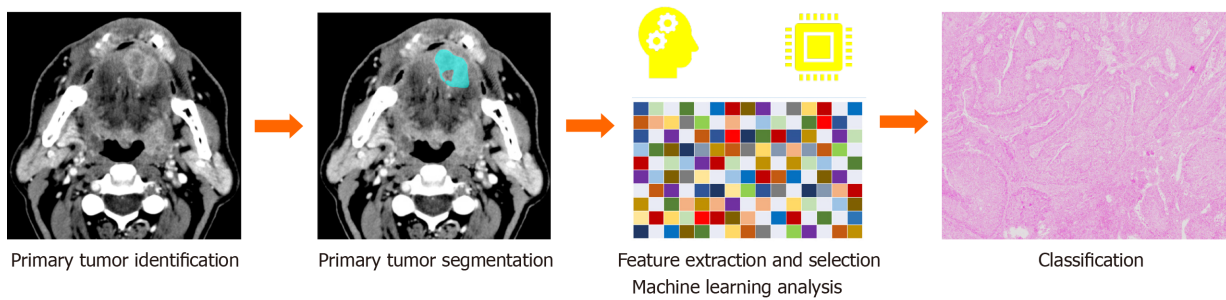


Figure 2 A schematic diagram of a radiomic and machine learning workflow pipeline applied to contrast-enhanced computed tomography images.

Treatment monitoring

Temporal follow-up of tumors as well as the treatment response are active fields of research of AI technology to find accurate models for evaluation of efficient anticancer therapies that increase the progression-free survival of patients. In this regard, excellent results have been obtained using AI radiomics MRI-based models in predicting survival and recurrence-free survival in breast cancer^[25]. Moreover, the development of AI models has been explored in breast cancer imaging to assess predictive image-based phenotypes for precision medicine, in particular to predict the response to neoadjuvant chemotherapy (NAC). In a recent study, Sutton *et al*^[26] explored the usefulness of a combined radiomics MRI-based and molecular subtype-based ML model in assessing the complete pathological response (pCR) to NAC; their AI model accurately predicted pCR on MRI with an AUC of 0.88 and showed that the performance in predicting pCR increased when radiomics features were combined with molecular subtype in comparison of the solely molecular subtype results^[26].

CHALLENGES AND FUTURE DIRECTIONS

AI techniques still have to face some issues to be incorporated in clinical practice. Of note, large datasets containing annotated images are needed for training of DL algorithms, but standardized imaging workflow lacks^[15]. Complex AI functions are not easily interpreted by healthcare providers, and this “black box” nature could affect the acceptance of AI programs, also from the ethical and legal points of view^[27]. Moreover, variability across multi-center and multi-vendor should be addressed with future studies sharing more reliable and robust validation^[28].

Despite these drawbacks, AI incorporation into cancer imaging has been boosting the shift of oncology towards a precision diagnostics and personalized cancer treatment. Indeed, as previously discussed, recent literature evidence pointed out the emerging role of AI in supporting all cancer imaging pathways from screening programs to diagnostic and prognostic tasks, offering new methods to increase radiologists’ performance in order to improve oncological care environment. Furthermore, the integration of AI into molecular pathological epidemiology can aid in developing pathologic signatures to stratify patients’ risk and predict biological tumor behavior by using clinical, radiological and pathological data^[29]. In the future, collaborations between different expertise figures, such as oncologists, epidemiologists, radiologists, pathologists and data scientists, should be encouraged to achieve harmonized and integrated development of AI systems in cancer research.

CONCLUSION

We have provided an overview of AI integration in cancer imaging, focusing on the basics of this disruptive technology and on the significant results obtained in improving clinical and radiological workup for oncological patients. Although, more evidence is still demanding the outlook of AI in cancer imaging remains bright.

REFERENCES

- Lakhani P, Prater AB, Hutson RK, Andriole KP, Dreyer KJ, Morey J, Prevedello LM, Clark TJ, Geis JR, Itri JN, Hawkins CM. Machine Learning in Radiology: Applications Beyond Image Interpretation. *J Am Coll Radiol* 2018; **15**: 350-359 [PMID: 29158061 DOI: 10.1016/j.jacr.2017.09.044]
- Verde F, Stanzione A, Romeo V, Cuocolo R, Maurea S, Brunetti A. Could Blockchain Technology Empower Patients, Improve Education, and Boost Research in Radiology Departments? *J Digit Imaging* 2019; **32**: 1112-1115 [PMID: 31197561 DOI: 10.1007/s10278-019-00246-8]
- Choy G, Khalilzadeh O, Michalski M, Do S, Samir AE, Pianykh OS, Geis JR, Pandharipande PV, Brink JA, Dreyer KJ. Current Applications and Future Impact of Machine Learning in Radiology. *Radiology* 2018; **288**: 318-328 [PMID: 29944078 DOI: 10.1148/radiol.2018171820]
- Goldenberg SL, Nir G, Salcudean SE. A new era: artificial intelligence and machine learning in prostate cancer. *Nat Rev Urol* 2019; **16**: 391-403 [PMID: 31092914 DOI: 10.1038/s41585-019-0193-3]
- Yang YJ, Bang CS. Application of artificial intelligence in gastroenterology. *World J Gastroenterol* 2019; **25**: 1666-1683 [PMID: 31011253 DOI: 10.3748/wjg.v25.i14.1666]
- Chartrand G, Cheng PM, Vorontsov E, Drozdal M, Turcotte S, Pal CJ, Kadoury S, Tang A. Deep Learning: A Primer for Radiologists. *Radiographics* 2017; **37**: 2113-2131 [PMID: 29131760 DOI: 10.1148/rg.2017170077]
- Sheth D, Giger ML. Artificial intelligence in the interpretation of breast cancer on MRI. *J Magn Reson Imaging* 2020; **51**: 1310-1324 [PMID: 31343790 DOI: 10.1002/jmri.26878]
- Ming C, Viassolo V, Probst-Hensch N, Chappuis PO, Dinov ID, Katapodi MC. Machine learning techniques for personalized breast cancer risk prediction: comparison with the BCRAT and BOADICEA models. *Breast Cancer Res* 2019; **21**: 75 [PMID: 31221197 DOI: 10.1186/s13058-019-1158-4]
- Ming C, Viassolo V, Probst-Hensch N, Dinov ID, Chappuis PO, Katapodi MC. Machine learning-based lifetime breast cancer risk reclassification compared with the BOADICEA model: impact on screening recommendations. *Br J Cancer* 2020; **123**: 860-867 [PMID: 32565540 DOI: 10.1038/s41416-020-0937-0]
- Greffier J, Hamard A, Pereira F, Barrau C, Pasquier H, Beregi JP, Frandon J. Image quality and dose reduction opportunity of deep learning image reconstruction algorithm for CT: a phantom study. *Eur Radiol* 2020; **30**: 3951-3959 [PMID: 32100091 DOI: 10.1007/s00330-020-06724-w]
- Montagnon E, Cerny M, Cadrin-ChÃnevert A, Hamilton V, Derennes T, Ilinca A, Vandenbroucke-Menu F, Turcotte S, Kadoury S, Tang A. Deep learning workflow in radiology: a primer. *Insights Imaging* 2020; **11**: 22 [PMID: 32040647 DOI: 10.1186/s13244-019-0832-5]
- McKinney SM, Sieniek M, Godbole V, Godwin J, Antropova N, Ashrafian H, Back T, Chesus M, Corrado GC, Darzi A, Etemadi M, Garcia-Vicente F, Gilbert FJ, Halling-Brown M, Hassabis D, Jansen S, Karthikesalingam A, Kelly CJ, King D, Ledam JR, Melnick D, Mostofi H, Peng L, Reicher JJ, Romera-Paredes B, Sidebottom R, Suleyman M, Tse D, Young KC, De Fauw J, Shetty S. International evaluation of an AI system for breast cancer screening. *Nature* 2020; **577**: 89-94 [PMID: 31894144 DOI: 10.1038/s41586-019-1799-6]
- RodrÃguez-Ruiz A, Krupinski E, Mordang JJ, Schilling K, Heywang-KÃrbrunner SH, Sechopoulos I, Mann RM. Detection of Breast Cancer with Mammography: Effect of an Artificial Intelligence Support System. *Radiology* 2019; **290**: 305-314 [PMID: 30457482 DOI: 10.1148/radiol.2018181371]
- Nam JG, Park S, Hwang EJ, Lee JH, Jin KN, Lim KY, Vu TH, Sohn JH, Hwang S, Goo JM, Park CM. Development and Validation of Deep Learning-based Automatic Detection Algorithm for Malignant Pulmonary Nodules on Chest Radiographs. *Radiology* 2019; **290**: 218-228 [PMID: 30251934 DOI: 10.1148/radiol.2018180237]
- Cuocolo R, Caruso M, Perillo T, Ugga L, Petretta M. Machine Learning in oncology: A clinical appraisal. *Cancer Lett* 2020; **481**: 55-62 [PMID: 32251707 DOI: 10.1016/j.canlet.2020.03.032]
- Deig CR, Kanwar A, Thompson RF. Artificial Intelligence in Radiation Oncology. *Hematol Oncol Clin North Am* 2019; **33**: 1095-1104 [PMID: 31668208 DOI: 10.1016/j.hoc.2019.08.003]
- Zhang L, Mohamed AA, Chai R, Guo Y, Zheng B, Wu S. Automated deep learning method for whole-breast segmentation in diffusion-weighted breast MRI. *J Magn Reson Imaging* 2020; **51**: 635-643 [PMID: 31301201 DOI: 10.1002/jmri.26860]
- Zhang Y, Chen JH, Chang KT, Park VY, Kim MJ, Chan S, Chang P, Chow D, Luk A, Kwong T, Su MY. Automatic Breast and Fibroglandular Tissue Segmentation in Breast MRI Using Deep Learning by a Fully-Convolutional Residual Neural Network U-Net. *Acad Radiol* 2019; **26**: 1526-1535 [PMID: 30713130 DOI: 10.1016/j.acra.2019.01.012]
- Gitto S, Cuocolo R, Albano D, Chianca V, Messina C, Gambino A, Ugga L, Cortese MC, Lazzara A, Ricci D, Spairani R, Zanchetta E, Luzzati A, Brunetti A, Parafioriti A, Sconfienza LM. MRI radiomics-based machine-learning classification of bone chondrosarcoma. *Eur J Radiol* 2020; **128**: 109043 [PMID: 32438261 DOI: 10.1016/j.ejrad.2020.109043]
- Romeo V, Maurea S, Cuocolo R, Petretta M, Mainenti PP, Verde F, Coppola M, Dell'Aversana S, Brunetti A. Characterization of Adrenal Lesions on Unenhanced MRI Using Texture Analysis: A Machine-Learning Approach. *J Magn Reson Imaging* 2018; **48**: 198-204 [PMID: 29341325 DOI: 10.1002/jmri.25954]
- Stanzione A, Ricciardi C, Cuocolo R, Romeo V, Petrone J, Sarnataro M, Mainenti PP, Improta G, De Rosa F, Insabato L, Brunetti A, Maurea S. MRI Radiomics for the Prediction of Fuhrman Grade in Clear Cell Renal Cell Carcinoma: a Machine Learning Exploratory Study. *J Digit Imaging* 2020 [PMID: 32314070 DOI: 10.1007/s10278-020-00336-y]
- Beig N, Khorrami M, Alilou M, Prasanna P, Braman N, Orooji M, Rakshit S, Bera K, Rajiah P, Ginsberg J, Donatelli C, Thawani R, Yang M, Jacono F, Tiwari P, Velcheti V, Gilkeson R, Linden P, Madabhushi A. Perinodular and Intranodular Radiomic Features on Lung CT Images Distinguish Adenocarcinomas from Granulomas. *Radiology* 2019; **290**: 783-792 [PMID: 30561278 DOI: 10.1148/radiol.2018180910]
- Romeo V, Cuocolo R, Ricciardi C, Ugga L, Cocozza S, Verde F, Stanzione A, Napolitano V, Russo D, Improta G, Elefante A, Staibano S, Brunetti A. Prediction of Tumor Grade and Nodal Status in Oropharyngeal and Oral Cavity Squamous-cell Carcinoma Using a Radiomic Approach. *Anticancer Res*

- 2020; **40**: 271-280 [PMID: [31892576](#) DOI: [10.21873/anticancerres.13949](#)]
- 24 **Stanzione A**, Cuocolo R, Del Grosso R, Nardiello A, Romeo V, Travaglino A, Raffone A, Bifulco G, Zullo F, Insabato L, Maurea S, Mainenti PP. Deep Myometrial Infiltration of Endometrial Cancer on MRI: A Radiomics-Powered Machine Learning Pilot Study. *Acad Radiol* 2020 [PMID: [32229081](#) DOI: [10.1016/j.acra.2020.02.028](#)]
 - 25 **Reig B**, Heacock L, Geras KJ, Moy L. Machine learning in breast MRI. *J Magn Reson Imaging* 2020; **52**: 998-1018 [PMID: [31276247](#) DOI: [10.1002/jmri.26852](#)]
 - 26 **Sutton EJ**, Onishi N, Fehr DA, Dashevsky BZ, Sadinski M, Pinker K, Martinez DF, Brogi E, Braunstein L, Razavi P, El-Tamer M, Sacchini V, Deasy JO, Morris EA, Veeraraghavan H. A machine learning model that classifies breast cancer pathologic complete response on MRI post-neoadjuvant chemotherapy. *Breast Cancer Res* 2020; **22**: 57 [PMID: [32466777](#) DOI: [10.1186/s13058-020-01291-w](#)]
 - 27 **Carter SM**, Rogers W, Win KT, Frazer H, Richards B, Houssami N. The ethical, legal and social implications of using artificial intelligence systems in breast cancer care. *Breast* 2020; **49**: 25-32 [PMID: [31677530](#) DOI: [10.1016/j.breast.2019.10.001](#)]
 - 28 **Thrall JH**, Li X, Li Q, Cruz C, Do S, Dreyer K, Brink J. Artificial Intelligence and Machine Learning in Radiology: Opportunities, Challenges, Pitfalls, and Criteria for Success. *J Am Coll Radiol* 2018; **15**: 504-508 [PMID: [29402533](#) DOI: [10.1016/j.jacr.2017.12.026](#)]
 - 29 **Ogino S**, Nowak JA, Hamada T, Milner DA Jr, Nishihara R. Insights into Pathogenic Interactions Among Environment, Host, and Tumor at the Crossroads of Molecular Pathology and Epidemiology. *Annu Rev Pathol* 2019; **14**: 83-103 [PMID: [30125150](#) DOI: [10.1146/annurev-pathmechdis-012418-012818](#)]



Basic Study

Predicting a live birth by artificial intelligence incorporating both the blastocyst image and conventional embryo evaluation parameters

Yasunari Miyagi, Toshihiro Habara, Rei Hirata, Nobuyoshi Hayashi

ORCID number: Yasunari Miyagi 0000-0003-0962-033X; Toshihiro Habara 0000-0003-3853-8044; Rei Hirata 0000-0002-2248-4224; Nobuyoshi Hayashi 0000-0001-6576-3066.

Author contributions: Miyagi Y, Habara T, R Hirata, and Hayashi N designed and coordinated the study; Miyagi Y and Hayashi N supervised the project; Habara T, and R Hirata acquired and validated data; Miyagi Y developed artificial intelligence software, analyzed and interpreted data, and wrote draft; Hayashi N set up project administration; Miyagi Y, Habara T, R Hirata, and Hayashi N wrote the manuscript; and all authors approved the final version of the article.

Institutional review board statement: The study was reviewed and approved by the Institutional Review Board at Okayama Couples' Clinic.

Conflict-of-interest statement: The authors declare no conflict of interest.

Data sharing statement: No informed consent was not obtained for data sharing. No additional data are available.

Open-Access: This article is an

Yasunari Miyagi, Department of Artificial Intelligence, Medical Data Labo, Okayama 703-8267, Japan

Yasunari Miyagi, Department of Gynecologic Oncology, Saitama Medical University International Medical Center, Hidaka 350-1298, Saitama, Japan

Toshihiro Habara, Rei Hirata, Nobuyoshi Hayashi, Department of Reproduction, Okayama Couples' Clinic, Okayama 701-1152, Japan

Corresponding author: Yasunari Miyagi, MD, PhD, Director, Professor, Surgeon, Department of Artificial Intelligence, Medical Data Labo, 289-48 Yamasaki, Naka ward, Okayama 703-8267, Japan. ymiyagi@mac.com

Abstract

BACKGROUND

The achievement of live birth is the goal of assisted reproductive technology in reproductive medicine. When the selected blastocyst is transferred to the uterus, the degree of implantation of the blastocyst is evaluated by microscopic inspection, and the result is only about 30%-40%, and the method of predicting live birth from the blastocyst image is unknown. Live births correlate with several clinical conventional embryo evaluation parameters (CEE), such as maternal age. Therefore, it is necessary to develop artificial intelligence (AI) that combines blastocyst images and CEE to predict live births.

AIM

To develop an AI classifier for blastocyst images and CEE to predict the probability of achieving a live birth.

METHODS

A total of 5691 images of blastocysts on the fifth day after oocyte retrieval obtained from consecutive patients from January 2009 to April 2017 with fully deidentified data were retrospectively enrolled with explanations to patients and a website containing additional information with an opt-out option. We have developed a system in which the original architecture of the deep learning neural network is used to predict the probability of live birth from a blastocyst image and CEE.

RESULTS

open-access article that was selected by an in-house editor and fully peer-reviewed by external reviewers. It is distributed in accordance with the Creative Commons Attribution NonCommercial (CC BY-NC 4.0) license, which permits others to distribute, remix, adapt, build upon this work non-commercially, and license their derivative works on different terms, provided the original work is properly cited and the use is non-commercial. See: <http://creativecommons.org/licenses/by-nc/4.0/>

Manuscript source: Invited manuscript

Received: August 24, 2020

Peer-review started: August 24, 2020

First decision: September 13, 2020

Revised: September 19, 2020

Accepted: September 19, 2020

Article in press: September 19, 2020

Published online: September 28, 2020

P-Reviewer: Boon CS, Hou Y, Karmazanovsky GG

S-Editor: Wang JL

L-Editor: A

P-Editor: Li JH



The live birth rate was 0.387 (= 1587/4104 cases). The number of independent clinical information for predicting live birth is 10, which significantly avoids multicollinearity. A single AI classifier is composed of ten layers of convolutional neural networks, and each elementwise layer of ten factors is developed and obtained with 42792 as the number of training data points and 0.001 as the L2 regularization value. The accuracy, sensitivity, specificity, negative predictive value, positive predictive value, Youden J index, and area under the curve values for predicting live birth are 0.743, 0.638, 0.789, 0.831, 0.573, 0.427, and 0.740, respectively. The optimal cut-off point of the receiver operator characteristic curve is 0.207.

CONCLUSION

AI classifiers have the potential of predicting live births that humans cannot predict. Artificial intelligence may make progress in assisted reproductive technology.

Key Words: Artificial intelligence; Blastocyst; Deep learning; Live birth; Machine learning; Neural network

©The Author(s) 2020. Published by Baishideng Publishing Group Inc. All rights reserved.

Core Tip: The feasibility of predicting live birth by artificial intelligence (AI) combining blastocyst images and conventional embryo evaluation parameters (CEE) is investigated because there is no human method to predict live birth from blastocyst image. Deep learning of blastocyst images is performed by using the original conventional neural network, and the elementwise layer network is used for independent CEE factors to develop a single AI classifier, the accuracy, sensitivity, specificity and area under the curve values used to predict live birth by the AI are 0.743, 0.638, 0.789, and 0.740, respectively.

Citation: Miyagi Y, Habara T, Hirata R, Hayashi N. Predicting a live birth by artificial intelligence incorporating both the blastocyst image and conventional embryo evaluation parameters. *Artif Intell Med Imaging* 2020; 1(3): 94-107

URL: <https://www.wjgnet.com/2644-3260/full/v1/i3/94.htm>

DOI: <https://dx.doi.org/10.35711/aimi.v1.i3.94>

INTRODUCTION

The achievement of live birth is the goal of assisted reproductive technology in reproductive medicine. Miscarriage or embryo developmental failure can cause cost and time loss, and bring the negative psychological outcome to the patient. Although the morphological structures have been studied, the prognosis of the developmental ability of oocytes has not yet been found^[1]. Time-lapse microscopy and conventional morphological evaluations recently studied are not sufficient to ensure the thriving of the embryo after transfer^[2]. The feasibility of investigating time-lapse imaging has not yet been established. Preimplantation genetic testing for aneuploidy^[3,4], which is an invasive procedure for embryos, is the subject of ethical considerations. Since embryos are genetically heterogeneous, the chromosomal profile of biopsy samples does not always reflect the rest of the profile^[5]. After all, no method has been established in practice to use morphological analysis and/or non-morphological analysis to predict the live birth of a blastocyst.

Recently, artificial intelligence (AI) has been developed^[6] and investigated as a diagnostic tool in reproductive medicine. *e.g.*, predicting the viability of embryos can lead to a sensitivity of 70.1% for viable embryos, and a specificity of 60.5% for non-viable embryos^[7]. A report showed that the AI classifier was used to classify images of mature blastocysts, which appeared to be the final stage prior to freezing or transfer, and the most important embryo stage for evaluating assisted reproductive technology demonstrated the potential for predicting the probability of live birth^[8]. Our report (2019) is used to apply deep learning in convolutional neural networks (CNN) to the prediction of live births^[9-12] to blastocyst images classified by maternal age,

demonstrated that the accuracy, sensitivity, specificity, positive predictive value, and negative predictive value area under the curve (AUC) were 0.732, 0.673, 0.753, 0.404, 0.862 and 0.726, respectively^[13]. To the best of our knowledge, these are unique values for predicting live birth through image recognition of blastocyst images. We have previously reported live birth predictions using multivariate logistic regression function in combination with conventional embryo evaluation (CEE) (*e.g.* maternal age, body mass index, *etc.*) and the application of deep learning, which was applied to blastocyst images that were also classified by age; this method was defined as a combination method^[13,14] in which the accuracy, sensitivity, specificity, positive predictive value, negative predictive value, and AUC value for all ages were 0.721, 0.779, 0.704, 0.400, 0.885 and 0.773, respectively (2019). This combination method seemed to be better than CEE.

AI can be trained through images and non-images (such as numbers^[15]) simultaneously. The classifier made by AI can convert data composed of image data and non-image data into a confidence score, which is an estimated probability of belonging to a target category (such as a live birth category). Therefore, when inputting images and non-images, an AI classifier trained on image and non-image data can generate confidence scores. The AI feature that can convert images into probabilities seems to be an outstanding advantage. Compared with AI classifiers trained only by images, AI classifiers trained with more information (including image and non-image data) may show better results. Then it may be necessary to investigate whether a single AI classifier of deep learning might demonstrate better predictability than the combination method when applied to both the blastocyst image and independent CEE factors, which were not classified by age but included age, to predict a live birth. Although it is necessary to use a combination method to create multiple AI classifiers, it is not necessary to classify a single AI classifier by age as an independent factor of CEE^[16,17]. Therefore, we constructed the original neural network architecture of the AI classifier as a pilot study and demonstrated the feasibility of the classifier compared with the combination method.

MATERIALS AND METHODS

Patients and data preparation

The study collected images of blastocysts with morphological features and clinical information obtained from consecutive patients at the Okayama Couples' Clinic from January 1, 2009, to April 30, 2017, with completely deidentified data were enrolled. Only elective single embryo transfer is performed. Track all blastocysts to confirm whether the result is a live birth or a non-live birth. This retrospective study was approved by the Institutional Review Board (IRB) of Okayama Couples' Clinic (IRB number 18000128-5). This non-interventional study provides patients with the option to opt-out with additional information on the clinic's website.

CEE

All blastocysts with clinical information and morphological features, such as maternal age, body mass index, past embryo transfer time, *in vitro* fertilization time, anti-Müllerian hormone value, FSH value, blastocyst grade on day 3, embryo cryopreservation day, Trophoblast grade, inner cell mass grade, number of blastomeres on the 3rd day after insemination, the average diameter of blastocysts, antral follicle count, the existence of immune sterility, the existence of oviduct infertility, the existence of endometriosis, insemination procedures, ovarian stimulation method, the grade of smooth endoplasmic reticulum cluster, degree of blastocyst expansion, presence of vacuoles, refractile body, male age, and male body mass index, were collected to evaluate the outcome of live birth *vs* non-live birth. This information was provided by doctors and embryologists engaged in clinical practice for over twenty years and who have implemented standard laboratory practices related to embryo morphological evaluations according to the 2011 international consensus meeting^[18].

The relationships between each factor in CEE and live birth were assessed. Then, we obtained univariate regression functions. Significant factors without multicollinearity which indicated a state of strong correlations between variables were selected as independent factors to predict live birth.

Blastocyst images

As a routine conventional microscopic observation at magnification of 400 times, a single clear image of the blastocyst is captured at about 115 h after insemination or about 139 h if the blastocyst is less than approximate 120 μm in diameter. According to a published report^[14], each image is cropped into a square and then saved in size of 50 \times 50 pixels to provide the best accuracy. The picture has been de-identified so as not to identify the person.

Preparation for AI

The deidentified data set included all the factors in CEE, images of the blastocysts that resulted in miscarriages, non-live births, or live births were transferred to the AI system off-line.

AI classifier

AI classification programs were developed as shown in Figure 1. AI classifiers which were made up of both CNN^[19-24] with L2 regularization^[25,26] and elementwise functions that apply a function to each element of a tensor for each factor of the CEE to obtain the probability of predicting a live birth or non-live birth, as shown in Figure 1. We introduced deep learning for images with a published CNN architecture except for a softmax layer^[14]. The CNN in the image consisted of 10 Layers with a combination of convolutional layers with multiple kernel sizes^[27-29], pooling layers^[30-33], flattened layers^[34], linear layers^[35,36] and rectified linear layers unit layers^[37,38]. On the other hand, we also performed elementwise functions that we reported for the CEE factors^[14].

Then, all tensors from the convolutional network for image and scholars by the elementwise functions for the factors of the CEE were catenated and inputted into a batch normalization layer^[39]. Then, the data was placed in a linear layer and a softmax layer^[40,41] which presented the probability of live birth or non-live birth.

The appropriate number of training datasets was investigated by evaluating the accuracies using the ten-fold cross-validation method^[42-44]. Firstly, all data were divided into test datasets and training datasets randomly in a ratio of one to nine. Four-fifths of the training data set was used as the AI training dataset. The remainder, one-fifth, of the dataset, was defined as the validation dataset. The AI training dataset, validation dataset, and non-overlapping test dataset were created in this fashion. The AI classifier was trained by an AI training dataset with concurrent validation by the validation dataset, and then the AI classifier was evaluated with the test dataset. The training dataset is augmented by rotating images, as is often performed in the AI classifier process known as data augmentation, because the blastocyst image processing with any degree of rotation can produce images, resulting in different vector data of the same category^[14]. Repeat this procedure ten times to incorporate all the data. Investigate the number of training data points until the accuracy value is the largest possible while keeping the variance of the accuracy value as small as possible. Therefore, this process can temporarily display an appropriate amount of training data to more accurately verify the prediction. Then, by varying the hyperparameters and the number of training data points, the best AI classifier showing the best accuracy was finally selected during the early stopping procedure. By comparing with the combination method, the feasibility of the new method is evaluated.

Development environment

The tools and conditions for development used are as follows: Intel Core i5 running Windows 10 (Redmond, WA, United States), 32 GB (Santa Clara, CA, United States) and NVIDIA GeForce GTX 1080 Ti (Santa Clara, CA, United States) and Wolfram Language 12.0 (Wolfram Research, Champaign, IL, United States).

Statistical analysis

Wolfram Language 12.0 is used for all statistical analyses. One-way analysis of variance test and univariate regression analysis was used. $P < 0.05$ was considered to indicate statistical significance.

RESULTS

Clinical information and morphological features

There were 5691 blastocysts, among which the outcome of live birth and non-live birth were 1587/4104, respectively. Images, morphological feature data, and clinical

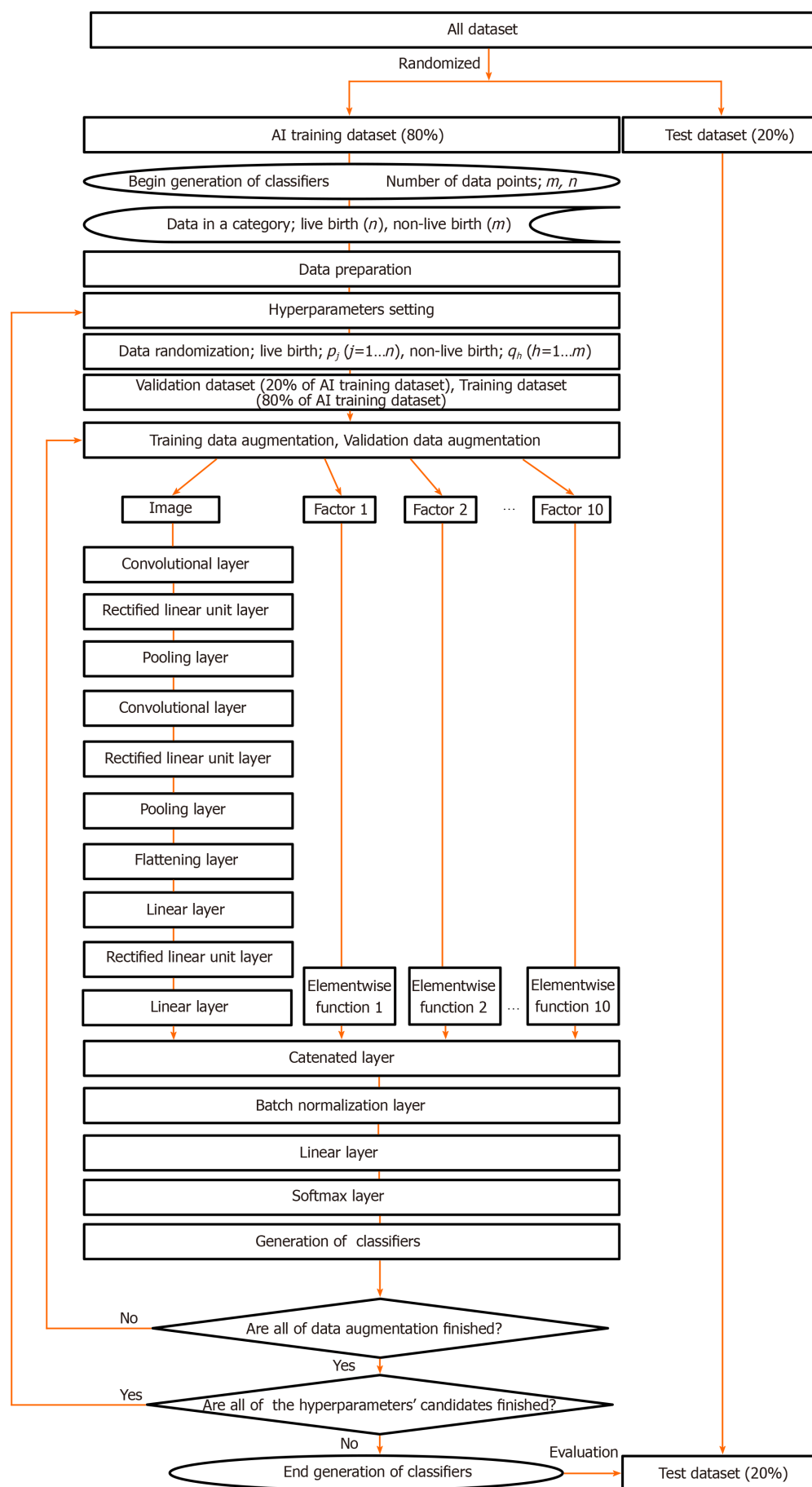


Figure 1 Flowchart for generating the artificial intelligence classifiers. The artificial intelligence classifier consisted of a combination of 10 Layers of a

convolutional neural network for an image and each elementwise layer often significant factors of the conventional embryo evaluation (CEE) that we had reported^[14]. The ten factors chosen as independent factors to predict live birth were age, the number of embryo transfers, anti-Müllerian hormone concentration, day-3 blastomere number, grade on day 3, embryo cryopreservation day, inner cell mass, trophoctoderm, average diameter, and body mass index. The functions in the elementwise layer for each factor of the CEE are shown as formulas in [Table 1](#). The image processing and ten factors of the conventional embryo evaluation tensor were combined at the catenated layer. AI: Artificial intelligence.

information were obtained. The live birth rate was 0.387. [Table 1](#) shows the independent clinical information and morphological features for predicting live births. The mean \pm SD/median/range for age, number of embryo transfers, anti-Müllerian hormone concentration (ng/mL), day-3 blastomere number, grade on day 3 (class A = 1, B = 2, C = 3, D = 4), embryo cryopreservation day (day 5 = 1, day 6 = 2), inner cell mass (A = 1, B = 2, C = 3), trophoctoderm (A = 1, B = 2, C = 3), average diameter (μ m) and body mass index (kg/m^2) were $35.75 \pm 4.78/36/20-48$; $2.75 \pm 2.36/2/1-30$; $3.91 \pm 3.54/2.94/0.0-32.2$; $8.03 \pm 1.74/8/2-17$; $1.87 \pm 0.57/2/1-4$; $1.20 \pm 0.40/1/1-2$; $1.58 \pm 0.55/2/1-3$; $2.01 \pm 0.75/2/1-3$; $154.77 \pm 24.12/153.8/81.3-242.5$; and $21.30 \pm 3.16/20.6/13.9-43.3$, respectively.

Univariate regression functions

The univariate regression functions in order to use at the elementwise layer in the neural network for each were as follows: Age, $k/[1 + \text{Exp}(\beta_0 + \beta_1 x)]$, $\beta_0 = -10.742$, $\beta_1 = 0.284$, $k = 0.451$; number of embryo transfers, $1/[1 + \text{Exp}(\beta_0 + \beta_1 x)]$, $\beta_0 = 0.635$, $\beta_1 = 0.156$; anti-Müllerian hormone concentration (ng/mL), $1/[1 + \text{Exp}(\beta_0 + \beta_1 x)]$, $\beta_0 = 1.282$, $\beta_1 = 0.062$; day-3 blastomere number, $k/(2\pi\sigma^2)^{0.5} \text{Exp}[(x-m)^2/(2\sigma^2)]$, $\sigma = 4.668$, $m = 11.624$, $k = 4.643$; grade on day 3 (class A = 1, B = 2, C = 3, D = 4), $k/[1 + \text{Exp}(\beta_0 + \beta_1 x)]$, $\beta_0 = -7.967$, $\beta_1 = 2.584$, $k = 0.319$; embryo cryopreservation day (day 5 = 1, day 6 = 2), $\beta_0 + \beta_1 x$; $\beta_0 = 0.435$, $\beta_1 = -0.131$; inner cell mass (A = 1, B = 2, C = 3), $\beta_0 + \beta_1 x$, $\beta_0 = 0.479$, $\beta_1 = -0.131$; trophoctoderm (A = 1, B = 2, C = 3), $\beta_0 + \beta_1 x$; $\beta_0 = 0.526$, $\beta_1 = -0.124$; averaged diameter (μ m), $1/[1 + \text{Exp}(\beta_0 + \beta_1 x)]$, $\beta_0 = 2.623$, $\beta_1 = -0.011$; and body mass index (kg/m^2), $1/[1 + \text{Exp}(\beta_0 + \beta_1 x)]$, $\beta_0 = -0.631$, $\beta_1 = 0.079$.

The approximate number of training data points

Overview of the accuracy profile as a function of the approximate number of training data points to study the appropriate amount of training data are shown in the left panel of [Figure 2](#). The accuracy values were classified with L2 regularization values. High accuracies were obtained when the number of training data points was between 25605 and 45468. The mean of standard deviation of each parameter in the training data set are 0.0163, 0.0090, 0.0082, 0.0075, 0.009, 0.0121, 0.0086, and 0.0071, respectively. Although there is training data, there is no significant difference in standard deviation ($P = 0.223$ by one-way analysis of variance test). The same data were converted to a two-dimensional contour plot of accuracy as a function of the number of training data points and the number of L2-regularization values (right panel in [Figure 2](#)). The brighter area that indicated higher accuracy was observed when the number of the training data points was between 25605 and 45468 and when the L2-regularization values were less than 0.1.

AI classifier

Therefore, the best AI classifier is investigated. When the number of training data points is between 25605 and 45468 and the L2-regularization values are less than 0.1, the best AI classifier will exist. Finally, the best AI classifier was obtained with 42792 training data points and 0.001 L2 regularization values. The accuracy, sensitivity, specificity, positive predictive value, negative predictive value, Youden J index^[45] and area under the curve (mean \pm SE) obtained by the AI classifier are 0.743, 0.638, 0.789, 0.573, 0.831, 0.427 and 0.740 ± 0.031 , respectively, as shown in [Table 2](#). The optimal cut-off point of the receiver operator characteristic (ROC) curve^[46] is 0.207. The classification time per case is less than 0.2 s.

DISCUSSION

Here, a single AI classifier for deep learning with CNN using blastocyst images and elementwise layers using independent factors of the morphological features and clinical information of the CEE is developed. When the patient's age is less than 39 years old, this integrated AI classifier is superior to the combination method in terms

Table 1 The morphological features and clinical information of 5691 blastocysts and the univariate regression formulas^[13] of the independent factors for predicting the probability of live birth

Independent factors	mean \pm SD	Median	Minimum	Maximum	Formulas	Coefficients
Age	35.75 \pm 4.78	36	20	48	$k/[1 + \text{Exp}(\beta_0 + \beta_1 x)]$	$\beta_0 = -10.742 \pm 4.106$ ($P = 0.0089$); $\beta_1 = 0.284 \pm 0.109$ ($P = 0.0088$); $K = 0.451$
Number of embryo transfers procedures in the past	2.75 \pm 2.36	2	1	30	$1/[1 + \text{Exp}(\beta_0 + \beta_1 x)]$	$\beta_0 = 0.635 \pm 1.158$ ($P = 0.584$); $\beta_1 = 0.156 \pm 0.123$ ($P = 0.204$)
Anti-Müllerian hormone concentration (ng/mL)	3.91 \pm 3.54	2.94	0.0	32.2	$1/[1 + \text{Exp}(\beta_0 + \beta_1 x)]$	$\beta_0 = 1.282 \pm 2.640$ ($P = 0.627$); $\beta_1 = 0.062 \pm 0.139$ ($P = 0.678$)
Day-3 blastomere number	8.03 \pm 1.74	8	2	17	$k/(2\pi\sigma^2)^{1/2} \text{Exp}(-(x-m)^2/(2\sigma^2))$	$\sigma = 4.668 \pm 0.773$ ($P = 4.179 \times 10^{-5}$); $m = 11.624 \pm 0.663$ ($P = 1.969 \times 10^{-10}$); $K = 4.643 \pm 0.611$ ($P = 3.91 \times 10^{-6}$)
Grade on day 3 (Class A = 1, B = 2, C = 3, D = 4)	1.87 \pm 0.57	2	1	4	$k/[1 + \text{Exp}(\beta_0 + \beta_1 x)]$	$\beta_0 = -7.967 \pm 8.012$ ($P = 0.320$); $\beta_1 = 2.584 \pm 2.582$ ($P = 0.317$); $K = 0.319$
Embryo cryopreservation day (Day 5 = 1, Day 6 = 2)	1.20 \pm 0.40	1	1	2	$\beta_0 + \beta_1 x$	$\beta_0 = 0.435$; $\beta_1 = -0.131$
Inner cell mass (A = 1, B = 2, C = 3)	1.58 \pm 0.55	2	1	3	$\beta_0 + \beta_1 x$	$\beta_0 = 0.479 \pm 0.037$ ($P = 0.049$); $\beta_1 = -0.131 \pm 0.017$ ($P = 0.083$)
Trophoblast (A = 1, B = 2, C = 3)	2.01 \pm 0.75	2	1	3	$\beta_0 + \beta_1 x$	$\beta_0 = 0.526 \pm 0.002$ ($P = 0.0026$); $\beta_1 = -0.124 \pm 0.001$ ($P = 0.005$)
Average diameter (μm)	154.77 \pm 24.12	153.8	81.3	242.5	$1/[1 + \text{Exp}(\beta_0 + \beta_1 x)]$	$\beta_0 = 2.623 \pm 5.312$ ($P = 0.621$); $\beta_1 = -0.011 \pm 0.030$ ($P = 0.723$)
Body mass index (kg/m^2)	21.30 \pm 3.16	20.6	13.9	43.3	$1/[1 + \text{Exp}(\beta_0 + \beta_1 x)]$	$\beta_0 = -0.631 \pm 0.844$ ($P = 0.454$); $\beta_1 = 0.079 \pm 0.035$ ($P = 0.026$)

Each formula was determined to fit the data distribution. Coefficients are shown as the mean \pm SE.

Table 2 Discrimination ability of the best classifier of the original neural network architecture comparing the combination method^[13]

Patient age (yr)	Accuracy	Sensitivity	Specificity	PPV	NPV	AUC	95%CI of the AUC	Cut-point
AI in this study								
All ages	0.743	0.638	0.789	0.573	0.831	0.740	0.681-0.801	0.207
The combination method ^[13]								
All ages	0.721	0.779	0.704	0.400	0.885	0.773	0.655-0.888	0.213
< 35	0.616	0.652	0.592	0.515	0.719	0.655	0.600-0.707	0.388
35-37	0.671	0.786	0.612	0.508	0.849	0.723	0.653-0.793	0.281
38-39	0.732	0.758	0.725	0.455	0.908	0.791	0.693-0.889	0.219
40-41	0.801	0.700	0.816	0.350	0.950	0.806	0.687-0.925	0.142
≥ 42	0.784	1.000	0.773	0.171	1.000	0.888	0.713-1.063	0.037

The number of the training data was 42792 consisted of both a blastocyst image and ten factors of conventional embryo evaluation (CEE). The value of the combination method was a function of multivariate logistic regression with CEE and artificial intelligence for predicting probability for live birth from an image of the blastocyst in patients categorized by age. The optimal cut-point of live birth was the value corresponding to the point with the lowest distance to the upper-left corner of the receiver operator characteristic curve^[46]. The accuracies, sensitivities, and specificities were obtained by using cut-points. PPV: Positive predictive value; NPV: Negative predictive value; AUC: Area under the time concentration curve.

of accuracy in predicting which embryo to transfer to obtain a live birth.

The accuracy value of predicting live birth is 0.743. We have previously reported that the accuracy values of predicting live birth through the CEE/AI/combined method are 0.631/0.647/0.616, 0.687/0.675/0.671, 0.725/0.697/0.732, 0.714/0.776/0.801 and 0.910/0.866/0.784 for the age categories of < 35, 35-37, 38-39, 40-41 and ≥ 42 years, respectively^[13]. Our report provides 0.721 ± 0.077 (mean \pm SD) as

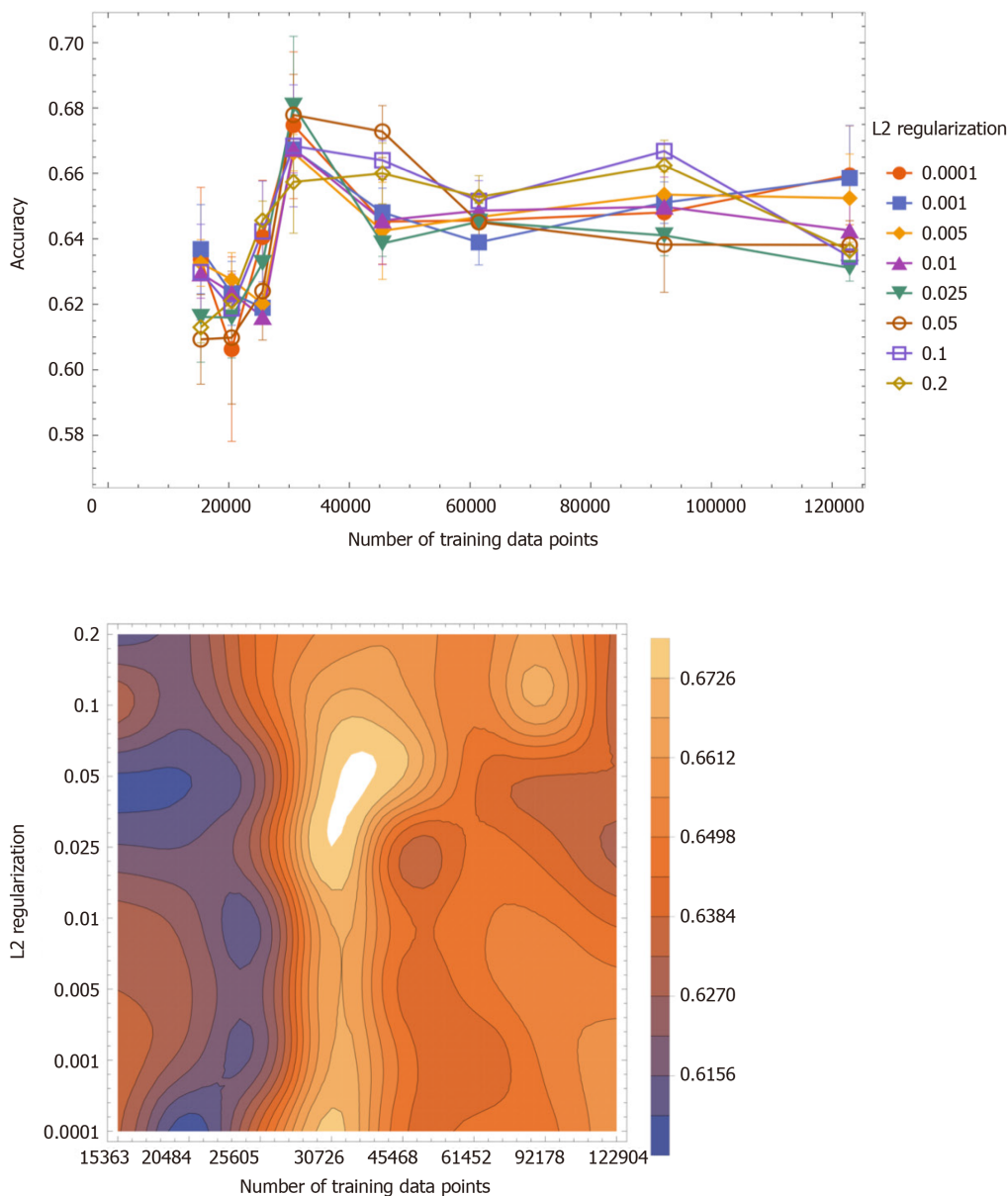


Figure 2 The accuracy value (mean \pm SD) as a function of the number of training data points. The accuracy values were classified with L2 regularization values: 0.0001, 0.001, 0.005, 0.01, 0.025, 0.05, 0.1 and 0.2. High accuracy values were obtained when the number of training data was between 25605 and 45468 (left panel). The two-dimensional contour plot of the accuracy value as a function of the training data and L2 regularization values (right panel). The brighter area indicates higher accuracy. High accuracy values were observed when the number of the training data was between 25605 and 45468 and when L2 regularization values were less than 0.1.

the accuracy value. The combination method is the multivariate logistic function, the CEE probability generated by the multivariate logistic regression, and the confidence score generated by AI and the deep learning of CNN independently. However, the AI classifier in this study used both blastocyst images and CEE factors including age. These two different methods used the same data set composed of blastocyst images and CEE factors, and there was no significant difference in accuracy ($P = 0.52$). Therefore, in this study, the accuracy value of 0.743 as a predictor of live birth seems to be close to the average accuracy of the combination method. In this study, the results on the accuracy value are superior to the combination method that was classified by maternal age (when the patient's age is less than 39 years old); when the patient's age is greater than 39 years old, the classification method is inferior. Regarding the accuracy value, if the AI classifier in this study is used, it will be better for patients younger than 39 years old, as shown in Table 2.

Although there is no other way to predict live births, compared with AI in other medical classifiers, this single AI classifier does not seem to be good enough. The accuracy value of the AI classifier has been published, and were 0.997 for the breast cancer diagnosis^[47]; 0.83-0.90 for the early diagnosis of Alzheimer's disease^[48]; 0.83 for

urological dysfunctions^[49]; 0.72^[50], 0.50^[51], 0.823^[52] and 0.941^[53] for colposcopy diagnosis; 0.83 for the orthopedic trauma diagnosis^[54]; and 0.98 for the morphological quality of blastocysts with the evaluation by the embryologist^[55]. In one report, due to the probability of live births, images of embryos classified as poor and good were scored 0.509 and 0.614, respectively^[55]. The AI classifier fails to notice clinical obstacles to achieving delivery, such as uterine factors^[56] (*e.g.*, uterine leiomyoma^[57] and endometrial polyps^[58]), endometriosis^[59], ovarian function^[60], oviduct obstruction^[61,62], immune disorders^[63,64] and the uterine microbiota^[65,66]), so the prediction of blastocyst outcome through images can never reach 100%. Therefore, in this study, using 0.743 as the accuracy value for predicting live birth, as the application of AI in medicine, seems to be a moderately good result.

The values of AUC, sensitivity, and specificity are the most important statistical data for evaluating binary classification test methods because these values are independent of the distribution of the patient. The AUC in this study was 0.740 ± 0.031 (mean \pm SE). In our report, the AUC values of predicted live births done by CEE/AI/combination methods are 0.651/0.634/0.655, 0.697/0.688/0.723, 0.771/0.728/0.791, 0.788/0.743/0.806 and 0.820/0.837/0.888 for the age categories of < 35, 35-37, 38-39, 40-41, and ≥ 42 years, respectively^[13].

The reported AUC of the combination method is 0.773 ± 0.088 (mean \pm SD). There was no significant difference between the AUC value of the AI classifier and the average AUC value of the combination method ($P = 0.41$). However, in this study, when the patient is younger than 37 years old, the results of the AUC value may be superior to the combination method, and when the patient is older than 37 years old, the results are inferior. Regarding AUC, if the AI classifier in this study is used, it will be better for patients younger than 37 years old. The published AUC value of the AI classifier with deep learning is 0.66, which can predict live birth^[13]; 0.65 predicts live birth without aneuploidy^[8]; 0.74 classifies embryos into three categories^[64]; 0.826^[52] for colposcopy by image, and 0.941^[53] for colposcopy by image combined with HPV. Therefore, in this study, as an AI application in medicine, an AUC value of 0.740 seems to be a moderately good result.

The sensitivity of this study is 0.638. In our report, the sensitivity of CEE/AI/combination method to age category is 0.580/0.530/0.652, 0.714/0.655/0.786, 0.727/0.697/0.758, 0.700/0.650/0.700, and 0.667/0.833/1.000 for the age categories of < 35, 35-37, 38-39, 40-41, and ≥ 42 years, respectively^[13]. The sensitivity of this combination method is 0.779 ± 0.134 (mean \pm SD). The sensitivity of this study is inferior to the combination method ($P < 0.019$) and lower than the combination method of any age category.

The specificity of this study was 0.789. In our report, the specificities of CEE/AI/combination methods are 0.665/0.724/0.592, 0.673/0.685/0.612, 0.725/0.697/0.725, 0.716/0.794/0.816, and 0.922/0.867/0.773 for the age categories of < 35, 35-37, 38-39, 40-41, and ≥ 42 years, respectively^[13]. The specificity of the combination method in the report is 0.704 ± 0.098 (mean \pm SD). Although there is no significant difference, the specificity of this study is superior to the combination method ($P = 0.052$). Except for 40-41 years old, the specificity of the combination method of any age category is higher.

In this study, Youden's J index^[45] was 0.427. Youden's J index (sensitivity plus specificity -1) is a statistical value that is very valuable for dichotomous diagnostic tests, and can sometimes be used for ROC analysis. In our report, the Youden's J index values of the CEE/AI/combination methods are 0.245/0.254/0.244, 0.387/0.340/0.398, 0.452/0.394/0.483, 0.416/0.444/0.516, and 0.589/0.700/0.773 for the age categories of < 35, 35-37, 38-39, 40-41, and ≥ 42 years, respectively^[13]. The combination method in the report yielded 0.483 ± 0.193 (mean \pm SD). There is no significant difference in Youden's J index ($P = 0.519$). However, in this study, the results of the Youden's J index may be superior to the combination method when the patient is younger than 37 years old, and inferior to the combination method when the patient is older than 37 years old. Regarding Youden's J index, if the AI classifier in this study is to be used, it will be better for patients younger than 37 years old. A report has been published on the Youden's J index value of the medical AI classifier. The index of LSIL/HSIL diagnosed by deep learning colposcopy is 0.682^[52] and 0.789^[53], while the index for predicting live birth is 0.30 without aneuploidy^[8].

As for the accidental evaluation and comparison of AI only used for blastocyst images^[13], its accuracy, sensitivity, specificity, positive predictive value, negative predictive value, Youden's J index, and AUC value are 0.732/0.721/0.743, 0.673/0.779/0.638, 0.753/0.704/0.789, 0.404/0.400/0.831, 0.862/0.885/0.573, 0.426/0.482/0.427 and 0.726/0.773/0.740 by AI for blastocyst image only/AI as the combination method/AI in this study. We hope that the AI or combination method in

this study will be better than other methods, but there seems to be no outstanding AI. Although the AI in this study seemed to demonstrate tendency that was superior for specificity and positive predictive value, and inferior for sensitivity and negative predictive value and AI for blastocyst image only seemed to be superior to AI in this study for negative predictive value and the value of the AUC, there was no significant superiority among the three types of AI classifiers. This result might suggest that medical imaging as the morphological features of the blastocyst was the most important among the significant parameters in the dataset. Non-image parameters may not contribute much to predicting live birth, but there is one thing. Therefore, multi-image data sets such as time-lapse photography of AI may be good candidates for predicting live births in the future. In this study, only a single image was evaluated, but it is known through time-lapse image analysis that morphology is not a static parameter, so it will be evaluated by multiple images in the future. In further research, the application of artificial intelligence consists of different neural network architectures that can process images and non-images in multiple time series at the same time, which may be better applied to time-lapse evaluation, because it has not yet shown the established method of predicting live birth. Without the intervention of more complex statistical methods, or preferably by AI applications, it may be difficult to analyze multiple data composed of images and non-images.

Not only is there no gold standard method for making neural network architectures for general targets but also images. However, the following neural networks for general image recognition have made progress: LeNet^[68] (in 1998), AlexNet^[40] (in 2012), GoogLeNet^[36] (in 2014), ResNet^[69] (in 2015), and Squeeze-and-Excitation networks^[70] (in 2017). In this study, the image of the blastocyst was analyzed using CNN, and the scholar data of CEE was converted at the elementwise layers that have a function for each factor. After connecting these outputs, by using several network layers, the probability of live birth or non-live birth can be generated at the end of the neural network through the softmax function. The AI of the neural network can evaluate not only images but also non-image data. Compared with traditional statistics, this function of artificial intelligence seems to be advanced. When evaluating images through traditional statistical data, humans should define some image features (such as morphological shape and hue) before analysis, and then extract and quantitatively convert them into tensor data. Although the criteria for extracting certain features from images are indispensable for using traditional statistical data, the universality of the definition cannot be proven. On the other hand, artificial intelligence can evaluate images without any standard to extract certain features. Therefore, it is expected that AI can predict live birth through blastocyst images and CEE factors. As far as we know, there are no reports about the simultaneous use of image and non-image data for live birth prediction.

The ability of the AI classifier neural network, which consists of the CNN for the image and elementwise functions for the scholarly values of the CEE factors in this study, was almost similar to that of the published combination method^[13]. The AI classifier in this study demonstrated insignificant superiority in terms of specificity, significant inferiority in terms of sensitivity, and similarity in terms of accuracy, Youden J index, and AUC. However, comparing the accuracy of the AI in this study and the combination method in patients aged 35 to 37 years in a validation study, the required sample size would be 9497000 with 0.05 and 0.20 alpha and beta errors, respectively. Also, for the AI classifier of the neural network composed of CNN for the image and some networks for the non-image data, modifications in the network architecture, hyperparameters, and an increase in the number of datasets are expected. Although further prospective studies may be required, this AI model appeared to have the potential for clinical applicability. Also, this AI classifier was a single classifier that could be easier to improve in the future, although the five AI classifier combination method would be more difficult to improve because it would require a data set for each age category, resulting in a higher number of data sets would lead. The AI classifier can display the ranking of the blastocysts to predict a live birth with decimal places, and it helps embryologists and clinicians select the blastocyst for embryo transfer. There can be a quick diagnosis of the prediction over a distance without expensive equipment when the image and CEE parameters are transmitted over the internet.

Since there is theoretically an infinite number of probabilities for the construction of the neural network architecture and numerous combinations of statistical functions, further investigations for patients are worthwhile. By selecting the hyperparameters and setting the random seed value within the program in various ways, the result can be changed, *e.g.*, the prediction accuracy can be a little better or a little worse. Similar statements can be made about the dataset. If one uses the same deep neural network

architecture and a different training dataset, for example, provided by a different institute, the prediction accuracy differs. This is one of the aspects of current AI technology. The AI in this study had not been tested for external data as an institutional joint research to validate the generalization ability. In the field of AI technology, a critical statistical method for evaluating the relative superiority of predictive ability between two classifiers is not well established. Therefore, at least the clear superiority in prediction accuracy, the advantages of the network architecture, or a wider variety of datasets that were included in the analysis should be considered before conventional practical use. To improve the AI classifier in the future and to examine not only conventional static values such as accuracy, but also robustness, stability, and reliability. It may be necessary to use the multiple-image data of blastocytes obtained by time-lapse methods from other institutes to evaluate the prediction accuracy, the increased amount of data, novel non-image data that would be significant and not yet discovered, such as genetic information or some patient biomarkers in the future, and the incorporation of the vastly improved neural network architecture.

CONCLUSION

Deep learning with a CNN for a blastocyst image and with networks of elementwise layers for independent CEE factors were used to develop the single AI classifier for predicting the probability of live birth. Due to the development of AI that does not harm the embryo, the embryo can be transferred after making the prediction. AI could bring benefits to the advancement of assisted reproductive technology.

ARTICLE HIGHLIGHTS

Research background

To acquire live births is the goal of assisted reproductive technology. No method has been established in practice to use non-morphological analysis and/or morphological analysis such as conventional morphological evaluations and time-lapse microscopy to predict the live birth of a blastocyst.

Research motivation

Artificial intelligence (AI) classifiers for blastocyst images to predict the live birth has been introduced in reproductive medicine recently.

Research objectives

The present study aimed to develop an AI classifier that combines blastocyst images and the morphological features and clinical information of the conventional embryo evaluation parameters such as maternal age to predict the probability of achieving a live birth.

Research methods

A total of 5691 images of blastocysts combined with conventional embryo evaluation parameters were used. A system in which the original architecture of the deep learning neural network was developed to predict the probability of live birth.

Research results

The number of independent clinical information for predicting live birth is 10. The best single AI classifier composed of ten layers of convolutional neural networks and each elementwise layer of ten factors was developed and obtained with 42792 as the number of training data points and 0.001 as the L2 regularization value. The accuracy, sensitivity, specificity, negative predictive value, positive predictive value, Youden J index, and area under the curve values for predicting live birth were 0.743, 0.638, 0.789, 0.831, 0.573, 0.427, and 0.740, respectively.

Research conclusions

AI classifiers have the potential of predicting live births that humans cannot predict. AI that can be trained by both morphological and non-morphological information may make progress in assisted reproductive technology.

Research perspectives

Due to the development of AI that does not harm the embryo, the embryo can be transferred after making the prediction. AI could bring benefits to the advancement of assisted reproductive technology.

ACKNOWLEDGEMENTS

The authors would like to express their sincere gratitude to the anonymous reviewers for their useful comments and suggestions on how to improve the quality of this paper.

REFERENCES

- 1 **Rienzi L**, Vajta G, Ubaldi F. Predictive value of oocyte morphology in human IVF: a systematic review of the literature. *Hum Reprod Update* 2011; **17**: 34-45 [PMID: 20639518 DOI: 10.1093/humupd/dmq029]
- 2 **Kirkegaard K**, Ahlström A, Ingerslev HJ, Hardarson T. Choosing the best embryo by time lapse versus standard morphology. *Fertil Steril* 2015; **103**: 323-332 [PMID: 25527231 DOI: 10.1016/j.fertnstert.2014.11.003]
- 3 **Dahdouh EM**, Balayla J, Audibert F; Genetics Committee; Wilson RD; Audibert F; Brock JA; Campagnolo C; Carroll J; Chong K; Gagnon A; Johnson JA; MacDonald W; Okun N; Pastuck M; Vallée-Pouliot K. Technical Update: Preimplantation Genetic Diagnosis and Screening. *J Obstet Gynaecol Can* 2015; **37**: 451-463 [PMID: 26168107 DOI: 10.1016/s1701-2163(15)30261-9]
- 4 **Brezina PR**, Kutteh WH. Clinical applications of preimplantation genetic testing. *BMJ* 2015; **350**: g7611 [PMID: 25697663 DOI: 10.1136/bmj.g7611]
- 5 **Gleicher N**, Metzger J, Croft G, Kushnir VA, Albertini DF, Barad DH. A single trophectoderm biopsy at blastocyst stage is mathematically unable to determine embryo ploidy accurately enough for clinical use. *Reprod Biol Endocrinol* 2017; **15**: 33 [PMID: 28449669 DOI: 10.1186/s12958-017-0251-8]
- 6 **Miyagi Y**, Fujiwara K, Oda T, Miyake T, Coleman RL. Development of New Method for the Prediction of Clinical Trial Results Using Compressive Sensing of Artificial Intelligence. *J Biostat Biometric App* 2018; **3**: 203
- 7 **VerMilyea M**, Hall JMM, Diakiw SM, Johnston A, Nguyen T, Perugini D, Miller A, Picou A, Murphy AP, Perugini M. Development of an artificial intelligence-based assessment model for prediction of embryo viability using static images captured by optical light microscopy during IVF. *Hum Reprod* 2020; **35**: 770-784 [PMID: 32240301 DOI: 10.1093/humrep/deaa013]
- 8 **Miyagi Y**, Habara T, Hirata R, Hayashi N. Feasibility of artificial intelligence for predicting live birth without aneuploidy from a blastocyst image. *Reprod Med Biol* 2019; **18**: 204-211 [PMID: 30996684 DOI: 10.1002/rmb2.12267]
- 9 **Fukushima K**. Neocognitron: a self organizing neural network model for a mechanism of pattern recognition unaffected by shift in position. *Biol Cybern* 1980; **36**: 193-202 [PMID: 7370364 DOI: 10.1007/BF00344251]
- 10 **Hubel DH**, Wiesel TN. Receptive fields and functional architecture of monkey striate cortex. *J Physiol* 1968; **195**: 215-243 [PMID: 4966457 DOI: 10.1113/jphysiol.1968.sp008455]
- 11 **Hubel DH**, Wiesel TN. Receptive fields of single neurones in the cat's striate cortex. *J Physiol* 1959; **148**: 574-591 [PMID: 14403679 DOI: 10.1113/jphysiol.1959.sp006308]
- 12 **Schmidhuber J**. Deep learning in neural networks: an overview. *Neural Netw* 2015; **61**: 85-117 [PMID: 25462637 DOI: 10.1016/j.neunet.2014.09.003]
- 13 **Miyagi Y**, Habara T, Hirata R, Hayashi N. Feasibility of predicting live birth by combining conventional embryo evaluation with artificial intelligence applied to a blastocyst image in patients classified by age. *Reprod Med Biol* 2019; **18**: 344-356 [PMID: 31607794 DOI: 10.1002/rmb2.12284]
- 14 **Miyagi Y**, Habara T, Hirata R, Hayashi N. Feasibility of deep learning for predicting live birth from a blastocyst image in patients classified by age. *Reprod Med Biol* 2019; **18**: 190-203 [PMID: 30996683 DOI: 10.1002/rmb2.12266]
- 15 **Miyagi Y**, Miyake T. Potential of deep learning for predicting fetal weight of Japanese. *Acta Med Okayama* 2020; In press
- 16 **Weiss RV**, Clapauch R. Female infertility of endocrine origin. *Arq Bras Endocrinol Metabol* 2014; **58**: 144-152 [PMID: 24830591 DOI: 10.1590/0004-2730000003021]
- 17 **Shirasuna K**, Iwata H. Effect of aging on the female reproductive function. *Contracept Reprod Med* 2017; **2**: 23 [PMID: 29201428 DOI: 10.1186/s40834-017-0050-9]
- 18 **Alpha Scientists in Reproductive Medicine and ESHRE Special Interest Group of Embryology**. The Istanbul consensus workshop on embryo assessment: proceedings of an expert meeting. *Hum Reprod* 2011; **26**: 1270-1283 [PMID: 21502182 DOI: 10.1093/humrep/der037]
- 19 **Bengio Y**, Courville A, Vincent P. Representation learning: a review and new perspectives. *IEEE Trans Pattern Anal Mach Intell* 2013; **35**: 1798-1828 [PMID: 23787338 DOI: 10.1109/TPAMI.2013.50]
- 20 **LeCun YA**, Bottou L, Orr GB, Müller KR. Efficient Backprop. In: Montavon G, Orr GB, Müller KR, editors. Neural networks: Tricks of the trade. Berlin, Heidelberg: Springer, 2012: 9-48 [DOI: 10.1007/978-3-642-35289-8_3]
- 21 **LeCun Y**, Bottou L, Bengio Y, Haffner P. Gradient-Based Learning Applied to Document Recognition. *Proc IEEE* 1998; **86**: 2278-2324 [DOI: 10.1109/5.726791]
- 22 **LeCun Y**, Boser B, Denker JS, Henderson D, Howard RE, Hubbard W, Jackel LD. Backpropagation Applied to Handwritten Zip Code Recognition. *Neural Comput* 1989; **1**: 541-551 [DOI: 10.1162/neco.1989.1.4.541]

- 10.1162/neco.1989.1.4.541]
- 23 **Serre T**, Wolf L, Bileschi S, Riesenhuber M, Poggio T. Robust object recognition with cortex-like mechanisms. *IEEE Trans Pattern Anal Mach Intell* 2007; **29**: 411-426 [PMID: 17224612 DOI: 10.1109/TPAMI.2007.56]
 - 24 **Wiatowski T**, Bölcskei H. A Mathematical Theory of Deep Convolutional Neural Networks for Feature Extraction. *IEEE Trans Inf Theory* 2017; **64**: 1845-1866 [DOI: 10.1109/TIT.2017.2776228]
 - 25 **Srivastava N**, Hinton G, Krizhevsky A, Sutskever I, Salakhutdinov R. Dropout: A Simple Way to Prevent Neural Networks from Overfitting. *J Mach Learn Res* 2014; **15**: 1929-1958
 - 26 **Nowlan SJ**, Hinton GE. Simplifying Neural Networks by Soft Weight-Sharing. *Neural Comput* 1992; **4**: 473-493 [DOI: 10.1162/neco.1992.4.4.473]
 - 27 **Bengio Y**. Learning Deep Architectures for AI, Founds Trends® in Mach Learn. Boston: Now Publishers Inc, 2009: 1-127
 - 28 **Mutch J**, Lowe DG. Object Class Recognition and Localization Using Sparse Features with Limited Receptive Fields. *Int J Comput Vis* 2008; **80**: 45-57 [DOI: 10.1007/s11263-007-0118-0]
 - 29 **Neal RM**. Connectionist Learning of Belief Networks. *Artif Intell* 1992; **56**: 71-113 [DOI: 10.1016/0004-3702(92)90065-6]
 - 30 **Ciresan DC**, Meier U, Masci J, Gambardella LM, Schmidhuber J. Flexible, High Performance Convolutional Neural Networks for Image Classification. Proceedings of the Twenty-Second International Joint Conference on Artificial Intelligence; July 16-22; Barcelona, Spain. Menlo Park: AAAI Press, 2011: 1237-1242
 - 31 **Scherer D**, Müller A, Behnke S. Evaluation of Pooling Operations in Convolutional Architectures for Object Recognition. In: Diamantaras K, Duch W, Iliadis LS, editors. Artificial Neural Networks – ICANN 2010. Lecture Notes in Computer Science. Berlin, Heidelberg: Springer, 2010: 92-101 [DOI: 10.1007/978-3-642-15825-4_10]
 - 32 **Huang FJ**, LeCun Y. Large-Scale Learning with Svm and Convolutional for Generic Object Categorization. In: 2006 IEEE Computer Society Conference on Computer Vision and Pattern Recognition; 2006 June 17-22; New York, USA. IEEE, 2006: 284-291 [DOI: 10.1109/CVPR.2006.164]
 - 33 **Jarrett K**, Kavukcuoglu K, Ranzato M, LeCun Y. What Is the Best Multi-Stage Architecture for Object Recognition? In: 2009 IEEE 12th international conference on computer vision; 2009 Sep 29-Oct 2; Kyoto, Japan; IEEE, 2009: 2146-2153 [DOI: 10.1109/ICCV.2009.5459469]
 - 34 **Zheng Y**, Liu Q, Chen E, Ge Y, Zhao JL. Time Series Classification Using Multi-Channels Deep Convolutional Neural Networks. In: Li F, Li G, Hwang S, Yao B, Zhang Z, editors. Web-Age Information Management. WAIM 2014. Lecture Notes in Computer Science. Cham: Springer, 2014: 298-310 [DOI: 10.1007/978-3-319-08010-9_33]
 - 35 **Mnih V**, Kavukcuoglu K, Silver D, Rusu AA, Veness J, Bellemare MG, Graves A, Riedmiller M, Fidjeland AK, Ostrovski G, Petersen S, Beattie C, Sadik A, Antonoglou I, King H, Kumaran D, Wierstra D, Legg S, Hassabis D. Human-level control through deep reinforcement learning. *Nature* 2015; **518**: 529-533 [PMID: 25719670 DOI: 10.1038/nature14236]
 - 36 **Szegedy C**, Liu W, Jia Y, Sermanet P, Reed S, Anguelov D, Erhan D, Vanhoucke V, Rabinovich A. Going Deeper with Convolutions. Proceedings of the IEEE conference on computer vision and pattern recognition; 2015 June 7-12; Boston, USA. Computer Vision Foundation, 2015: 1-9
 - 37 **Glorot X**, Bordes A, Bengio Y. Deep Sparse Rectifier Neural Networks. Proceedings of the Fourteenth International Conference on Artificial Intelligence and Statistics (AISTATS) 2011; 2011 Apr 11-13; Lauderdale, USA. AISTATS, 2011: 315-323
 - 38 **Nair V**, Hinton GE. Rectified Linear Units Improve Restricted Boltzmann Machines. Proceedings of the 27th international conference on machine learning (ICML-10); 2010 June 21-24; Haifa, Israel. Omni press, 2010: 807-814
 - 39 **Ioff, S**, Szegedy C. Batch Normalization: Accelerating Deep Network Training by Reducing Internal Covariate Shift. Available from: <https://arxiv.org/abs/1502.03167v3>
 - 40 **Krizhevsky A**, Sutskever I, Hinton GE. Imagenet Classification with Deep Convolutional Neural Networks. In: Pereira F, Burges CJC, Bottou L, Weinberger KQ, editors. Proceedings of the 25th International Conference on Neural Information Processing Systems; 2012 Dec 3-8; Lake Tahoe, USA. Red Hook: Curran Associates Inc., 2012: 1097-1105
 - 41 **Bridle JS**. Probabilistic Interpretation of Feedforward Classification Network Outputs, with Relationships to Statistical Pattern Recognition. In: Soulié FF, Héroult J, editors. Neurocomputing. Berlin, Heidelberg: Springer, 1990: 227-236 [DOI: 10.1007/978-3-642-76153-9_28]
 - 42 **Kohavi R**. A Study of Cross-Validation and Bootstrap for Accuracy Estimation and Model Selection. In: Proceedings of the 14th international joint conference on Artificial intelligence; 1995 Aug 20-25; Montreal, Canada. San Francisco: Morgan Kaufmann Publishers Inc, 1995: 1137-1145
 - 43 **Schaffer C**. Selecting a Classification Method by Cross-Validation. *Mach Learn* 1993; **13**: 135-143 [DOI: 10.1007/BF00993106]
 - 44 **Refaeilzadeh P**, Tang L, Liu H. Cross-validation. In: Liu, L, Özsu, MT, editors. Encyclopedia of database systems. New York: Springer, 2009: 532-538
 - 45 **Youden WJ**. Index for rating diagnostic tests. *Cancer* 1950; **3**: 32-35 [PMID: 15405679 DOI: 10.1002/1097-0142(1950)3:1<32::AID-CNCR2820030106>3.0.CO;2-3]
 - 46 **Unal I**. Defining an Optimal Cut-Point Value in ROC Analysis: An Alternative Approach. *Comput Math Methods Med* 2017; **2017**: 3762651 [PMID: 28642804 DOI: 10.1155/2017/3762651]
 - 47 **Litjens G**, Sánchez CI, Timofeeva N, Hermsen M, Nagtegaal I, Kovacs I, Hulsbergen-van de Kaa C, Bult P, van Ginneken B, van der Laak J. Deep learning as a tool for increased accuracy and efficiency of histopathological diagnosis. *Sci Rep* 2016; **6**: 26286 [PMID: 27212078 DOI: 10.1038/srep26286]
 - 48 **Ortiz A**, Munilla J, Górriz JM, Ramírez J. Ensembles of Deep Learning Architectures for the Early Diagnosis of the Alzheimer's Disease. *Int J Neural Syst* 2016; **26**: 1650025 [PMID: 27478060 DOI: 10.1142/S0129065716500258]
 - 49 **Gil D**, Johnsson M, Chamizo JMG, Paya AS, Fernandez DR. Application of Artificial Neural Networks in the Diagnosis of Urological Dysfunctions. *Expert Syst Appl* 2009; **36**: 5754-5760 [DOI:

- 10.1016/j.eswa.2008.06.065]
- 50 **Simões PW**, Izumi NB, Casagrande RS, Venson R, Veronezi CD, Moretti GP, da Rocha EL, Cechinel C, Ceretta LB, Comunello E, Martins PJ, Casagrande RA, Snoeyer ML, Manenti SA. Classification of images acquired with colposcopy using artificial neural networks. *Cancer Inform* 2014; **13**: 119-124 [PMID: 25374454 DOI: 10.4137/CIN.S17948]
 - 51 **Sato M**, Horie K, Hara A, Miyamoto Y, Kurihara K, Tomio K, Yokota H. Application of deep learning to the classification of images from colposcopy. *Oncol Lett* 2018; **15**: 3518-3523 [PMID: 29456725 DOI: 10.3892/ol.2018.7762]
 - 52 **Miyagi Y**, Takehara K, Miyake T. Application of deep learning to the classification of uterine cervical squamous epithelial lesion from colposcopy images. *Mol Clin Oncol* 2019; **11**: 583-589 [PMID: 31692958 DOI: 10.3892/mco.2019.1932]
 - 53 **Miyagi Y**, Takehara K, Nagayasu Y, Miyake T. Application of deep learning to the classification of uterine cervical squamous epithelial lesion from colposcopy images combined with HPV types. *Oncol Lett* 2020; **19**: 1602-1610 [PMID: 31966086 DOI: 10.3892/ol.2019.11214]
 - 54 **Olczak J**, Fahlberg N, Maki A, Razavian AS, Jilert A, Stark A, Sköldenberg O, Gordon M. Artificial intelligence for analyzing orthopedic trauma radiographs. *Acta Orthop* 2017; **88**: 581-586 [PMID: 28681679 DOI: 10.1080/17453674.2017.1344459]
 - 55 **Khosravi P**, Kazemi E, Zhan Q, Malmsten JE, Toschi M, Zisimopoulos P, Sigaras A, Lavery S, Cooper LAD, Hickman C, Meseguer M, Rosenwaks Z, Elemento O, Zaninovic N, Hajirasouliha I. Deep learning enables robust assessment and selection of human blastocysts after in vitro fertilization. *NPJ Digit Med* 2019; **2**: 21 [PMID: 31304368 DOI: 10.1038/s41746-019-0096-y]
 - 56 **Sanders B**. Uterine factors and infertility. *J Reprod Med* 2006; **51**: 169-176 [PMID: 16674011]
 - 57 **Ikhena DE**, Bulun SE. Literature Review on the Role of Uterine Fibroids in Endometrial Function. *Reprod Sci* 2018; **25**: 635-643 [PMID: 28826369 DOI: 10.1177/1933719117725827]
 - 58 **Taylor E**, Gornel V. The uterus and fertility. *Fertil Steril* 2008; **89**: 1-16 [PMID: 18155200 DOI: 10.1016/j.fertnstert.2007.09.069]
 - 59 **Tomassetti C**, D'Hooghe T. Endometriosis and infertility: Insights into the causal link and management strategies. *Best Pract Res Clin Obstet Gynaecol* 2018; **51**: 25-33 [PMID: 30245115 DOI: 10.1016/j.bpobgyn.2018.06.002]
 - 60 **Christ JP**, Gunning MN, Palla G, Eijkemans MJC, Lambalk CB, Laven JSE, Fauser BCJM. Estrogen deprivation and cardiovascular disease risk in primary ovarian insufficiency. *Fertil Steril* 2018; **109**: 594-600.e1 [PMID: 29605405 DOI: 10.1016/j.fertnstert.2017.11.035]
 - 61 **Arronet GH**, Eduljee SY, O'Brien JR. A nine-year survey of Fallopian tube dysfunction in human infertility. *Fertil Steril* 1969; **20**: 903-918 [PMID: 5361465 DOI: 10.1016/s0015-0282(16)37205-3]
 - 62 **Segars JH**, Herbert CM 3rd, Moore DE, Hill GA, Wentz AC, Winfield AC. Selective fallopian tube cannulation: initial experience in an infertile population. *Fertil Steril* 1990; **53**: 357-359 [PMID: 2298319 DOI: 10.1016/s0015-0282(16)53296-8]
 - 63 **Practice Committee of the American Society for Reproductive Medicine**. The role of immunotherapy in in vitro fertilization: a guideline. *Fertil Steril* 2018; **110**: 387-400 [PMID: 30098685 DOI: 10.1016/j.fertnstert.2018.05.009]
 - 64 **Hong YH**, Kim SJ, Moon KY, Kim SK, Jee BC, Lee WD, Kim SH. Impact of presence of antiphospholipid antibodies on in vitro fertilization outcome. *Obstet Gynecol Sci* 2018; **61**: 359-366 [PMID: 29780778 DOI: 10.5468/ogs.2018.61.3.359]
 - 65 **Moreno I**, Simon C. Relevance of assessing the uterine microbiota in infertility. *Fertil Steril* 2018; **110**: 337-343 [PMID: 30098680 DOI: 10.1016/j.fertnstert.2018.04.041]
 - 66 **Kroon SJ**, Ravel J, Huston WM. Cervicovaginal microbiota, women's health, and reproductive outcomes. *Fertil Steril* 2018; **110**: 327-336 [PMID: 30098679 DOI: 10.1016/j.fertnstert.2018.06.036]
 - 67 **Campbell A**, Fishel S, Bowman N, Duffy S, Sedler M, Thornton S. Retrospective analysis of outcomes after IVF using an aneuploidy risk model derived from time-lapse imaging without PGS. *Reprod Biomed Online* 2013; **27**: 140-146 [PMID: 23683847 DOI: 10.1016/j.rbmo.2013.04.013]
 - 68 **LeCun Y**, Haffner P, Bottou L, Bengio Y. Object Recognition with Gradient-Based Learning. In: Forsyth DA, Mundy JL, di Gesù V, Cipolla R. Shape, contour and grouping in computer vision. Lecture Notes in Computer Science 1681. Berlin, Heidelberg: Springer, 1999: 319-345 [DOI: 10.1007/3-540-46805-6_19]
 - 69 **He K**, Zhang X, Ren S, Sun J. Deep Residual Learning for Image Recognition. In: Proceedings of the IEEE conference on computer vision and pattern recognition; 2016 June 27-30; Las Vegas, USA. IEEE, 2016: 770-778 [DOI: 10.1109/CVPR.2016.90]
 - 70 **Hu J**, Shen L, Sun G. Squeeze-and-Excitation Networks. In: Proceedings of the IEEE conference on computer vision and pattern recognition; 2018 June 18-23; Salt Lake City, USA. IEEE, 2018: 7132-7141 [DOI: 10.1109/CVPR.2018.00745]



Published by **Baishideng Publishing Group Inc**
7041 Koll Center Parkway, Suite 160, Pleasanton, CA 94566, USA

Telephone: +1-925-3991568

E-mail: bpgoffice@wjgnet.com

Help Desk: <https://www.f6publishing.com/helpdesk>

<https://www.wjgnet.com>

